
Perovskite oxyfluorides: A study on the topochemical fluorination of the Ba-Fe-O model system for possible SOFC cathode applications

Zur Erlangung des Grades eines Doktors der Naturwissenschaften (Dr. rer. nat.)
Genehmigte kumulative Dissertation von Stephan Wollstadt aus Offenbach am Main
Tag der Einreichung: 29.6.2021, Tag der Prüfung: 31.8.2021

1. Gutachten: Prof. Dr. Oliver Clemens
2. Gutachten: Prof. Dr. Wolfgang Ensinger
Darmstadt



TECHNISCHE
UNIVERSITÄT
DARMSTADT

Materials and Earth
Sciences Department
Materialdesign durch
Synthese

Perovskite oxyfluorides: A study on the topochemical fluorination of the Ba-Fe-O model system for possible SOFC cathode applications

Accepted cumulative doctoral thesis by Stephan Wollstadt

1. Review: Prof. Dr. Oliver Clemens
2. Review: Prof. Dr. Wolfgang Ensinger

Date of submission: 29.6.2021

Date of thesis defense: 31.8.2021

Darmstadt

Bitte zitieren Sie dieses Dokument als:

URN: urn:nbn:de:tuda-tuprints-urn:nbn:de:tuda-tuprints-197805

URL: <http://tuprints.ulb.tu-darmstadt.de/19780>

DOI: <https://doi.org/>-

Dieses Dokument wird bereitgestellt von tuprints,

E-Publishing-Service der TU Darmstadt

<http://tuprints.ulb.tu-darmstadt.de>

tuprints@ulb.tu-darmstadt.de

Available under only the rights of use according to UrhG.

”A scientist in his laboratory is not a mere technician: he is also a child confronting natural phenomena that impress him as though they were fairy tales.”
– Marie Curie

Erklärungen laut Promotionsordnung

§8 Abs. 1 lit. c PromO

Ich versichere hiermit, dass die elektronische Version meiner Dissertation mit der schriftlichen Version übereinstimmt.

§8 Abs. 1 lit. d PromO

Ich versichere hiermit, dass zu einem vorherigen Zeitpunkt noch keine Promotion versucht wurde. In diesem Fall sind nähere Angaben über Zeitpunkt, Hochschule, Dissertationsthema und Ergebnis dieses Versuchs mitzuteilen.

§9 Abs. 1 PromO

Ich versichere hiermit, dass die vorliegende Dissertation selbstständig und nur unter Verwendung der angegebenen Quellen verfasst wurde.

§9 Abs. 2 PromO

Die Arbeit hat bisher noch nicht zu Prüfungszwecken gedient.

Darmstadt, 29.6.2021

S. Wollstadt

Zusammenfassung

Gegenstand dieser kumulativen Doktorarbeit war die Untersuchung topochemischer Modifikationen des anionischen Teilgitters im kubischen Perowskittyp $\text{BaFeO}_{2.5}$ innerhalb des Ba-Fe-O-F Modellsystems. Der Fokus lag auf der topochemischen Fluorierung des reinen Oxids zusammen mit einer umfassenden Untersuchung der kinetischen, magnetischen und elektrochemischen Eigenschaften des Oxyfluoridsystems $\text{BaFeO}_{2.5-x/2}\text{F}_x$ ($x = 0, 0.333, 1$). Oxyfluoride könnten eine Lösung sein hin zum Betrieb von Festoxid-Brennstoffzellen bei mittleren oder sogar niedrigen Temperaturen, da durch die Fluorierung die Aktivierungsenergie für die Sauerstoffreduktionsreaktion im Kathodenmaterial verringert sowie die Leitung von Sauerstoffionen erhöht werden kann. Aber auch die topochemische Oxidation führte zu einem neuen Einblick in mögliche Koordinationen des Übergangsmetallkations $\text{Fe}^{3+/4+}$ zusammen mit mehreren Redox-Phasenübergängen unter oxidierender Atmosphäre in Kombination mit der Ausordnung von Sauerstoffvakanzan. Das Ba-Fe-O-F System wurde als Modellsystem gewählt aufgrund des bereits vorhandenen Wissens über fluorierete Phasen innerhalb des Systems und ihrer Struktur in Abhängigkeit zur Fluorstöchiometrie. Das Ba-Fe-O-System zeigt verschiedene Modifikationen vom Perowskittyp mit variierender Sauerstoffstöchiometrie im Bereich von $2,5 < x < 3$, ausgehend von BaFeO_x , mit entsprechenden Oxidationsstufen von $\text{Fe}^{3+/4+}$. Die Verbindungen, welche auf einer kubischen Struktur basieren, können mithilfe Gruppen-Untergruppen-Beziehungen beschrieben werden, wobei die Raumgruppe $Pm\bar{3}m$ die Aristotypstruktur ist. Bisher haben alle diese Verbindungen eine 5- oder 6-fach Koordination des Fe^{4+} -Kations gemein. Es konnte eine neue Modifikation von $\text{Ba}_3\text{Fe}_3\text{O}_8$ ($\text{BaFeO}_{2.667}$) identifiziert werden, welche in der $P2_1/m$ -Raumgruppe kristallisiert und ein Fe^{4+} -Kation in einer 4-fachen Koordinationsumgebung, einem Tetraeder, aufweist. Bisher wurde der $\text{Fe}^{4+}\text{O}_4^{4-}$ -Tetraeder nur für einige andere oxidische Verbindungen außerhalb der Perovskitfamilie gefunden. Innerhalb des Tetraeders nimmt das Fe^{4+} den High-Spin-Zustand mit einer elektronischen Konfiguration $e^2t_2^2$ an und hat einen Gesamtspin von $S = 2$. Ferner wurde gezeigt, dass diese Verbindung isotypisch zu der bereits veröffentlichten und gut beschriebenen Oxyfluoridverbindung $\text{Ba}_3\text{Fe}_3\text{O}_7\text{F}$ ($\text{BaFeO}_{2.333}\text{F}_{0.333}$) ist, welche dieselbe Raumgruppe und Superzelle mit ähnlichen Gitterparametern und Atompositionen aufweist. Daraus lässt sich folgern, dass das Konnektivitätsschema und die Koordinierung der Sauerstoffpolyeder und Eisenkationen

in der Formel $\text{Ba}_3(\text{Fe}^{3+}\text{O}_{6/2})(\text{Fe}^{3+}\text{O}_{5/2})(\text{Fe}^{4+}\text{O}_{3/2}\text{O}_{1/1})$ zusammengefasst werden kann. Die kinetischen Untersuchungen der Interdiffusionsreaktion von $\text{BaFeO}_{2.5}$ und BaFeO_2F zur Bildung von $\text{BaFeO}_{2.333}\text{F}_{0.333}$ wurden mithilfe von in-situ Röntgenbeugung bei verschiedenen Temperaturen unter isothermen experimentellen Bedingungen durchgeführt. Die relativen Gewichtsanteile der beteiligten Phasen wurden durch quantitative Rietveld-Verfeinerungen extrahiert und somit konnte der Reaktionsverlauf über die Zeit abgebildet werden. Die kinetische Analyse ergab eine Reaktion erster Ordnung mit temperaturabhängigen Diffusionswegen und Kristallisationsprozessen. Die Anwendung eines Diffusionsmodells basierend auf der Boltzmann-Matano-Methode und das quadratische Mittel der Eindringtiefe führte zur Berechnung eines Interdiffusionskoeffizienten. Dies ermöglichte die Bestimmung des Sauerstoffions als geschwindigkeitsbestimmendes Anion dieser Interdiffusionsreaktion. Der eher einfache Ansatz auf Basis der Röntgenbeugung ergab aufschlussreiche Einblicke in die Reaktionskinetik der Interdiffusion in Oxyfluoriden.

Da Oxyfluoride die Verwendung von Brennstoffzellen bei mittleren und niedrigen Temperaturen ermöglichen könnten, wurde der Einfluss der topochemischen Fluorierung auf elektrochemische und auch magnetische Eigenschaften untersucht. Zu diesem Zweck wurden symmetrische Filme mit den Zusammensetzungen $\text{BaFeO}_{2.5-x/2}\text{F}_x$ ($x = 0, 0.333, 1$) als Kathodenmaterialien synthetisiert und elektrochemisch untersucht. Zur Einstellung eines spezifischen Fluorgehalts des Films wurde eine neue Methode durch Interdiffusion entwickelt. Eine partielle Fluorierung der Kathode ($\text{BaFeO}_{2.333}\text{F}_{0.333}$) führte zu einer Änderung des limitierenden Prozesses, von der Sauerstoffionenleitung durch das Material hin zur Limitierung durch die Sauerstoffreduktion und -inkorporation an der verfügbaren Oberfläche. Auf der anderen Seite zeigte die vollständig fluorierte Kathode (BaFeO_2F) eine um mehrere Größenordnung geringere Sauerstoffionenleitung, was auf die Nichtexistenz von Sauerstofffehlstellen zurückzuführen ist, welche für die Aufnahme von Sauerstoff aus der Atmosphäre und die Leitung von Sauerstoffionen erforderlich sind.

Die Anpassung der magnetischen Eigenschaften durch topochemische Fluorierung wurde an dünnen Filmen aus BaFeO_2F untersucht und mit Filmen aus $\text{BaFeO}_{2.5}$ verglichen. Die oxidischen Filme wurden mit PLD epitaktisch auf SrTiO_3 gewachsen, wodurch es aufgrund von Gitterfehlanpassungen zu einer Dehnung des Films kam, und topochemisch fluoriert wurden. Das Ziel dieser Studie war es, den Einfluss von eingebrachtem Fluor auf den gedehnten Film zu untersuchen, da durch die Fluorierung nicht-zentrosymmetrische Konfigurationen um das Fe^{3+} -Kationen gebildet werden können, welche zur Ausbildung von mutiferroischen Eigenschaften führen. Vergleichbare Ergebnisse von Messungen an Pulverproben deuteten auf dieses Verhalten hin. Die Fluorierung führte zu keiner Verschlechterung der Filmqualität, unabhängig von den zwei gewählten Verfahren zur topochemischen Fluorierung. Des Weiteren konnte gezeigt werden, dass die Filme homogen fluoriert wurden, ohne dass Fluor im Substrat gefunden werden konnte. Obwohl

es möglich war, einkristalline Filme zu synthetisieren, zeigten die Ergebnisse eine Entspannung der Elementarzelle hin zu nahezu perfekter kubischer Symmetrie und deuteten auf die Bildung einer *trans*-Konfiguration hin, d. h. die Fluorionen besetzen die gegenüberliegenden Ecken des FeO_4F_2 -Oktaeders. Somit ergab die scheinbare Zentrosymmetrie eine Abnahme der Anisotropie in der antiferromagnetischen Ordnung sowie eine leichte Verkipfung der magnetischen Momente, aber keine multiferroischen Eigenschaften.

Abstract

The subject of this cumulative doctoral thesis was the investigation of topochemical modifications of the anionic sublattice of the cubic perovskite-type compound $\text{BaFeO}_{2.5}$ within the Ba-Fe-O-F model system. The focus lay on the topochemical fluorination of the pure oxide combined with an extensive investigation of kinetic, magnetic and electrochemical analysis of the oxyfluoride system $\text{BaFeO}_{2.5-x/2}\text{F}_x$ ($x = 0, 0.333, 1$) depending on the fluorine content. Oxyfluorides might be suitable for enabling the operation of solid oxide fuel cells (SOFCs) at intermediate or even low temperatures by decreasing the activation energy for the oxygen reduction reaction in the cathode material as well as by improving transport kinetics of oxygen ions. But also the topochemical oxidation led to a new insight into possible coordination of the transition metal cation $\text{Fe}^{3+/4+}$ and showed revealing redox reactions under oxidizing atmosphere. The Ba-Fe-O-F system was chosen to be most suitable as a model system due to the already existing knowledge about fluorinated phases within the system and their structural connection to the fluorine stoichiometry.

The Ba-Fe-O system exhibits various perovskite-type modifications with varying oxygen stoichiometry in the range of $2.5 < x < 3$ accompanied by the corresponding changes of valence states of $\text{Fe}^{3+/4+}$. The cubic-based structures can be described by group-subgroup relations with respect to the cubic perovskite structure type with the aristotype symmetry $Pm\bar{3}m$. So far, these compounds have in common a 5- or 6-fold coordination of the Fe^{4+} cation. In this work, a new modification of $\text{Ba}_3\text{Fe}_3\text{O}_8$ ($\text{BaFeO}_{2.667}$), crystallizing in the $P2_1/m$ space group, could be identified exhibiting a Fe^{4+} cation within a 4-fold coordination (tetrahedron) environment. Hitherto, the $\text{Fe}^{4+}\text{O}_4^{4-}$ tetrahedron was so far only reported for a few oxidic compounds other than perovskites. Within the tetrahedron, the Fe^{4+} adopts the high spin state with an electronic configuration $e^2t_2^2$ and a total spin of $S = 2$. Further, it was revealed that this compound was isotypic to the already reported and well-described oxyfluoride compound $\text{Ba}_3\text{Fe}_3\text{O}_7\text{F}$ ($\text{BaFeO}_{2.333}\text{F}_{0.333}$), sharing the same space group and super-cell with comparable, but distinguishable, lattice and atomic parameters. From this it follows, that the connectivity scheme and coordination environment of the oxygenpolyhedra and iron cations could be summed up in the formula $\text{Ba}_3(\text{Fe}^{3+}\text{O}_{6/2})(\text{Fe}^{3+}\text{O}_{5/2})(\text{Fe}^{4+}\text{O}_{3/2}\text{O}_{1/1})$.

The kinetic studies of the interdiffusion reaction of $\text{BaFeO}_{2.5}$ and BaFeO_2F forming

BaFeO_{2.333}F_{0.333} were performed with the help of in-situ X-ray diffraction at different temperatures with isothermal experimental conditions. Weight fractions extracted by quantitative Rietveld refinements were utilized to image the reaction over time. Kinetic analysis revealed a first order reaction with temperature-dependent diffusion paths and crystallization processes. The application of a diffusion model based on the Boltzmann-Matano method and the root mean-squared penetration depth allowed the estimation of an interdiffusion coefficient which allowed the assignment of oxygen to be the rate limiting species. The rather simple approach on the base of X-ray diffraction yielded satisfying insights into the reaction kinetics of interdiffusion in oxyfluorides.

Since oxyfluorides may be possible candidates for intermediate and low temperature SOFCs, the impact of topochemical fluorination on electrochemical and also magnetic properties was studied. For this purpose symmetrical films with BaFeO_{2.5-x/2}F_x ($x = 0, 0.333, 1$) as cathode materials were synthesized and investigated. For this purpose, a new synthesis technique for the precise adjustment of the fluorine stoichiometry based on interdiffusion was developed. The results for a partial fluorinated cathode showed a change in transport kinetics towards an increase in bulk transport of oxygen ions together with a limitation of the process by the utilized surface area. On the other side, the fully fluorinated cathode (BaFeO₂F) exhibited very poor electrochemical performance, which can be assigned to the absence of oxygen vacancies which are required for oxygen exchange with the atmosphere and the conduction of oxygen ions.

Investigations of powder samples of the oxyfluoride BaFeO₂F suggest non-centrosymmetric environments around the Fe³⁺ cation which cause multiferroic properties. The tailoring of magnetic properties by topochemical fluorination was studied on thin films of BaFeO₂F and compared to BaFeO_{2.5} films. The oxide films were epitaxially grown by PLD on SrTiO₃ substrates which caused a straining due to the lattice mismatch inside the film and topochemically fluorinated. The aim was to investigate the influence of incorporated fluorine on the strained film by forming non-centrosymmetric environments around Fe³⁺ cations yielding possible multiferroic properties as suggested from powder samples. The chosen fluorination methods did not lead to a worsening of the film quality. Further, it could be shown that the films were homogeneously fluorinated without any fluorine incorporation into the substrate material. Although it was possible to synthesize such single crystalline films, the results showed a relieve of the unit cell towards almost perfect cubic symmetry and suggested the formation of a *trans* configuration, i.e., fluorine sitting on opposite sites of the FeO₄F₂ octahedron. Thus, the apparent centrosymmetry yielded a decrease of anisotropy in antiferromagnetic ordering as well as a slight ferromagnetic canting of the magnetic moments, but no multiferroic properties.

Acknowledgements

I would like to take the chance to thank everyone who accompanied me on my long journey throughout these years and who contributed to this work.

First and foremost, I would like to thank Prof. Dr. Oliver Clemens for offering me the chance to conduct this work in his research group. I thank him for his endless support during these four years and some months and his unrestricted trust in my work and skills - despite some football disagreements. Under his supervision and constant nurturing of my curiosity, I was able to develop myself and my work. Sincere thanks for all the input and discussions and pushing this work into its current form.

Further, I would like to thank Prof. Dr. Wolfgang Ensinger for being co-examiner of this work. I enjoyed the talks and discussions during weekly lunch meetings on Thursday. Special thanks to Prof. Ensinger for taking care of us after the lab moved to Stuttgart. I would also like to thank Prof. Dr. Lambert Alff and Prof. Dr. Barbara Albert for agreeing to be part of my examination committee.

I would like to express my gratitude to my research group *Materialdesign durch Synthese* (now *Chemische Materialsynthese* at University of Stuttgart) for the great company and constant scientific exchange - especially Aamir Waidha for the delightful discussions about the Ba-Co/Fe-O system and other perovskites. Being part of this group made my time at the Technical University of Darmstadt very special and entertaining. Special thanks to Akash Nair and Jasim Ali for their scientific work and contributions to this work during their Advanced Research Lab and Master's Thesis projects. Also a very special thanks to Maria Walker for her always friendly supportive and reliable teamwork.

This work would not have achieved these results without the support and cooperation from/with members of the workshop at the Materials Science department. Special thanks to Michael Weber and Jochen Rank for their perfect work and support during technical maintenance, electrical issues, but also the manufacturing of the impedance sample holder. Their expertise were of striking help and contributed to my scientific knowledge. Further, I would express my thanks towards Claudia Fasel, who supported my work by TG/DTA measurements several times combined with extensive discussion and analysis, and towards Jean-Christophe Jaud for helping me out in XRD issues.

Further, I would like to thank my close friends and colleagues Lukas Zeinar, Christian

Lampa, Tobias Stohr and Manuel Donzelli for their support and making the time enjoyable and fun, even during the hard times, but also scientific exchange about different research topics.

Also special thanks to all my collaborators who supported my work with measurements and scientific input: Prof. Dr. Roger de Souza (discussion about JMA analysis), Dr. Yuji Ikeda and Prof. Dr. Blazej Grabowski (DFT calculations), Dr. Abhshek Sarkar and Dr. Robert Kruk (Mössbauer spectroscopy), Dr. Sami Vasala (SQUID measurements), Humera Siddiqui (atmospheric furnace).

Finally, I want to thank friends and my family who supported me during this time. My deepest thanks towards Adalie B. who put up with me during the final year.

I gratefully acknowledge the funding by the German Research Foundation (DFG) within the Emmy Noether program (CL551/2-1).

Preface - Licensing Information and Personal Contribution

The presented cumulative thesis includes the articles published in peer-reviewed journals. The articles have been adapted to the format of the thesis in order to match the corporate design of TU Darmstadt. The supplementary information have been included directly into the text for a more structured appearance. Grammar and/or spelling mistakes found were corrected. The content of each publication remained unchanged. In the following, the licensing information of each publication and statements of personal contribution will be given. The licensing information is additionally given on the first page of each publication inside the thesis.

1. **Structural and magnetic properties of newly found $\text{BaFeO}_{2.667}$ synthesized by oxidizing $\text{BaFeO}_{2.5}$ obtained via nebulized spray pyrolysis**

Stephan Wollstadt, Yuji Ikeda, Abhishek Sarkar, Sami Vasala, Claudia Fasel, Lambert Alff, Robert Kruk, Blazej Grabowski, Oliver Clemens; *Inorganic Chemistry*
<https://doi.org/10.1021/acs.inorgchem.1c00434>

Reprinted (adapted) with permission from Wollstadt, S., Ikeda, Y., Sarkar, A., Vasala, S., Fasel, C., Alff, L., Kruk, R., Grabowski, B., and Clemens, O. "Structural and Magnetic Properties of $\text{BaFeO}_{2.667}$ Synthesized by Oxidizing $\text{BaFeO}_{2.5}$ Obtained via Nebulized Spray Pyrolysis." *Inorganic Chemistry* 60.15 (2021): 10923-10933. Copyright 2021 American Chemical Society.

The synthesis and experiments for structural characterization (XRD) and electrochemical impedance experiments were planned and carried out by myself. DT/TGA measurements were conducted by Claudia Fasel. Ab initio DFT calculations and evaluation were performed by Dr. Yuji Ikeda and Prof. Dr. Blazej Grabowski. Mössbauer measurements and fitting were carried out by Dr. Abhishek Sarkar and Dr. Robert Kruk. Magnetic SQUID measurements and discussion were done by Dr. Sami Vasala. Combination of results from the different techniques, interpretation and setting into context by myself. Writing and composing the journal article were primarily done

by myself and proofread by Prof. Dr. Oliver Clemens. All co-authors contributed basic text and figures.

2. On the Impact of the Degree of Fluorination on the ORR Limiting Processes within Iron Based Catalysts: A Model Study on Symmetrical Films of Barium Ferrate

Stephan Wollstadt, and Oliver Clemens, *Materials*

<https://doi.org/10.3390/ma13112532>

Reproduced under the *Creative Commons CC BY 4.0* license from Wollstadt, Stephan, and Oliver Clemens. "On the Impact of the Degree of Fluorination on the ORR Limiting Processes within Iron Based Catalysts: A Model Study on Symmetrical Films of Barium Ferrate." *Materials* 13.11 (2020): 2532.

The experiments were carried out by myself under the supervision of Prof. Dr. Oliver Clemens. The synthesis, characterization and data analysis were done by myself. Writing and composing the journal article were done by myself with final discussion with Prof. Dr. Oliver Clemens.

3. Synthesis and characterisation of fluorinated epitaxial films of BaFeO₂F: Tailoring magnetic anisotropy via a lowering of tetragonal distortion

A. Nair, S. Wollstadt, R. Witte, S. Dasgupta, P. Kehne, L. Alff, P. Komissinskiy and O. Clemens, *RSC Advances*

<https://doi.org/10.1039/C9RA08039B>

Reproduced under the *Creative Commons CC BY-NC 3.0* license from Nair, A., Wollstadt, S., Witte, R., Dasgupta, S., Kehne, P., Alff, L., Komissinskiy, P., and Clemens, O. (2019). Synthesis and characterisation of fluorinated epitaxial films of BaFeO₂F: Tailoring magnetic anisotropy via a lowering of tetragonal distortion. *RSC Advances*, 9(64), 37136-37143 with permission from the Royal Society of Chemistry.

My focus lied on helping with target synthesis, topochemical fluorination of epitaxial films and structural characterization. Synthesis and experiments for structural characterization (XRD) were carried out by Akash Nair under my supervision, as well as the supervision of Dr. Philipp Kehne, Dr. Philipp Komissinskiy and Prof. Dr. Oliver Clemens. Dr. Ralf Witte performed Mössbauer spectroscopy. Dr. Supratik Dasgupta carried out magnetic measurements. Writing and composing of the journal were mainly carried out by Akash Nair. All co-authors contributed by discussion and feedback.

4. **A kinetic study of the interdiffusion of fluorine and oxygen in the perovskite-type barium ferrate system $\text{BaFeO}_{2.5-x}\text{F}_{2x}$**

Stephan Wollstadt, Roger A. De Souza, and Oliver Clemens, *The Journal of Physical Chemistry C*

<https://doi.org/10.1021/acs.jpcc.0c10174>

Reprinted (adapted) with permission from Wollstadt, Stephan, Roger A. De Souza, and Oliver Clemens. "Kinetic Study of the Interdiffusion of Fluorine and Oxygen in the Perovskite-Type Barium Ferrate System $\text{BaFeO}_{2.5-x}\text{F}_{2x}$." *The Journal of Physical Chemistry C* 125.4 (2021): 2287-2298. Copyright 2021 American Chemical Society. The basic idea for the underlying experiment was given by Prof. Dr. Oliver Clemens. Planning and execution as well as the extensive kinetic and interdiffusion analysis were done by myself. Prof. Dr. Roger de Souza suggested the application of the Johnson-Mehl-Avrami model, which was then realized by myself. Writing and composing the journal article was done by myself. Prof. Dr. Oliver Clemens and Prof. Dr. Roger de Souza were involved in final discussion and revision.

Contents

Zusammenfassung	vii
Abstract	xi
Acknowledgements	xiii
Preface	xv
1. Introduction	1
1.1. SOFC research	3
1.2. Structure of this work	4
2. Fundamentals	7
2.1. Perovskite structure	7
2.1.1. ABX_3 crystal structure	7
2.1.2. Jahn-Teller distortion	9
2.1.3. Oxygen vacancy ordering	11
2.1.4. Topochemical fluorination of perovskite oxides	13
2.1.5. Oxygen ion conduction in perovskite materials	15
2.1.6. Magnetic properties of perovskite materials	16
2.2. ^{57}Fe Mössbauer spectroscopy	19
2.3. Principles of diffusion	20
2.3.1. Fick's laws of diffusion	20
2.3.2. Boltzmann-Matano analysis	22
2.4. X-ray diffraction	23
2.4.1. Generation of diffraction radiation	24
2.4.2. Principles of powder diffraction	25
2.4.3. Experimental setups for powder XRD	31
2.4.4. Intensity and shape of reflections inside powder diffraction patterns	31
2.4.5. Thin film X-ray diffraction techniques	34
2.4.6. Fundamental parameter approach	35

2.4.7. Rietveld Refinement method	36
2.4.8. X-ray diffraction and Rietveld refinement within this work	38
2.5. Electrochemical impedance spectroscopy	39
2.5.1. Fundamentals of electrochemical impedance spectroscopy	39
2.5.2. Models for SOFC cathodes	44
2.5.3. EIS and SOFC models within this work	48
3. Topochemical reactions affecting the anion lattice inside the model system barium ferrate	49
3.1. Structural and magnetic properties of newly found BaFeO _{2.667} synthesized by oxidizing BaFeO _{2.5} obtained via nebulized spray pyrolysis	63
3.1.1. Introduction	65
3.1.2. Experimental	66
3.1.3. Results and discussion	69
3.1.4. Conclusions	83
3.1.5. Acknowledgments	85
3.2. On the Impact of the Degree of Fluorination on the ORR Limiting Processes within Iron Based Catalysts: A Model Study on Symmetrical Films of Barium Ferrate	87
3.2.1. Introduction	89
3.2.2. Experimental	93
3.2.3. Results and Discussion	96
3.2.4. Conclusion	113
3.3. Synthesis and characterisation of fluorinated epitaxial films of BaFeO ₂ F: Tailoring magnetic anisotropy <i>via</i> a lowering of tetragonal distortion	115
3.3.1. Introduction	117
3.3.2. Experimental	118
3.3.3. Results and discussion	121
3.3.4. Conclusions	130
3.3.5. Acknowledgments	130
3.4. A kinetic study of the interdiffusion of fluorine and oxygen in the perovskite-type barium ferrate system BaFeO _{2.5-x} F _{2x}	131
3.4.1. Introduction	133
3.4.2. Experimental	135
3.4.3. Results and discussion	136
3.4.4. Conclusion	151
3.4.5. Acknowledgments	152



3.5. Supplemental and additional topics	153
3.5.1. Phases inside the system Ba-Fe-O-F	153
3.5.2. Group-subgroup relations of the structural changes observed by topochemical reactions	155
3.5.3. Oxygen cycling and morphological influences	157
3.5.4. Reduced fluorine doping	166
4. Conclusion	169
5. Outlook	171
A. EIS sample holder	191
B. TOPAS INP Example	193
C. Atomic positions in BaFeO_{2.5} and BaFeO_{2.333}F_{0.333}/BaFeO_{2.667} for Sec. 3.5.2	199
D. EIS data for Sec. 3.5.3	201

List of Figures

1.1. Schematic of a solid oxide fuel cell highlighting the basic working principle and illustrating the critical process of oxygen ion reduction and conduction.	3
2.1. Schematic structural configurations for perovskite structures: a) ideal cubic perovskite (<i>A</i> - yellow, <i>B</i> - blue, <i>X</i> - red); b) corner sharing of anion octahedra in cubic symmetry; c) face sharing polyhedra for purely hexagonal stacking and d) alternating face and corner sharing polyhedra for a sequence of hexagonal and cubic stacking. Unit cell borders are schematically shown.	8
2.2. a) Geometrical scheme of the shape and direction of <i>d</i> orbitals. b) Ligand field energy level diagram of the Jahn-Teller distortion of high-spin Fe^{4+} inside an octahedral (elongation and compression) and a possible tetrahedral ligand field.	10
2.3. 5- and 4-fold coordinations of transition metal cations (Mn, Zn, Fe) in a) $\text{CaMnO}_{2.5}$ [30] (square-pyramid), b) BaZnO_2 [31] (tetrahedron) and c) SrFeO_2 [32] (square-planar). $\text{BaFeO}_{2.5}$ [33] (d) contains three different iron coordinations: 6-fold, 5-fold and 4-fold. The vacancies (grey balls) form a channel-like network inside the large unit cell.	12
2.4. Structures of the topochemically fluorinated compounds of $\text{BaFeO}_{2.5}$: a) $\text{BaFeO}_{2.333}\text{F}_{0.333}$ [12] and b) BaFeO_2F [11]. Vacancies are coloured in grey and the relaxation of the anion from the ideal cubic position (black) is marked as a red arrow.	14
2.5. a) Oxygen vacancy inside a BX_6 octahedron and b) the diffusion path of an oxygen ion vacancy following a random path through the bulk.	15
2.6. Depiction of the exchange interactions inside an iron containing perovskite for a) superexchange ($\text{Fe}^{3+} + \text{S} \leftrightarrow \text{Fe}^{3+} - \text{S}$) and b) double exchange interaction ($\text{Fe}^{3+} + \text{S} \leftrightarrow \text{Fe}^{4+} + \text{S}$).	18
2.7. Mössbauer spectrum with one sextet and a doublet. The doublet exhibits an isomer shift δ	20
2.8. Concentration profile of a diffusion couple at time <i>t</i> with the C^* at location x^* with starting concentrations C_L and C_R	23

2.9. Electron transition according to the selection rules resulting in the characteristic X-ray spectrum, with the characteristic peaks for $K_{\alpha/\beta}$ and the accompanying bremsstrahlung. Implementing a β -filter (dotted line) leads to a filtered X-ray spectrum.[53, 57]	26
2.10. Elastic scattering of X-ray waves: (a) geometric illustration of Bragg's law, (b) elastic scattering at electron density (schematic) of an atom.	29
2.11. Geometrical construction of the Ewald's sphere. The two diffracted waves \vec{k}_1 and \vec{k}_2 spanning the diffraction cones 1 and 2, satisfying the diffraction condition with the reciprocal lattice vector $\vec{d}_{hkl,1}^*$ and $\vec{d}_{hkl,2}^*$, respectively. The diffraction cones form so-called Debye-Scherrer rings on a detector plane, named after early inventors of diffraction cameras.	30
2.12. Schematic concept of a) Bragg-Brentano geometry and b) weakening of penetrating X-ray beam coupled with decrease of detectable intensity.	32
2.13. Example simulation of a) one RC element and c) two RC elements. The Nyquist plots (a,c) show one and two semicircles, respectively, and the Bode plots (b,d) show one and two maxima in the phase angle, respectively, while the amount of impedance rises correspondingly. The simulation parameters for the single RC element are $R_s = 50 \Omega$ and $R = 50 \Omega$ and for the double RC element $R_s = 50 \Omega$, $R_1 = 40 \Omega$ and $R_2 = 25 \Omega$	42
2.14. R-CPE elements with different values for $\alpha = 1, 0.9, 0.8, 0.6$. The depression of the semicircle in the Nyquist plot (a) leads to a decrease in imaginary impedance, but also to a dispersion of the maximum in the phase angle (b), while the the slope of $ Z $ is equal to α	44
2.15. Different morphologies of cathodes with the special cases of a) Pt, b) dense and c) porous cathode configurations and its impact on the impedance spectroscopy response with the corresponding formalism and equivalent circuits. Note that the serial resistance includes the electrolyte response.	45
3.1. Defect structure of (a) $\text{BaFeO}_{2.5}$ ($P2_1/c$) and (b) $\text{BaFeO}_{2.33}\text{F}_{0.33}$ ($P2_1/m$) with bars/crosses indicating oxygen vacancy channels/relaxations [12, 33], (c) depicts a defect free structure of BaFeO_2F ($Pm\bar{3}m$).[83] Below the structural representations, the XRD patterns of each phase are given, with highest intensity reflection groups shown in insets.	51
3.2. NSP experimental setup with the schematical precipitation process. Taken from Pub. 3 [83].	52

3.3. Reaction routes for the low and high temperature NSP process with the post treatment processes leading to powders with hollow sphere and fine grain morphology, respectively. Only the fine grain powder was suitable for film synthesis.	53
3.4. HT-XRD of BaFeO _{2.5} under oxygen atmosphere with indicated phase changes and the structural model of BaFeO _{2.667} (<i>P2₁/m</i>) created by DFT calculations with iron coordinations highlighted (“o” - octahedron, “p” - square pyramid; “t” - tetrahedron). Figure is recreated from Fig. 3.7 and Fig. 3.9 in Sec. 3.1.	55
3.5. Topochemical fluorination of oxidic films to achieve (a) partially fluorinated BaFeO _{2.333} F _{0.333} YSZ8 BaFeO _{2.333} F _{0.333} via an interdiffusion approach and (b) fully fluorinated BaFeO ₂ F YSZ8 BaFeO ₂ F via the vapor transport related technique.	57
3.6. Scheme of the interdiffusion process inside the powder mixture. The phase changes can be tracked by high temperature XRD (e.g. at temperatures of 380 °C and 480 °C).	60
3.7. Results of the high temperature XRD study: (a,c,e) depict the results of BaFeO _{2.5} under oxygen; (b,d,f) depict the results of BaFeO _{2.667} under air. (a,b) show the XRD pattern over the whole temperature range with the emerging configurations. (c,d) highlight the corresponding phase fractions as calculated by Rietveld refinements. (e,f) showcase the evolving pseudocubic lattice parameters (and simultaneously the volume per formula unit <i>V_{f.u.}</i>) with straight lines emphasizing the linear thermal expansion.	71
3.8. TG/DTA measurement of pure BaFeO _{2.5} performed under pure oxygen atmosphere, complementary to the HTXRD experiment depicted in Figure 3.7 a,c,e.	72
3.9. Primitive cell of Ba ₃ Fe ₃ O ₈ . Green, brown and red spheres represent Ba, Fe, and O atoms, respectively. The labels on the Fe atoms show their coordination environments; “o”, “t” and “p” indicate an octahedral, tetrahedral, and pyramidal coordination, respectively.	74
3.10. a) Characteristic XRD reflexes for BaFeO _{2.5} , BaFeO _{2.667} and BaFeO _{2.333} F _{0.333} . Ambient XRD data of BaFeO _{2.667} and corresponding Rietveld fit based on the positional parameters found for b) BaFeO _{2.333} F _{0.333} [12] and c) calculated by DFT for BaFeO _{2.667}	76
3.11. ⁵⁷ Fe Mössbauer spectra of room temperature and at 10 K of BaFeO _{2.667}	77
3.12. ⁵⁷ Fe Mössbauer spectra of BaFeO _{2.667} recorded at room temperature. (SI)	77

3.13.a) Field cooled and zero field cooled curves and b) Field-dependent magnetization of $\text{BaFeO}_{2.667}$ at various temperatures with the coercivity at 10 K shown in the inset.	83
3.14.a) Energetically most stable G-type AFM ordering of $\text{Ba}_3\text{Fe}_3\text{O}_8$, with only the Fe atoms shown. The red and the blue arrows indicate spin-up and spin-down magnetic moments, respectively. For each Fe atom, its six neighboring Fe atoms have opposite magnetic moments; b) <i>ab initio</i> computed energies of $\text{Ba}_3\text{Fe}_3\text{O}_8$ as a function of U_{eff} . For each U_{eff} , the energy of the NM phase is set as the reference.	84
3.15. Field cooled and zero field cooled curves (left) and Field-dependent magnetization of $\text{BaFeO}_{2.81}$ at various temperatures (right).	85
3.16. Defect structure of (a) $\text{BaFeO}_{2.5}$ ($P2_1/c$) and (b) $\text{BaFeO}_{2.67}/\text{BaFeO}_{2.33}\text{F}_{0.33}$ ($P2_1/m$) with bars/crosses indicating oxygen vacancy channels/relaxations [12, 33], (c) depicts a defect free structure of BaFeO_2F ($Pm\bar{3}m$). Though $\text{BaFeO}_{2.67}$ is confirmed to have the same overall anion content $\text{BaFeX}_{2.67}$ than $\text{BaFeO}_{2.33}\text{F}_{0.33}$, neutron diffraction studies are yet needed to confirm the identical vacancy ordering pattern within the $\sqrt{6} \times \sqrt{2} \times \sqrt{3}$ monoclinic superstructure of the cubic perovskite modification.	92
3.17. NSP experimental setup with the schematical precipitation process.	94
3.18. Topochemical fluorination of oxidic films to achieve (a) partial fluorinated $\text{BaFeO}_{2.33}\text{F}_{0.33} \text{YSZ8} \text{BaFeO}_{2.33}\text{F}_{0.33}$ via an interdiffusion approach and (b) fully fluorinated $\text{BaFeO}_2\text{F} \text{YSZ8} \text{BaFeO}_2\text{F}$ via the vapor transport related technique.	95
3.19. XRD of as-prepared NSP powder and after the calcination step at 900 °C.	97
3.20. SEM micrographs of (a) as-prepared NSP powder at 750 °C and (b) after calcination at 900 °C.	97
3.21. Zeta potential measurement of an aqueous solution of BFO in the pH range from 2–10.	98
3.22. XRD pattern of as-synthesized water-containing BFO and SEM micrograph of the dried BFO.	99
3.23. Variable temperature XRD of BaFeO_2F under argon, 690–730 °C.	100
3.24. Variable temperature XRD of $\text{BaFeO}_{2.33}\text{F}_{0.33}$ under argon, 570–630 °C.	101
3.25. XRD of as-prepared films with sputtered Au electrodes on top after topochemical oxidation and fluorination.	103
3.26. SEM before (a) and after (b) sintering. EDX (c) of a topochemically fluorinated BFOF film, mapping the main elements of the used materials: Zr, Y, Ba, Fe, F.	104

3.27. (a,c,e) Nyquist and (b,d,f) Bode plots of symmetrical films of BFO, BFOF33 and BFOF. The recorded data are represented by symbols, while the fits are drawn with solid lines.	107
3.28. Comparison of fitting models describing diffusive and/or capacitive responses for (a) BFO' and (b) BFOF33, where each, (a) and (b), contain a comparison of the used models inside Nyquist and Bode plots.	108
3.29. Logarithmic plot of the area specific resistance. Dashed fitting lines highlight the behavior in case of BFOF33 (●) and BFOF (▲). BFO/BFO' (■) exhibits a bend trajectory. Hollow symbols represent the temperatures with open semicircles.	110
3.30. Schematic of the penetration of the utilization region δ into the electrode in dependency of its thickness L with the corresponding impedance models: (a) depicts the relation represented by Equation 3.5; (b) illustrates the case discussed for Equation 3.15.	111
3.31. Arrhenius plot for the conductivity of BFO/BFO' (■), BFOF33 (●) and BFOF (▲). Dashed lines represent the performed fit for the activation energy.	113
3.32. Representation of drop fluorination method of fluorination as carried out on BFO films. The figure is recreated and related to the scheme shown in ref. [47].	119
3.33. Vapour transport process carried out on as-grown oxygen deficient BFO placed downstream from PVDF pellets in a heated alumina tube in the presence of a flowing carrier gas. The figure is recreated and related to the scheme shown in ref. [47].	119
3.34. (a) High resolution X-ray diffractograms of an as-deposited BFO (black) and fluorinated BFOF (red) films on SrTiO ₃ substrate (b) Expanded view of the (001) BFO and BFOF reflections.	122
3.35. a) XRD $2\theta - \theta$ patterns of the BFO film and BFOF films on STO. b) Expanded view of the 001 reflection. (SI)	122
3.36. Rocking curve scans of the (002) reflection of a film of BFO (a) and BFOF (b). (SI)	123
3.37. X-ray Reciprocal Space Mapping of the (a) BFO and (b) drop-fluorinated BFOF films measured around (103) STO reflection.	124
3.38. Normalized concentration-depth profile for BFOF-VT. (SI)	125
3.39. Normalized concentration-depth profile for BFOF film corresponding to all the elements observed in XPS spectra.	126
3.40. ⁵⁷ Fe conversion electron Mössbauer spectrum recorded from (a) BFO and (b) BFOF at room temperature.	126

3.41. Dependences of the magnetization from the applied magnetic field at 10 K for (a) non-fluorinated BFO and (c) drop-fluorinated BFOF films. Temperature dependence of the magnetization for (b) BFO and (d) BFOF films, measured at the applied magnetic field of 200 Oe in field-cooled (FC black) and zero-field-cooled (ZFC red) regimes. The data were corrected for the diamagnetic contribution of the SrTiO ₃ substrate.	129
3.42. Group-subgroup relationship of the cubic aristotype and its monoclinic derivative structures.	137
3.43. Comparison of the coordination of iron inside the vacancy ordered structures of BaFeO _{2.5} (a,b) and BaFeO _{2.333} F _{0.333} (c,d). 5- and 6-fold coordinated iron atoms are surrounded by blue polyhedra, while yellow polyhedra mark tetrahedrally coordinated iron atoms. The tetrahedra form a channel-like vacancy ordering inside BaFeO _{2.5}	138
3.44. Selected ranges of the X-ray diffraction patterns of (a) BFO, (b) BFOF33 and (c) BFOF.	138
3.45. Rietveld refinements of the mixtures at RT and at the end of the isothermal experiments at 380 °C and 480 °C with the refined phase fractions (BFO – green, BFOF – red, BFOF33 – blue) for the angular ranges 29 – 33° 2θ and 42 to 46° 2θ. The overall refinement is coloured in black. The differences are given underneath (grey dotted line). For a better signal to noise ratio, the last 4 patterns for each temperature were merged and the refined phase fractions can be found in Table 3.12.	140
3.46. Phase fractions over time upon heating at the different temperatures from 380 °C to 480 °C, (a) – (f).	143
3.47. (a) reduced time plot for the extracted weight percentages of BFOF33 (inset: depiction of the maximum phase fractions over corresponding temperature); (b) linearization of the reaction constant <i>k</i> for first order reaction mechanism for the formation of BFOF33 with corresponding fits (dotted lines); (c) linearized Arrhenius plot of <i>k</i> (<i>T</i>) with corresponding fit (dotted line).	144
3.48. Fitting of JMA model (red) on XRD data (black) combined with the corresponding crystallite volume (blue) of BFOF33 phase for 380 – 480 °C, (a) – (f). The crystallite size is described as the volume weighted average column length from the integral width of the reflections <i>L_{Vol}</i> (IB).	146
3.49. Schematic diffusion process during an isothermal experiment at different times. The concentration profiles of fluorine and oxygen are coloured in red and green, respectively.	147

3.50. SEM micrographs of (a) pristine powder and (b,c) powder after the isothermal interdiffusion experiment at temperatures of 380 and 480 °C, respectively.	148
3.51. (a) Penetration depth over time based on equation 3.30 with linear fits to extract the diffusion coefficient; (b) Arrhenius plot of the extracted diffusion coefficients.	151
3.52. Shortened symmetry tree for the cubic aristotype $Pm\bar{3}m$ and the monoclinic subgroups $P2_1/c$ and $P2_1/m$ with the corresponding transformation matrices and with $P4/mmm$ indicated as a possible route for the transition between both monoclinic phases.	156
3.53. Anion ordering in a $3\times 3\times 3$ supercell of $BaFeO_{2.5}$ viewing along (a) a -axis, (b) b -axis and (c) c -axis. The oxygen vacancies are depicted as grey balls with pink connections highlighting the formed oxygen vacancy channels. A detailed list of the atomic positions is given in Tab. C.2.	158
3.54. Anion ordering in a $3\times 3\times 3$ supercell of $BaFeO_{2.333}F_{0.333}/BaFeO_{2.667}$ viewing along (a) a -axis, (b) c -axis and (c) b -axis. The anion vacancies are depicted as grey balls with pink connections highlighting the formed oxygen vacancy channels. Dark red balls indicate the ideal anion position and black arrows show the displacement after relaxation leading to additional vacancy positions. A detailed list of the atomic positions is given in Tab. C.1.	159
3.55. Schematic synthesis route for the preparation of low and high temperature NSP powder and the subsequent film preparation. For both powders and the film the crystallite size and the synthesis temperature are given.	161
3.56. Cyclic TG measurement of $BaFeO_{2.5}$ prepared by NSP at 1050 °C under pure oxygen between 420 and 650 °C. The start of the measurement is marked with a star and the end with a diamond. Dotted and dashed lines are guides for the eye to highlight important features. The cyclic measurement is compared to the TG measurement presented in Sec. 3.1. For both powders the crystallite size (CS) and the synthesis temperature (NSP-T) are given.	163
3.57. Area specific resistance of a four-times cycled symmetrical film of $BaFeO_{2.5}$ and $BaFeO_{2.667}$. The heating and cooling ramps are indicated by solid and hollow symbols, respectively. The dashed line highlights the non-linear behaviour of the area specific resistance.	164
3.58. XRD of symmetrical films of $BaFeO_{2.667}$ on YSZ8 coated with Au electrode, recorded before (a) and after (b) the high temperature impedance spectroscopy under oxygen. The * indicates a slight impurity of $BaCO_3$	165
3.59. XRD of the composite film before (a) and after (b) the electrical impedance measurement (c). The composite (red circles) is compared to a pure oxide film (black squares).	168

A.1. EIS sample holder.	191
D.1. Electrical impedance spectra (Nyquist and Bode plots) of BaFeO _{2.667} symmetrical films at the temperatures a) 440°C, b) 460 °C and c) 480 °C. The number denominates the cycle, while h and c indicate heating and cooling, respectively.	201
D.2. Electrical impedance spectra (Nyquist and Bode plots) of BaFeO _{2.667} symmetrical films at the temperatures a) 500°C, b) 520 °C and c) 540 °C. The number denominates the cycle, while h and c indicate heating and cooling, respectively.	202

List of Tables

2.1. Comparison of three types of radiation used in diffraction experiments; f - atomic scattering function, s - $\sin \theta/\lambda$, Z - atomic number [53].	26
2.2. Interpretation of capacitance values in relation to their possible physical origin [5, 76].	43
3.1. DFT optimized internal atomic positions of G-AFM $P2_1/m$ $Ba_3Fe_3O_8$ with $U_{\text{eff}} = 2.5$ eV. For Fe atoms, the coordination environments are indicated. .	74
3.2. Lattice parameters optimized in DFT calculations and with XRD measurements. For XRD, the parameters were obtained with fixing the atomic positions either to those of isotypic $BaFeO_{2.333}F_{0.333}$ [116] or those of our DFT results. Fits are shown in Figure 3.10 b,c.	75
3.3. Fitting parameters for the ^{57}Fe Mössbauer spectrum of $BaFeO_{2.667}$ recorded at 10 K.	75
3.4. Fitting parameters for the ^{57}Fe Mössbauer spectroscopy at room temperature. (SI)	76
3.5. Bond valence sums (BVS) [155] calculated for different cations. Magnetic moments on atoms derived from the Bader analysis (Table 3.6) are also shown for comparison.	79
3.6. <i>Ab initio</i> computed atomic properties of FM $BaFeO_3$ and G-AFM $Ba_3Fe_3O_8$ with $U_{\text{eff}} = 2.5$ eV based on the Bader analysis [127]. For the Fe atoms, the coordination environments are also shown. The order of inequivalent sites is the same as in [12]. ν : atomic volume. q : atomic charge. $ m $: absolute value of the atomic magnetic moment. (SI)	81
3.7. Lattice parameters and cell volume per formula unit Z of $BaFeX_y$ ($X = O, F$) for the sintered and topochemically modified films.	103
3.8. Activation energies as calculated from the Arrhenius plots in Figure 3.29. .	112
3.9. Calculated lattice parameters of the films from RSM.	123
3.10. Fitting parameters for the ^{57}Fe Mössbauer spectra for BFO.	128
3.11. Fitting parameters for the ^{57}Fe Mössbauer spectra for BFOF.	128

3.12. Weight percentages of the quantitative Rietveld analysis of the isothermal experiments at RT and for the merged final four measurements.	142
3.13. Johnson-Mehl-Avrami kinetic from fitting the model on the recorded XRD data of BFOF33.	142
3.14. Average interdiffusion coefficients extracted from the squared penetration depth plots.	151
3.15. Unit cell volume per formula unit V_Z and space groups (SG) for selected topochemically modified phases inside the systems Ba-Fe-O and Ba-Fe-O-F.	155
3.16. Crystallite sizes of the investigated sample powders and films depending on the synthesis temperature.	162
3.17. Lattice parameter and volume weighed crystallite sizes of $\text{BaFeO}_{2.667}$ before and after the cyclic impedance spectroscopy. The volume per formula unit $V_{f.u.}$ is given related to the volume of one $\text{BaFeO}_{2.667 \pm d}$ unit.	167
C.1. Atomic parameters of $\text{BaFeO}_{2.333}\text{F}_{0.333}$ [12] used for Fig. 3.54 plus the anion vacancies.	199
C.2. Atomic parameters of $\text{BaFeO}_{2.5}$ [33] used for Fig. 3.53 plus the oxygen vacancies.	200

List of Acronyms and Symbols

Acronyms

ASR	area specific resistance
AFC	alkaline fuel cell
AFM	antiferromagnetic
BFO	BaFeO _{2.5}
BFO'	BaFeO _{2.67}
BFO(OH)	BaFeO _{2.5-x} (OH) _{2x}
BFOF33	BaFeO _{2.333} F _{0.333}
BFOF	BaFeO ₂ F
BSCF	Ba _{0.5} Sr _{0.5} Co _{1-x} Fe _x O _{3-δ}
BVS	bond valence sum
CPE	constant phase element
DTA	differential thermal analysis
EDX	energy dispersive X-ray
EIS	electrical impedance spectroscopy
FM	ferromagnetic
GDC	gadolinium doped ceria
GOF	goodness of fit
Gsu	Gerischer impedance element (suppressed)
HT-XRD	high temperature X-ray diffraction
HTK	Hochtemperatur Ofen-Kammer
JMA	Johnson-Mehl-Avrami
LSC	La _{1-x} Sr _x CoO _{3-δ}
LSF	La _{1-x} Sr _x FeO _{3-δ}
LSM	La _{0.8} Sr _{0.2} MnO ₃
MCFC	molten carbonate fuel cell
MIEC	mixed ionic-electronic conductor
NM	non-magnetic
NSP	nebulized spray pyrolysis

ORR	oxygen reduction reaction
PAFC	phosphoric acid fuel cell
PEMFC	polymer electrolyte membrane fuel cell
PVDF	polyvinylidene difluoride
SEM	scanning electrode microscopy
SLM	standard liter per minute
SOFC	solid oxide fuel cell
SQUID	superconducting quantum interference device
STO	SrTiO ₃
TCU	temperature control unit
TG	thermogravimetric
TPB	triple phase boundary
VT-XRD	variable temperature X-ray diffraction
YSZ/YSZ8	yttria-stabilized zirconia (8-Mol.% Y ₂ O ₃)
XRD	X-ray diffraction

Symbols

α	exponent of an CPE element
B_{hf}	hyperfine field splitting
C	capacitance (Sec. 2.5)
$C_{L,chem}$	chemical capacitance depending on film thickness L
C	Curie constant
χ	susceptibility
δ	utilization region inside the electrode
D	diffusion coefficient
\tilde{D}	interdiffusion coefficient
E_a	activation energy
f	atomic form factor
$F(\phi)$	structure factor
$G(\theta)$	geometry, structure and extrinsic sample factor
hkl	Miller indices
$I(t)/I(\omega)$	time/frequency dependent current
I_{hkl}	measured X-ray intensity
\mathbf{J}	vector of flux of particles
\vec{k}	wavevector of X-rays
L	inductance (Sec. 2.5)

L	electrode thickness (Sec. 3.2)
l_δ	utilization depth of an electrode with thickness L
L	particle size (Sec. 3.4)
λ	wavelength of X-rays
Λ	wavelength function (PSF)
LP_θ	Lorentz polarization factor
μ_B	Bohr magneton
μ_{eff}	effective magnetic moment
n_{JMA}	Avrami exponent
∇C	concentration gradient vector
Ω	instrumental broadening function (PSF)
ϕ	exponent of fractal Gerischer model
ϕ	Weiss constant
$PSF(\theta)$	peak shape function
Ψ	specimen function (PSF)
R	resistance
R_{chem}	chemical resistance
R_s	serial resistance
R_{Bragg}	reflection intensity-based R-factor
R_{wp}	weighted profile R-factor
s	scaling factor
t_{chem}	time constant for electrochemical reactions
T_N	Néel temperature
τ_{RC}	relaxation time in impedance spectroscopy
θ	defraction angle
U_{rm}	effective Coulomb interaction potential
$V(t)/V(\omega)$	time/frequency dependent voltage
$V_{\text{f.u.}}$	unit cell volume per formula unit
w_p	weight fraction of phase p
Z_{chem}	impedance of an electrochemical process

1. Introduction

The principle of an electrochemical cell has a long history. The effect of the inverted hydrolysis was first discovered by Sir William Grove, a Welsh physicist and barrister, in 1838. Grove worked on the improvement of conventional batteries, which were recently developed by the Italian professor Alessandro Volta in 1800, and found the generation of an electric voltage by combining sheet iron and unglazed porcelain plates submerged in a solution of copper sulphate and diluted acid [1]. This invention later was enhanced and developed to a power supply, called "gaseous battery", suitable for mass production. Simultaneously, the German physicist Christian F. Schönbein described his invention of a first basic fuel cell by bringing in contact two solutions of acidulated water, one with dissolved hydrogen, separated by a membrane. He underlined the importance of platinum as a connector of the two solutions, which was declared to be a necessity in order to generate a measurable current [2]. However, it took almost a century until the fuel cell as a reliable power supply could prove its worth. An alkaline fuel cell developed by the General Electric Company generated the power for the Gemini V mission inside the Gemini project by the NASA in 1965 [3]. The requirement of a steady and enduring supply of power during the mission denied the use of batteries, which were used prior in short-term missions.

During the development and advances in the field of solid oxide fuel cells, it was shown that the oxygen reduction reaction and oxygen ion conduction are the rate limiting factors. Thus, to increase the performance of solid oxide fuel cells and make them available for applications on a daily base, different materials are investigated to push the limitations towards new borders. Some of those materials belong to the material class of the so-called perovskite-type oxides.

Perovskite is the name of the mineral structure of calcium titanium oxide (CaTiO_3), which was discovered in the Ural mountains in 1839 by Gustav Rose and subsequently described and named after the Russian mineralogist Lev A. Perovski (1792 – 1856). The perovskite structure offers a huge variety of possibilities for applications and may be the answer for some of nowadays problems in energy related fields of research. Though the perovskite is referred to the highest symmetric cubic arrangement, the very first perovskite, CaTiO_3 , crystallizes in the orthorhombic space group $Pbnm$ with the lattice parameters $a = 5.39 \text{ \AA}$,

$b = 5.45 \text{ \AA}$ and $c = 7.65 \text{ \AA}$ comprising four formula units. This structural divergence is depending on the atomic radii of the metal cations and the anions participating in the compound formation.

SOFCs are efficient devices for generating electrical power from the conversion of chemical fuels. They consist of a dense electrolyte, which acts as a membrane for oxygen ion conduction and an electronic separator between the porous electrodes. These electrodes, anode and cathode, are responsible for the oxygen reduction reaction and ion conduction (cathode) and the reaction between oxygen and hydrogen ions (anode). Both electrodes are required to exhibit sufficient electronic conduction in order to enable the general energy generation and the oxygen ion reduction reaction at the cathode side [4]. A drawback of earlier oxide cathode materials was the lack of the desired electrocatalytic activity, thus, platinum as a catalyst material was required, but also a high operating temperature was required to reduce the overpotential inside the cell by providing sufficient activation energy for the oxygen reduction reaction and oxygen ion conduction. Current research focuses on the development of perovskite materials which possess sufficient ionic and electronic conduction, so-called mixed ionic-electronic conductors (MIEC), while exhibiting electrocatalytic activity to replace the expensive platinum. But also the reduction of operating temperature is a much sought-after goal, since lower operating temperatures reduce the material erosion and the cost for safety measures [4, 5]. Promising perovskite oxides for cathode materials in SOFCs are $\text{Ba}_{0.5}\text{Sr}_{0.5}\text{Co}_{0.2}\text{Fe}_{0.8}\text{O}_{3-\delta}$, $\text{La}_{1-x}\text{Sr}_x\text{MnO}_{3-\delta}$ (LSM) or $\text{La}_{0.6}\text{Sr}_{0.4}\text{Co}_{0.2}\text{Fe}_{0.8}\text{O}_{3-\delta}$ (LSCF) [4, 6–9].

Besides the cation doping, another way to reduce the operating temperature is the introduction of fluorine into the anion sublattice of the MIEC cathode materials [10]. By this, the activation energy for oxygen reduction reaction and oxygen ion conduction is supposed to be lowered due to the manipulation of the bond properties between anions and transition metal cation. Fluorine possesses the highest electronegativity of 4, which leads to weakened Coulombic forces between oxygen anions and the transition metal cations [10].

This work focuses on the investigation of topochemical modifications of the cubic perovskite-type compound $\text{BaFeO}_{2.5}$ within the Ba-Fe-O-F model system. Upon the introduction of fluorine, the Ba-Fe-O-F model system exhibits distinct phases depending on the fluorine stoichiometry, which are well-studied [11, 12]. This knowledge about structure, which is directly connected to the fluorine stoichiometry, simplifies the electrochemical investigations, but also bypasses the indistinguishability of the anions.

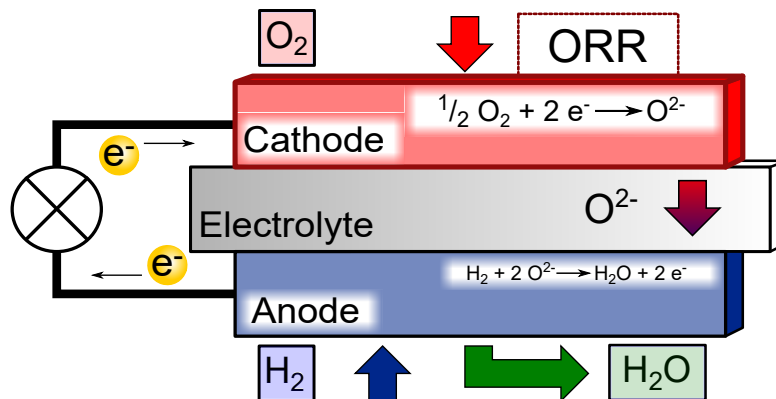


Figure 1.1.: Schematic of a solid oxide fuel cell highlighting the basic working principle and illustrating the critical process of oxygen ion reduction and conduction.

1.1. SOFC research

Today the research in the field of SOFC focuses on the creation of low (400 – 600 °C) and intermediate (600 – 800 °C) temperature oxygen ion conductors on the base of perovskite-type materials. Fig. 1.1 illustrates the basic working principle of a fuel cell and highlights the critical process of oxygen reduction and ion conduction. Besides oxygen, the cathode material also has to conduct electrons and as a result, the usage of so-called mixed ionic-electronic conductors was introduced. Reducing the operation temperature of a SOFC below 800 or even 600 °C would allow the usage of less expensive materials for safety measures and sealing. As a result, it would be much easier to implement SOFCs into everyday life. However, by reducing the working temperature, the polarization resistance rises since the provided energy may not meet the required activation energies for oxygen reduction reaction and ion conduction. Thus, the electrodes, especially the cathode where the oxygen reduction and conduction takes place, have to be improved to fulfill the demands for high performance. Besides the electrodes, the electrolyte material has to exhibit purely oxygen ion conduction. Yttria-doped zirconia (with 8 mol.% Y) has proven to be a suitable material, but also other materials such as gadolinium doped ceria (GDC) or samaria-doped ceria (SDC) are under consideration [13, 14]. Ferrite-based cathodes exhibit high oxygen permeability and electrocatalytic activity, but also show higher current densities compared to state-of-the-art manganese based cathodes [15, 16]. Promising candidates for cathode applications are compounds from the Ba-Sr-Co-Fe system ($\text{Ba}_{0.5}\text{Sr}_{0.5}\text{Co}_{0.2}\text{Fe}_{0.8}\text{O}_{3-\delta}$) [4, 17] or LaMO_3 , where La may also be substituted by

an alkaline metal like Sr and M is typically a transition metal cation [4, 18, 19]. Recent advances towards the desired goal were made by introducing the new strategy of anion doping. By this, the oxygen inside the perovskite is replaced by another anion, such as the halide ions fluorine (F^-) or chlorine (Cl^-), while the doping with fluorine showed the most promising results [10, 20]. The idea behind the doping with fluorine is the weakening of the oxygen bond between the anion and the transition metal cation, thus, lowering the activation energy for the oxygen ion conduction. Fluorine possesses the highest electronegativity with 4 compared to oxygen with 3.44. Thus, it forms a strong gradient of electronic attraction towards itself and away from the near oxygen anions [10]. However, the stability at elevated temperatures of some oxyfluoride materials is still a big concern, due to irreversible decomposition into metal fluoride and other products [10, 21]. Such decomposition would result in the destruction of the device. Besides the high temperature stability, the analysis of oxyfluorides also raises problems due to the following reasons: Oxygen and fluorine are indistinguishable by most characterization methods, such as X-ray or neutron diffraction due to similar scattering lengths [22, 23], which would offer a non-destructive characterization. On the other side, fluorine and oxygen can be distinguished by XPS or EDX, by either sputtering or cross-sectional measurements.

1.2. Structure of this work

The cumulative part of this thesis contains four publications:

1. **Sec. 3.1: Structural and magnetic properties of newly found $BaFeO_{2.667}$ synthesized by nebulized spray pyrolysis suitable for oxygen storage**
2. **Sec. 3.2: On the Impact of the Degree of Fluorination on the ORR Limiting Processes within Iron Based Catalysts: A Model Study on Symmetrical Films of Barium Ferrate**
3. **Sec. 3.3: Synthesis and characterisation of fluorinated epitaxial films of $BaFeO_2F$: Tailoring magnetic anisotropy via a lowering of tetragonal distortion**
4. **Sec. 3.4: A kinetic study of the interdiffusion of fluorine and oxygen in the perovskite-type barium ferrate system $BaFeO_{2.5-x}F_{2x}$**

This cumulative thesis is structured aiming for a connection between synthesis conditions, electrochemical and magnetical properties and the interdiffusion kinetics and thermodynamics of the oxyfluoride system Ba-Fe-O-F. Prior to the publications, Sec. 2 covers the fundamentals on which this work is based on. A general summary of the publications is given in Sec. 3 prior to the publications, where the content of each publication is put into greater context. The publications are adapted to the design and format of this cumulative thesis and adequate reference for the online version will be given.

This cumulative thesis aims for a better understanding of the impact of topochemical fluorination and the investigation of the anion sublattice inside the cubic perovskite-type system Ba-Fe-O-F. For this purpose, the cubic perovskite model system Ba-Fe-O was chosen, since its oxyfluoride phases $\text{BaFeO}_{2.333}\text{F}_{0.333}$ and BaFeO_2F are well studied and structurally understood. In addition, these phases exhibit well distinguishable structures, thus, bypassing the indistinguishability of the anions enabling an indirect determination of anion dynamics.

The main results of this thesis are discussed inside the publications in Sec. 3 with a preceding synopsis which connects the publications and sums up the key findings of each. The first publication contains the characterization and description of the newly found modification of $\text{BaFeO}_{2.667}$, which was found during the work on the electrochemical properties of symmetrical films of the oxide and oxyfluorides. These films are subjects of the second publication, which also highlights synthesis conditions for preparing symmetrical films of $\text{BaFeO}_{2.5}$, $\text{BaFeO}_{2.333}\text{F}_{0.333}$ and BaFeO_2F , but also investigates the metastability of the oxyfluoride compounds. Further, this second publication aims for the investigation of the electrochemical properties of these phases depending on the fluorine content. Afterwards, the third publication introduces epitaxial films of $\text{BaFeO}_{2.5}$ and BaFeO_2F and investigates the magnetical properties of these phases. The last publication investigates the interdiffusion reaction between $\text{BaFeO}_{2.5}$ and BaFeO_2F forming $\text{BaFeO}_{2.333}\text{F}_{0.333}$. Here, insights into kinetical and thermodynamical aspects were gained by isothermal diffraction experiments, which provide important insights on their potential use within SOFCs.

During the work on this topics, further results were generated delivering additional insights into the matter, which have not been published, but are important in the context of this thesis. These results are given after the publications and form the foundation for pursuing discussions which could not be addressed inside the publications. These discussion can be separated into four topics dealing with the phase formations inside the Ba-Fe-O-F system with respect to their symmetry, group-subgroup relations within oxidation and reduction of the phases $P2_1/c$, $P2_1/m$ and $P4/mmm$, the influence of crystallite sizes on reactivity and phase stability, and the preparation and examination of a fluorinated film with the composition $\text{BaFeO}_{2.43}\text{F}_{0.13}$.

2. Fundamentals

2.1. Perovskite structure

This section will introduce the perovskite-type structure and explain the layout of this special type of (oxide) material. Further, it will cover electronic configurations and the Jahn Teller distortion arising from the degeneration of electronic states. It will also highlight the oxygen vacancy ordering inside perovskite-type compounds, especially in $\text{BaFeO}_{2.5}$ which is the key compound in this work. Afterwards, the anion (fluorine) doping of oxide perovskites will be introduced and different synthesis approaches of the topochemical fluorination will be discussed, while special attention is drawn towards the topochemical fluorination products of $\text{BaFeO}_{2.5}$. The section will be closed with a description of oxygen ion conduction and magnetic ordering inside the perovskite lattice. The following discussion is based on references [24–28].

2.1.1. ABX_3 crystal structure

The general form of the perovskite is ABX_3 , with A being a large cation, predominantly an alkaline earth metals (SrTiO_3 , GdFeO_3), but sometimes also precious metals like Ag, B representing transition metal cations and X being anions, most popular are oxygen anions for oxidic metal compounds. Fig. 2.1.1 a shows a perovskite with the general formula of ABX_3 adopting the ideal cubic aristotype symmetry. In general, the atoms on the A -site occupy the corners forming a primitive cubic lattice, while the B -site lies in the center of the cell surrounded by the anion octahedra, with four anions arranged in a square-planar configuration and two anions on the apical sites, all located on the centres of the cubic faces, yielding the coordination numbers for A and B to be 12 and 6, respectively, with polyhedra sharing corners between unit cells (Fig. 2.1.1 b). The A cations form together with their oxygen neighbours closed packed AO_3 layers in the $[1\ 1\ 1]$ direction. Due to this high symmetry in ideal perovskite structures, isotropic properties can be expected. The bond lengths inside the BX_6 octahedron are equal for each $B^{4+} - O^{2-}$ bond and the bond angles are either 90° or 180° for the $O^{2-} - B^{4+} - O^{2-}$ bond. Thus, the atomic positions for an ideal cubic $Pm\bar{3}m$ perovskite can be given as:

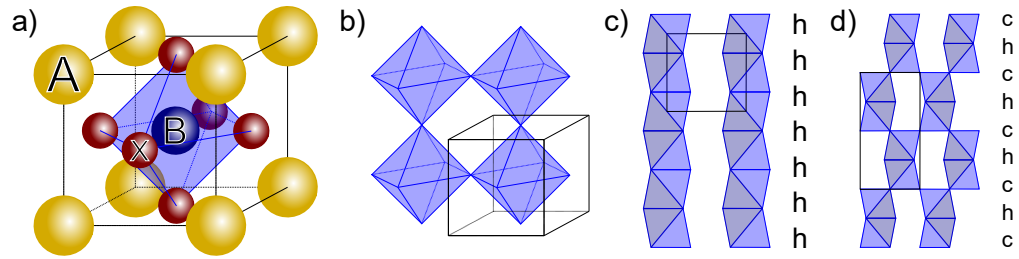


Figure 2.1.: Schematic structural configurations for perovskite structures: a) ideal cubic perovskite (A - yellow, B - blue, X - red); b) corner sharing of anion octahedra in cubic symmetry; c) face sharing polyhedra for purely hexagonal stacking and d) alternating face and corner sharing polyhedra for a sequence of hexagonal and cubic stacking. Unit cell borders are schematically shown.

- A: $3a - (0, 0, 0)$
- B: $3b - (1/2, 1/2, 1/2)$
- X: $3c - (1/2, 1/2, 0)$

A cubic perovskite can be characterized by the *ccp* stacking of its AO_3 layers, what differentiates it from the similar brownmillerite structure. However, a lot of perovskite structures are deduced from or close to the general form $ABX_{3-\delta}$ with δ being the amount of introduced oxygen vacancies, thus, the structures start to deviate from the ideal cubic symmetry. In general, the structural changes arise from the ionic radii of participating species or the arrangement of the BX_6 octahedra, where this octahedra may also be reduced to polyhedra with lower coordination number for $\delta > 0$.

From a crystallographic point of view, the ideal cubic structure does not allow any changes of the atomic positions, thus, a change in symmetry is required for altering atomic positions which is also accompanied by the tilting of the anion octahedron and/or a reduction of the coordination number. These changes in symmetry are highly dependent on the ionic radii of the respective species and can be well predicted by the Goldschmidt tolerance factor t :

$$t = \frac{(r_A + r_X)}{\sqrt{2}(r_B + r_X)}, \quad (2.1)$$

where r is the ionic radii for each ionic species. For the ideal case with oxygen anions occupying X , the formula yields $1 \geq t > 0.9$. For $0.9 \geq t > 0.71$ the structure distorts in a lower symmetric system, such as octahedral or tetrahedral, while for $t > 1$, the perovskite

may adopt the hexagonal symmetry.

The hexagonal symmetry inside perovskite systems deviates in terms of the stacking order. While cubic perovskite crystals exhibit a *ccp* stacking order, a hexagonal perovskite features a hexagonal closed packing (*hcp*) or a sequence of *hcp* and *ccp* stacking of AX_3 layers. The stacking order leads to purely face-sharing octahedra or alternating face- and corner-sharing polyhedra, see Fig. 2.1.1 c,d.

The BX_6 octahedra are also responsible for physical properties which are based on the electronic configuration of the transition metal *B*-cation which is on the other hand influenced by the anion octahedron. In principle, the BX_6 octahedra can be modified in three different ways:

- *B*-cation displacement
- BX_6 rotation/tilt
- BX_6 distortion

The displacement of the *B*-cation occurs if the cation is too small for the octahedral site, while the octahedron itself undergoes an elongation or compression. Such a displacement leads to a symmetrical change towards a tetragonal, trigonal or orthorhombic unit cell. The symmetry change is additionally accompanied by the generation of a permanent electric dipole moment, which is necessary for pyroelectric and (anti)ferroelectric effects. In contrast, if the *A*-cation is too small, the BX_6 octahedron tends to tilt/rotate in order to compensate for the free volume generated by the small cation. The result is a reduction of crystal symmetry. For more information the reader is referred to [24].

A special case is the distortion of the BX_6 octahedron due to either $\delta > 0$ or displacements of the *B*-cation. The octahedron can distort itself in shapes of elongated or compressed octahedra but also to square planar or square pyramidal configurations, accompanied with the loss of bonding between *B* and *X* ions. These distortions are the result of electronic interactions of the cation and anion electron orbitals. The driving force is the reduction of energy by the deformation of the polyhedron in order to remove the degeneration of the electronic ground state. The best-known distortion is the Jahn-Teller distortion which will be discussed in the following.

2.1.2. Jahn-Teller distortion

The Jahn-Teller effect states that a molecule with a symmetrical atomic configuration, such as the BX_6 octahedron in perovskites, and a degenerate ground state (i.e. multiple energetically equivalent ground states), is unstable and will undergo a distortion to remove

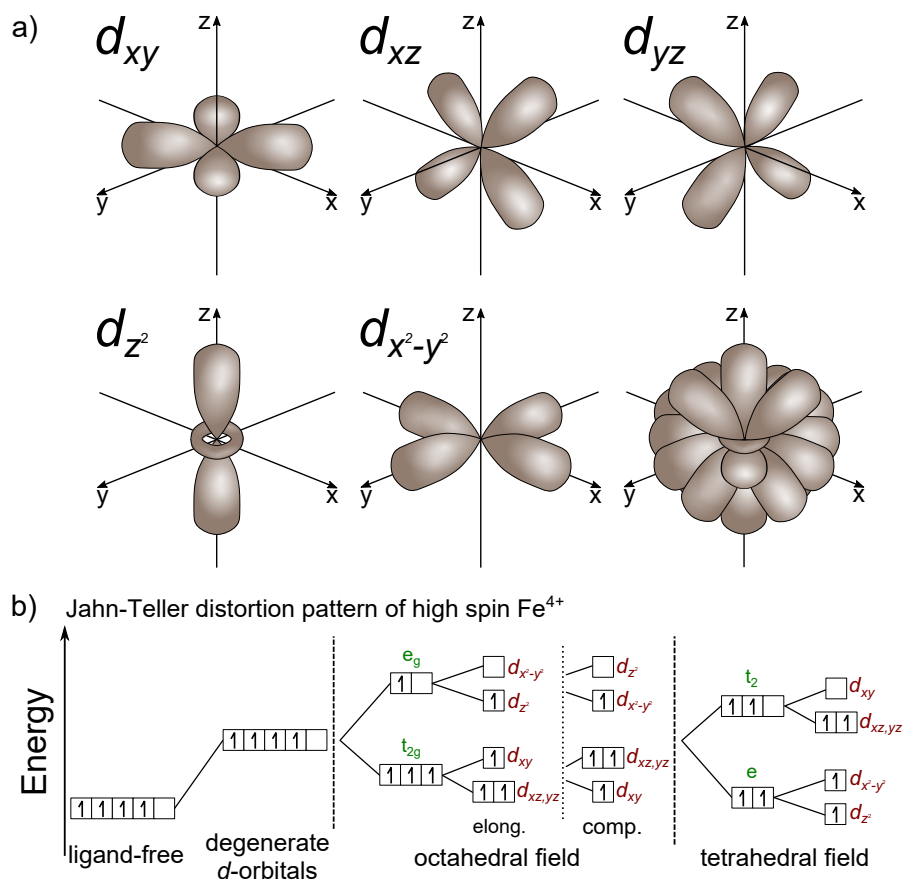


Figure 2.2.: a) Geometrical scheme of the shape and direction of d orbitals. b) Ligand field energy level diagram of the Jahn-Teller distortion of high-spin Fe^{4+} inside an octahedral (elongation and compression) and a possible tetrahedral ligand field.

this electronic degeneracy. From this it follows that transition metal cations such a d -electron configuration are more stable inside distorted octahedrons (or polyhedrons). Such cations are called Jahn-Teller ions. Upon the insertion of the Jahn-Teller cation, for example high-spin Fe^{4+} , into the octahedron, the d orbitals, schematically shown in Fig. 2.2 a, split from a spherical-symmetry into two different energy levels with the electronic configuration $t_{2g}^3 e_g^1$ as depicted in Fig. 2.2 b. The highest double degenerate energy level, the e_g level, contains the d_{z^2} and $d_{x^2-y^2}$ orbitals, while the lower triply degenerate t_{2g} level contains the d_{xy} , d_{xz} and d_{yz} orbitals. The energy difference arises from the stronger inter-electronic repulsion between the e_g orbitals and the donor electrons from the X -ligands. The octahedron may undergo either an elongation or a compression to lower the net-energy of the ligand field. Which distortion the octahedron experiences, depends on the occupation of the e_g orbitals. If the electron occupies the $d_{x^2-y^2}$ orbital, the equatorial orbitals (d_{xy} , d_{xz} and d_{yz}) will then be repelled leading to the compression of the octahedron. On the other hand, an occupation of the d_{z^2} orbital leads to the elongation of the octahedron, since only the axial orbitals will be repelled. Another case is the distortion of a tetrahedral coordination scheme. Here, the energy levels of the orbitals are swapped, due to the different arrangement of the ligands around the center B cation. On the other side, in case of a tetrahedral distortion, the d_{z^2} and $d_{x^2-y^2}$ orbitals possess a lower energy, while the equatorial orbitals d_{xy} , d_{xz} and d_{yz} are higher in energy. This leads to the electronic configuration $e^2 t_2^2$ for high spin Fe^{4+} .

2.1.3. Oxygen vacancy ordering

In case of small concentrations of defects in the anion sublattice, the defects can be assumed to be distributed randomly without interaction. However, for higher defect concentrations, the defects form an ordered arrangement in order to minimize the lattice energy [29]. Besides the formation of cluster or microdomains, the arrangement of vacancies can lead to long-range ordering which induces the formation of new compounds and structures. The vacancy concentration is a function of the oxygen partial pressure and annealing temperature. In case of perovskites with the general formula $ABO_{3-\delta}$, the oxygen vacancy concentration directly affects the coordination of the transition metal cation leading to square-pyramidal or tetrahedral coordination polyhedra. The ordering of such oxygen vacancies directly influence the properties, such as magnetic ordering, which depend on the interaction between the transition metal cation and the direct oxygen neighbours. Fig. 2.3 a,b,c showcase compounds which possess transition metal cations solely coordinated inside a square-pyramid ($\text{CaMnO}_{2.5}$ [30]), tetrahedron (BaZnO_2 [31]) and square-planar (SrFeO_2 [32]), respectively. A high amount of vacancies ($\delta = 0.5$) may change the crystal class, e.g. $\text{BaFeO}_{2.5}$ is a complex oxygen vacancy ordered perovskite,

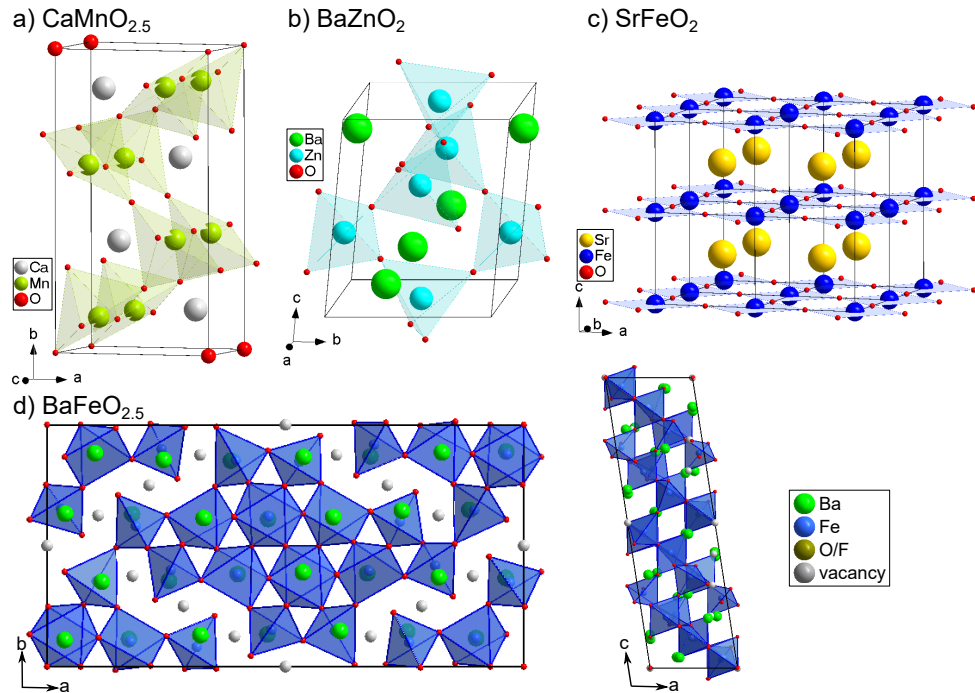
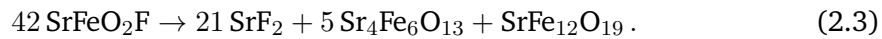


Figure 2.3.: 5- and 4-fold coordinations of transition metal cations (Mn, Zn, Fe) in a) $\text{CaMnO}_{2.5}$ [30] (square-pyramid), b) BaZnO_2 [31] (tetrahedron) and c) SrFeO_2 [32] (square-planar). $\text{BaFeO}_{2.5}$ [33] (d) contains three different iron coordinations: 6-fold, 5-fold and 4-fold. The vacancies (grey balls) form a channel-like network inside the large unit cell.

while the perovskite CaFeO_3 can be reduced to the brownmillerite-structure $\text{CaFeO}_{2.5}$. $\text{BaFeO}_{2.5}$ exhibits three independent iron positions which possess a 6-fold, 5-fold and 4-fold coordination with the corresponding coordination polyhedra as showcased in Fig. 2.3 d. The vacancies form a channel-like network and extend the size of the unit cell reaching 28 formula units per unit cell [33]. Further, this vacancy ordering leads to a symmetry decrease from $Pm\bar{3}m$ (BaFeO_3) [34]) down to monoclinic $P2_1/c$. In contrast, $\text{CaFeO}_{2.5}$ forms the perovskite-related brownmillerite structure [35] where the oxygen vacancies form alternating sheets of FeO_6 octahedra and FeO_4 tetrahedra. The parent symmetry $Pm\bar{3}m$ is reduced to $Pcmm$ with the general formula $\text{Ca}_2\text{Fe}_2\text{O}_5$. The vacancy ordering within $\text{BaFeO}_{2.5}$ and the oxyfluoride $\text{BaFeO}_{2.333}\text{F}_{0.333}$ (see below) are central aspects for the discussion of the experimental results within this work.

2.1.4. Topochemical fluorination of perovskite oxides

The insertion of halides, predominantly fluoride (F^-), introduces a singly negatively charged anion. Especially the combination of oxygen and fluoride in oxyfluoride perovskites promises enhanced properties, such as oxygen ion conduction by lowering the activation energy. Fluoride has the highest electronegativity, thus, influencing the bond characteristics of the $O^{2-} - B^{4+} - F^-$ bond. However, some oxyfluoride materials are metastable and require the preparation via a topochemical treatment [10]. Further, this metastability demands an application below their decomposition temperature, which has to be taken into account for the application as cathode materials for SOFCs. The decomposition of fluorinated perovskite oxides can be used in some cases to estimate the fluorine content. For $BaFeO_2F$ and $SrFeO_2F$ [36] it was shown that the decomposed products can be quantified by Rietveld analysis and thus, the composition can be proven according to



The insertion of fluorine into the anion sublattice may cause the transition metal cation to change its valence state. According to [37], the response of the host lattice can be separated into

- **Reductive exchange:** one O^{2-} anion is substituted with **one** F^- anion, resulting in the reduction of the transition metal cation
- **Anion exchange:** one O^{2-} anion is substituted with **two** F^- anions, leading to no change of the oxidation state
- **Oxidative exchange:** fluorine anions are inserted into interstitial sites, increasing the oxidation state of the transition metal cation.

In this work, the fluorination of $BaFeO_{2.5}$ leads to no change in the oxidation state of Fe^{3+} and thus, the fluorination follows the general formula $BaFeO_{2.5-x/2}F_x$ [11, 12, 38–40]. In the cubic perovskite-type system, only two oxyfluoride phases are possible: $BaFeO_{2.333}F_{0.333}$ and $BaFeO_2F$ [12]. The incorporation of fluorine into $BaFeO_{2.5}$ leads to a symmetry change due to the partial or full occupation of oxygen vacancies: $BaFeO_{2.333}F_{0.333}$ crystallizes in $P2_1/m$ (Fig. 2.4 a), which is a vacancy ordered structure, while $BaFeO_2F$ possesses the space group $Pm\bar{3}m$ (Fig. 2.4 b). The anion vacancies in $BaFeO_{2.333}F_{0.333}$ are indicated as grey balls. In addition to the anion vacancies, one anion

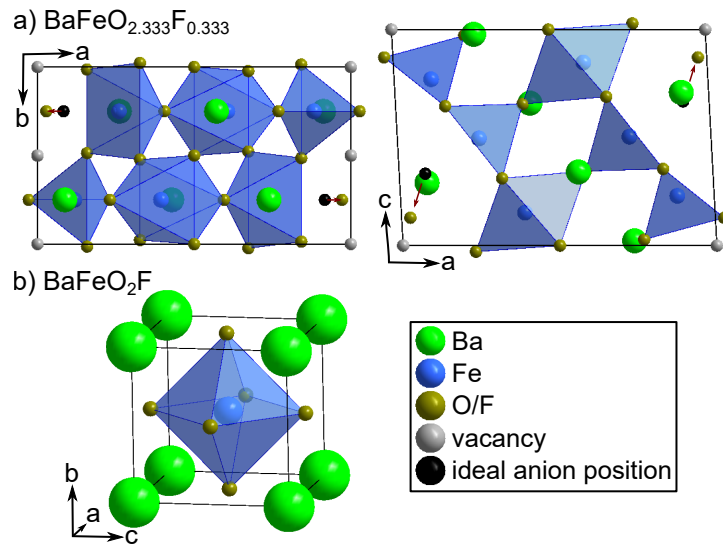


Figure 2.4.: Structures of the topochemically fluorinated compounds of $\text{BaFeO}_{2.5}$: a) $\text{BaFeO}_{2.333}\text{F}_{0.333}$ [12] and b) BaFeO_2F [11]. Vacancies are coloured in grey and the relaxation of the anion from the ideal cubic position (black) is marked as a red arrow.

position is shifted (indicated by red arrows) what results in the formation of the tetrahedral and square-pyramidal coordinations around the Fe cations. The type of fluorination to be used depends on the transition metal species and their electronic configuration of the to-be-fluorinated compound. The transition metal cation can act as an electron donor if its density of states and the states of the oxygen are close to the Fermi level. Otherwise, only the oxygen can be substituted. For example, Sr_2TiO_4 can only be fluorinated to $\text{Sr}_2\text{TiO}_3\text{F}_2$ [41, 42], while Sr_2CuO_3 can be fluorinated to $\text{Sr}_2\text{CuO}_2\text{F}_{2+x}$ [43, 44]. Depending on the desired fluorination reaction (reductive/oxidative/substitutive), a variety of fluorination agents are available [21], which subsequently require an oxidizable or reducible cation, while a substitutive fluorination requires available vacancies which can be occupied by one fluorine. Highly oxidative fluorination agents are fluorine gas and XeF_2 , but especially fluorine gas requires special equipment and handling and the oxidative strength may easily lead to the decomposition of the target phase. For a reductive fluorination, the polymer agents polyvinylidenedifluoride (PVDF) [45] and polytetrafluoroethylene (PTFE) [46] can be used which also guarantee a less aggressive fluorination reaction. The fluorination reaction takes place at around 350 – 450 °C where

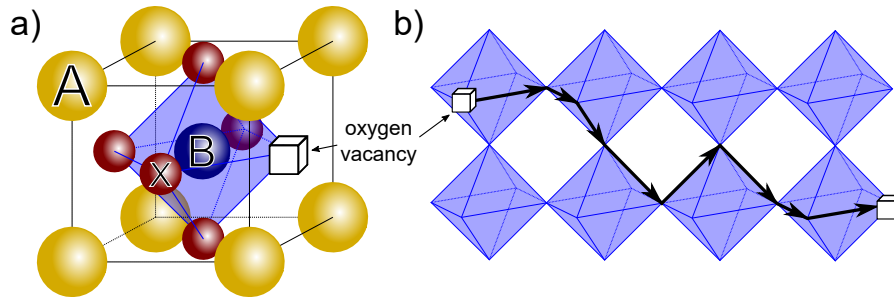


Figure 2.5.: a) Oxygen vacancy inside a BX_6 octahedron and b) the diffusion path of an oxygen ion vacancy following a random path through the bulk.

the polymers decompose into smaller fractions of their polymer chains, though, the reaction is not fully understood yet, but it is assumed that HF is formed during the process. The use of these polymers allow for a homogeneous mixture with the precursor powder or they can be dissolved and then coated on sample material [21, 47]. Nevertheless, the usage of these polymers under an inert atmosphere require a post-annealing under an oxidative atmosphere to burn away carbon residuals.

Another hypothetical method could be the fluorination via interdiffusion, which was not examined, yet, but will be presented in Sec. 3.2. It relies on the concentration gradient between the oxyfluoride and the oxide, where the oxyfluoride serves as the fluorination agent. Here, it was used to prepare $BaFeO_{2.333}F_{0.333}$ by the heterogeneous interdiffusion of $BaFeO_{2.5}$ and $BaFeO_2F$, but also to adjust the fluorine content inside a porous film by a homogeneous interdiffusion of $BaFeO_{2.333}F_{0.333}$ and $BaFeO_{2.5}$ to form $BaFeO_{2.333}F_{0.333}$ inside the film.

2.1.5. Oxygen ion conduction in perovskite materials

The ideal perovskite oxide contains a perfectly stoichiometric octahedron of the form BX_6 . However, in reality the number of anions can deviate leading to a more general formula $ABO_{3-\delta}$, where δ accounts for the number of oxygen vacancies with a value between $0 \leq \delta \leq 1$. The non-stoichiometry of oxygen is thereby a function of temperature and oxygen partial pressure in the surrounding atmosphere, but can also be influenced greatly by the choice of the A and B site cations [24, 27].

The oxygen ion conduction inside perovskite materials relies on the random hopping of oxygen ions into oxygen vacancies or, from a different angle, random hopping of oxygen vacancies from one oxygen lattice site to the next [24]. According to [24], ionic

conductivity inside a perovskite can be described with an Arrhenius-type equation:

$$\sigma T = \sigma_0 \exp\left(\frac{-E_A}{RT}\right), \quad (2.4)$$

where σ is the ionic conductivity, T the temperature, σ_0 the pre-exponential factor and E_A the activation energy. In addition, the formation of oxygen ion vacancies depends on the oxygen partial pressure in the surrounding atmosphere. Thus, the number of vacancies is proportional to the oxygen partial pressure

$$[V_{O^{\cdot\cdot}}] \propto p_{O_2}^{-1/2}. \quad (2.5)$$

Fig. 2.5 a and b depicts an oxygen vacancy inside a cubic perovskite unit cell and its path through the bulk with corner sharing octahedra, respectively. From this it becomes evident that on the one side, the amount of vacancies defines the oxygen ion conduction and on the other side, the symmetry plays an important role in such a way that it dictates the diffusion path. A big advantage of the perovskite crystal system is that its structural integrity is maintained upon higher oxygen non-stoichiometries in contrast to other crystal systems, thus rendering the possibility of high oxygen ion transport. However, oxygen vacancies may be arranged in an ordered manner stabilizing a superstructure or pinned at their lattice site. These factors are detrimental for oxygen ion conduction since these vacancies are unable to participate in the conduction process, thus, the true amount of conducting vacancies is lower than expected from the oxygen (vacancy) stoichiometry and the simple path (Fig. 2.5) is obstructed leading to higher activation energies. It requires a high activation energy to break up the ordering leading to sudden increase of oxygen ion conduction at a certain transition temperature.

2.1.6. Magnetic properties of perovskite materials

An extensive description about magnetism can be found within *Perovskites: Structure-Property Relationships* by Richard J.D. Tilley (Wiley, 2016) [24]. Magnetism in perovskite materials arises from the incorporation of cations showing paramagnetism due to their magnetic moment. Typical magnetic cations are transition metal and lanthanide cations since their d and f shells are only partially filled. In addition, the configuration of the incorporated cations influences the strength of the magnetic moment by adjusting the energy levels of the orbitals (vide supra). In case of $3d$ transition metals, the magnetic moment arises solely from the electron spin and this adjustment leads to the formation of either high spin, intermediate spin or low spin configuration which directly affects the total magnetic moment. The magnetic behaviour is then estimated by the orientation/arrangement of the spins in relation to each other. This ordering is temperature-dependent

and perovskite materials show usually paramagnetic ordering at elevated temperatures. The arrangement at elevated temperatures is dynamic and the orientation of dipoles is continually changing without any interactions. In a magnetic field, these spins will align along the magnetic flux perturbed by thermal motion with a susceptibility following the Curie law:

$$\chi = \frac{C}{T}, \quad (2.6)$$

with C being the Curie constant and T the temperature. The so-called Curie Temperature T_C marks the transition temperature above which ferromagnetic perovskites transform to paramagnetic ordering. In contrast, the antiferromagnetic ordering is transformed into the paramagnetic ordering above the Néel temperature T_N . Well above these temperatures, the paramagnetic susceptibility of ferromagnetic and antiferromagnetic perovskites obey the modified Curie-Weiss laws:

$$\chi = \frac{C}{T - T_C} \quad (\text{ferromagnetism}) \quad (2.7)$$

$$\chi = \frac{C}{T + \phi} \quad (\text{antiferromagnetism}), \quad (2.8)$$

where ϕ is the Weiss constant. A reciprocal fit of $\chi^{-1}(T)$ of the paramagnetic region allows the determination of the Curie temperature or Weiss constant. From the Curie constant C it is possible to calculate the effective magnetic moment μ_{eff} , according to

$$C = \frac{n \cdot \mu_B^2}{3k_B} \cdot \mu_{\text{eff}}^2, \quad (2.9)$$

where n is the number of magnetic atoms and μ_B the Bohr magneton.

2.1.6.1. Exchange interactions

The ordering of magnetic moments below the corresponding transition temperatures requires a certain interaction between the magnetic cations and diamagnetic anions (oxygen/fluorine) of the perovskite material. The magnetic cations inside a cubic perovskite are coordinated inside an octahedron of oxygen (or fluorine) anions which are corner-shared among neighbouring octahedra. This sharing allows the exchange interaction between the electrons of the d orbitals of the cations and the electrons of p orbitals of the anions. Thereby, the exchange interaction can be separated into superexchange and double-exchange interaction which correspond to antiferromagnetic and ferromagnetic ordering, respectively.

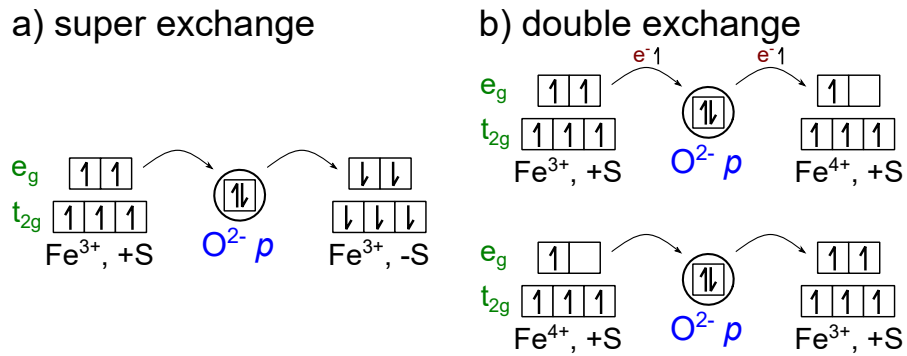


Figure 2.6.: Depiction of the exchange interactions inside an iron containing perovskite for a) superexchange ($\text{Fe}^{3+} +\text{S} \leftrightarrow \text{Fe}^{3+} -\text{S}$) and b) double exchange interaction ($\text{Fe}^{3+} +\text{S} \leftrightarrow \text{Fe}^{4+} +\text{S}$).

The superexchange interaction induces an antiparallel spin alignment between two isoelectronic cations due to the up and down spin of the intermediate anion. From this it follows that most perovskites with a single type of magnetic cation are antiferromagnetic [24]. The spin ordering can form certain patterns which are called A-, C-, E- and G-type ordering depending on the macroscopic arrangement of the spins throughout the whole crystal. For example, the A-type ordering exhibits ferromagnetic ordering along the (001) planes where neighbouring planes are aligned antiparallel. On the other side, in an G-type ordered crystal, each cation has six antiparallel oriented neighbours. On the other hand, the double-exchange mechanism describes the real transfer of an electron from one transition metal cation to an adjacent anion, which already possesses a filled *d*-shell and, in order to accept the transferred electron, has to donate one of its electrons to the next transition metal cation. The key here is that the participating transition metal cations exhibit different oxidation states with high spin electrons. Double-exchange always leads to a ferromagnetic ordering.

2.1.6.2. Spin irregularities

In some materials, the spin ordering can not be resolved due to competing interactions between cations with valence states of more than two (which would otherwise allow an ordering via double or superexchange). This leads to a dynamic reorientation of spins which is described as spin glass behaviour. It results from a disorder between paramagnetic cations and was found for Ru or Mn containing perovskites [24]. The magnetic order of spins can also deviate from perfection by a small tilting or canting

of a small angle leading to spin canting. This spin canting occurs in antiferromagnetic lattices and results in a weak ferromagnetic coupling due to the canted spins. The spin canting may depend on the type of cation and leads to specific types of orderings within compounds with multiple cation types.

2.2. ^{57}Fe Mössbauer spectroscopy

The characterization technique Mössbauer spectroscopy is based on the recoilless emission and resonant absorption of γ -radiation by atomic nuclei. The Mössbauer effect describes the process of the recoilless absorption and fluorescence where the whole energy of an absorbed γ -quantum is used to excite the atomic nucleus, which then releases a γ -quantum with the exact same energy upon relaxation. Experimentally this is utilized to by combining the emission of γ -radiation with the Doppler-effect and measuring the transmitted (through sample material) γ -radiation. The Doppler-effect leads to a shift of the sharp line width of the γ -radiation. This shift compensates the perturbations of chemical and physical environment onto the specimen nuclei which influence the detailed positions of the core energy levels. It allows for a precise description of magnetic, chemical and structural properties.

In reality, the nuclei are perturbed by electric and magnetic fields created by the surrounding electrons and atoms. This perturbation or nuclear hyperfine interaction leads to a shift, the isomer shift δ , and splitting, due to the splitting of degenerate energy levels, of the observed Mössbauer lines. The isomer shift arises from different electron and charge distributions around isomers and its value is related to a reference absorber (usually α -Fe). The splitting can be divided into electric quadrupole and magnetic dipole interaction. The electric quadrupole splitting arises from the interaction of the magnetic spins with the electric field gradient, thus, leading to a degeneration of the single ground states into two substates. In contrast, the magnetic field hyperfine field splitting leads to a sextet due to the degeneration into six substates. All these interactions may be observed as a combined effect, e.g. the center of a sextet or doublet is shifted due to the isomer shift. Fig. 2.7 depicts a sextet and a doublet inside a Mössbauer spectrum. The doublet exhibits a significant isomer shift δ .

As a source material ^{57}Co has shown to exhibit the highest possible activity and narrow line width. ^{57}Co decays by electron capture¹ into ^{57}Fe . [28]

The Mössbauer spectroscopy allows the characterization of the chemical and magnetic environment around Fe, and thus, the Fe-cation itself, especially the oxidation state can be identified by comparison with known compounds. It was used within this thesis to

¹The nucleus captures an inner shell electron and converts a proton into a neutron.

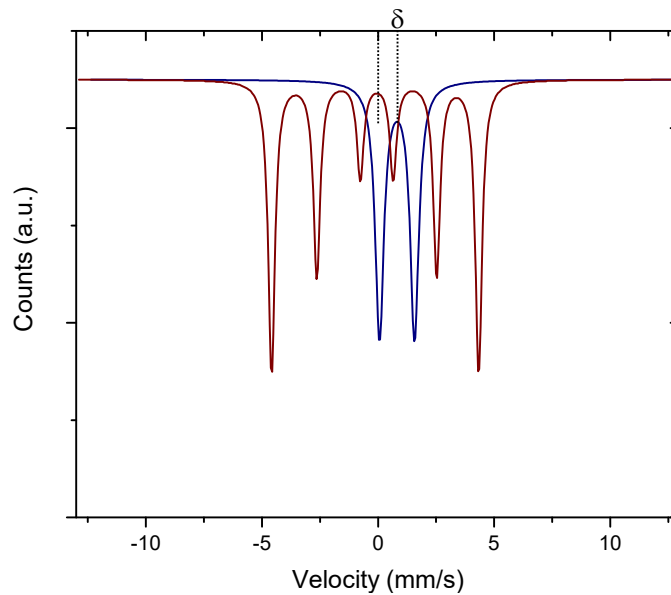


Figure 2.7.: Mössbauer spectrum with one sextet and a doublet. The doublet exhibits an isomer shift δ .

investigate the iron coordination within the newly found modification of $\text{BaFeO}_{2.667}$ in Sec. 3.1 (measured and evaluated by Dr. Abhishek Sarkar and Dr. Robert Kruk) and the magnetic ordering and anion coordination of/around the Fe-cation inside epitaxial $\text{BaFeO}_{2.5}$ and BaFeO_2F in Sec. 3.3 (measured and analysed by Dr. Ralf Witte).

2.3. Principles of diffusion

This section will outline Fick's laws of diffusion together with an elevated analysis model developed by Matano [48] on the base of Boltzmann's improvement of Fick's second law [49–51].

2.3.1. Fick's laws of diffusion

Diffusion is the movement of particles driven by a gradient in concentration and is a thermally activated process. Fick came up with the concept of a connecting parameter between particle flux and gradient in chemical concentration, leading to Fick's **first** law of

diffusion:

$$\mathbf{J} = -D\nabla C, \quad (2.10)$$

with \mathbf{J} being the vector of flux of particles and ∇C their concentration gradient vector, which always points towards the most rapid increase. D is the diffusion coefficient and is a factor of proportionality which interconnects the underlying process of equalization in concentration. The equation of continuity describes the change in the particle flux over time

$$-\nabla \mathbf{J} = \frac{\partial C}{\partial t} \quad (2.11)$$

and is needed to formulate Fick's **second** law of diffusion, which is a combination of the first law and the continuity law:

$$\frac{\partial C}{\partial t} = \nabla \cdot (D\nabla C), \quad (2.12)$$

which simplifies to

$$\frac{\partial C}{\partial t} = D\Delta C, \quad (2.13)$$

if the diffusion is independent of concentration and in this case D is linear.

The first and second law may be simplified in one dimensional diffusion direction:

$$J_x = -D \frac{\partial C}{\partial x} \quad (2.14)$$

$$\frac{\partial C}{\partial t} = D \frac{\partial^2 C}{\partial x^2}. \quad (2.15)$$

In any case, the second law is a linear second-order partial differential equation, which requires the knowledge of initial and boundary conditions.

If the diffusion depends on the concentration of the participating species, Fick's second law becomes more complex, since it loses its linearity and the diffusion coefficient D becomes also concentration dependent and turns into the interdiffusion coefficient \tilde{D} :

$$\frac{\partial C}{\partial t} = \frac{\partial C}{\partial x} \left[\tilde{D}(C) \frac{\partial C}{\partial x} \right]. \quad (2.16)$$

This equation cannot be solved analytically for an arbitrary concentration dependence of $\tilde{D}(C)$. However, the Boltzmann-Matano analysis is one of the few methods which offers a way to calculate $\tilde{D}(C)$ from concentration-depth profiles and will be introduced in the next subsection.

2.3.2. Boltzmann-Matano analysis

Boltzmann transformed the nonlinear partial differential equation 2.16 for \tilde{D} being a function of $C(x)$ alone. For this purpose he introduced the variable

$$\eta \equiv \frac{x}{2\sqrt{t}}, \quad (2.17)$$

which combines x and t . By inserting this variable into eqn. 2.16 eventually transforms Fick's second law into an ordinary differential equation:

$$-2\eta \frac{dC}{d\eta} = \frac{d}{d\eta} \left[\tilde{D}(C) \frac{dC}{d\eta} \right]. \quad (2.18)$$

This form of Fick's second law now allows to extract the interdiffusion coefficient \tilde{D} from an experimental concentration-depth profile $C(x)$. Matano provided appropriate boundary conditions by considering a diffusion couple (two semi-infinite bars in contact) at time $t = 0$, from which the conditions then yield

$$C = C_L \quad \text{for} \quad (x < 0, t = 0), \quad (2.19)$$

$$C = C_R \quad \text{for} \quad (x > 0, t = 0). \quad (2.20)$$

During a diffusion experiment, a concentration profile $C(x)$ develops after a time t . This profile can be measured on the basis of a cross section of the diffusion zone. By applying the boundary conditions, eqn. 2.18 yields

$$\tilde{D}(C^*) = -2 \frac{\int_{C_L}^{C^*} \eta dC}{(dC/d\eta)_{C=C^*}}, \quad (2.21)$$

which then becomes -after back transformation into space and time coordinates- the Boltzmann-Matano equation:

$$\tilde{D}(C^*) = -\frac{1}{2t} \frac{\int_{C_L}^{C^*} (x - x_M) dC}{(dC/dx)_{C^*}}. \quad (2.22)$$

Note that x_M describes the position of the Matano plane which is the average distance weighed concentration, meaning equal integrals on the left and right hand side of the plane, and is added after the experiment. By setting the Matano plane as the origin of the x -axis ($x_M = 0$), it can simply be found by

$$\int_{C_R}^{C_M} x dC + \int_{C_M}^{C_L} x dC = 0. \quad (2.23)$$

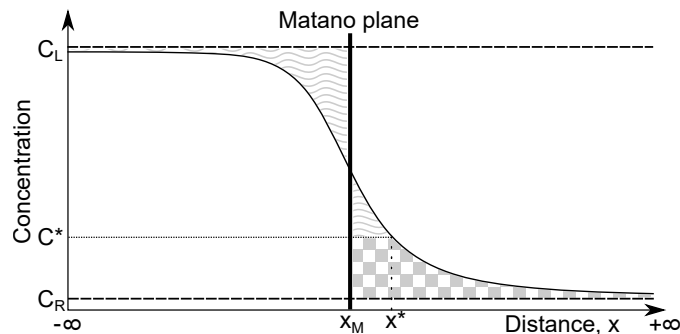


Figure 2.8.: Concentration profile of a diffusion couple at time t with the C_* at location x_* with starting concentrations C_L and C_R .

Fig. 2.8 illustrates the Boltzmann-Matano equation. Eqn. 2.22 holds true for an infinite system, thus, the diffusion must not reach the borders of the system. For a detailed derivation the reader is kindly referred to the literature [51, 52].

2.4. X-ray diffraction

The term diffraction describes the interaction of a wave when encountering an object or aperture resulting in the generation of a pattern behind that object. The shape of that pattern is thereby depending on the wavelength of the incident wave and the geometrical properties of the object resulting in the phenomena of constructive or destructive interference. Thus, one can extract information about the diffracting object by analysing the as-generated pattern. The important point is that the waves themselves do not produce an image of the object, but "shadow" which contains geometrical information.

In the following, the principles of radiation generation and powder diffraction of X-rays will be discussed. The diffraction with X-rays is one of the core methods inside this work. It allows for an easy and fast, but also comprehensive evaluation of structural properties. In addition, a brief discussion of thin film diffraction with X-rays will be given.

The chapter will be concluded with the introduction of the Rietveld method, which is a powerful tool for analysing powder diffraction data and extracting crystallographic information.

The phenomena of X-ray diffraction and its derived applications can be found in various text books which are used to give a small overview over this topic in the following [53–56].

2.4.1. Generation of diffraction radiation

The application of short-wave electromagnetic radiation, such as X-rays or moving electrons and neutrons, allows the analysis of unit cell dimensions and distances inside a crystallographic lattice. Due to the atomic radii of a few tenths of Ångstrom up to several Ångstroms, those short-wave radiation coincides with the atomic sizes. The pseudo-infinite configuration of a crystal lattice serves as a suitable object for diffraction of such incoming electromagnetic waves. Table 2.1 compares the three types of electromagnetic waves. Since the diffraction via X-rays is one of the core evaluation methods within this work, the main attention will be drawn onto the field of X-rays. Though, the three types can be used complementary to gain a broader overview and a full set of information from the sample material.

For the generation of X-ray radiation two different possibilities are available. Though, both rely on the acceleration or deceleration of charge. The first and simple one, is the generation of X-rays inside a sealed X-ray tube. Here, electrons are emitted from a electrically heated cathode, such as a tungsten filament, and accelerated by an electrical potential towards cooled anode, such as copper or molybdenum. The typical potential is maintained at 30 to 60 kV and the current through the cathode lies between 10 to 50 mA. Upon impact of the electrons on the anode, the electrons penetrate the material and are decelerated by interaction with electrostatic fields of the anode atoms. The deceleration results in the emission of bremsstrahlung (1 - 2 %), due to the change of their momentum, and mainly heat (98 - 99 %). Simultaneously, the incoming electrons may ionize the atoms of the anode material, either by direct exchange of energy or other high-energy radiation, such as high-energy bremsstrahlung, leading to the ejection of a core-shell electron. The excited atom can return to the energetic ground state, by filling the core-shell electron vacancy by an electron from another shell. This electron transition releases energy by the emission of an X-ray with wavelength characteristic to the anode material. Such electron transitions are bound to selection rules, schematically shown in Figure 2.9, leading to the unique X-ray spectrum characteristic for the anode material. The selection rules are as follows:

- transitions inside one main shell are forbidden, for the principal quantum number² n must hold $\Delta n \neq 0$.
- the angular momentum quantum number l is only allowed to change by ± 1 ; $\Delta l = 0$

²Quantum numbers: n - principal quantum number, describes the distance between electron and core, i.e. the shell; l - angular momentum quantum number, describes the angular momentum and shape of the orbital; j - total angular momentum quantum number, it combines the spin s and the angular momentum l of a particle.

forbidden.

- the total angular momentum quantum number j can change by ± 1 and 0.

From these selection rules, the emitted X-ray radiation can be named. If a hole in the K -shell is filled, then the radiation is called K -radiation, while the indices α and β describe from which shell the electron drops: α stands for a neighbouring shell ($\Delta n = 1$) and β for any other ($\Delta n > 1$). In addition, the numerics 1, 2,... signal a transition from varying (total) angular momentum quantum numbers. Figure 2.9 also shows, how an X-ray spectrum is filtered, when leaving the X-ray tube. Such filters are made out of materials which have an absorption edge close to the K_β wavelength, reducing the intensity below this edge by a tremendous amount. They come to use in a powder diffraction experiment, where monochromatic radiation together with a maximum of the ratio of intensity in characteristic radiation and bremsstrahlung are desired (both kinds of radiation are depending on the excitation potential). In case of a Cu anode, this maximum is reached at 36 kV. The combination of $K_{\alpha 1}$ and $K_{\alpha 2}$ is acceptable, since the removal of $K_{\alpha 2}$ component would drastically reduce the overall outgoing intensity, and thereby increasing the time for a satisfying experimental result. The angular divergence of the outgoing beam can be reduced by collimation. A high divergence leads to broad and asymmetric reflections. Both, collimation and monochromatization, have to be done carefully without unnecessary loss of intensity, thus, a trade-off has to be found. Basic experimental setups will be discussed later. Another method, which is in principle similar, is the use of a rotating anode. Here, the anode rotates at a high speed, while cooled with water. The rotation and cooling increase the amount of bombarded cooled anode area, thus, enabling a higher power input and simultaneously a higher X-ray beam intensity. The second method for producing X-ray radiation for experimental use, is the so-called synchrotron radiation source, which are the most powerful sources for X-rays. X-ray radiation is harvested from charged particles moving on a circular orbit. These particles are routed by a magnetic field accelerating the particles towards the center of the ring and are moving at a relativistic speed. Due to the constant change of momentum, the particle flux emits a constant spectrum of X-rays tangentially to its movement, which is of brilliant quality and coherence. However, the huge drawback are the immense costs for maintaining a synchrotron source. Nevertheless, synchrotron radiation sources are a highly desired, but the availability is restricted to selected synchrotron sites.

2.4.2. Principles of powder diffraction

Max von Laue firstly described the discovery of diffraction of X-rays proving the wave-like nature of X-rays [58, 59]. Before discussing the principles of powder diffraction, one

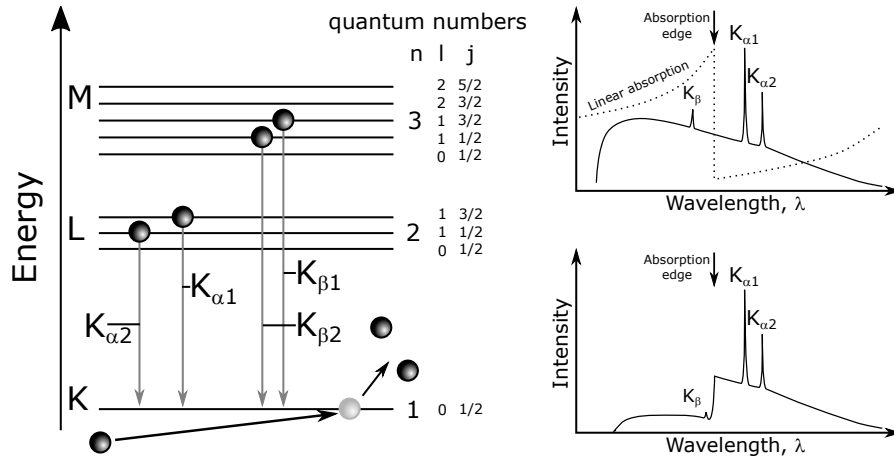


Figure 2.9.: Electron transition according to the selection rules resulting in the characteristic X-ray spectrum, with the characteristic peaks for $K_{\alpha/\beta}$ and the accompanying bremsstrahlung. Implementing a β -filter (dotted line) leads to a filtered X-ray spectrum.[53, 57]

Table 2.1.: Comparison of three types of radiation used in diffraction experiments; f - atomic scattering function, s - $\sin \theta/\lambda$, Z - atomic number [53].

	X-rays (conv./synch.)	Neutrons	Electrons
Nature	wave (photon)	particle (fermion)	particle (fermion)
Scattering by	electron density	nuclei and magnetic spins of electrons	electrostatic potential
Scattering function	$f(s) \propto Z$	f is constant at all s	$f(s) \propto Z^{1/3}$
Wavelength range, λ	0.5 - 2.5/0.1 - 10 Å	1 Å	0.02 - 0.05 Å
Wavelength selection	fixed, $K_{\alpha,\beta}$ /variable	variable	variable
Lattice image	reciprocal	reciprocal	reciprocal/direct
Use to determine atomic structure	relative simple	relative simple	very complex
Theory of diffraction	kinematical	kinematical	dynamical

has to consider the interaction of X-rays with matter and how to approach this "black box" first. In general, the interaction of X-rays with matter can be approached via two different theoretical assumptions: kinematical and dynamical diffraction. The kinematical diffraction describes that an X-ray beam is only diffracted once inside a crystal and does not diffract more than once with the crystal lattice. Thus, the interaction between beam and crystal is negligibly small. This requires the powder to fulfil several preconditions. The crystals inside the powder have to consist out of several smaller units, crystallites, which have to be slightly misaligned to guarantee a statistically sufficient distribution of each orientation. This misalignment has to be large enough so that the beam does not interact with matter outside such crystallites. The kinematical theory is applied to X-ray and neutron scattering (see Table 2.1), since it describes the interaction of X-rays with a powder (mosaic of many crystallites) simple and accurate. On the other side, the theory of dynamical diffraction states that the beam is allowed to interact with matter more than once, including scattering and other interactions. Hence, this theory necessitates a much more complex mathematical description.

A crystal lattice is a (near) infinite arrangement of stacked atoms in periodic order. The periodicity and arrangement allow the X-ray beam to be diffracted in such a way that an interference pattern can be observed. The observed diffraction pattern is the transformation of the lattice into an image in reciprocal space. Hence, in order to become a real image of the lattice, the pattern has to be transformed back into real space. Further, a diffraction of a lattice will be represented by a point in reciprocal space, though, the reciprocal lattice (arrangement of diffraction points) maintains the symmetry of the real lattice. The concept of a reciprocal lattice was first introduced by Ewald in 1921 [60]. Further, Ewald introduced the concept of the Ewald's sphere, which states that an elastically scattered wave with wavelength λ and wavevector \vec{k} produces a diffraction if the end of the scattered wave with vector \vec{k}' coincides with a point in reciprocal space, by moving the sphere by the length of \vec{k} away from the origin. Here the wavevectors \vec{k} and \vec{k}' have the same length $1/\lambda$ and the angle between \vec{k} and \vec{k}' is 2θ . This will be discussed in detail later this section.

Determining factors for a successful scattering are the wavelength λ , the lattice distance d and the incident angle θ . In 1913, this relation was formulated by Lawrence Bragg and his father William Bragg [61], and thus named Bragg's law of X-ray diffraction (which can be easily transferred into the Laue condition):

$$2d \sin \theta = n\lambda. \quad (2.24)$$

This formalism is depicted in Figure 2.10 a, though, this is a sufficient simplification of the diffraction of X-rays at atoms. So far the centre of diffraction was not defined precisely

and simply assigned to the atom as a whole. In fact, scattering occurs at the electron distribution around a nucleus. Figure 2.10 b schematically shows the diffraction at an atom by assuming a spherical electron distribution around the nucleus. At this point it may be noted that the interaction of an X-ray with an electron leads to the formation of a Hertzian dipole, thus, emitting a wave in every direction with the same frequency and wavelength as the incident X-ray wave. Thus, the angular dependency is directly related to the electron distribution around the core. This type of scattering is also called coherent scattering and the coherent wave has a phase difference of π . Scattering of the electron shell is called atomic scattering factor or atomic form factor f and is the Fourier transformation of the electron density around a nucleus³. This scattering ability is a function of the wavelength and the atomic form factor of each element can be found in *International tables for crystallography* [62]. From this it follows that the scattered amplitude is the result of the interference of multiple spherical waves. The thermal motion t of an atom leads to small deviations of the diffraction condition due to the movement of the refraction center. The frequency of thermal motion is much smaller, than the X-ray wave frequency, hence, a correcting factor has to be added. This factor is called Debye-Waller factor and respects the average center position of an atom. The considerations for 1-dimensional diffraction can easily be expanded into the 3-dimensional case. By placing an arbitrary amount of atoms N in a well-defined periodic distance in one dimension, their intensity functions overlap and produce a well-defined diffraction pattern at certain points in diffraction (reciprocal) space, requiring one integer for their description (h). The diffraction of a unit cell, which is the smallest unit of a 3-dimensional periodic arrangement of atoms, with a certain number of identical atoms, produces a diffraction pattern, which requires three independent integers, the so-called Miller indices (h, k, l). This can be formalised by:

$$I_{1D}(\phi) \propto f^2(\phi) \frac{\sin^2 N h \pi}{\sin^2 h \pi} \rightarrow I_{3D}(\phi) \propto f^2(\phi) \frac{\sin^2 N_1 h \pi}{\sin^2 h \pi} \frac{\sin^2 N_2 k \pi}{\sin^2 k \pi} \frac{\sin^2 N_3 l \pi}{\sin^2 l \pi}. \quad (2.25)$$

Since unit cells often contain more than one atom, the atomic scattering function $f(\phi)$ has to be extended to the so-called structure factor $F(\phi)$. The structure factor has to be expressed in terms of the Miller indices (hkl) and thus is written as

$$I_{3D}(\phi) \propto F^2(hkl) \frac{\sin^2 U_1 h \pi}{\sin^2 h \pi} \frac{\sin^2 U_2 k \pi}{\sin^2 k \pi} \frac{\sin^2 U_3 l \pi}{\sin^2 l \pi}, \quad (2.26)$$

where $U_{1,2,3}$ is the number of unit cells in the specific direction. If the unit cell contains a number of atoms (j) of more than one element, the structure factor has to be extended

³For an extensive derivation the reader is referred to [57]

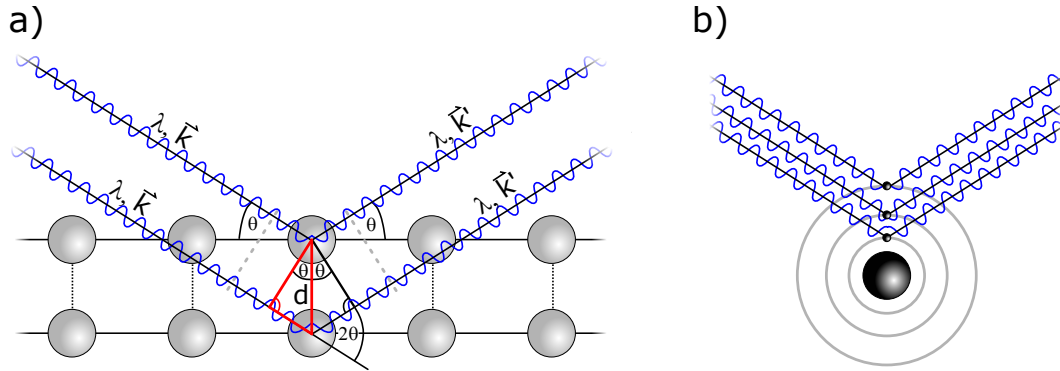


Figure 2.10.: Elastic scattering of X-ray waves: (a) geometric illustration of Bragg's law, (b) elastic scattering at electron density (schematic) of an atom.

respecting the scatter ability $f^j(s)$ of each atom (j), the level of occupation g^j inside the unit cell and their positions ($\mathbf{x}^j = (x^j, y^j, z^j)$). The structure factor has to account for the change in phase angle of the beam being diffracted at different scattering points. Hence, it turns into an imaginary number and can also be written as a vector. This so-called structure amplitude F_{hkl} can be written as

$$F_{hkl} = \sum_{j=1}^n g^j f^j(s) \exp[2\pi i(hx^j + ky^j + lz^j)], \quad (2.27)$$

with s is $\sin \theta_{hkl}/\lambda$. The imaginary product $i\pi(hx^j + ky^j + lz^j)$ describes the phase angle of the diffracted wave at the j th atom inside the unit cell. Thus, the structure factor is given as the absolute value of the vector $|F_{hkl}|^2$.

A measured intensity is mostly a relative value and not absolute, hence, a scaling factor s has to be introduced which, for example, is connected to the number of unit cells U . Further, different geometrical and instrumental effects and such effects arising from the sample properties aside the structural factor also influence the scattered intensity. They may be summed up in the factor $G(\theta)$, which is a function of the diffraction angle θ . Thus, the overall measured intensity can be written as

$$I_{hkl} = s \times G(\theta) \times |F_{hkl}|^2. \quad (2.28)$$

The Bragg's law gave a first geometrical interpretation of constructive interference conditions. By combining Bragg's law and the Ewald's sphere, the origin of a powder pattern of a polycrystalline sample can be understood. Figure 2.10 a depicts the diffraction condition

for the 2-dimensional case. In a 3-dimensional case, the condition $\vec{k}' - \vec{k} = \vec{d}_{hkl}^*$ holds true in such a way that the ends of \vec{k}' and \vec{d}_{hkl}^* form a ring at the surface of the Ewald's sphere perpendicular to \vec{k} assuming the amount of crystallites satisfying the diffraction condition to be near infinity. This ring is the base of a cone inside the Ewald's sphere which apex coincides with the centre of the Ewald's sphere and the wavevectors \vec{k}' form the mantle, thus, the angle of the cone takes the value 4θ . Figure 2.11 depicts this construction for a polycrystalline sample. The intensity of a Debye-Scherrer ring can be assumed to be

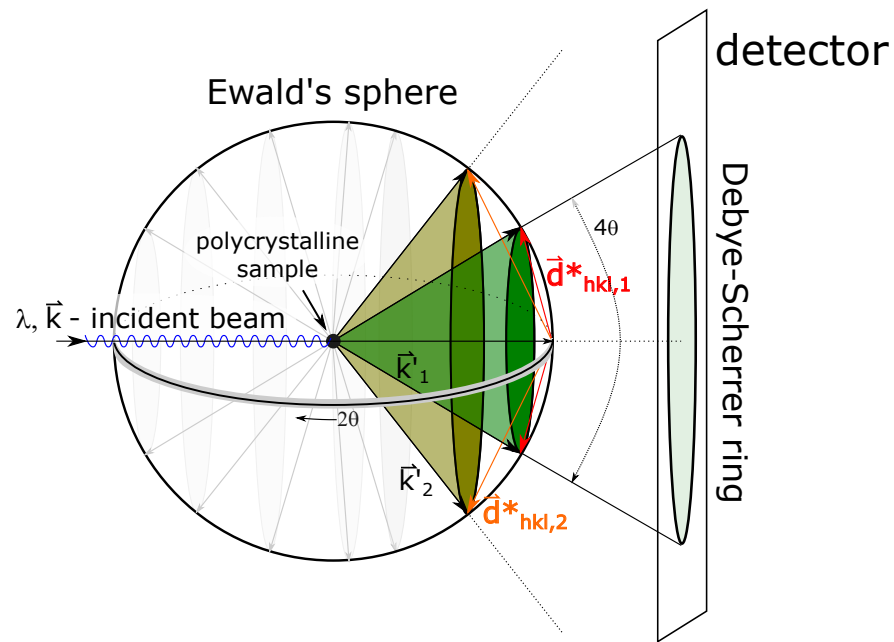


Figure 2.11.: Geometrical construction of the Ewald's sphere. The two diffracted waves \vec{k}'_1 and \vec{k}'_2 spanning the diffraction cones 1 and 2, satisfying the diffraction condition with the reciprocal lattice vector $\vec{d}_{hkl,1}^*$ and $\vec{d}_{hkl,2}^*$, respectively. The diffraction cones form so-called Debye-Scherrer rings on a detector plane, named after early inventors of diffraction cameras.

constant along its circumference. Hence, only a small rectangle of the whole range is measured in a diffraction experiment in dependency of 2θ (see Figure 2.11), which yields the standard powder diffraction pattern.

Equation 2.28 states that the relative intensity of a reflection depends not only on the Miller indices, but also on other contributions perturbing the delta-function of the Bragg's law.

These contributions are also depending on the diffraction angle 2θ . The understanding of such a powder diffraction pattern will be discussed in Sec. 2.4.4.

2.4.3. Experimental setups for powder XRD

One of the most common setups is the Bragg-Brentano geometry. This geometry allows for a rapid analysis of sample material combined with a high intensity, but is susceptible for preferred orientation. Figure 2.12 a) schematically shows a Bragg-Brentano configuration with moving source and detector around the sample position. Source and detector are mounted on the goniometer circle in such a way that the focal point of the source and receiving slit of the detector coincide with the circumference of the goniometer circle with the sample in its center. In addition, their movement is coupled to each other. Source, sample and detector form the focussing circle ensuring the sample surface to be at the central point. The radius of the focus circle is inversely proportional to θ . Various slits can be applied to manipulate the divergent X-ray beam. First, a soller slit after the X-ray tube can be installed to reduce the divergence of the beam. Sollers slits are a stack of parallel high absorbing metal platelets, which extract the divergent share of the X-ray beam by only allowing waves with a very small divergence to pass through. A divergence slit is additionally needed to control the irradiated area of the sample surface by limiting the beam dimension inside the focussing circle. On the detector side, a receiving slit can be applied to control the area contributing to the detector signal. In addition, another soller slit can be installed to cut out highly divergent shares of the X-ray beam. The total number of slits and their aperture can be freely chosen, depending on the desired measurement. However, the usage of slits reduce the overall intensity of the beam and thus, increase the measurement time for a satisfying result. On the other side, the irradiated area and detectable beam intensity also depends on the radius of the focussing circle. A large focussing circle, and thus a low diffraction angle θ , leads to a very large area of irradiation what is directly linked to a high intensity and vice versa. Although the total volume may be equivalent, the absorption of X-rays $\tau(\theta)$ inside the sample material and the beam being scattered at lattices closer to the surface, lead to a lower detectable intensity, as schematically shown in Figure 2.12 b). To overcome this intrinsic disadvantage of the angular dependency of intensity, slits with variable aperture can be used to increase the passing intensity with increasing measurement angle.

2.4.4. Intensity and shape of reflections inside powder diffraction patterns

The measured powder diffraction pattern contains several reflections differing in position, shape and intensity. First, the position depends on the chosen wavelength and the

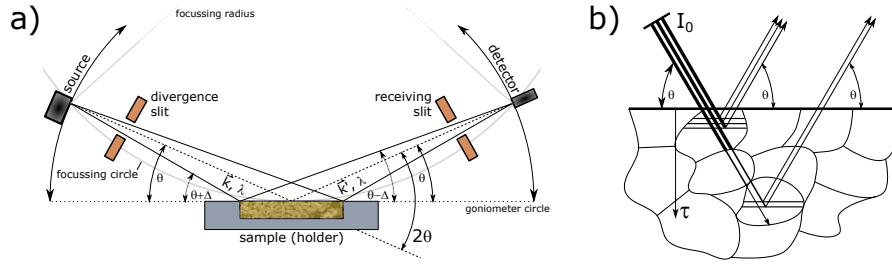


Figure 2.12.: Schematical concept of a) Bragg-Brentano geometry and b) weakening of penetrating X-ray beam coupled with decrease of detectable intensity.

interplanar distance d_{hkl} of the crystal. The latter one is a function of the lattice parameters and Miller indices, which are subjected to Bragg's condition, as discussed above. Other factors perturbing the theoretical peak position origin from instrumental sources, namely the axial divergence of the diffracting beam, sample displacement, misalignment of source or detector and absorption.

The observed shapes of reflections can be mathematically described by the so-called peak shape function (PSF) which is a convolution of three functions: instrumental broadening Ω , wavelength Λ and specimen itself Ψ , plus a certain background b :

$$PSF(\theta) = \Omega(\theta) \otimes \Lambda(\theta) \otimes \Psi(\theta) + b(\theta). \quad (2.29)$$

In a first approximation, the PSF for describing the shape properly is a (Pseudo-)Voigt function, which weights the Lorentzian and Gaussian contributions and accounts for the centrosymmetry of reflection peaks. The sample function Ψ , which is of interest in terms of material characterization, will be discussed in the following. Instrumental broadening Ω and wavelength contributions Λ to the PSF and their determination will be summed up in the fundamental parameter approach (2.4.6).

Ideally, the specimen function is a δ function with discrete reflexes. In reality, deviations from the kinematical model and physical properties of the specimen crystal can affect the peak width. Small and/or strained crystallites lead to a substantial broadening of the observed reflection. Both show an angular dependency, where crystallite size (τ) effects are more predominant at low values while microstrain (ϵ) at higher values of θ . These isotropic influences can be described in by the Scherrer equation:

$$\beta = \frac{\lambda}{\tau \cdot \cos \theta} \quad (2.30)$$

and

$$\beta = k \cdot \epsilon \cdot \tan \theta, \quad (2.31)$$

where k depends on the definition of ϵ and β is the excess width in addition to the other contributions. Beside this, anisotropic peak broadening occurs, when an exceptional anisotropic straining in one direction within the crystal exists. It may be described by spherical harmonics or the Stephens' model [63].

Asymmetry of a peak usually arises at low angles due to instrumental factors, but also due to the non-zero curvature of the Debye-rings. Asymmetry of peaks lead to a broadening of the peak towards the low angle side, while the high angle side remains unaffected. Instrumental factors, such as axial divergence and non-ideal specimen geometry, are the major parts and can be reduced by a proper alignment of the setup and by reducing the axial divergence of the beam (e.g. soller slits). Further, it can be taken into account via the fundamental parameter approach covered in the next section.

On the other side, the observed intensity of a reflection can be given by extending the Equation 2.28 to:

$$I_{hkl} = K \times p_{hkl} \times L_{\theta} \times P_{\theta} \times A_{\theta} \times T_{hkl} \times E_{hkl} \times |F_{hkl}|^2, \quad (2.32)$$

where p_{hkl} is the multiplicity factor, which accounts for the multiplicity of eventual symmetrically equivalent points in reciprocal lattice. L_{θ} is the Lorentz multiplier and P_{θ} the polarization factor, which are also combined into LP_{θ} , the Lorentz polarization factor. On the one hand, it accounts for the density of equivalent reciprocal lattice points on the Ewald's sphere, what is proportional to $1/\sin \theta$. On the other hand it respects the even distribution of intensity along the Debye-Scherrer ring, which results in a cutting of observed intensity, due to the interception of the ring by the detector slit, thus, being direct proportional to $1/\sin 2\theta$. A_{θ} is the absorption of the incident and diffracted beams, qualitatively schematized in Figure 2.11. T_{hkl} is the preferred orientation factor, accounting for a possible deviation from the random distribution of lattice orientations. E_{hkl} is the extinction multiplier, treating deviations from the kinematical theory⁴. Thus, the observed intensity can be divided into angular dependences, indicated by the subscript θ , and lattice depend functions, indicated by (hkl) as subscripts, i.e. a Bragg angle dependence means a dependency upon the length of the corresponding lattice vector d^*_{hkl} , while a function of (hkl) additionally includes the direction of the corresponding lattice vector d^*_{hkl} .

⁴ T_{hkl} and E_{hkl} were not observed throughout the scope of this work and will therefore be neglected.

2.4.5. Thin film X-ray diffraction techniques

Polycrystalline films on polycrystalline substrates can be compared to powder diffraction samples in such a way that the arrangement of lattice planes in polycrystalline films of sufficient thickness is as random as in polycrystalline powder samples. Hence, the outcome of XRD experiments on such films have a lot in common with powder samples with one exception. The absorption of x-rays travelling through the film material results in a lowered intensity for layered structures or the substrate. Hence, a quantitative analysis can not be done solely relying on the observed intensities.

X-ray diffraction measurements on thin films is a powerful tool to describe several properties depending on the film morphology. A variety of techniques exist to characterize film thickness, out-of-plane lattice parameter, surface roughness and film orientation. Thereby, two different methods are applicable which differ in the coupling of incident and refracted beam. The symmetrical coupling is the same as for powder diffraction ($\theta/2\theta$) and in case of single crystalline epitaxial films yields the out-of-plane lattice parameter. In contrast, the asymmetrical coupling is determined by a fixed incident beam angle ω which is kept at a very low angle (several degrees or less) and the detector is used to collect refraction data over the whole range of 2θ . This latter method yields information of crystal lattices inclined with the substrate surface. Throughout this work, symmetrical coupling was used for thin film analysis.

In contrast, epitaxial films differ in terms of morphology. The term "epitaxial" describes the growth of a layer consisting of a single crystalline structure on a substrate material in such a way that growing crystal and substrate have ideally the same orientation. A $2\theta/\theta$ scan of an epitaxial film exhibits additional features. Beside the observable hkl -reflection, the reflections are accompanied by the so-called Laue oscillations visible on each side of the reflection peak and are a measure for the thickness of the layers. The thickness can be calculated from the adjacent positions of Laue oscillation satellites [64]:

$$t = \frac{\lambda}{2[\sin(\theta_i) - \sin(\theta_{i-1})]} \quad (2.33)$$

Another method to analyse the film thickness is the so-called X-ray reflectivity (XRR) measurement at low angles θ . Total reflection of an incident X-ray beam occurs below a critical angle θ_c resulting in an intensity plateau. In the region around the critical angle ($\theta \approx \theta_c$), a transition occurs and the intensity decreases following the so-called Porod slope [65]. Once crossed, the observed intensity exhibits characteristic intensity oscillations which are called Kiessig fringes [66]. These fringes are connected to interference of reflected and refracted beams as a multiple of the wavelength λ and allow for an estimation of the film thickness. The relation can be compared to Bragg's law and similarly yields the

spacing between film surface and film-substrate interface. Thereby, the distance between two fringes are inversely proportional to the film thickness:

$$2\theta_{i+1} - 2\theta_i \approx \lambda/t, \quad (2.34)$$

from which it follows that the measurable thickness is limited to a maximum value. Further, this method is vulnerable to surface roughness and inhomogeneities in thickness. Here it may be noted that the calculations for the thickness of the film by Laue and Kiessig differ by the fact that the Laue oscillations are caused by crystalline influence, i.e. stacked lattices contributing to the refraction, while the Kiessig fringes are caused by the presence of two surfaces/interfaces. In addition, the thickness can be estimated from Scherrer's equation 2.30 assuming a perfect crystal with a single scattering domain.

In theory, an epitaxial grown film is assumed to be a perfect single crystal, however, in reality lattice planes may be misaligned. This misalignment, also called the mosaicity of a film, can be measured via an ω or rocking curve measurement. During a rocking curve experiment, the source and detector are fixed to an angle at which the Bragg condition is fulfilled and only the source is moved by a small fraction causing the incident beam to vary by $\Delta\omega$. This rocking around the incident angle leads to refraction at misaligned lattice planes and thus, to a broadening of the Bragg reflection.

The preceding thin film techniques for epitaxial films offer only out-of-plane characterization. In contrast, the so-called reciprocal space mapping (RSM) renders the possibility to measure in-plane properties of epitaxial films. An RSM is the sum of multiple ω -measurements which angular dependencies are transferred into directions of the reciprocal space. The result is a two dimensional depiction of the reciprocal space which allows for an estimation of the corresponding in-plane lattice parameter.

2.4.6. Fundamental parameter approach

The fundamental parameter approach [67, 68] aims for a description of the instrumental Ω and emission Λ function. By measuring a substantially ideal sample, which crystallite size and microstrain do not contribute to line broadening, the sample function Ψ approaches its ideal δ -function shape - or at least the contributions are known. A common standard is LaB₆ with known crystallite size and strain effects. Thus, the remaining line profile broadening can be traced back to instrumental and emission characteristics. This deconvolution of the PSF and the fixing of the first two functions, allows for a proper determination of broadening by the specimen function of any other sample.

2.4.7. Rietveld Refinement method

The Rietveld refinement method is crystal structure refinement method using a least-square minimizing procedure to refine structural parameters [69–72]. With that said, this method does not aim to refine whole patterns, but rather parameters included in a to-be-refined crystal structure. It is necessary to already provide a crystal structure model prior to the first refinement steps, since no effort is made in advance to allocate observed intensities or to deconvolute overlapping reflections, which is simultaneously a feature of this method. The method does not yield a definite structural solution, but can be of tremendous help in finding one. In addition, this method respects influences of instrument and radiation source, thus such information have also to be given prior to a refinement. On the other hand, the method allows for a direct feedback over refined parameters during the refinement procedure. The method revolves around the least-square minimisation of the residual S_y :

$$S_y = \sum_i w_i (y_{i,obs} - y_{i,calc})^2 \rightarrow \text{minimisation}, \quad (2.35)$$

with $w_i = 1/y_{i,obs}$, $y_{i,obs}$ being the observed intensity at step i and $y_{i,calc}$ being the calculated intensity at the i th step. In principle, the intensity of a reflection is depending on factors being a function of either θ or (hkl) (see also Equation 2.32). Thus, the calculated intensity at step i is a combination of those functions plus contributions from neighbouring reflections, yielding a sum with the Miller indices (hkl) , represented as H , as its argument plus a background intensity:

$$y_{i,calc} = s \sum_H p_{hkl} \times LP_\theta \times A_\theta \times T_{hkl} \times E_{hkl} \times \phi(2\theta_i - 2\theta_{hkl}) \times |F_{hkl}|^2 + y_{i,bg}, \quad (2.36)$$

where s is the scaling factor, ϕ is the peak shape function and $y_{i,bg}$ is the background intensity at the i -th step. The background intensity $y_{i,bg}$ can be fitted with a polynomial of order m :

$$y_{i,bg} = \sum_m b_m \cdot (2\theta_i)^m. \quad (2.37)$$

The application of the least-squares minimisation method leads to a set of normal equations which contain the differentials of all calculated intensities $y_{i,calc}$ with respect to every refineable parameter. The set of normal equations can be solved by inversion of the normal

matrix M_{jk} .

$$M_{jk} = - \sum_i 2w_n \left[(y_{i,obs} - y_{i,calc}) \cdot \frac{\partial^2 y_{i,calc}}{\partial x_j \partial x_k} - \left(\frac{\partial y_{i,calc}}{\partial x_j} \right) \cdot \left(\frac{\partial y_{i,calc}}{\partial x_k} \right) \right], \quad (2.38)$$

where $x_{j/k}$ are the sets of refineable parameters, which create an $m \times m$ matrix with m being the number of refined parameters. Due to the non-linearity of the residual of S_y , the minimum is found iteratively by applying the difference Δx_k on the set of refineable parameters with the aim to potentially improve the starting model. The difference Δx_k is calculated by:

$$\Delta x_k = \sum M_{ij}^{-1} \cdot \frac{\partial S_y}{\partial x_k}. \quad (2.39)$$

This procedure will be repeated until a convergence criterion is satisfied. In order to avoid implausible or false minima (results), carefully chosen constraints to the refined parameters have to be applied to minimize the flexibility of the model. But also the starting model should already provide a sufficient well approximation. The amount of refineable parameters may further lead to unwanted perturbation or interference of the result when refined at once. Thus, the refinement of too many parameters in one step should be avoided. In addition, the background can be minimized by well prepared samples or correctly chosen experimental conditions. The quality of the found fit can be described by different R -indices, the GOF (goodness of fit) and by inspecting the difference curve between observed and calculated intensity, $y_{i,obs}$ and $y_{i,calc}$, respectively. The most important R -indices are the R_{wp} (weighted profile) and R_{Bragg} (reflection intensity-based) values:

$$R_{wp} = \sqrt{\frac{\sum_n w_n (y_{i,obs} - y_{i,calc})^2}{\sum_n w_n (y_{i,obs})^2}} \quad (2.40)$$

$$R_{Bragg} = \frac{\sum_k |I_{k,obs} - I_{k,calc}|}{\sum_k (I_{k,obs})}, \quad (2.41)$$

where I_k is the intensity of the Bragg reflex k at the of the refinement. The GOF is the ratio of the R_{wp} and R_e (R expected):

$$GOF = \frac{R_{wp}}{R_e} = \sqrt{\frac{\sum_n w_n (y_{i,obs} - y_{i,calc})^2}{N - P}} = \sqrt{\frac{S_y}{N - P}}, \quad \text{with} \quad R_e = \sqrt{\frac{N - P}{\sum_n w_n (y_{i,obs})^2}}, \quad (2.42)$$

where N and P are the number of measurement points and refined parameters, respectively. The inspection of the difference curve is a rather qualitative procedure without a precise parameter, but it allows a graphical assessment of the fit. Since the Rietveld method relies on mathematical peak shape functions, instrumental influences and good approximation of the to-be-refined structural model, it is possible to evaluate the quality of the performed fit and it highlights fundamental incorrect input information.

Together with the qualitative phase analysis, the Rietveld refinement renders the possibility to extract the weight fractions from the XRD data. This quantification uses the above introduced scaling factor s to calculate the weight fractions w_p of each phase p in a multiphase mixture with the phases q . A precondition to achieve reliable values is the homogeneity of the examined powder guaranteeing an even distribution of each phase throughout the whole sample.

$$w_p = \frac{s_p \cdot (Z_p M_p V_p)}{\sum_q s_q \cdot (Z_q M_q V_q)}, \quad (2.43)$$

with Z , M and V being the number of atoms in the unit cell, the molar mass and the volume of the unit cell, respectively. From this it follows that the crystal phases of each phase have to be known as well as that amorphous phases/fractions are omitted. Another method is the usage of a known external standard which is added to the sample material, such as corundum. A present amorphous phase leads to an overestimation of the added standard from which it is possible to calculate the true phase fractions. The software used for Rietveld refinements throughout this cumulative thesis is Topas version 5 and later version 6 [73]. Besides the GUI guided operation, it offers a mode based on an input script known as INP format. This input script allows for an easy analysis of a batch of XRD patterns, though, it may require the application of constraints to avoid physically unreasonable results. The setting up of such an INP file is straightforward since the "language" relies on case sensitive plain text. Appendix B contains an commented example INP script as it was used for the evaluation of the *in situ* XRD data obtained in Sec. 3.4.

2.4.8. X-ray diffraction and Rietveld refinement within this work

X-ray diffraction coupled with Rietveld refinement are the core characterization technique within this work. Besides basic structural characterization via ambient measurements throughout the whole work, high-temperature *in situ* measurements under selected atmospheres provided insights into phase formation and structural integrity in Sec. 3.2 and 3.1. Further, set of isothermal high-temperature *in situ* measurements were utilized in Sec. 3.4 to investigate interdiffusion mechanisms inside the Ba-Fe-O-F system. The structural

dependency of the compounds inside the model system allowed for a precise estimation of the fluorine content, thus, facilitating the preparation of the desired samples. For all XRD measurements, Rietveld refinements were performed to draw the most information from the resulted patterns. Especially, the possibility of batch refinements with the help of input files (see Appendix B).

2.5. Electrochemical impedance spectroscopy

The electrochemical impedance spectroscopy (EIS) is one of the numerous techniques to investigate electrochemical properties of materials. The peculiarity of this technique is the gathering of information in dependency of the frequency. In contrast to time-dependent measurement techniques, EIS is able to pinpoint phenomena inside the specimen due to the frequency dependency. However, this may also pose problems in understanding and also in proper analysis of the gathered data. Information from EIS have to be unwrapped by complex mathematics and can easily be misinterpreted. This section will introduce basic principles of electrochemical impedance spectroscopy [74] as well as mathematical models created for the analysis of solid oxide fuel cell cathodes [5, 75] which are crucial for the discussion in Sec. 3.2.

2.5.1. Fundamentals of electrochemical impedance spectroscopy

The impedance $Z(\omega)$ is a term which describes the complex resistance of a material upon the application of a frequency dependent voltage $V(\omega)$. This relation is formulated by Ohm's law for alternating current:

$$Z(\omega) = \frac{V(\omega)}{I(\omega)}, \quad (2.44)$$

with ω as the angular frequency and $I(\omega)$ being the current passing through the resistor. The impedance of an *ideal* resistor is purely real, and therefore $Z = R$ applies. The total impedance of a system is the sum of all serial resistors:

$$Z_{\text{total}}(\omega) = \sum_i Z_i(\omega). \quad (2.45)$$

In contrast to a resistor, a capacitor accumulates charge Q over time, since current cannot flow through it. Hence, the capacitance C can simply be described by

$$\frac{dV(t)}{dt} = \frac{I(t)}{C} \quad \text{or equivalent} \quad V(t)C = \int_0^t I(t)dt. \quad (2.46)$$

The third element is the inductor, which describes the generation of an opposing current when current is flowing through leading to a change in potential. The inductance L is described by

$$\frac{V(t)}{L} = \frac{dI(t)}{dt} \quad \text{or equivalent} \quad I(t)L = \int_0^t V(t)dt. \quad (2.47)$$

In electrical impedance spectroscopy, an sinusoidal voltage is applied:

$$V(t) = V_0 \sin(\omega t), \quad (2.48)$$

with V_0 being the amplitude of the applied signal, $\omega = 2\pi f$ with f as frequency and ϕ being the phase shift. This sinusoidal signal renders the possibility to display the voltage and current as a complex quantity. This complex numbers can be split into real and imaginary parts which are related to real (cosine) and reactive (sine) power:

$$V(t) = V_0 \sin(\omega t) = V_0(\cos(\omega t) + j \cdot \sin(\omega t)) = V_0 \cdot e^{j(\omega t)} \quad (2.49)$$

$$I(t) = I_0 \sin(\omega t + \phi) = I_0(\cos(\omega t + \phi) + j \cdot \sin(\omega t + \phi)) = I_0 \cdot e^{j(\omega t - \phi)}, \quad (2.50)$$

with ϕ being the phase shift between voltage and current. The representation as an exponential function is the Euler transformation. Inserting the exponential function in equation 2.46 and 2.47 yields the complex relation for capacitor and inductor⁵

$$\frac{I(t)}{C} = \frac{dV(t)}{dt} = V_0 \cdot e^{j(\omega t)} \cdot j\omega = V(t)j\omega \Rightarrow Z_C = \frac{V(t)}{I(t)} = \frac{1}{j\omega C} \quad (2.51)$$

$$\frac{V(t)}{C} = \frac{dI(t)}{dt} = I_0 \cdot e^{j(\omega t - \phi)} \cdot j\omega = I(t)j\omega \Rightarrow Z_L = \frac{V(t)}{I(t)} = j\omega L. \quad (2.52)$$

For any impedance, the following formalism holds true:

$$Z = \frac{V(t)}{I(t)} = \frac{V_0}{I_0} \cdot e^{j\phi} = |Z| \cos(\phi) + j \cdot |Z| \sin(\phi) = Z' \cos(\phi) + j \cdot Z'' \sin(\phi), \quad (2.53)$$

where Z' and Z'' represent the real and imaginary party of the impedance, respectively. During an impedance spectroscopy experiment, a sinusoidal voltage $V(t)$ like in eqn. 2.49 is applied to the specimen and the current response $I(t)$ (eqn. 2.50) is recorded. From this,

⁵This relation uses the following transformations of the complex quantity j : $e^{-j \cdot \pi/2} = \cos(-\pi/2) + j \sin(-\pi/2) = -j$ and $e^{j \cdot \pi/2} = \cos(\pi/2) + j \sin(\pi/2) = j$. The arguments of the sine and cosine function $-\pi/2$ and $\pi/2$ are equivalent to a phase shift of -90° and $+90^\circ$ between potential and current at a capacitor and an inductor, respectively.

the impedance response of the whole system is calculated after eqn. 2.53. A common way to plot the impedance data is in the form of Cole-Cole (Nyquist) and Bode plots. The Nyquist plot separates the absolute value of the impedance vector with the frequency as the function parameter, thus, the (negative) imaginary part of the impedance ($-Z_{img}$) is plotted versus the real part (Z_{real}). In contrast, the Bode plot displays the absolute value of the impedance $|Z|$ and the phase angle ϕ complementarily plotted over the logarithmic frequency f . The combination of the complex plane plot and the two Bode diagrams delivers sufficient information to find a well-fitting description of the phenomenon. Figure 2.13 exemplifies the result of two different simulated impedance spectroscopy measurements. Typically, the impedance response of a specimen forms a semicircle (or more) in the Nyquist plot and one corresponding maximum in the phase angle plot of the Bode diagram. This semicircle-like shape arises from the capacitive nature of phenomena found in materials, such as the accumulation of charge at interfaces or grain boundaries, combined with the intrinsic resistance of the charge transportation. Such semicircles can be characterized by using appropriate fitting models containing equivalent circuits, most commonly (depending on the investigated system) a capacitor and resistor in parallel per phenomenon, as shown in Figure 2.13 for example simulations of one RC element (a,b) and two RC elements in series (c,d). Such an RC circuit impedance model can be described by

$$Z_{RC}(\omega) = \frac{R}{1 + j \cdot \omega RC}. \quad (2.54)$$

The resistance of such an element is simply the difference of the intercepts with the real axis, i.e. the diameter of the semicircle. In most cases, an additional resistance is connected in series which sums up pure ohmic resistances in the observed frequency range. For an infinite frequency, the impedance of the RC element becomes zero, since the impedance of the capacitor becomes zero, and thus, the impedance of the system is just the serial resistance R_s . For a frequency approaching zero, the impedance becomes real ($Z = R_s + R$), since a direct current is flowing through the system. The frequency found at the apex of the semicircle is the break-point in the Bode diagram and is given by the time constant τ_{RC} of the element:

$$\omega_{apex} = \frac{1}{\tau_{RC}} = \frac{1}{RC}. \quad (2.55)$$

The time constant of a system is a measure for the decrease of a current within the system, e.g. a small time constant means faster current decay. If the system contains more than one element, like in Fig. 2.13 c, the semicircles can be identified easily, if the time constants of each semicircle, here $\tau_{RC,1}$ and $\tau_{RC,2}$, are well separated. If the time constants are similar, the semicircles overlap and an evaluation becomes more difficult. In such

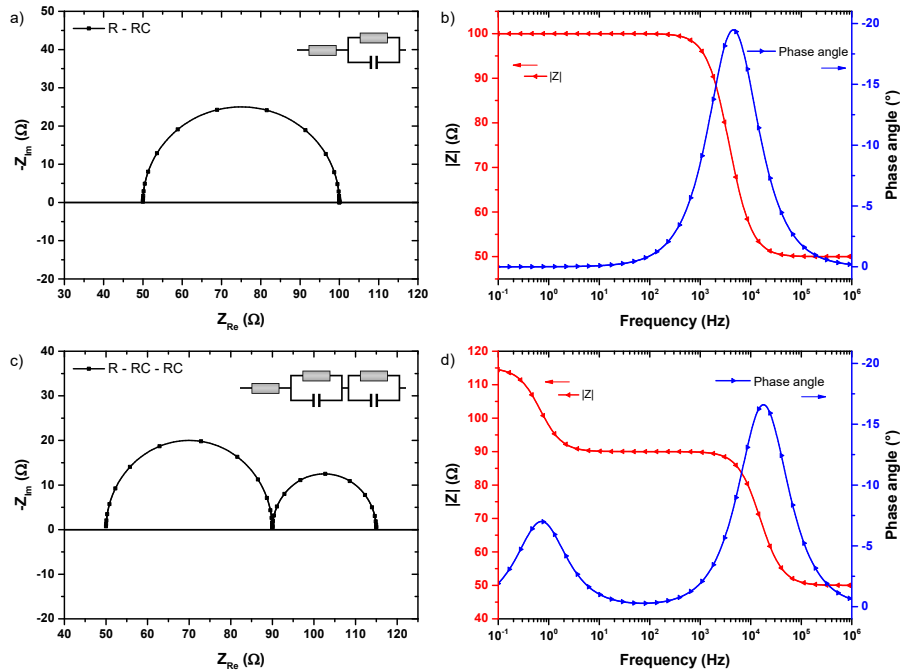


Figure 2.13.: Example simulation of a) one RC element and c) two RC elements. The Nyquist plots (a,c) show one and two semicircles, respectively, and the Bode plots (b,d) show one and two maxima in the phase angle, respectively, while the amount of impedance rises correspondingly. The simulation parameters for the single RC element are $R_s = 50 \Omega$ and $R = 50 \Omega$ and for the double RC element $R_s = 50 \Omega$, $R_1 = 40 \Omega$ and $R_2 = 25 \Omega$.

cases, the distribution of relaxation times (DRT) can help to find the physically reasonable amount of elements. In principle, the DRT is found by modelling an impedance spectrum by an infinite amount of RC -elements which yields a statistical distribution of relaxation times. In solid-state ionics an RC circuit is associated with a well-defined process or phenomenon. For systems with similar resistances, the phenomena may be distinguished if their capacitances differ sufficiently. The capacitances found in solid-state ionics strongly depend of their physical origin, thus making electrical impedance spectroscopy a powerful tool to characterize such processes. Table 2.2 lists typical capacitance values for selected physical processes [76]. In reality, the capacity impedance response of processes deviate from the above introduced idealized case. The observed perfect semicircle changes to a depressed semicircle which then can be described by a so-called constant phase element

Table 2.2.: Interpretation of capacitance values in relation to their possible physical origin [5, 76].

Capacitance (F)	Physical origin
10^{-12}	bulk material
10^{-11} – 10^{-8}	grain boundary
10^{-9} – 10^{-7}	surface layer
10^{-7} – 10^{-5}	sample-electrode interface
10^{-4}	electrochemical reactions
10^{-1}	oxygen stoichiometric polarisation in the bulk of a MIEC thin film electrode ⁶

(CPE). The impedance of a CPE is given by:

$$Z_Q(\omega) = \frac{1}{Q \cdot (j\omega)^\alpha}, \quad (2.56)$$

with Q being the admittance value and α a measure for the deviation from the perfect semicircle. For an ideal capacitor the phase angle is -90° while for a CPE this phase angle is lowered to $-(90^\circ \cdot \alpha)$, thus, the depression is a rotation of the impedance vector relocating the center below the real axis, as depicted in Fig. 2.14 a. Further, the slope of the absolute value of the impedance becomes α and the maximum of the phase angle is shifted to higher frequencies (Fig. 2.14). The impedance of an RQ or $R|CPE$ element becomes

$$Z_{RQ} = \frac{R}{1 + RQ(j\omega)^\alpha}, \quad (2.57)$$

with the time constant τ_{RQ}

$$\tau_{RQ} = \sqrt[\alpha]{RQ}, \quad (2.58)$$

which leads to the corresponding relaxation frequency by inserting eqn. 2.58 into eqn. 2.55:

$$f_Q = \frac{1}{2\pi\tau_{RQ}} = \frac{1}{2\pi \sqrt[\alpha]{RQ}}. \quad (2.59)$$

The origin of the CPE can be ascribed to surface heterogeneity [77, 78] or to continuously distributed time-constants for charge-transfer reactions [79, 80].

The "real" capacity of a CPE element can be calculated after

$$C_Q = \sqrt[\alpha]{R^{1-\alpha} \cdot Q}. \quad (2.60)$$

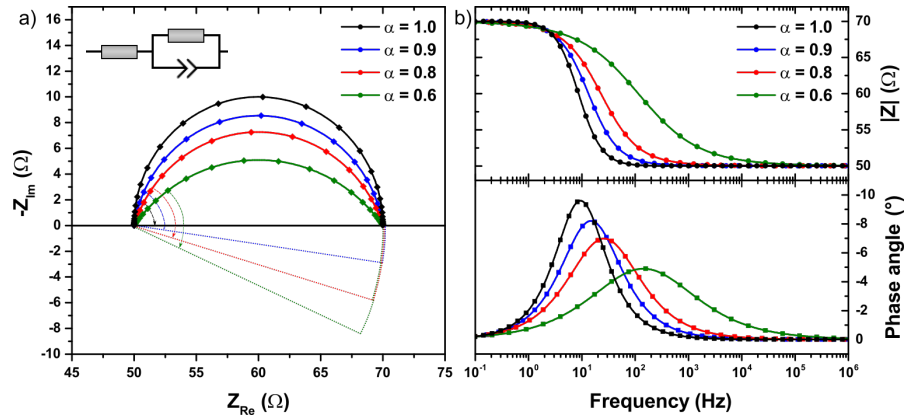


Figure 2.14.: R-CPE elements with different values for $\alpha = 1, 0.9, 0.8, 0.6$. The depression of the semicircle in the Nyquist plot (a) leads to a decrease in imaginary impedance, but also to a dispersion of the maximum in the phase angle (b), while the the slope of $|Z|$ is equal to α .

In principle, most phenomena can be described by $R|CPE$ elements. However, a lot of processes are more complex and thus require more complex impedance models, e.g. when the observed phenomenon includes chemical reactions or a coupled reaction of diffusion and subsequent chemical reaction. On the other hand, such models allow for a more detailed description of such processes accompanied with a comprehensive gain of information about the specimen.

2.5.2. Models for SOFC cathodes

This section will discuss the impedance models for cathode materials of solid oxide fuel cells (SOFC) observed during electrochemical impedance spectroscopy. The above section introduced the basics of EIS, but in reality, some observations require more sophisticated approaches. These approaches will be discussed on the base of cathode materials for SOFC. In principle, it will be differentiated between dense and porous cathodes made of mixed ionic-electronic conductors (MIEC), which differ in terms of electrochemical properties. The following discussion will primarily be based on the work of S.B. Adler et al. [5, 19, 75] to which the reader is referred to for further reading. Divergent sources will be marked explicitly.

The underlying electrochemical process of an operating cathode in a SOFC is the reduction

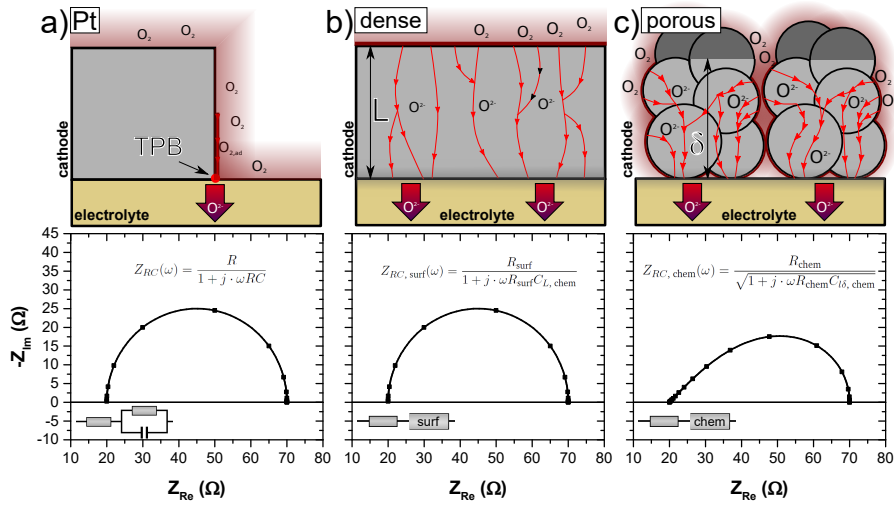


Figure 2.15.: Different morphologies of cathodes with the special cases of a) Pt, b) dense and c) porous cathode configurations and its impact on the impedance spectroscopy response with the corresponding formalism and equivalent circuits. Note that the serial resistance includes the electrolyte response.

of atmospheric oxygen to bulk oxygen which can be described with the half-cell reaction



These oxygen ions migrate through the SOFC and undergo the recombination reaction at the other side of the SOFC at the anode. The reduction of oxygen is the more studied reaction, since the activation of this reaction is observed to be the more complex and harder to activate reaction inside a SOFC.

Prior to oxide materials, platinum was the material of choice for fuel cell cathodes, due to its catalytic properties for oxygen reduction. Since platinum is no oxygen ion conductor itself, the gas phase has to be in contact with platinum and the electrolyte at once, thus, forming the so called triple phase boundary (TPB). This one dimensional geometrical concept of an electrochemical reaction region proved to be a valuable phenomenological description which could explain the observed high capacitances at lower frequencies that could not be ascribed to traditional interfacial capacitances but rather to the accumulation of oxygen ions from gas phase and counter charges. Fig. 2.15 sketches the kinetic and electrochemical processes of such a Pt electrode together with the arising impedance response, which can be fitted with a single R|C-element. The performance of a fuel cell

electrode increases with the length of the TPB. However, the reaction steps which occur in the vicinity are not yet fully understood, especially which step is rate limiting, though, they must include adsorption of oxygen molecules from the gas phase, diffusion of such on the surface and finally the catalytic dissociation and reduction reaction followed by the incorporation into the electrolyte. Experiments with porous Pt (and other precious metals like Ag or Au) electrodes showed that the adsorption and diffusion of oxygen onto the Pt surface and towards the TPB played a significant role for the overall reaction kinetics. In addition it was also shown in case of Ag that diffusion of oxygen also occurs through the bulk of the metal electrode, though it exhibits poor catalytic activity. The porosity made the co-limitation of kinetics (reduction reaction and incorporation at TPB) and mass transfer (adsorption and transportation of oxygen species) visible. In terms of electrical impedance it means the Nyquist plots exhibits an equal contribution of real and imaginary parts of the impedance leading to a $\sim 45^\circ$ slope of the plot in the medium frequency range. The above mentioned processes can be transferred onto perovskite mixed ionic-electronic conductors with the special focus on bulk properties. Some MIEC materials combine the electronic/ionic conduction with sufficient catalytic activity to become suitable for SOFC cathode applications - in addition to be a low-cost alternative to Pt. $\text{La}_{1-x}\text{Sr}_x\text{CoO}_{3-\delta}$ (LSC), $\text{La}_{1-x}\text{Sr}_x\text{FeO}_{3-\delta}$ (LSF) and $\text{La}_{1-x}\text{Sr}_x\text{MnO}_{3-\delta}$ (LSM) are two of the most studied and well-understood materials, with LSM being the most favored material for SOFC cathodes. They exhibit metallic and semiconducting/semimetallic properties at elevated temperatures guaranteeing a sufficient electronic conduction, while simultaneously offering enough oxygen vacancies for a high oxygen ion conduction. Experiments on thin films showed that, by offering such pathways through bulk material, the performance of cathodes scale to some extent with their thickness, thus, the overall reaction (adsorption, diffusion and exchange reaction) is drawn away from the TPB and occurs over the whole electrode/electrolyte interface. Their impedance response showed perfect semicircles at low frequencies which were possible to be analysed assuming that the absorption of oxygen at the gas/film interface is the rate limiting step due to the purely capacitive response. This case is schematically shown in Fig. 2.15 b. Here, the oxygen reduction can again be split into two reactions: first, the absorption of oxygen at the gas/film interface coupled with the subsequent transportation through the bulk and second, the exchange of oxygen ions at the electrode/electrolyte interface. The first step can also be associated with a chemical capacitance (due to the chemical potential being the driving force), which is a measure of how much of the bulk takes part during the oxygen reduction reaction and is normally much larger than interface/surface capacitances. In impedance spectroscopy, the semicircle observed for a dense thin film with surface-limiting conditions, can simply

be described by

$$Z_{RC,\text{surf}}(\omega) = \frac{R_{\text{surf}}}{1 + j \cdot \omega R_{\text{surf}} C_{L,\text{chem}}}, \quad (2.62)$$

with R_{surf} is the surface resistance associated with the oxygen reduction at the gas/surface interface and $C_{L,\text{chem}}$ is the corresponding chemical capacitance which is solely determined by the oxygen stoichiometry changes in the film with total thickness L ($C \propto L$). Note that this formalism is comparable to eqn. 2.54.

On the other side, a porous film of MIEC for cathode application is a much more complex case. So far, only one possible reaction path was discussed. In general, for porous cathodes, there are several reaction pathways possible. The most relevant for this work is the absorption of oxygen at the gas/electrode interface, the subsequent reduction of oxygen ions and incorporation into the bulk material followed by the conduction of ions through the bulk. Another pathway would be adsorption (and reduction) at the surface of the electrode followed by diffusion of oxygen species towards the TPB/electrolyte. However, only the first case will be considered and is schematically depicted in Fig. 2.15 c with the corresponding impedance response. The performance of this bulk pathway depends on the one hand on the exchange kinetics at the gas/electrode interface, but on the other hand on the bulk transportation. Assuming a process co-limited by bulk transportation and surface chemistry, i.e. exchange/reduction of oxygen, the impedance response $Z_{RC,\text{chem}}$ and for semi-infinite (thick) porous electrode can be described by:

$$Z_{RC,\text{chem}}(\omega) = \frac{R_{\text{chem}}}{\sqrt{1 + j \cdot \omega R_{\text{chem}} C_{l\delta,\text{chem}}}}. \quad (2.63)$$

$Z_{RC,\text{chem}}$ is a convolution chemical contributions, R_{chem} and $C_{l\delta,\text{chem}}$ are the characteristic resistance and capacitance, respectively. These parameters depend highly on the morphology of the electrode, such as porosity, tortuosity and surface area. This impedance model has the shape of a half tear-drop and is called "Gerischer" impedance, due to its first description by Gerischer in 1951 for oxygen absorption/exchange on a metallic membrane [81]. Compared to the case of a dense film, the capacitance in the present case depends on a so-called "utilization" length l_δ which represents the penetration depth of an electro-active region into the electrode starting from the electrolyte. This "utilization" length l_δ depends on a surface resistance comparable to R_{surf} and the surface area. It was found that the performance of an electrode was improved up to a thickness of 10 - 15 μm [82]. This peculiarity emphasizes the discrepancy between the TPB concept and porous MIEC cathodes and highlights the importance of bulk properties.

As a conclusion, the overall polarization impedance response of an electroactive electrode,

dense or porous, on an electrolyte can be summed up by:

$$Z_{\text{pol}} = R_{\text{electrolyte}} + Z_{\text{interfaces}} + Z_{\text{chem}} , \quad (2.64)$$

where $Z_{\text{interfaces}}$ combines the charge-transfer resistances/impedances and Z_{chem} represents the non-charge-transfer chemical processes, namely oxygen absorption/reduction and ion diffusion. For comparison, the polarization resistance (real part of impedance) of a measured specimen is related to the participating area, the so-called area specific resistance (ASR), which is given by:

$$R_{\text{ASR}} = R_{\text{pol}} \cdot A_{\text{electrode}} , \quad (2.65)$$

with $A_{\text{electrode}}$ being the total area of the used electrodes. R_{ASR} is hence given in units of Ωcm^2 .

2.5.3. EIS and SOFC models within this work

Electrical impedance spectroscopy is the key technique for investigating the electrochemical performance of the prepared porous symmetrical films in Sec. 3.2. With the help of the Gerischer impedance model developed by Adler et al., the porous cathodes were characterized.

3. Topochemical reactions affecting the anion lattice inside the model system barium ferrate

In the following, a list of all publications inside this work will be given and afterwards a summary will highlight the important aspects and results of each publication in the context of synthesis, topochemical modification and investigation of the model system Ba-Fe-O-F.

1. **Sec. 3.1: Structural and magnetic properties of newly found $\text{BaFeO}_{2.667}$ synthesized by oxidizing $\text{BaFeO}_{2.5}$ obtained via nebulized spray pyrolysis**
2. **Sec. 3.2: On the Impact of the Degree of Fluorination on the ORR Limiting Processes within Iron Based Catalysts: A Model Study on Symmetrical Films of Barium Ferrate**
3. **Sec. 3.3: Synthesis and characterisation of fluorinated epitaxial films of BaFeO_{2}F : Tailoring magnetic anisotropy via a lowering of tetragonal distortion**
4. **Sec. 3.4: A kinetic study of the interdiffusion of fluorine and oxygen in the perovskite-type barium ferrate system $\text{BaFeO}_{2.5-x}\text{F}_{2x}$**

The aims of this work were to investigate the influences of topochemical fluorination of $\text{BaFeO}_{2.5}$ onto the electrochemical properties and to understand interdiffusion kinetics inside this system. Doping of the anion sublattice of the cathode material is another solution besides cation doping towards low and intermediate temperature solid oxide fuel cells, and the most promising anion is fluorine due to its electronegativity. Though $\text{BaFeO}_{2.5}$ itself shows limited suitability as such a cathode material, it offers a very important advantage

over state-of-the-art cathode materials, such as $\text{Ba}_{0.5}\text{Sr}_{0.5}\text{Co}_{0.2}\text{Fe}_{0.8}\text{O}_{3-\delta}$, $\text{La}_{1-x}\text{Sr}_x\text{MnO}_{3-\delta}$ (LSM) or $\text{La}_{0.6}\text{Sr}_{0.4}\text{CoO}_{3-\delta}$ (LSC).

Conventional compounds exhibit a cubic perovskite structure, which makes it difficult or even impossible to resolve incorporated fluorine after topochemical modifications. In contrast, monoclinic $\text{BaFeO}_{2.5}$ forms two distinct oxyfluoride structures depending on the fluorine stoichiometry: $\text{BaFeO}_{2.333}\text{F}_{0.333}$ ($P2_1/m$) and BaFeO_2F ($Pm\bar{3}m$). Thus, each of the three compounds can simply be identified by XRD what is synonymous with a precise estimation of the fluorine content. Fig. 3.1 depicts the three structures (taken from the publication in Sec. 3.2 [83]) together with their XRD patterns. $\text{BaFeO}_{2.5}$ ($P2_1/c$) crystallizes in a complex monoclinic structure with an ordering of the oxygen vacancies with one unit cell containing 28 formula units of $\text{BaFeO}_{2.5}$. On the other hand, $\text{BaFeO}_{2.333}\text{F}_{0.333}$ ¹ ($P2_1/m$) possesses a different symmetry with 6 formula units of $\text{BaFeO}_{2.5}$ inside the monoclinic unit cell, and is also oxygen vacancy ordered. Both monoclinic structures are subgroups of the aristotype structure $Pm\bar{3}m$ (BaFeO_2F) [12, 33]. With the aid of this peculiarity of the Ba-Fe-O-F system, it can be used as a model system for investigating the impact of topochemical fluorination onto electrochemical properties and it can also help to understand interdiffusion kinetics and mechanisms. The iron oxidation state of Fe^{3+} is maintained for each fluorine stoichiometry due to the substitutional topochemical fluorination. Further, the oxygen vacancy concentration is already known due to the structural characterizations in [11, 12, 33] which are of importance for oxygen reduction and conduction. In addition, oxyfluorides may offer special multiferroic properties due to their influence onto the coordination of the transition metal cation inside the perovskite.

The synthesis of monoclinic $\text{BaFeO}_{2.5}$ was done via the nebulized spray pyrolysis (NSP). With this technique it is possible to synthesize nanocrystalline powder with a high phase purity [84–86]. It requires the precursor salts $\text{Ba}(\text{NO}_3)_2$ and $\text{Fe}(\text{NO}_3)_3 \cdot 9 \text{H}_2\text{O}$ to be dissolved in an aqueous solution. This solution is then nebulized by an ultrasonic membrane and carried by an argon stream through a reactor which was kept at a temperature of 1050 °C. The principle setup is sketched in Fig. 3.2 (taken from [83] within this work) together with the precipitation process. The NSP process and a general discussion of the synthesis of $\text{BaFeO}_{2.5}$ can be found the Sec. 3.2. It is crucial that the system is free of air because the powder is prone to take up CO_2 and form BaCO_3 as well as additional oxygen may lead to a different phase, e.g. $6\text{H-BaFeO}_{2.5+y}$ [39]. Within these synthesis and electrochemical studies, it was found that the fluorine free BaFeO_{3-d} ($d \leq 0.5$) system was not fully understood. Due to the susceptibility towards the oxygen partial pressure, a new

¹Inside the publication in Sec. 3.2, $\text{BaFeO}_{2.333}\text{F}_{0.333}$ had to be changed to $\text{BaFeO}_{2.33}\text{F}_{0.33}$ during the revision process.

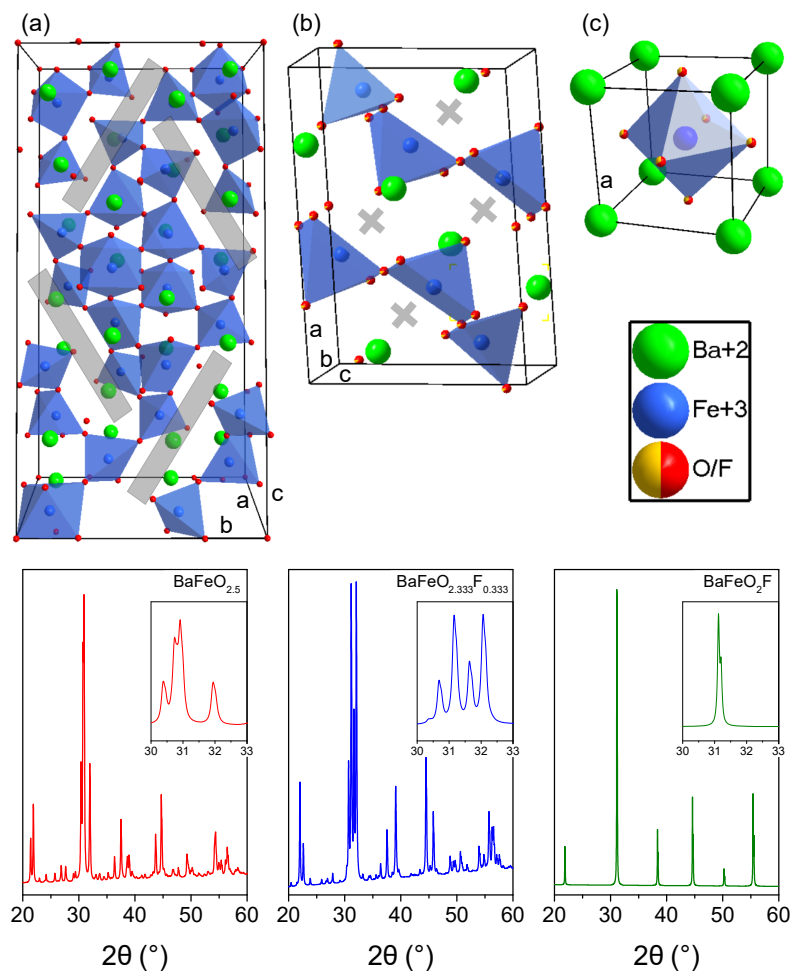


Figure 3.1.: Defect structure of (a) $\text{BaFeO}_{2.5}$ ($P2_1/c$) and (b) $\text{BaFeO}_{2.333}\text{F}_{0.333}$ ($P2_1/m$) with bars/crosses indicating oxygen vacancy channels/relaxations [12, 33], (c) depicts a defect free structure of BaFeO_2F ($Pm\bar{3}m$).[83] Below the structural representations, the XRD patterns of each phase are given, with highest intensity reflection groups shown in insets.

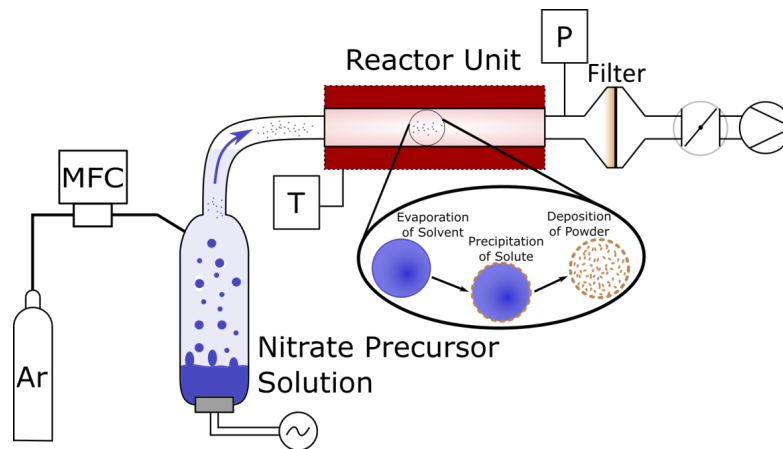


Figure 3.2.: NSP experimental setup with the schematical precipitation process. Taken from Pub. 3 [83].

modification of $\text{BaFeO}_{2.667}$ was found and later characterized, where it was shown that this modification is isotopic to $\text{BaFeO}_{2.333}\text{F}_{0.333}$ ($P2_1/m$) with the same vacancy ordering scheme. In contrast to the NSP process, a solid state approach requires several long heating steps with intermediate milling treatments [33]. However, solid state routes offer the availability of a much higher powder output (NSP roughly 1 - 3 g per run) and thus was chosen as the synthesis route for thin film targets for pulsed laser deposition (PLD) processes. The PLD synthesis was performed under the supervision of Dr. Philipp Kehne. The work on epitaxial films of BaFeO_2 grown by PLD and their fluorination was part of the Master's thesis of Akash Nair.

A characteristic of the NSP technique is the hollow-sphere morphology as well as the hydration of the as-synthesized powder. Though the dehydration can simply be done by heating the powder at an elevated temperature ($\sim 450^\circ\text{C}$) under an inert atmosphere, the morphology of the as-synthesized powder was an issue on the route towards intact films for subsequent measurements. The hollow-sphere morphology prevented the powder to sinter onto the YSZ substrate, thus, an alternative synthesis procedure had to be developed. Previously, this was achieved by the usage of NaCl as a reaction additive what lead to a fine grained morphology [87–89]. However, the chlorine prohibited the formation of monoclinic $\text{BaFeO}_{2.5}$ and promoted the formation the formation of hexagonal $\text{BaFeO}_{2.5}$ by incorporation of Cl into the lattice [90].

Another approach was the abandoning of the idea of a high temperature reaction process towards a low temperature synthesis. This was done by reducing the synthesis temperature

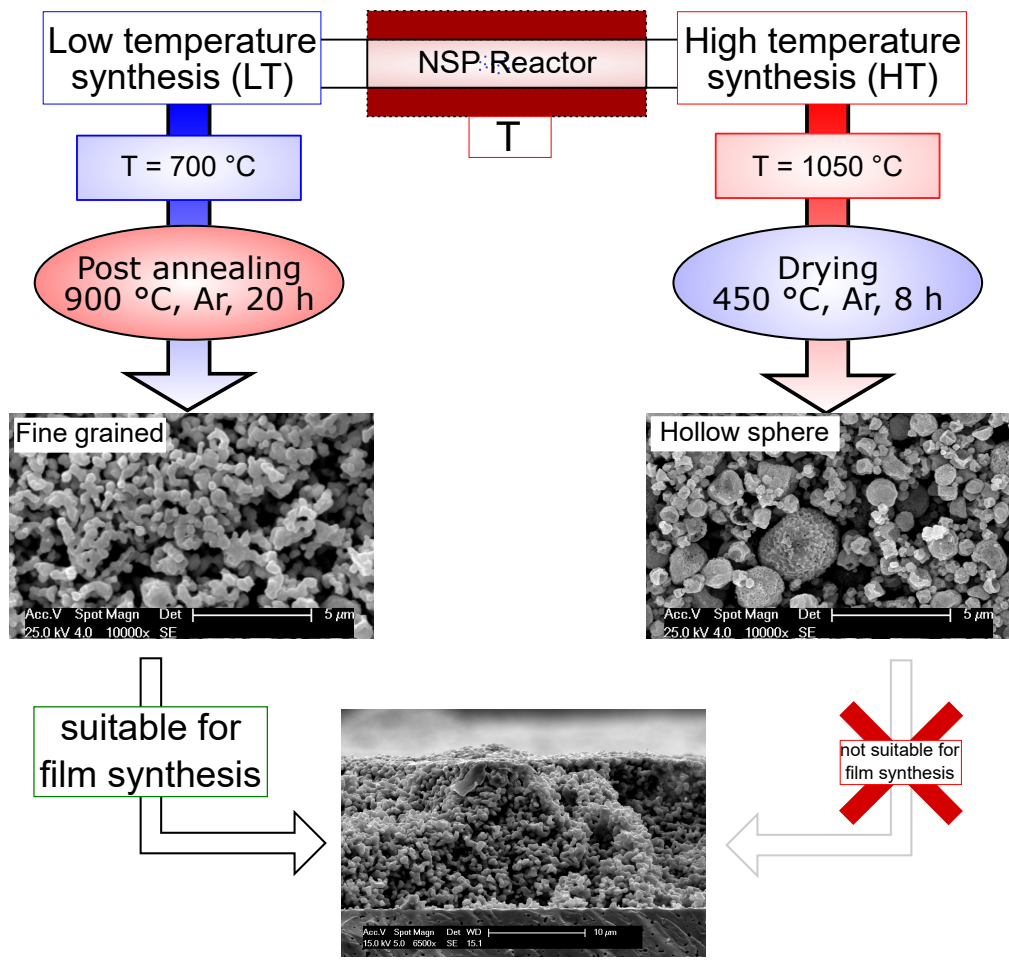


Figure 3.3.: Reaction routes for the low and high temperature NSP process with the post treatment processes leading to powders with hollow sphere and fine grain morphology, respectively. Only the fine grain powder was suitable for film synthesis.

of the NSP reactor from 1050 °C down to 700 °C, what led to unreacted nanocrystalline powder containing mainly the precursor salts, but a subsequent annealing at 900 °C under Ar yielded fine grained powder, which was suitable for the desired film synthesis. Both synthesis routes for the powder are schematically drawn in Fig. 3.3. As deposition method for coating the YSZ8 button-substrates (diameter 1 cm, thickness 500 μm) with pristine powder to prepare polycrystalline films, spin coating was found to be the method of choice. For that purpose, the zeta potential of BaFeO_{2.5} dispersed in an acidic dispersion was estimated and HNO₃ was used as dispersant (HCl led to the formation of hexagonal BaFeO_{2.5-x}Cl_{x/2} upon drying). In addition, it should be noted that during the synthesis process, BaFeO_{2.5} showed to be very unstable in aqueous media if traces of water were inside the powder, either adhesive or incorporated. In these cases, BaFeO_{2.5} decomposed very fast and formed a highly alkaline solution (pH = 14) what indicates the formation of Ba²⁺(OH⁻)₂. Symmetrical films prepared by spin coating exhibited a thickness of roughly 13 μm and a high porosity. During the porous film preparations, it turned out that no buffering layer was needed which would prevent the interdiffusion of substrate material into the film or vice versa.

The next milestone to reach was the topochemical fluorination of as-prepared symmetrical films of BaFeO_{2.5}. The oxyfluoride compounds found within the cubic-perovskite Ba-Fe-O system are metastable, thus requiring the topochemical fluorination but also the estimation of a decomposition temperature for finding an upper working temperature limit when investigating the electrochemical performance of each compound as a cathode. It turned out that BaFeO_{2.333}F_{0.333} does not decompose but rather transforms into a hexagonal structure above a temperature of 590 °C with very little formation of BaF₂, while BaFeO₂F decomposes above 710 °C into BaF₂ and BaFe₂O₄.

Besides the knowledge about crystal structure and stoichiometry, it is also necessary to understand the oxidation/reduction behaviour of each compound. During the experiments, before any fluorine was added, another structure of a pure oxide BaFeO_{2.5+x} was observed. The structure could be fitted with the structural model for BaFeO_{2.333}F_{0.333} (*P*2₁/*m*), what led to the assumption that the observed oxide phase possesses a similar anion occupation and vacancy ordering and thus could be described as BaFeO_{2.667}. This composition was present during and after the electrochemical investigation of BaFeO_{2.5} films, thus a detailed characterization of this phase in Sec. 3.2 was needed to discuss the electrochemical performance which required the interpretation of the data in the context of the structural and compositional knowledge of this phase. Further experiments were performed to unravel its properties, presented in Sec. 3.1. First, the formation of this phase was studied by high temperature XRD under pure oxygen as shown in Fig. 3.4. The results showed a surprising redox behaviour of BaFeO_{2.5}/BaFeO_{2.667}. Under pure oxygen at ~250 °C, BaFeO_{2.5} turned into BaFeO_{2.667}, which was well describable by the same structural model

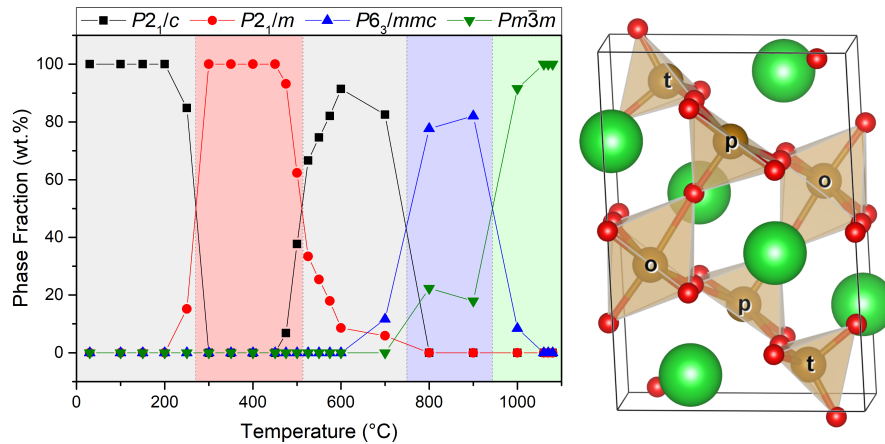


Figure 3.4.: HT-XRD of $\text{BaFeO}_{2.5}$ under oxygen atmosphere with indicated phase changes and the structural model of $\text{BaFeO}_{2.667}$ ($P2_1/m$) created by DFT calculations with iron coordinations highlighted ("o" - octahedron, "p" - square pyramid; "t" - tetrahedron). Figure is recreated from Fig. 3.7 and Fig. 3.9 in Sec. 3.1.

as $\text{BaFeO}_{2.333}\text{F}_{0.333}$ ($P2_1/m$), and at higher temperature, $\text{BaFeO}_{2.667}$ turned back into $\text{BaFeO}_{2.5}$. This phase change from $P2_1/c$ into $P2_1/m$ came with a reduction in unit cell volume by $\sim 3\%$. The high temperature XRD measurements could be well supported by TG/DTA measurements under pure oxygen, conducted by Claudia Fasel. There, it could be shown that this phase formation was accompanied by oxygen uptake and release and consequently, the iron oxidation state changed partially towards $4+$ in a total ratio of 1:2 compared to Fe^{3+} . From this, the question arose, where the Fe^{4+} is allocated, since the $\text{BaFeO}_{2.333}\text{F}_{0.333}$ ($P2_1/m$) model contains three independent iron positions which are differently coordinated: octahedral (CN = 6), square pyramidal (CN = 5) and tetragonal (CN = 4) coordinations were possible. For uncovering the coordination of Fe^{4+} , DFT calculations were performed in collaboration with Prof. Blazej Grabowski and Dr. Yuji Ikeda. The results suggested Fe^{4+} to be coordinated inside the tetrahedron, which was not reported for a mixed-valent perovskite oxide before. The structural model created from the DFT data is also shown in Fig. 3.4. Additional Mössbauer spectroscopy measurements were performed in cooperation with Dr. Robert Kruk and Dr. Abhishek Sarkar. The measurements supported the findings of the DFT calculations. The 6- and 5-fold coordinated iron positions exhibited similar isomer shifts and hyperfine field splitting compared to $\text{BaFeO}_{2.5}$ and $\text{BaFeO}_{2.333}\text{F}_{0.333}$, while the 4-fold coordinated iron could be identified as high-spin Fe^{4+} . From this, $\text{BaFeO}_{2.667}$ can be described by the coordination

and connectivity scheme $\text{Ba}_3(\text{FeO}_{6/2})(\text{FeO}_{5/2})(\text{FeO}_{3/2}\text{O}_{1/1})$. Inside Sec. 3.1, an extensive overview over different iron coordinations in perovskite-type compounds is given. The magnetic ordering within $\text{BaFeO}_{2.667}$ was found to be of the G-AFM ordering type, which is the same ordering as found for the other Ba-Fe-O-F compounds. Magnetic measurements were performed by Dr. Sami Vasala. During the performed experiments, it was found that the system could be even further oxidized by simply cooling it under the oxygen atmosphere forming a seemingly tetragonal phase with the composition $\text{BaFeO}_{2.81}$.

During the experiments in Sec. 3.1, the cyclic TG measurements of high temperature NSP powder exhibited a different oxygen uptake and release behaviour than the previously used low temperature powder. It turned out that the crystallite size between the investigated powders differed leading to the assumption that, additionally to the powder morphology, its crystallite size may have an influence on kinetic properties. Though not included in the publication, the work went beyond structural characterization and electrical properties were determined. The estimation of the crystallite size from XRD yielded a crystallite size of ~ 23 nm and ~ 63 nm for the high and low temperature powder, respectively. This crystallite size dependency will be discussed in Sec. 3.5.3 after the presentation of the publications. With this additional oxide phase identified, the topochemical fluorination of the mother compound $\text{BaFeO}_{2.5}$ prepared as symmetrical polycrystalline and asymmetrical epitaxial films will be presented.

The development of suitable reaction conditions for the topochemical fluorination of films of $\text{BaFeO}_{2.5}$ was another milestone during this work. In principle, the full and partial fluorination can easily be done by low temperature fluorination with PVDF [11, 12]. For conventional powders, the precursor oxide powder is mixed in the desired stoichiometric ratio of PVDF and then heated at 400 °C for 24 h under flowing nitrogen or argon. As a logical consequence, this method could not be applied to the porous or epitaxial films. The easier fluorination was the full fluorination of $\text{BaFeO}_{2.5}$ to BaFeO_2F , since this process does not require the precise supply of the fluorination agent. For this purpose, two routes are possible which can be found in literature [47] and will be described in the following. The first one, is the vapor fluorination method. Here, the sample film was placed inside a tube furnace with a small amount of PVDF deposited before it in such a way that during the heating procedure, the PVDF decomposed and fluorine containing fractions of the polymer were carried by a gas stream (nitrogen or argon) over the sample surface. This guaranteed an evenly fluorinated material, however, it could not be applied in such a way that a specific amount of fluorine could be incorporated. The second possibility for a fully fluorination is the covering of the film surface with a solution of dissolved PVDF in acetone. This method is suitable for furnaces without a flowing gas stream. Both methods might lead to the overfluorination if the fluorination is continued even though the sample material is already fully fluorinated, i.e., decomposition into BaF_2 . Both methods were

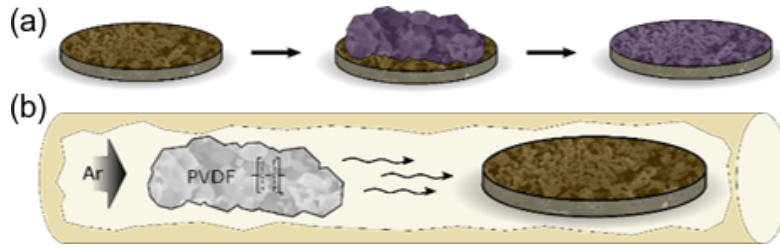
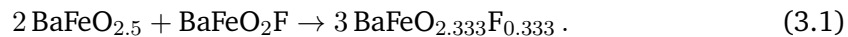


Figure 3.5.: Topochemical fluorination of oxidic films to achieve (a) partially fluorinated $\text{BaFeO}_{2.333}\text{F}_{0.333}|\text{YSZ8}|\text{BaFeO}_{2.333}\text{F}_{0.333}$ via an interdiffusion approach and (b) fully fluorinated $\text{BaFeO}_2\text{F}|\text{YSZ8}|\text{BaFeO}_2\text{F}$ via the vapor transport related technique.

investigated and compared for the epitaxial film preparation in Sec. 3.3, but did not show any differences with respect to quality, structure and composition, while only the vapor fluorination method was used for the fluorination of the porous film. Both methods could not be used for the preparation of partially fluorinated porous films, since both methods do not allow a controlled adjustment of the fluorine content. Thus, another method had to be developed, which is included in the work on synthesis and electrical characterization of porous films presented in Sec. 3.2 and was inspired by the work on the interdiffusion reaction, which is presented in Sec. 3.4. There, the interdiffusion reaction of $\text{BaFeO}_{2.5}$ and BaFeO_2F forming $\text{BaFeO}_{2.333}\text{F}_{0.333}$ was investigated following the interdiffusion reaction:



The fact that a distribution of fluorine inside this system is possible, lead to the idea to partially fluorinate a porous film with the composition $\text{BaFeO}_{2.5}$ by simply covering it with a large amount of $\text{BaFeO}_{2.333}\text{O}_{0.333}$ powder and annealing it at a temperature of 400 – 500 °C. Here, this powder served as a reservoir of the correct fluorine to oxygen ratio, which is then applied to the film material due to the concentration gradient. This new interdiffusion technique and the vapor fluorination method are schematically shown in Fig. 3.5 a,b, respectively, taken from Sec. 3.2. The even distribution of fluorine throughout the film could be shown by EDX of the cross section and XPS depth profiling in case of the porous (Sec. 3.2) and epitaxial (Sec. 3.3) films, respectively. After the adjustment of the right fluorine content, the porous films were investigated by electrochemical impedance spectroscopy under a pure oxygen atmosphere in a temperature range of 400 °C to 600 °C. For this purpose a special sample holder was constructed (see Sec. A). The electrochemical characterization of an SOFC cathode in Sec. 3.2 via impedance spectroscopy requires a set of suitable mathematical models to describe each aspect of the material adequately.

The processes occurring during the oxygen reduction reaction and oxygen ion transport together with a large variety of cathode morphologies lead to specific capacitive responses, which cannot be approached by models containing only CPE contributions. As introduced in Sec. 2.5, in the special case of a porous MIEC cathode as investigated in this work, a mathematical model is already available created by Adler et al. [75] based on the work of Gerischer [81], which combines the incorporation of oxygen ions at the gas/cathode interface and the transport of oxygen ions through the bulk material into one element. These two phenomena lead to the very distinct half tear-drop shaped EIS response. The bulk diffusion generates the linear part in the mid-frequency range, while the oxygen ion exchange produces the capacitive response in the low-frequency range inside the Nyquist plot.

The impedance spectroscopy yielded three different responses for the three compositions. The pure oxide showed the typical but slightly depressed Gerischer-type shape, while $\text{BaFeO}_{2.333}\text{F}_{0.333}$ showed a semicircle-like response, both in a comparable range of resistance together with identifiable contributions of charge exchanges. In contrast, BaFeO_2F showed very large resistances and a response consisting out of several contributions. The response of the purely oxidic film could be well described by the Gerischer-type impedance model developed by Adler et al. though, it had to be slightly modified by turning it into a “fractal” expression, comparable to the distribution of relaxation times turning a pure capacitance into a CPE element. During these experiments, the oxide exhibited a non-Arrhenius behaviour, which was attributed to the phase change to $\text{BaFeO}_{2.667}$ by incorporation of oxide ions into the lattice. On the other side, the partial fluorinated film could neither be fitted by an ideal or the fractal Gerischer impedance model. It exhibited purely semicircle-like characteristics, but showed an ideal Arrhenius behaviour. This semicircle response in case of cathodes for SOFCs could be attributed to a shift of the limiting factor towards a surface limitation of the oxygen reduction and transportation process. Fluorine, as the more mobile anion due to its monovalency, what was also shown inside the kinetics study in Sec. 3.4, might be able to allocate an oxygen vacancy in order to allow an oxygen ion to move. In addition, the fluorination led to a phase stabilization, as also shown in Sec. 3.5.4, where an even lower degree of fluorination is discussed. In contrast, the fully fluorinated film showed an ASR several magnitudes higher than the previous films with a lower fluorine content. This drastic increase could be attributed to the lack of oxygen vacancies due to the full occupation of the anion sublattice after the fluorination. Oxygen vacancies are necessary in order to allow the uptake of atmospheric oxygen and to conduct oxygen ions. On the other hand, the oxygen vacancy ordering in the monoclinic phases leads to a rigid anion sublattice which may also hinder the oxygen ion conduction.

In contrast to the polycrystalline films, the epitaxial films of $\text{BaFeO}_{2.5}$ and BaFeO_2F were

investigated in order to proof a possible multiferroic behaviour due to lattice distortions introduced by fluorination. Additional to XRD analysis, Mössbauer spectroscopy and magnetical measurements were performed on the films. The incorporated fluorine lead to a displacement of the iron cation inside the unit cells in powder samples which exhibited no long range anion ordering. However, XRD and RSM measurements of the oxide and fluorinated films showed that the fluorination lead to a relaxation of the strained lattice invoked by the mismatch between film and substrate. The Mössbauer study revealed that the fluorination leads to a more isotropic orientation of spins, which is in correspondence to the strain relaxation, while the spins of the oxide were parallel to out-of-plane direction. Further, the results suggested a *trans*-configuration, i.e. centrosymmetric, of the $\text{Fe}^{3+}\text{O}_4\text{F}_2$ octahedron, thus, no Fe cation displacement would be possible. In contrast, the overall magnetic ordering remained unchanged in a G-AFM ordering with a small canting of spins.

The diffusion and interdiffusion of anions inside the Ba-Fe-O-F system is crucial for understanding synthesis conditions and oxygen ion conduction. A lot of the work done in Sec. 3.2 was driven by the general concept of interdiffusion coupled with anion movement during electrochemical processes. The work in Sec. 3.4 deepens the understanding of such interdiffusion reactions and investigates thermodynamic and kinetic properties. The Ba-Fe-O-F system offers a unique chance to explore such underlying fundamentals due to the structural dependency on the fluorine content. The reaction of $\text{BaFeO}_{2.5}$ and BaFeO_2F to $\text{BaFeO}_{2.333}\text{F}_{0.333}$ involves three distinct structures, which can be identified easily by XRD, thus, overcoming the basic problem of distinguishing the participating anions. XRD and neutron diffraction cannot be applied to distinguish between O^{2-} and F^- since they are equal in their electron configuration ($1s^2 2s^2 2p^6$) and their similar scattering lengths (5.803(4) fm and 5.654(1) fm for oxygen and fluorine, respectively [23]) and atomic form factors [21, 22]. A key feature of this study is the indirect resolution of diffusing oxygen and fluorine anions via tracking of the weight fractions of specific crystal structures (Fig. 3.1) by XRD and Rietveld refinement on the progressing reaction. Thus, it bypasses the above mentioned restrictions and enables the usage of a rather simple method. The experimental plan involved isothermal high temperature XRD to monitor the interdiffusion reaction depending on temperature. Based on the metastability and electrochemical performance highlighted in Sec. 3.4, a temperature window of 380 – 480 °C with 20 °C with XRD scans in a timed interval were chosen. The collected XRD patterns were then evaluated by a batch Rietveld refinement based on an input script (see Sec. B). The to-be-investigated powder was in every case a 2:1 mixture of $\text{BaFeO}_{2.5}$ and BaFeO_2F to satisfy the general interdiffusion reaction (Eqn. 3.1). Fig. 3.6 illustrates the basic idea of the experimental work in Sec. 3.4. The formation of $\text{BaFeO}_{2.333}\text{F}_{0.333}$ at selected temperatures, and by this the interdiffusion of the anions, was monitored by the

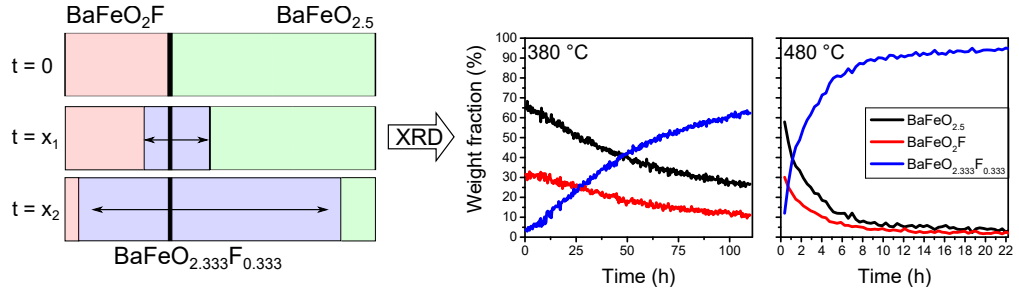


Figure 3.6.: Scheme of the interdiffusion process inside the powder mixture. The phase changes can be tracked by high temperature XRD (e.g. at temperatures of 380 °C and 480 °C).

extraction of the corresponding weight fractions from the XRD patterns.

The analysis followed three different approaches, the first one investigated the thermodynamical order and activation energy of the reaction, the second one applied the empirical formula developed by Johnson, Mehl and Avrami (in cooperation with Prof. Dr. Roger de Souza) which yielded insights into the reaction path inside the material, and the third and last method was the application of a diffusion model based on the Boltzmann-Matano method and the deduced root mean-squared displacement developed by Dayananda [52]. The reaction was found to be of first order with an activation energy of 0.47(1) eV based on the time and temperature-dependent changes in the weight fractions of each phase. Subsequently, the weight fraction data was used to fit the Johnson-Mehl-Avrami (JMA) model [91, 92]:

$$\gamma(t) = (1 - e^{k_{JMA} t^{n_{JMA}}}) \quad (3.2)$$

With $\gamma(t)$ being the phase fraction percentage of $\text{BaFeO}_{2.333}\text{F}_{0.333}$ at time t , n_{JMA} the Avrami exponent and k_{JMA} the rate constant of formation. The fitting of the data set yielded a diffusion controlled reaction, with a phase formation mechanism depending on temperature. At the lower temperatures, the transformation starts along the grain boundaries while for higher temperatures, the transformation directly penetrates into the bulk. Despite that, the crystallite size remained unaffected, what points towards no recrystallization during the interdiffusion reaction.

For the last analysis approach, the particle size of the powder before and after the lowest and highest temperature measurement was analysed by SEM. It was also shown that no particle growth occurred during the interdiffusion reaction and hence, the product particles are morphologically identical to the educt particles. Knowing the particle size

L_{particle} , the interdiffusion coefficient $\tilde{D}_{\text{BaFeO}_{2.333}\text{F}_{0.333}/\text{C}}$ could then be calculated by fitting the transformed data to the following equation:

$$x_{\text{BaFeO}_{2.333}\text{F}_{0.333}/\text{C}} = C_{V,\text{BaFeO}_{2.333}\text{F}_{0.333}} \cdot L_{\text{particle}} = \sqrt{2\tilde{D}_{\text{BaFeO}_{2.333}\text{F}_{0.333}/\text{C}}t}. \quad (3.3)$$

Here, $x_{\text{BaFeO}_{2.333}\text{F}_{0.333}/\text{C}} = C_{V,\text{BaFeO}_{2.333}\text{F}_{0.333}} \cdot L_{\text{particle}}$ describes the penetration depth of the product phase into the educt phases, with $C_{V,\text{BaFeO}_{2.333}\text{F}_{0.333}}$ being the overall concentration. For the application of this formalism, it was assumed that the particles of the educt phases were evenly distributed in such a way that the local stoichiometry satisfies Eqn. 3.1. By this, the diffusion occurred over the grain boundary between the particles with zero net mass flux. The fitting yielded then interdiffusion coefficients with an order of magnitude of $10^{-13}\text{cm}^2/\text{s}$ and following an Arrhenius-type behaviour. Thus, the extraction of the activation energy for the interdiffusion resulted in a value of $E_{a,\tilde{D}} = 0.46(2)$ eV, which is comparable to the reaction rate activation energy of $0.47(1)$ eV. The study was conducted to gain insight into the interdiffusion behaviour of oxide and fluoride anions. Based on the presented results, it was possible to assign the oxygen anion as the rate limiting species. After the publications, Sec. 3.5 will pick up some questions which could not be addressed inside the publications. It will contain discussions about

- phase formations inside the Ba-Fe-O-F system with respect to their symmetry
- symmetry relations within oxidation and reduction of the phases $P2_1/c$, $P2_1/m$ and $P4/mmm$
- influence of crystallite sizes on reactivity and phase stability
- preparation and examination of a fluorinated film with the composition $\text{BaFeO}_{2.43}\text{F}_{0.13}$

· *Phase formations inside the Ba-Fe-O-F system with respect to their symmetry* The investigated system Ba-Fe-O-F was shown to either form structures with a symmetry of $P2_1/c$, $P2_1/m$ and $Pm\bar{3}m$ during the experiments, which were of importance. Especially the formation of $P2_1/m$ for the structurally isotopic compositions $\text{BaFeO}_{2.333}\text{O}_{0.333}$ and $\text{BaFeO}_{2.667}$ raised the question what is the controlling factor for this specific phase formations. This question will qualitatively discussed based on the occupation of the anion sublattice and oxygen vacancy ordering.

· *Symmetry relations within oxidation and reduction of the phases $P2_1/c$, $P2_1/m$ and $P4/mmm$*

The oxidation of $P2_1/m$ towards $P4/mmm$ will be discussed with respect to symmetry changes along the branches of the corresponding symmetry tree. As highlighted during

the works in Sec. 3.1 and 3.4, the symmetry relations between $P2_1/c$ and $P2_1/m$ are connected via the aristotype symmetry $Pm\bar{3}m$, while the observed symmetry $P4/mmm$ can be found on both branches below the aristotype.

· *Influence of crystallite sizes on reactivity and phase stability*

The impact of the crystallite size on specific properties, such as sintering or oxygen release/uptake as shown above, will be with the cyclic measurements of TG and EIS under oxygen atmosphere coupled with XRD analysis performed within the experimental framework of Sec. 3.1. The different synthesis procedures found during this work, lead to samples with differing crystallite sizes, especially in case of the powders synthesized via the low and high temperature synthesis route.

· *Preparation and examination of a fluorinated film with the composition $BaFeO_{2.43}F_{0.13}$*

The system Ba-Fe-O-F either forms the structures $P2_1/c$, $P2_1/m$ and $Pm\bar{3}m$, the question about the performance of a low fluorinated film with a fluorine stoichiometry less than $BaFeO_{2.333}F_{0.333}$ was not addressed during the work in Sec. 3.2. The results there suggested a change in limitation from bulk transport to surface exchange, thus, a further reduction of the fluorine content may have a yet unknown impact on the electrochemical performance. The results of the study on the low fluorinated film will be presented and discussed.

3.1. Structural and magnetic properties of newly found $\text{BaFeO}_{2.667}$ synthesized by oxidizing $\text{BaFeO}_{2.5}$ obtained via nebulized spray pyrolysis

Stephan Wollstadt ^{a,d}, Yuji Ikeda ^b, Abhishek Sarkar ^{c,e}, Sami Vasala ^d, Claudia Fasel ^f, Lambert Alff ^g, Robert Kruk ^c, Blazej Grabowski ^b, Oliver Clemens ^{a,*}

^a University of Stuttgart, Institute for Materials Science, Materials Synthesis Group, Heisenbergstraße 3, 70569 Stuttgart, Germany

^b University of Stuttgart, Institute for Materials Science, Department of Materials Design, Pfaffenwaldring 55, 70569 Stuttgart, Germany

^c Karlsruher Institut für Technologie, Institut für Nanotechnologie, Hermann-von-Helmholtz-Platz 1, 76344 Eggenstein Leopoldshafen, Germany

^d Technical University of Darmstadt, Institut für Materialwissenschaft, Fachgebiet Materialdesign durch Synthese, Alarich-Weiss-Straße 2, 64287 Darmstadt, Germany

^e Technical University of Darmstadt, Institut für Materialwissenschaft, Gemeinschaftslabor Nanomaterialien, Alarich-Weiss-Straße 2, 64287 Darmstadt, Germany

^f Technical University of Darmstadt, Institut für Materialwissenschaft, Fachgebiet Disperse Feststoffe, Alarich-Weiss-Straße 2, 64287 Darmstadt, Germany

^g Technical University of Darmstadt, Institut für Materialwissenschaft, Advanced Thin Film Technology, Alarich-Weiss-Straße 2, 64287 Darmstadt, Germany

* Corresponding Author: oliver.clemens@imw.uni-stuttgart.de

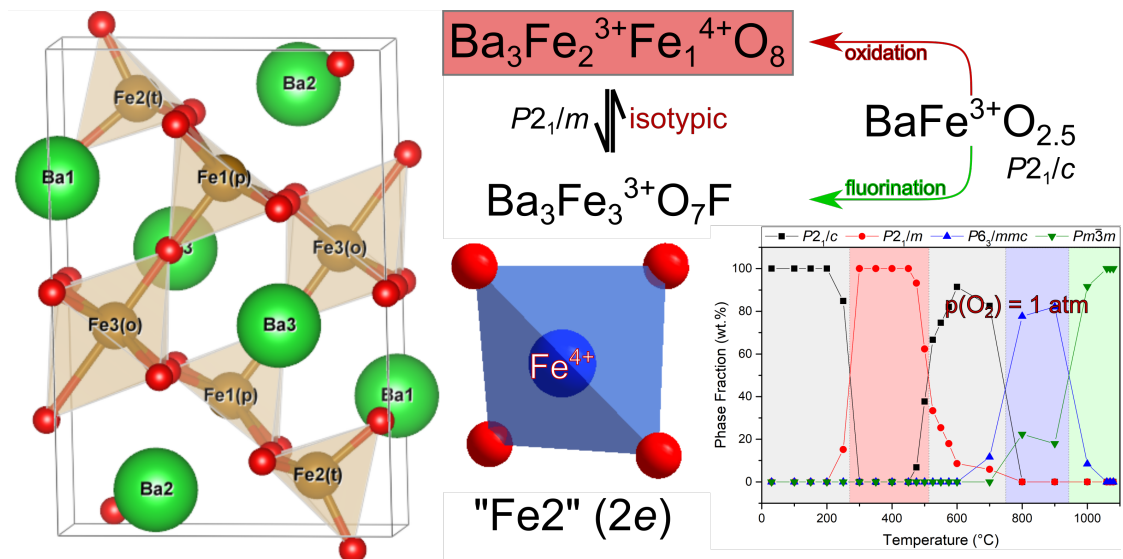
Received: 11 February 2021; Published online: 9 July 2021; Published in issue: 2 August 2021

Reprinted (adapted) with permission from Wollstadt, S., Ikeda, Y., Sarkar, A., Vasala, S., Fasel, C., Alff, L., Kruk, R., Grabowski, B., and Clemens, O. "Structural and Magnetic Properties of $\text{BaFeO}_{2.667}$ Synthesized by Oxidizing $\text{BaFeO}_{2.5}$ Obtained via Nebulized Spray Pyrolysis." *Inorganic Chemistry* 60.15 (2021): 10923-10933. Copyright 2021 American Chemical Society.

The supplementary information is directly included into the text and marked with (SI).

DOI: <https://doi.org/10.1021/acs.inorgchem.1c00434>

Abstract A new vacancy-ordered perovskite-type compound $\text{Ba}_3\text{Fe}_3\text{O}_8$ ($\text{BaFeO}_{2.667}$) was prepared by oxidizing $\text{BaFeO}_{2.5}$ ($P2_1/c$) with the latter compound obtained by a spray-pyrolysis technique. The structure of $\text{Ba}_3\text{Fe}_3\text{O}_8$ was found to be isotypic to $\text{Ba}_3\text{Fe}_3\text{O}_7\text{F}$ ($P2_1/m$) and can be written as $\text{Ba}_3\text{Fe}_2^{3+}\text{Fe}_1^{4+}\text{O}_8$. Mössbauer spectroscopy and *ab initio* calculations were used to confirm mixed iron oxidation states, showing allocation of the tetravalent iron species on the tetrahedral site and octahedral as well as square pyramidal coordination for the trivalent species within a G-type antiferromagnetic ordering. The uptake and release of oxygen was investigated over a broad temperature range from RT to 1100 °C under pure oxygen and ambient atmosphere via a combination of DTA/TG and variable temperature diffraction measurements. The compound exhibits a strong lattice enthalpy driven reduction to monoclinic and cubic $\text{BaFeO}_{2.5}$ at elevated temperatures.



3.1.1. Introduction

Perovskite oxides offer themselves as candidates for a vast variety of applications, such as cathode materials for solid oxide fuel cells (SOFC) [4, 18, 93, 94], membranes [95, 96] and oxygen storage [97]. The oxide perovskite as a crystal type is defined by the general formula ABO_3 where A is an alkaline, alkaline earth or rare earth metal cation, and B a transition metal cation [98]. Lattice oxygen can also be partially replaced by e.g. halide anions, like F^- [10, 99] or Cl^- [100, 101], even to large extents [102] opening up other fields of applications.

Iron-based perovskite oxides can be reduced and oxidized, resulting in a change of the oxidation state of the transition metal ion from 4+ to 3+. In many cases by reducing the transition metal completely to the trivalent state, the perovskite changes into the defect-ordered brownmillerite structure [103, 104], e.g. $SrFeO_3$ (cubic perovskite) reduced to $SrFeO_{2.5}$ (brownmillerite) [105, 106]. Further, even lower oxidation states are possible that maintain a perovskite related structure (CaH₂-based reduction to $SrFeO_2$ with divalent iron) [107] and $Sr_{1-x}Ba_xFeO_2$ [108] with divalent iron.

Similarly, the perovskite-system Ba-Fe-O possesses a cubic closed-packed (*ccp*) related arrangement of Ba and Fe ions for $BaFeO_{2.5}$, while showing a highly complex vacancy ordered structure of the anions [33, 109, 110]. Between an oxygen content of 2.5 and 3, the Ba-Fe-O system exhibits a variety of structures with partial hexagonal closed-packed (*hcp*) stacking of BaO_{3-y} layers [111–113], such as trigonal $BaFeO_{2.64}$ ($R\bar{3}m$) [111] or the hexagonal $P6_3/mmc$ phases $BaFeO_{2.65}$ [114] and $BaFeO_{2.667}$ [113], which can be related to the Goldschmidt tolerance factor [115], which increases for $A = Ba$, and is position-dependent due to the different sizes of Fe^{3+} and Fe^{4+} . The Ba-Fe-O system can adopt a lot of different structures depending of the anion sub-lattice.

$BaFeO_{2.5}$ is susceptible towards topochemical reactions. Several different modifications can be found by introducing OH^- , F^- or more O^{2-} . For example, the fluorine containing cubic ($Pm\bar{3}m$) $BaFeO_2F$ [11] and monoclinic ($P2_1/m$) $Ba_3Fe_3O_7F$ ($BaFeO_{2.333}F_{0.333}$) [12, 116] are formed upon topochemical fluorination of the compound. Hydration of $BaFeO_{2.5}$ yields the orthorhombic ($Cmcm$) phases $BaFeO_{2.33}(OH)_{0.33}$ and $BaFeO_{2.25}(OH)_{0.5}$ [117, 118]. Further, $BaFeO_{2.5}$ can be topochemically oxidized with ozone to $BaFeO_3$ [34]. The oxidation state of the transition metal Fe adapts according to the oxygen content, from 3+ to 4+, which directly affects magnetic properties. $BaFe^{4+}O_3$ is ferromagnetic with a high Curie temperature, however, intrinsic oxygen vacancies change the local oxidation states of iron from 4+ to 3+ [34, 119]. In contrast, $BaFe^{3+}O_{2.5}$ exhibits an antiferromagnetic ordering [33].

We already acknowledged the possible existence of a new monoclinic phase in the oxidic Ba-Fe-O system with an assumed composition of $BaFeO_{2.667}$ in our previous work [83].

There are several reports mentioning a composition of $\text{BaFeO}_{2.667}$, crystallizing either in a hexagonal space group $P6_3/mmc$ [113], or possessing a triclinic structure [111, 120, 121], or adopting a rhombohedral structure [111] for a similar composition $\text{BaFeO}_{2.68}$. However, none of these reports were able to derive a precise structural model consistent with the diffraction data observed. In this article, we report a detailed characterization of the synthesis of $\text{BaFeO}_{2.667}$ together with its detailed monoclinic structure and magnetic properties, as well as the oxygen incorporation and reduction and the reversibility of this process. We found that the material shows unusual allocation of Fe^{4+} on a tetrahedrally coordinated site, with antiferromagnetic ordering as well as activity for reversible oxygen uptake and release, an important feature for electrocatalytic applications.

3.1.2. Experimental

3.1.2.1. Sample synthesis

Synthesis of fine-crystalline precursor material was performed by nebulized spray pyrolysis (NSP), described in more detail previously [85, 86]. The aqueous solution contained the precursor nitrate salts of barium and iron, $\text{Ba}(\text{NO}_3)_2$ (Sigma Aldrich, 99.99 %) and $\text{Fe}(\text{NO}_3)_3 \cdot 9 \text{H}_2\text{O}$ (Sigma Aldrich, 99.99 %), respectively. The salts were weighed in the stoichiometric ratio 1:1 and dissolved in deionized water. The mixture was stirred for one hour to establish a homogenous transparent yellowish solution. The ultrasonic nebulizer membrane (TDK, NB-59S-09S-0) was operated at a voltage of 48 V and current of 0.5 mA. The formed mist was carried with a constant gas flow of 2.5 SLM (standard liter per minute) of argon through the reactor furnace, which was set to a temperature of 700 °C. A barometer ensured a set pressure of 900 mbar. The powder was collected on a glass-fiber filter, which was held at a constant temperature of 140 °C to prevent water from condensing on the powder. The as-prepared powder was annealed in an air-tight furnace at a temperature of 900 °C under a constant stream of argon for 20 h. The target phase $\text{BaFeO}_{2.667}$ was obtained by oxidizing this starting powder at 400 °C in an oxygen atmosphere for 2 h with subsequent quenching to room temperature.

For high temperature impedance spectroscopy, symmetrical films were prepared by spin-coating annealed powder in an acidic dispersion (pH = 4) on YSZ8 button substrates (fuelcellmaterials, Nexceris, USA). The films were then sintered at 1060 °C under argon for 1 h. The film was oxidized at 400 °C in an oxygen atmosphere for 2 h with subsequent quenching to room temperature. Subsequently, both sides were coated with a sputtered Au electrode.

3.1.2.2. X-ray Diffraction Experiments

Ambient and high temperature X-ray diffraction (XRD) experiments were carried out on a Bruker D8 diffractometer (Bruker AXS, Karlsruhe, Germany) with Bragg-Brentano geometry and a Cu-K α source. For ambient measurements the angular range was set to 20° to 100° 2 θ with a step size of 0.02° and 1 second measurement time per step. The high temperature diffraction experiments were carried out in an HTK 1200 N temperature chamber with a TCU 1000 N (Anton Paar) temperature controller. The oxidation behavior of BaFeO_{2.5} was investigated under a pure oxygen atmosphere, while the stability of BaFeO_{2.667} was investigated under air. In order to obtain a satisfying quality of the patterns, the angular range was reduced to 20° to 60° 2 θ with a step size of 0.008° and 0.22 seconds per step. A constant oxygen flow ensured a homogenous oxygen atmosphere. The temperature range was set from room temperature to 1080 °C. Each obtained pattern was qualitatively and quantitatively evaluated and refined using the Rietveld method implemented in the software TOPAS 6 (Bruker AXS, Karlsruhe, Germany). Therefore, the instrumental contribution to the convolution function was extracted empirically from a set of fundamental parameters utilizing a reference scan of a LaB6 standard (NIST 660a).

3.1.2.3. TG/DTA

Thermogravimetric analysis and differential thermal analysis were carried out on a Netzsch STA 449C. The temperature range was set from room temperature to 1100 °C (5 °C/min) under flowing oxygen (40 ml/min).

3.1.2.4. Magnetic measurements

Magnetization measurements were done using a Quantum Design MPMS SQUID magnetometer. The sample powder was filled into a gelatin capsule and fixed into a plastic sample holding straw. Temperature dependent M(T) behavior was measured in zero-field-cooled (ZFC) and field-cooled (FC) modes between 10 K and 350 K at 1 T field. Also, field dependent M(H) measurements were done at 10, 80, 250 and 320 K between –5 T and 5 T with 0.1 T intervals.

3.1.2.5. ⁵⁷Fe Mössbauer spectroscopy

⁵⁷Fe Mössbauer spectroscopy measurements were performed in transmission geometry using a spectrometer with a moving source of ⁵⁷Co:Rh in transmission geometry using a triangular sweep of the velocity scale. Low temperature measurements were performed

using a liquid He flow cryostat. As conventionally done, the isomer shift is given relative to α -Fe at room temperature.

3.1.2.6. DFT calculations

In the present *ab initio* calculations for $\text{BaFeO}_{2.667}$ we considered the G-type antiferromagnetic (AFM) ordering as well as the ferromagnetic (FM) and the non-magnetic (NM) ordering. To achieve a commensurate sampling of all the magnetic configurations, a 56-atom supercell based on a $1 \times 1 \times 2$ expansion of the 28-atom primitive cell was employed in the present *ab initio* calculations.

The projector augmented wave method [122] and the generalized gradient approximation (GGA) of the Perdew–Burke–Ernzerhof (PBE) form [122] as implemented in the VASP code [123, 124] were applied in combination with the provided potentials [124]. The $5s5p6s$, $3d4s$ and $2s2p$ orbitals of Ba, Fe and O, respectively, were treated as valence states. The plane-wave cutoff was set to 550 eV. The reciprocal space of the 56-atom supercell was sampled by a Γ -centered $6 \times 8 \times 4$ mesh, and the Methfessel–Paxton scheme [125] with a smearing width of 0.1 eV was employed. Total energies were minimized until they were converged to within 10^{-5} eV per unit cell. Cell volume, cell shape, and internal atomic positions were optimized so that the forces on atoms and the stress components on the supercells are less than $2.5 \cdot 10^{-2}$ eV/Å and $1 \cdot 10^{-3}$ eV/Å³, respectively. The NM, FM, and G-AFM configurations were computed under the collinear spin-polarized condition. Strong on-site electron correlation was considered for the Fe d orbitals employing the rotationally invariant DFT+ U formalism of Dudarev *et al.* [126], with $U_{\text{eff}} \equiv U - J$ varied in a range of 0 eV to 6 eV. Volumes, charges, and magnetic moments of atoms were evaluated based on the Bader analysis [127] employing the Yu–Trinkle algorithm [128] as implemented by Henkelman *et al.* [129–131].

For comparison, similar calculations were performed on cubic $Pm\bar{3}m$ BaFeO_3 . Previous *ab initio* simulations found that, within the collinear spin polarization, the FM phase is thermodynamically more stable than the AFM phases at 0 K for BaFeO_3 [132–134], and we therefore focus on the FM phase for BaFeO_3 . The reciprocal space of the 5-atom cubic primitive unit cell was sampled by a Γ -centered $12 \times 12 \times 12$ mesh, and otherwise the same computational conditions as for $\text{Ba}_3\text{Fe}_3\text{O}_8$ were applied.

3.1.3. Results and discussion

3.1.3.1. Determination of optimized synthesis conditions for BaFeO_{2.667}

The diffraction experiments on the oxidation behavior under a pure oxygen atmosphere of monoclinic BaFeO_{2.5} prepared by NSP are presented in Figure 3.7 a,c,e. All compositions given are in good agreement with the weight changes observed in a DTA/TG measurement (see Figure 3.8 and an extensive discussion in SI). The compound starts to take up oxygen around 250 °C under the formation of a new phase BaFeO_{2.667} with monoclinic ($P2_1/m$) symmetry (see structural analysis discussed in section 3.1.3.3), with a diffraction pattern not reported before. During this oxidation, the unit cell shrinks due to the change in the valence of iron from the larger sized trivalent to the smaller sized tetravalent state [135, 136]. Oxygen is again released starting at 475 °C under the reformation of BaFeO_{2.5} ($P2_1/c$), where both phases coexist up to a temperature of ~580 °C. Around 750 °C the system changes into a mixture predominantly consisting out of the hexagonal $P6_3/mmc$ (BaFeO_{2.667}) [113] and a lower amount of a cubic phase ($Pm\bar{3}m$), and the latter becomes the main phase at a temperature of 1000 °C. The transformation to the oxygen richer phases with $P2_1/m$ or $P6_3/mmc$ symmetry is accompanied by a decrease of the pseudocubic lattice parameter apseudocubic, which is calculated from the cube root of the volume per BaFeO_{2.5+x} formula unit, $V_{f.u.}$. In contrast, the transformation of BaFeO_{2.5} $P2_1/c$ above 750 °C appears to turn into $Pm\bar{3}m$ due to a sufficient amount of thermal energy (see Figure 3.7). The changes in volume and the linear expansions from the pseudocubic lattice parameters of the different phases are highlighted in Figure 3.7 e.

The narrow stability range of the monoclinic phase with $P2_1/m$ symmetry (BaFeO_{2.667}) becomes also evident by heating the as-prepared BaFeO_{2.667} sample in air, i.e., reducing the oxygen partial pressure from 1 bar to 0.2 bar (see Figure 3.7 b,d,f). In air, BaFeO_{2.667} starts to release oxygen at around 300 °C, forming the monoclinic BaFeO_{2.5} phase ($P2_1/c$). It remains in this configuration until it eventually starts to transform to cubic $Pm\bar{3}m$ symmetry at around 800 °C, as already observed under oxygen atmosphere. This structural transition only reflects the breaking up of the long range oxygen vacancy order found for BaFeO_{2.5} ($P2_1/c$) [33]. During this transition, no other oxidized phase, e. g., a hexagonal modification, is formed as in the case of heating under oxygen, compare Figure 3.7 c and d, respectively. The maintenance of oxygen composition for the $P2_1/c$ to $Pm\bar{3}m$ transition is also indicated by the absence of a sudden change of the volume per formula unit, see Figure 3.7 e,f.

In contrast to the heating, the processes observed on cooling are not easily comparable via XRD and TG due to different kinetics of both processes. In addition, the phases which are observed on cooling can depend from the starting temperature chosen for cooling,

e. g., cooling 6H-BaFeO_{3-y} under oxygen does not result in the reversible formation of BaFeO_{2.667} [39], and this phase is then stable down to ambient temperature. Further, we found that cooling BaFeO_{2.667} slowly under oxygen results in an oxygen uptake under formation of tetragonal BaFeO_{2.81} between 200-300 °C, which can also be found as an impurity phase (see next section) depending on the detailed heating and cooling conditions chosen. Thus, the uptake of oxygen under transformation to BaFeO_{2.81} is a competing reaction when heating BaFeO_{2.667} in pure oxygen atmosphere. This is further similar to the oxygen uptake of BaFeO_{2.5} under formation of cubic BaFeO₃ at 150 °C when heating under ozone as reported by Hayashi *et al.* [34].

3.1.3.2. Detailed interpretation of TG/DTA measurements (SI)

The TG/DTA measurement reveals several phase transitions accompanied by either mass gain or loss. Figure 3.8 depicts the recorded data. The TG trajectory shows two big mass gains between 250 and 550 °C and between 750 and 950 °C, each time followed by a loss of weight towards its initial mass. However, the first mass gain is accompanied by a release of energy, while the second mass gain and loss are endothermic processes. It is noteworthy that up to 250 °C the sample loses weight until the first massive mass gain. These anomalies may be attributed to a loss of adhesive water. As seen in the HT-XRD (Figure 3.7 a,b), BaFeO_{2.5} undergoes several phase transitions which can be assigned to different oxygen stoichiometries and thereby different structures. Thus, the first massive mass gain corresponds to an incorporation of oxygen from the stoichiometric level of 2.5 to 2.667, followed by the release of the incorporated oxygen above 520 °C. By comparing the masses $m_{2.667}$ ($m_{BaFeO_{2.667}} = 235.89u$) at 340 °C and $m_{2.5}$ ($m_{BaFeO_{2.5}} = 233.17u$) at 675 °C, it becomes evident that the change in oxygen stoichiometry can be assigned to roughly 0.17. The difference between the two masses is about 1 %, which corresponds to a mass difference of 2.72 u or 0.17 oxygen atoms ($m_O = 15.999u$). The second mass gain is about 0.6 % and can be attributed to the formation of the oxygen richer hexagonal BaFeO_{2.67} ($P6_3/mmc$) and the cubic $Pm\bar{3}m$ phases as it was observed in the *in situ* XRD experiments. From the XRD experiments, it follows, that the phase ratios are about 80 % $P6_3/mmc$ to 20 % $Pm\bar{3}m$, which corresponds to an average mass of 235.9 u. Though, it might be straightforward to assume that the cubic $Pm\bar{3}m$ phase may be BaFeO₃, the TG/DTA measurement shows a loss of mass accompanied with a strong endothermic spike in the first derivative of the DTA signal. These suggest that the composition is more likely BaFeO_{2.5}. By this, the endothermic nature of this phase transition is based on resolving of the strong vacancy ordering which is characteristic for BaFeO_{2.5} [33] by providing thermal energy. Thus, the composition of the hexagonal phase is roughly equal to the BaFeO_{2.667} phase [113] and the cubic phase $Pm\bar{3}m$ possess an oxygen stoichiometry ≈ 2.5 , which

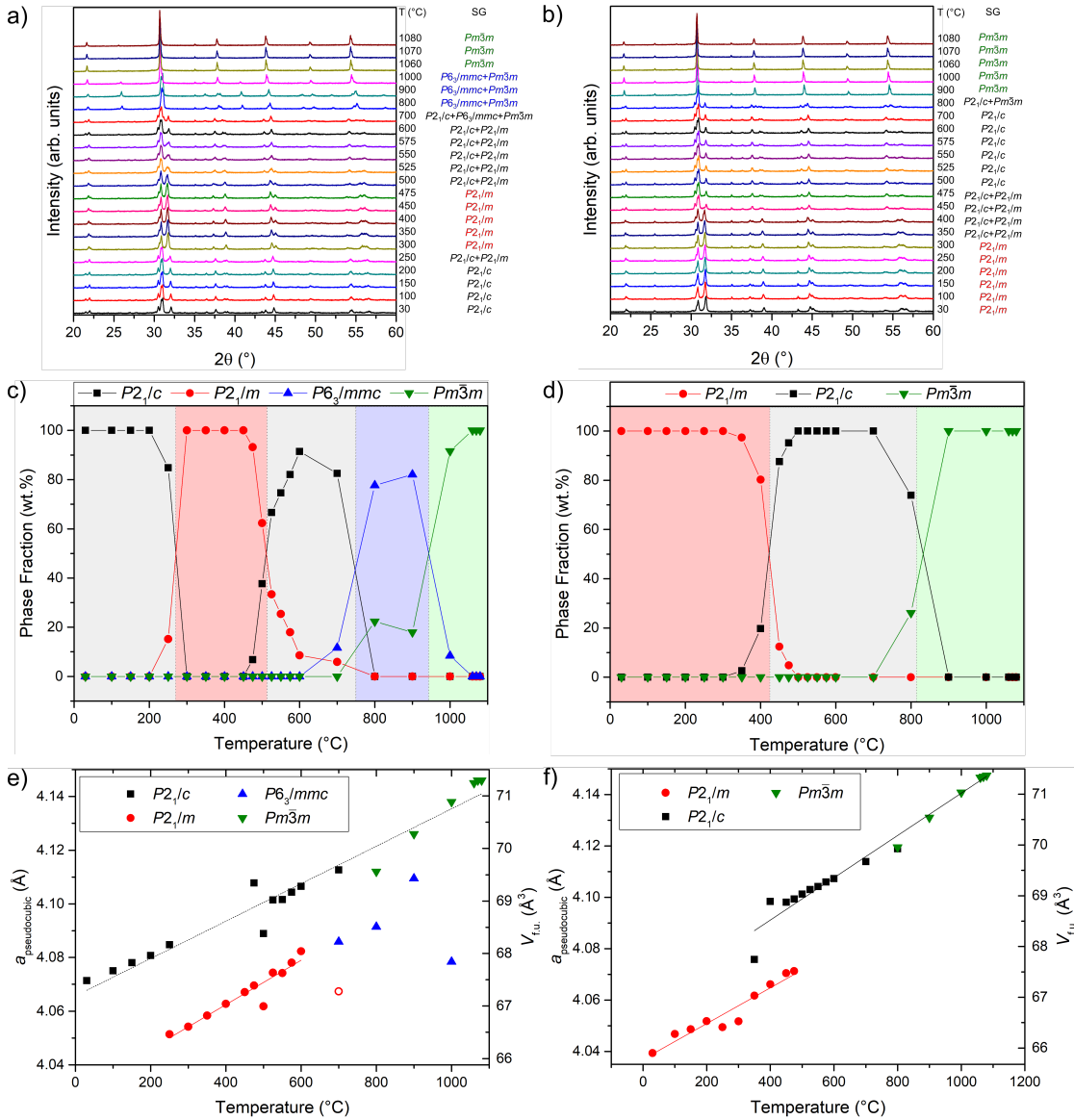


Figure 3.7.: Results of the high temperature XRD study: (a,c,e) depict the results of BaFeO_{2.5} under oxygen; (b,d,f) depict the results of BaFeO_{2.667} under air. (a,b) show the XRD pattern over the whole temperature range with the emerging configurations. (c,d) highlight the corresponding phase fractions as calculated by Rietveld refinements. (e,f) showcase the evolving pseudo-cubic lattice parameters (and simultaneously the volume per formula unit $V_{f.u.}$) with straight lines emphasizing the linear thermal expansion.

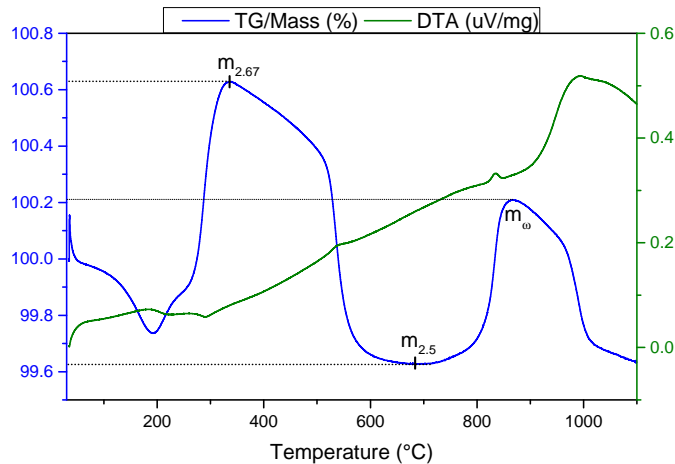


Figure 3.8.: TG/DTA measurement of pure $\text{BaFeO}_{2.5}$ performed under pure oxygen atmosphere, complementary to the HTXRD experiment depicted in Figure 3.7 a,c,e.

can also be connected to the observed pseudo-cubic lattice parameters in Figure 3.7 e,f.

3.1.3.3. Structural characterization of $\text{BaFeO}_{2.667}$

After obtaining optimized synthesis conditions, a long-time scan of $\text{BaFeO}_{2.667}$ was recorded at ambient temperature. Indexing of this pattern indicated the compound to crystallize in the monoclinic crystal system, with lattice parameters indicating a $\sqrt{6} \times \sqrt{2} \times \sqrt{3}$ supercell of the cubic perovskite type structure, i.e., a 6-fold superstructure of the cubic perovskite. To the best of our knowledge, this symmetry is known only for $\text{BaFeO}_{2.333}\text{F}_{0.333}$ [12, 116] as well as for $\text{BaCoO}_{2.667}$ [137], i.e., $2 \text{Ba}_3\text{M}_3\text{X}_8 = \text{Ba}_6\text{M}_6\text{X}_{16}$ for using integer chemical indexes, and both compounds have been found before by members of our group. Indeed, the pattern could be well fitted based on the structure found for $\text{BaFeO}_{2.333}\text{F}_{0.333}$ [12, 116]. In comparison to $\text{BaFeO}_{2.333}\text{F}_{0.333}$ ($V_{\text{oxyfluoride, f.u.}} = 67.10 \text{ \AA}^3$ [116]), $\text{BaFeO}_{2.667}$ ($V_{\text{oxide, f.u.}} = 66.47(2) \text{ \AA}^3$) exhibits a significantly smaller unit cell volume, which can be related to the smaller atomic radius of Fe^{4+} as compared to the single valence of the larger Fe^{3+} found in the oxyfluoride compound. The characteristic XRD reflexes in the range of 29 to 33° are shown in Figure 3.10 a to showcase the differences between the parent oxide $\text{BaFeO}_{2.5}$ and the oxidized $\text{BaFeO}_{2.667}$ and oxyfluoride $\text{BaFeO}_{2.333}\text{F}_{0.333}$. Since the monoclinic structure of $\text{BaFeO}_{2.5}$ is not directly related to the monoclinic structure of $\text{BaFeO}_{2.667}$ via a group-subgroup relationship (see symmetry trees given in references [12, 33, 138]), it is not possible to refine the reflection splitting pattern

observed for $\text{BaFeO}_{2.667}$ by adjusting the lattice parameters within the $P2_1/c$ structural model. Thus, it is possible to rule out such, at first glance likely, compositionally similar ordering variants. We acknowledge that in addition to the monoclinic phase, another perovskite-phase was observed in the powder quenched to room-temperature (P_4/mmm , $a = 3.981 \text{ \AA}$, $c = 4.010 \text{ \AA}$, $V = 63.53 \text{ \AA}^3$) with a weight fraction of around 10 %. This tetragonal structure is formed during the cooling process after oxidation and cannot be completely avoided by quenching to room temperature. Such a tetragonal barium ferrate was reported previously [111], and assigned to a composition of $\text{BaFeO}_{2.81}$ ($a = 3.978 \text{ \AA}$, $c = 4.003 \text{ \AA}$); thus it shows that the further uptake of oxygen on cooling can hardly be avoided completely.

Due to the fact that we could not get neutron data for the compound, which makes a precise determination of oxygen positions impossible, the atomic positions were derived by relaxing the structural model within the DFT calculations. Figure 3.9 shows the unit cell of the oxygen-vacancy-ordered $\text{BaFeO}_{2.667}$ ($\text{Ba}_3\text{Fe}_3\text{O}_8$) structure, based on O for F substitution of the structural model of $\text{BaFeO}_{2.333}\text{F}_{0.333}$. The structural parameters are listed in Table 3.1 and Table 3.2 (with $U_{\text{eff}} = 2.5 \text{ eV}$, which is close to the value used in [139] ($U - J = 2.4 \text{ eV}$) and reproduces a helical spin order in BaFeO_3 as observed in experiments). The structure obeys the symmetries of the space group $P2_1/m$ with $Z = 6$. Apart from changes of bond distances, as well as smaller changes of bond angles, no significant change was observed regarding the principle coordination environments. In particular, there are three symmetrically inequivalent sites for Fe, which are coordinated by O atoms in octahedral, pyramidal, and tetrahedral arrangements, respectively. Thus, the coordination scheme and connectivity of iron coordination polyhedra within $\text{BaFeO}_{2.667}$ can be described by the formula $\text{Ba}_3(\text{FeO}_{6/2})(\text{FeO}_{5/2})(\text{FeO}_{3/2}\text{O}_{1/1})$.

Both, the positional parameters of $\text{BaFeO}_{2.333}\text{F}_{0.333}$ as well as the DFT-optimized parameters for $\text{BaFeO}_{2.667}$ can be used to give a sufficiently good fit of the recorded diffraction patterns, as shown in Table 3.2 and Figure 3.10 b,c. Both, the coordination scheme as well as the presence of Fe^{4+} can be well confirmed by Mössbauer spectroscopy (see Figure 3.11 and Table 3.3, sextet 3). The Mössbauer spectrum of the compound was recorded at 10 K, at which the spectrum was easier to interpret than at ambient temperature (see Figure 3.12). At 10 K, the spectrum could be well described by three sextets with areas in the ratio of 1:1:1 (Table 3.3), agreeing well with iron being located on three different crystallographic sites with local symmetry $2e$. One of these sextets showed an isomer shift of 0.08 mm/s and a hyperfine field of 27.5(1) T, and we assign this sextet to the tetravalent iron species due to the following reasons: The reduction of the hyperfine field is well explained by the lower number of unpaired spins found for Fe^{4+} (d^4) as compared to Fe^{3+} (d^5). The isomer shift as well as the hyperfine field splittings are significantly reduced to what is found for the tetrahedrally coordinated Fe^{3+} species within the chemically similar

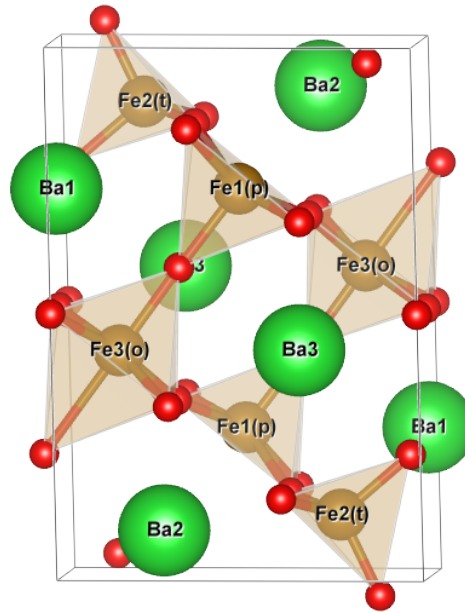


Figure 3.9.: Primitive cell of $\text{Ba}_3\text{Fe}_3\text{O}_8$. Green, brown and red spheres represent Ba, Fe, and O atoms, respectively. The labels on the Fe atoms show their coordination environments; “o”, “t” and “p” indicate an octahedral, tetrahedral, and pyramidal coordination, respectively.

Table 3.1.: DFT optimized internal atomic positions of G-AFM $P2_1/m$ $\text{Ba}_3\text{Fe}_3\text{O}_8$ with $U_{\text{eff}} = 2.5$ eV. For Fe atoms, the coordination environments are indicated.

Element	Wyckoff	Coordination	x	y	z
Ba	2e		0.271	1/4	0.987
	2e		0.911	1/4	0.716
	2e		0.573	1/4	0.336
Fe	2e	Fe1 pyramidal	0.270	1/4	0.489
	2e	Fe2 tetrahedral	0.881	1/4	0.233
	2e	Fe3 octahedral	0.574	1/4	0.827
O	2b		1/2	0	0
	2e		0.768	1/4	0.038
	2e		0.418	1/4	0.658
	2e		0.033	1/4	0.132
	4f		0.674	0.999	0.685
4f		0.846	0.991	0.383	

Table 3.2.: Lattice parameters optimized in DFT calculations and with XRD measurements. For XRD, the parameters were obtained with fixing the atomic positions either to those of isotypic $\text{BaFeO}_{2.333}\text{F}_{0.333}$ [116] or those of our DFT results. Fits are shown in Figure 3.10 b,c.

	DFT	XRD (atomic positions fixed)	
		$\text{BaFeO}_{2.333}\text{F}_{0.333}$ (isotypic to $\text{BaFeO}_{2.667}$)	based on DFT input
a (Å)	10.290	10.1597(2)	10.1621(2)
b (Å)	5.687	5.65021(15)	65.64942(14)
c (Å)	7.074	6.9524(2)	6.95256(19)
(°)	91.457	92.0529(17)	92.0490(19)
$V_{\text{f.u.}}$ (Å ³)	68.97	66.47(2)	66.48(2)
R_{wp} (%)		2.81	3.12
GOF		1.55	1.72

Table 3.3.: Fitting parameters for the ^{57}Fe Mössbauer spectrum of $\text{BaFeO}_{2.667}$ recorded at 10 K.

	Sextet 1 (blue)	Sextet 2 (green)	Sextet 3 (orange)
Area (%)	37(2)	29.5(1)	33.5(2)
Isomer shift (IS) (mm/s)	0.55(1)	0.31(1)	0.08(2)
Hyperfine field Bhf (T)	50.4(1)	47.0(1)	27.5(1)
Quadrupole splitting (mm/s)	-0.05(2)	-0.07(3)	-0.08(3)

compounds $\text{BaFeO}_{2.5}$ (0.15 – 0.23 mm/s, and 40.0 – 42.1 T) [33] or $\text{BaFeO}_{2.333}\text{F}_{0.333}$ (0.20 mm/s, and 42.0 T) [12]. The fact that the isomer shift is larger to what has been found for Fe^{4+} in Na_4FeO_4 (-0.140 mm/s [140]), Ba_2FeO_4 and Ba_3FeO_5 (-0.152 mm/s and -0.142 mm/s, respectively [141]), can be explained from the different bonding scenarios of the compounds. These compounds have isolated FeO_4^{4-} tetrahedra, which do not share edges or corners with other FeO_4^{4-} tetrahedra. Therefore, the oxygen ions provide a stronger degree of covalent bonding to the iron in compounds with non-linked FeO_4^{4-} tetrahedra, which reduces the isomer shift of the iron species in Na_4FeO_4 , Ba_2FeO_4 and Ba_3FeO_5 . The other two sextets both possess significantly higher isomer shifts and hyperfine fields of 0.31 mm/s and 0.55 mm/s and 50.4(1) T and 47.0(1) T, respectively. Both, hyperfine field and isomer shifts are well indicative for trivalent iron, similar to what has been found for the higher coordinated Fe^{3+} species in $\text{BaFeO}_{2.5}$ [33] and $\text{BaFeO}_{2.333}\text{F}_{0.333}$ [12]. Thus, one can conclude that charge ordering occurs in $\text{BaFeO}_{2.667}$ due to the significantly different site potentials induced by the different coordination environments. Thus, we discuss the allocation of the tetravalent iron species on one of the three different sites in the following. To do so, it is important to review what has been found for similar compounds previously.

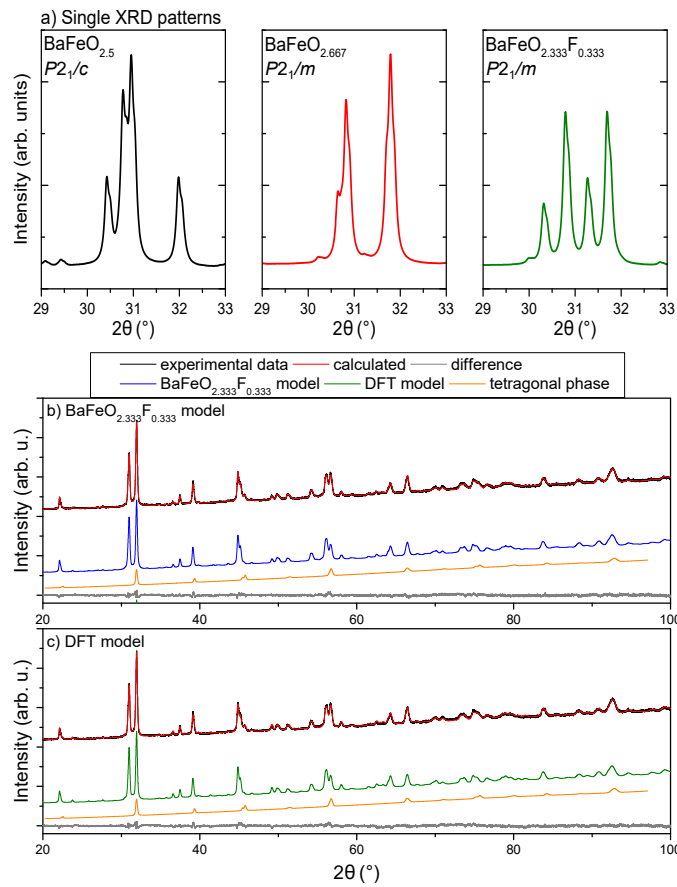


Figure 3.10.: a) Characteristic XRD reflexes for $\text{BaFeO}_{2.5}$, $\text{BaFeO}_{2.667}$ and $\text{BaFeO}_{2.333}\text{F}_{0.333}$. Ambient XRD data of $\text{BaFeO}_{2.667}$ and corresponding Rietveld fit based on the positional parameters found for b) $\text{BaFeO}_{2.333}\text{F}_{0.333}$ [12] and c) calculated by DFT for $\text{BaFeO}_{2.667}$.

Table 3.4.: Fitting parameters for the ^{57}Fe Mössbauer spectroscopy at room temperature. (SI)

	Singlet	Doublet 1	Doublet 2	Sextet 1	Sextet 2
Area (%)	20	25	23	10	22
Isomer shift (IS) (mm/s)	0.08	0.42	0.27	0.51	0.01
Hyperfine field B_{hf} (T)	-	-	-	47	28
Quadrupole splitting (mm/s)	-	1.5	0.71	-0.41	-0.07

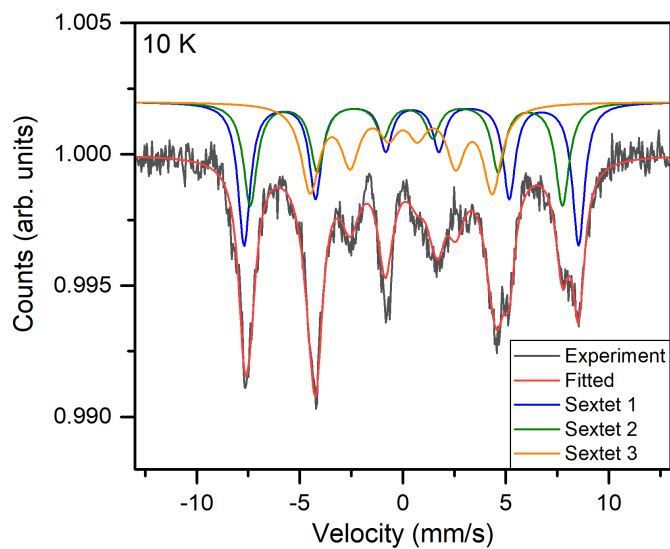


Figure 3.11.: ^{57}Fe Mössbauer spectra of room temperature and at 10 K of $\text{BaFeO}_{2.667}$.

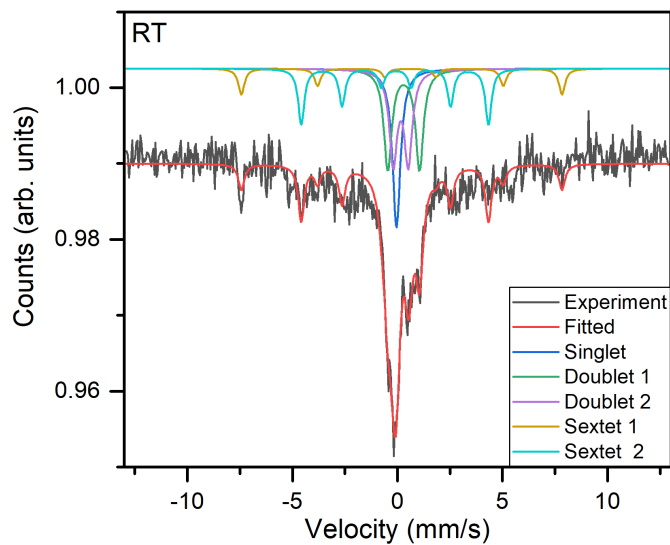


Figure 3.12.: ^{57}Fe Mössbauer spectra of $\text{BaFeO}_{2.667}$ recorded at room temperature. (SI)

First, for an octahedrally coordinated tetravalent iron ($\text{Fe}^{4+}\text{O}_{6/2}$), no strong tendency was found for distortion of the octahedron, though this would be in principle expected from the electron configuration $t_{2g}^3 e_g^1$ of high spin Fe^{4+} [142–145]. The high spin Fe^{4+} can be stabilized inside the square pyramidal coordination ($\text{Fe}^{4+}\text{O}_{5/2}$) as it has been observed for $\text{SrFeO}_{3-\delta}$ [146] next to octahedral coordination of the trivalent species ($\text{Fe}^{3+}\text{O}_{6/2}$) or inside $\text{BaY}_{0.5}\text{Fe}_{0.5}\text{O}_{2.75}$, where a square pyramidal coordination of Fe^{4+} is favored, while $\text{BaY}_{0.5}\text{Fe}_{0.5}\text{O}_{2.5}$ exhibits only octahedrally and tetrahedrally coordinated Fe^{3+} [145]. For $\text{Sr}_{1-x}\text{Ba}_x\text{FeO}_2$ ($0.4 \leq x \leq 1$) it was found that high spin Fe^{2+} ($S = 2$) is 4-fold coordinated inside a square-planar configuration [108]. By oxidizing $\text{CaAl}_{0.5}\text{Fe}_{0.5}\text{O}_{2.5+\delta}$, the tetrahedrally coordinated Fe^{3+} turns into Fe^{4+} , 5-fold coordinated inside a square pyramid [147]. Apart from perovskite type compounds, 4-fold coordinated high-spin Fe^{4+} was found within the compound Na_4FeO_4 [140], but it is also present within other non-perovskite-type compounds of the Ba-Fe-O system, namely in the Ba-rich Ba_2FeO_4 and Ba_3FeO_5 [141]. These structures are composed of isolated FeO_4^{4-} tetrahedra, as it was also reported for other Ba_2MO_4 compounds, with M being Ti, V, Cr or Co [148–154], with only small distortion of the tetrahedra due to Jahn-Teller active electron configuration. Inside the tetrahedron, Fe^{4+} adapts the electronic configuration $e^2 t_2^2$, with a total spin of $S = 2$, e.g. high spin, which is the only observed spin state in solid state materials [28]. On the other side, for similar compounds with smaller A-site cations, e.g. Sr_2FeO_4 [150], the Fe^{4+} cation coordination is an almost perfect octahedron, though the site symmetry of $4/mmm$ would allow for significant stretching of the octahedron. As a simple conclusion, the increase of coordination number for barium seems to induce the lowering of the coordination number for the tetravalent iron species within polyhedra of reduced coordination number.

To derive the most plausible allocation of the tetravalent iron atoms, bond valence sums [155] were calculated based on Fe-O distances derived from the structure optimized by the *ab initio* calculations. These calculations clearly indicate that Fe^{4+} is located on the tetrahedrally coordinated site (Fe2, see Table 3.5). This is in principle agreement with what we found for isotypic $\text{BaCoO}_{2.667}$ [137], in which d^5 configured Co^{4+} was also located on the tetrahedral site, and for which neutron diffraction data could be recorded in order to obtain precise Co-O bond distances. The magnetic moments derived from the Bader analysis (see Table 3.6) are found to be smaller than expected from the nominal oxidation numbers. Such a quantitative deviation is found also for transition metal oxides like TiO_2 [156] and actually under active discussion [157]. It is nevertheless noteworthy that the Bader-derived magnetic moments of Fe well distinguish the tetrahedrally coordinated site from the pyramidal or the octahedral site, consistently with BVS calculated from the DFT optimized model (again see Table 3.5).

Table 3.5.: Bond valence sums (BVS) [155] calculated for different cations. Magnetic moments on atoms derived from the Bader analysis (Table 3.6) are also shown for comparison.

Atom	Distances to oxygen (Å)	BVS	M (μ_B)
Ba1	1x 2.676	+2.32	
	2x 2.752		
	2x 2.763		
	1x 2.809		
	2x 2.877		
	2x 3.165		
Ba2	1x 2.744	+1.85	
	2x 2.836		
	2x 2.847		
	2x 2.949		
	2x 3.088		
	1x 3.165		
Ba3	1x 2.812	+2.12	
	2x 2.845		
	2x 2.851		
	2x 2.902		
	1x 2.946		
	2x 3.018		
Fe1 (pyramidal)	1x 1.916 2x 1.974 2x 2.047	+2.71	3.88
Fe2 (tetrahedral)	1x 1.742 1x 1.776 2x 1.852	+3.58	3.19
Fe3 (octahedral)	1x 1.971 2x 2.036 2x 2.038 1x 2.463	+2.61	3.94

The allocation of Fe^{4+} on the tetrahedral site is further in agreement with the Mössbauer data, where the B_{hf} values and isomer shifts for octahedral / square pyramidal coordination of Fe^{3+} are similar to what was found in $\text{BaFeO}_{2.5}$ [33] and $\text{BaFeO}_{2.333}\text{F}_{0.333}$ [12]. Thus, we conclude that although Jahn–Teller stabilizing coordination geometries (octahedral / square pyramidal) are available in the structural setting of $\text{BaFeO}_{2.667}$, there is a size-driven tendency of Fe^{4+} to be located on the tetrahedrally coordinated site. However, a conclusion about the distortion of the tetrahedron cannot be drawn due to a lack of fully reliable experimentally determined positional parameters of the anions. Further, it is also appropriate to discuss the structure found for $\text{BaFeO}_{2.667}$ with reference to earlier reported structural models for this compound. Though no diffraction data and details of powder preparation are presented in the early report from Mori in 1965 [158], we assume

that the author might have prepared this phase (which was described as triclinic-II) before by heating BaFeO_{2.5} (which was referred to as triclinic-I phase) between 400-500 °C in oxygen atmosphere. However, the lattice parameters reported ($a \approx b \approx 405.0$ pm, $c \approx 402.4$ pm, $\alpha \approx 91^\circ 44'$, $\beta \approx 88^\circ 16'$, $\gamma \approx 91^\circ 51'$) are implausible, since in such a small unit cell only compositions according to ABX_{3-n} ($n = 0, 1, 2, \text{ or } 3$) will be possible; clearly, the obtained splitting pattern cannot well describe the splitting of the main reflections and also does not cause superstructure reflections. The fact that many perovskite related barium ferrates were originally discovered in the 1960s, but could be only structurally solved in the early 90s or even later by neutron or electron diffraction, points to the high structural complexity found for this class of materials, the difficulty of growing single crystals due to the topochemical nature of the oxygen uptake / release, and the difficulty to solve such structures based on powder diffraction datasets previously.

3.1.3.4. Comments on Bader analysis of BaFeO₃ and BaFeO_{2.667} (SI)

Table 3.6 summarizes the *ab initio* computed atomic properties of BaFeO₃ and Ba₃Fe₃O₈ based on the Bader analysis. First, for FM BaFeO₃, it is confirmed that the Bader analysis can qualitatively reproduce the expected positive charges for Ba and Fe and negative charges for O. The absolute charge values are, however, much smaller than those predicted from nominal oxidation numbers (Ba²⁺, Fe^{3+/4+}, and O²⁻), which implies strong covalency in BaFeO₃. The magnetic moment of Fe is as high as 3.57 μ_B , indicating that the Fe cation is in a high-spin state.

We note that the Bader charge on Fe in BaFeO_{2.667} at the tetrahedral site is not substantially different from those at the octahedral and the pyramidal sites. This may be because the Bader charge of Fe at the tetrahedral site includes the contribution of the oxygen-vacancy region, as indicated by its Bader volume being even larger than that of the octahedral site. Namely, the contribution of the electrons in the oxygen-vacancy region may be largely included in the tetrahedral sites, which makes its Bader charge similar to those at the other Fe sites.

3.1.3.5. Magnetic characterization of BaFeO_{2.667}

Figure 3.13 a,b shows the magnetization of BaFeO_{2.667} as a function of temperature and the magnetization as a function of external field, respectively. Since the powder used for magnetic characterization also contains a small amount of tetragonal BaFeO_{2.81} (see previous sections), we also performed a magnetic characterization (see Figure 3.15 in Electronic Supplementary Material) of a BaFeO_{2.81} rich sample. From the significantly

Table 3.6.: *Ab initio* computed atomic properties of FM BaFeO₃ and G-AFM Ba₃Fe₃O₈ with $U_{\text{eff}} = 2.5$ eV based on the Bader analysis [127]. For the Fe atoms, the coordination environments are also shown. The order of inequivalent sites is the same as in [12]. ν : atomic volume. q : atomic charge. $|m|$: absolute value of the atomic magnetic moment. (SI)

	Element	Wyckoff	Coordination	ν (Å ³)	q (e)	$ m $ (μ _B)
BaFeO ₃	Ba	1a		20.34	1.57	0.02
	Fe	1b	octahedral	6.65	1.94	3.57
	O	3c		12.25	-1.17	0.14
Ba ₃ Fe ₃ O ₈	Ba	2e		22.28	1.55	0.00
		2e		23.94	1.58	0.01
		2e		21.91	1.54	0.00
	Fe	2e	pyramidal	8.33	1.81	3.88
		2e	tetrahedral	8.13	1.79	3.19
		2e	octahedral	7.54	1.83	3.94
	O	2b		13.01	-1.31	0.00
		2e		13.99	-1.19	0.11
		2e		13.01	-1.30	0.04
		2e		17.41	-1.15	0.13
		4f		13.60	-1.31	0.04
		4f		15.07	-1.27	0.10

different behavior, we conclude that the magnetic properties measured above 150 K, likely even above 80 K, most plausibly correspond to the monoclinic BaFeO_{2.667} phase with $P2_1/m$ symmetry, since BaFeO_{2.81} is paramagnetic with a very low overall magnetization above this temperature.

Above about 310 K, the magnetization curves of BaFeO_{2.667} in Figure 3.13 a,b show a plateau which might be a result of small (anti)ferromagnetic domains. Furthermore, close to 350 K, the zero-field-cooled magnetization increases slightly with increasing temperature, which could indicate an antiferromagnetic (possibly short-range) transition at higher temperatures. A Néel temperature above room temperature is also in agreement with the Mössbauer spectra recorded at room temperature (Figure 3.12), which show the presence of a dynamic sextet along with singlet and two doublets next to it. This indicates on-going loss of long-range magnetic ordering. At around 300 K, the magnetization curves show a ferromagnetic-like transition, which is probably due to weak ferromagnetism on top of the dominant antiferromagnetic order, as the magnetization measurements (Figure 3.13 b) do not show any saturation or hysteresis at 250 K. Below the transition at around 300 K, the FC and ZFC curves diverge notably, confirming a weak ferromagnetic (or a spin-glass-like) behavior, which is common in oxygen defect materials with canted or locally uncompensated spins [159]. At about 55 K there is a maximum visible in the ZFC curve and to a lesser extent in the FC curve (which both are not found for BaFeO_{2.81}), which

could be related either to gradual strengthening of the magnetic order with the decreasing temperature or presence of the magnetic coercivity. Indeed, at low temperatures, magnetic hysteresis was observed in the magnetization curves, with coercivity reaching about 0.7 T at 10 K, as shown in the inset in Figure 3.13 b. The $M(H)$ curve measured below and above the transitions (Figure 3.13 b) showed linear behavior without saturation, which again indicates a prevailing antiferromagnetic order with spin canting or locally uncompensated spins in the whole temperature range. However, we acknowledge that the behavior below 150 K cannot be fully assigned to $\text{BaFeO}_{2.667}$ with high certainty, due to a similar response of $\text{BaFeO}_{2.81}$ below 150 K, which might overlap with the magnetic feature of $\text{BaFeO}_{2.667}$. Previous experiments for barium ferrates such as $\text{BaFeO}_{2.5}$ [33] or $\text{BaFeO}_{2.333}\text{F}_{0.333}$ [12], which are both oxygen-vacancy-ordered derivatives of the cubic perovskite aristotype structure, found the G-AFM ordering according to the Wollan–Koehler notation [160]. This magnetic ordering is in general favoured for iron-based perovskites, due to the fact that the Fe-O-Fe bond angle only slightly deviates from 180° , thus inducing strong antiferromagnetic superexchange interactions [161]. Attempts were made to confirm the principle stability of an antiferromagnetic configuration over ferromagnetic and nonmagnetic configurations by *ab initio* calculations for $\text{BaFeO}_{2.667}$. Indeed, G-type AFM ordering (see Figure 3.14 a) was found to be energetically most stable as compared to the FM and the NM configurations (see Figure 3.14 b) regardless the U_{eff} value, giving good agreement to the observed experimental findings. Our DFT results also show that the ordered oxygen vacancies in $\text{Ba}_3\text{Fe}_3\text{O}_8$ change the stable magnetic state as compared to BaFeO_3 (i.e., of the perfect cubic perovskite without oxygen vacancies), for which the FM ordering is energetically more stable than various other AFM orderings within collinear spin polarized calculations [132–134]. Further, for G-type AFM $\text{Ba}_3\text{Fe}_3\text{O}_8$, all magnetic moments on Fe are larger than $3 \mu_B$ for all the sites, indicating again that the Fe cations are in high-spin states (see Table 3.5 and Table 3.6). Though the above made interpretation of the magnetic behavior observed experimentally is fully consistent with the DFT calculations and to what has been found previously on related iron-based perovskite, we acknowledge that further experiments, including temperature dependent neutron diffraction studies, would be required to achieve a final proof for the suggested magnetic behavior and a precise magnetic ordering temperature in special.

3.1.3.6. Magnetic measurements of $\text{BaFeO}_{2.81}$ (SI)

We performed an additional SQUID measurement on $\text{BaFeO}_{2.81}$ obtained by further oxidation during cooling of $\text{BaFeO}_{2.667}$ and it showed saturation and hysteresis only below 80 K; thus, we can conclude that our measurement is dominated by the properties of

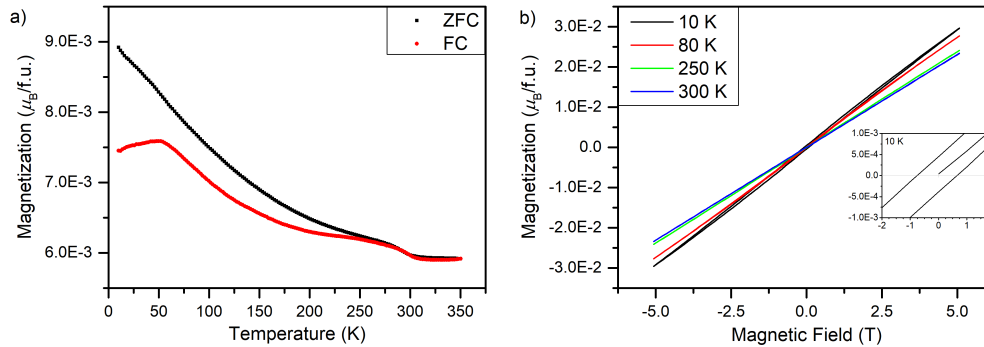


Figure 3.13.: a) Field cooled and zero field cooled curves and b) Field-dependent magnetization of $BaFeO_{2.667}$ at various temperatures with the coercivity at 10 K shown in the inset.

$BaFeO_{2.667}$ above 80 K. In addition, the low temperature magnetization appears to be one order of magnitude higher, compared to $BaFeO_{2.667}$. Above about 200 K the sample looks pretty much paramagnetic, but there are some interactions happening, as the inverse susceptibility is not linear. The M-H curves are linear, so no notable FM behaviour. Below 150 K the susceptibility increases, which looks like ferro- or ferrimagnetic transition. Also, at 80 and 10 K, the M-H curves show a small amount of saturation and at 10 K also some hysteresis. This can be due to ferro- or ferrimagnetism, but it is quite weak (small saturation magnetization). Below 70 K the FC and ZFC curves split, which looks like a spin-glass behaviour. Probably at low T the sample is either antiferromagnetic with spin canting, causing some ferromagnetic-like behaviour, or ferrimagnetic.

3.1.4. Conclusions

In this study, we have presented a detailed analysis of the structural, electric and magnetic properties of charge-ordered $BaFeO_{2.667}$, which reveals itself to be isotypic to $BaFeO_{2.333}F_{0.333}$. XRD experiments together with *ab initio* calculations confirm the structural model based on the space group $P2_1/m$. Mössbauer spectroscopy indicates three differently coordinated iron sites with Fe^{3+} being coordinated inside an octahedron and in a square pyramid, while Fe^{4+} is found to be coordinated inside of a tetrahedron. Magnetic measurements suggest an antiferromagnetic behavior, and *ab initio* GGA+*U* simulations also support the G-AFM ordering of $Ba_3Fe_3O_8$, and the Bader-analysis-obtained atomic magnetic moments on Fe as well as bond valence sums can be interpreted consistently with the expected oxidation numbers from the Mössbauer spectroscopy. Based on these results

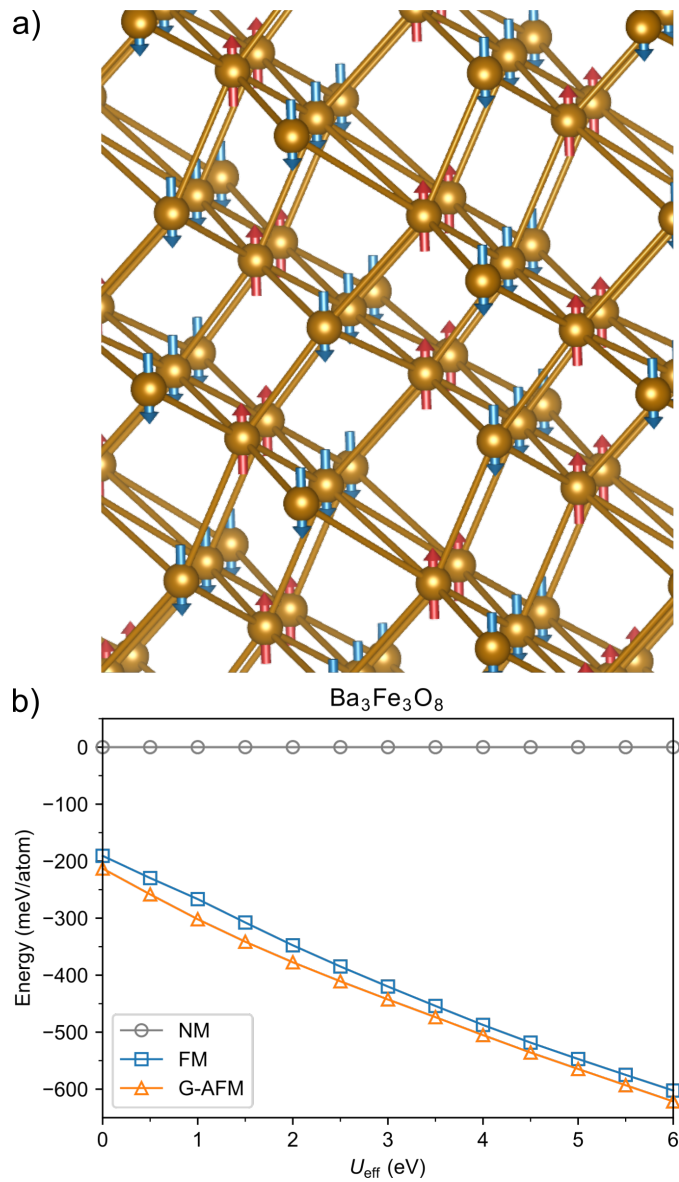


Figure 3.14.: a) Energetically most stable G-type AFM ordering of Ba₃Fe₃O₈, with only the Fe atoms shown. The red and the blue arrows indicate spin-up and spin-down magnetic moments, respectively. For each Fe atom, its six neighboring Fe atoms have opposite magnetic moments; b) *ab initio* computed energies of Ba₃Fe₃O₈ as a function of U_{eff} . For each U_{eff} , the energy of the NM phase is set as the reference.

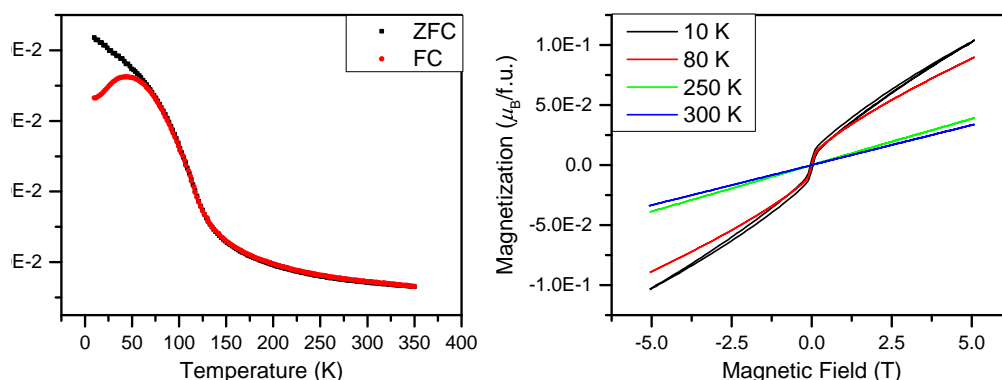


Figure 3.15.: Field cooled and zero field cooled curves (left) and Field-dependent magnetization of BaFeO_{2.81} at various temperatures (right).

we can state, to the best of our knowledge, that BaFeO_{2.667} exhibits the only tetrahedrally coordinated Fe⁴⁺ cation inside a vacancy ordered perovskite lattice, which is derived from the cubic aristotype structure.

The performed HT-XRD and TG/DTA experiments reveal the complex oxidation and reduction of the mother compound BaFeO_{2.5} and suggest a lattice enthalpy driven structural transition. On the other side, the high temperature cubic configuration is shown to preserve the oxygen stoichiometry while undergoing the strongly endothermic phase transition from the oxygen vacancy ordered $P2_1/c$ structure. In addition, the formation and stability of the presented oxidized phase seems to be strongly depending of the oxygen partial pressure as suggested by comparative HT-XRD experiments under air.

Further, we found that changes of the synthesis procedure can also alternate the oxygen uptake and release behavior of BaFeO_{2.667}, which alters the electrical properties of the material significantly, and we aim to address this finding in more detail in a follow-up study.

3.1.5. Acknowledgments

S.W. and O.C. acknowledge funding by the German Research Foundation (DFG) within CL551/2-1. Y.I. and B.G. acknowledge support by the state of Baden-Württemberg through bwHPC and the German Research Foundation (DFG) through grant no. INST 40/575-1 FUGG (JUSTUS 2 cluster) and funding from the European Research Council (ERC) under the European Union's Horizon 2020 research and innovation programme (grant agreement



no. 865855).

3.2. On the Impact of the Degree of Fluorination on the ORR Limiting Processes within Iron Based Catalysts: A Model Study on Symmetrical Films of Barium Ferrate

Stephan Wollstadt ¹ and Oliver Clemens ^{1,2,*}

¹ Fachgebiet Materialdesign durch Synthese, Institut für Materialwissenschaft, Technical University of Darmstadt, 64287 Darmstadt, Germany; wollstadt@md.tu-darmstadt.de

² Institut für Nanotechnologie, Karlsruher Institut für Technologie, Hermann-von-Helmholtz-Platz 1, 76344 Eggenstein Leopoldshafen, Germany

* Correspondence: oliver.clemens@md.tu-darmstadt.de; Fax: +49-6151-16-21991

Received: 24 April 2020; Accepted: 28 May 2020; Published: 3 June 2020

Reproduced under the *Creative Commons CC BY 4.0* license from Wollstadt, Stephan, and Oliver Clemens. "On the Impact of the Degree of Fluorination on the ORR Limiting Processes within Iron Based Catalysts: A Model Study on Symmetrical Films of Barium Ferrate." *Materials* 13.11 (2020): 2532.

DOI: <https://doi.org/10.3390/ma13112532>

Abstract In this study, symmetrical films of $\text{BaFeO}_{2.67}$, $\text{BaFeO}_{2.33}\text{F}_{0.33}$ and BaFeO_2F were synthesized and the oxygen uptake and conduction was investigated by high temperature impedance spectroscopy under an oxygen atmosphere. The data were analyzed on the basis of an impedance model designed for highly porous mixed ionic electronic conducting (MIEC) electrodes. Variable temperature X-ray diffraction experiments were utilized to estimate the stability window of the oxyfluoride compounds, which yielded a degradation temperature for $\text{BaFeO}_{2.33}\text{F}_{0.33}$ of 590 °C and a decomposition temperature for BaFeO_2F of 710 °C. The impedance study revealed a significant change of the catalytic behavior in dependency of the fluorine content. $\text{BaFeO}_{2.67}$ revealed a bulk-diffusion limited process, while $\text{BaFeO}_{2.33}\text{F}_{0.33}$ appeared to exhibit a fast bulk diffusion and a utilization region δ larger than the electrode thickness L (8 μm). In contrast, BaFeO_2F showed very area specific resistances due to the lack of oxygen vacancies. The activation energy for the uptake and conduction process of oxygen was found to be 0.07/0.29 eV (temperature range-dependent), 0.33 eV and 0.67 eV for $\text{BaFeO}_{2.67}$, $\text{BaFeO}_{2.33}\text{F}_{0.33}$ and BaFeO_2F , respectively.

Keywords: thin film fluorination; ORR catalysts; oxyfluorides; barium ferrate; impedance spectroscopy

3.2.1. Introduction

The currently rising awareness for the future need of clean and green energy increases the demand for energy storage and battery applications. Already existing systems like the well-known lithium ion batteries (LIB) and fuel cell based power sources experience an increase in interest. However, struggling with limited power output or high operating temperatures, these systems have to be revised and improved further to cope with future high-performance demands.

Nowadays fuel cell systems are based on several types of archetypes, including alkaline fuel cells (AFCs), phosphoric acid fuel cells (PAFCs), polymer electrolyte membrane fuel cells (PEMFCs), molten carbonate fuel cells (MCFCs) and solid oxide fuel cells (SOFCs). While PAFCs and PEMFCs require precious metals for their operability at low temperatures and AFCs, PAFCs and MCFCs suffer from corrosion problems due to their liquid electrolytes, SOFCs offer the cleanest and most efficient way to transform chemical into electrical energy [162]. SOFCs are characterized by all-solid components and hence, mostly high operating temperatures (>800 °C). However, the high operating temperature leads to cheaper building materials for electrolytes and electrodes such as perovskite type oxides. The high temperature can be an advantage in terms of performance; therefore, the focus on nowadays research lies on reducing it to intermediate temperatures of 500–700 °C, to limit disadvantageous reactions between cell components and thus, prolonging the cell lifetime. Current SOFCs are built of yttria-stabilized zirconia (YSZ) electrolyte, a $\text{La}_{0.8}\text{Sr}_{0.2}\text{MnO}_3$ (LSM) perovskite type cathode and a nickel–YSZ cermet anode [7, 10, 162]. A critical reaction in such fuel cells is the reduction of oxygen to oxide ions (oxygen reduction reaction, ORR), which requires the transfer of four electrons and is therefore a complex catalytic step [5]. For this reaction, a simple reduction of the operating temperature leads to an increase in cell polarization resistance due to the lack of activation energy [163, 164]. Attempts are made by the introduction of stacking multiple materials to profit from their specific characteristics [165] but also by utilizing nanoscale designs [85]. Further, the catalytic activity of the cathode is highly composition dependent, and tremendous efforts have been made to adopt the composition of the perovskite type catalyst by changing the La/Sr ratio or replacing Mn by other metals such as Fe or Co, both showing a strong impact on the average transition metal oxidation state. Recently, also doping of the anion sublattice of the cathode material was targeted [10, 166]. In this case, the introduction of anions alters the electronic structure, which directly affects the surface oxygen exchange and the oxygen bulk diffusion [167, 168]. Possible anionic dopants are F^- and Cl^- which reportedly increase the catalytic performance of perovskite oxides [100, 101].

For anion doping with fluoride, it is important to keep in mind that most of the perovskite type oxyfluoride materials are only metastable, and decompose into alkaline earth flu-

oxides and transition metal oxides at temperatures between 400–800 °C [10, 36]. In addition, it is normally not trivial to monitor the detailed fluorine content easily, since O^{2-} and F^- are indistinguishable within the commonly used powder diffraction methods [21, 37, 169]. The combination of difficult preparation, limited understanding of detailed compositional stability and challenging characterization of materials requires the analysis of systems with well-characterized fluorination behavior in order to develop basic knowledge on general structure-composition-property relationships.

Therefore, the aim of this study is to understand and elaborate the impact of the fluorine content and anion composition on a model system which is known to possess differently well characterized non-fluorinated and fluorinated phases with distinct fluorine contents. To do so, we target the system $BaFeO_xF_y$, for which the phases $BaFeO_{2.5}$ ($Ba_2Fe_2O_5$ [33]), $BaFeO_{2.67}$ ($Ba_3Fe_3O_8$, article in preparation), $BaFeO_{2.33}F_{0.33}$ ($Ba_3Fe_3O_7F$ [12, 116]) and $BaFeO_2F$ [11, 40] are known. The structures of these compounds can all be derived from the cubic perovskite type structure (aristotype); they distinguish by the detailed anion content, which leads to different distortion and ordering variants which are well distinguishable from the observed reflection splitting and superstructure reflections by powder diffraction. We emphasize already at this state the selection of these compounds is not based on high performance criteria since anion ordering is known for a potential negative impact on oxygen ion diffusion [170–172], but only on the fact of their well-known fluorination chemistry. Compounds of composition of, e.g., $Ba_{0.5}Sr_{0.5}Fe_{1-x}Co_xO_{3-y}F_y$ might be more suitable for their overall electrocatalytic activities, but are only poorly understood with respect to their fluorination behavior. In order to make the reader aware with the manifold phases found in the barium ferrate system and their structural and compositional behavior, these aspects will be summarized in the following:

$BaFeO_{2.5}$ (BFO) crystallizes in a vacancy ordered 28-fold supercell of the cubic perovskite structure with space group $P2_1/c$ [33]. The adaption of this monoclinic structure is highly dependent on the anion composition, and can only be found for compositions close to $BaFeO_{2.5+d}$ with $d < 0.01$ [173]. $BaFeO_{2.5}$ can be prepared by spray pyrolysis approaches [118, 174]; this method is known to provide powder morphologies for perovskite-type compounds which are suitable to prepare symmetrical films [85] on 8 mol %-yttria-stabilized zirconia button substrates (YSZ8), serving as the solid electrolyte. Only recently, we found that this phase can be topochemically oxidized to $BaFeO_{2.67}$ (BFO', space group $P2_1/m$) at 250 °C (article in preparation). Further, BFO can form two different oxyfluoride phases, $BaFeO_2F$ (BFOF, space group $Pm\bar{3}m$) or $BaFeO_{2.33}F_{0.33}$ (BFOF33, space group $P2_1/m$) on topochemical fluorination, which have already been well understood structurally and compositionally [11, 12]. For fluorine contents $2x$ between $1/3$ and 1 in the system $BaFeO_{2.5-x}F_{2x}$, two phase mixtures were observed [12]. $BaFeO_{2.67}$ and $BaFeO_{2.33}F_{0.33}$ are isotypic, but show a significantly difference in unit cell

volume, which makes them well distinguishable, and also allows to approximate potential intermediate compositions according to $\text{BaFeO}_{2.67-z}\text{F}_z$ ($0 \leq z \leq 1/3$) from the change of lattice parameters.

Further, since these compounds have only limited stability, it is not possible to use such oxyfluoride powders to sinter them into symmetrical films. Therefore, thin film suitable vapor transport related fluorination methods [175, 176] are used for the preparation of symmetrical films of BaFeO_2F , and extended by a newly developed interdiffusion approach for the preparation of symmetrical films of $\text{BaFeO}_{2.33}\text{F}_{0.33}$.

All the compounds differ with respect to their level of anion vacancies starting with the highest concentration $\text{BaFeO}_{2.5}\square_{0.5}$ ($P2_1/c$), $\text{BaFeO}_{2.67}\square_{0.33}$ ($P2_1/m$), $\text{BaFeO}_{2.33}\text{F}_{0.33}\square_{0.34}$ ($P2_1/m$) and $\text{BaFeO}_2\text{F}_1\square_0$ ($Pm\bar{3}m$), with \square representing an oxygen vacancy, as well as the average iron oxidation state (Fe^{3+} for BFO, BFOF33 and BFOF, $\text{Fe}^{3.33+}$ for BFO'). The oxidation states of iron were formerly investigated in [12, 33, 161] by Mößbauer spectroscopy and were found to be 3+ only for BFO and its fluorinated counterparts. The oxidation state of BFO' is 3.33+ in average, and has been confirmed by Mößbauer as well as thermogravimetric studies (*article in preparation*²). Figure 3.16 depicts the different structures highlighting the defect structure of the oxygen vacancies. Figure 3.16a shows the vacancy channels of BFO which would suggest a high oxygen ion mobility, however, due to the oxygen vacancy ordering, oxygen ions are highly immobile [33]. On the other hand, BFOF33 exhibits a different channel like vacancy ordering in Figure 3.16b, while BFOF (Figure 3.16c) is free of defects. It might be noteworthy that hitherto the defect structure of BFO' has not been investigated yet. Nevertheless, it is likely to be highly similar to BFOF33 due to the identical space group and super cell; however, the distribution of anions on the different anion sites needs to be confirmed by neutron diffraction experiments, but is of subordinate importance for the present study. The isotopic nature of $\text{BaFeO}_{2.67}$ and $\text{BaFeO}_{2.33}\text{F}_{0.33}$ could give an indication for the influence of fluorine incorporation without apparent change of the symmetry. In summary, the compounds are able to separate the influences of parameters important for the ORR, such as iron oxidation state, filling degree of the anion lattice and a potential impact of the fluoride ion itself due to its higher mobility than an oxide ion. This is elaborated in detail within this article by a combination of powder diffraction studies with temperature dependent impedance spectroscopy on symmetrical films on YSZ8. It was found that the data can be analyzed on the basis of impedance models describing the charge-transfer and non-charge-transfer process of a porous mixed ionic electronic conducting (MIEC) cathode, and that the filling degree of the anion lattice has indeed a major impact on the electrocatalytic properties of the samples.

²Valid back then. Currently under 2nd revision in *Inorganic Chemistry*, Sec. 3.1.

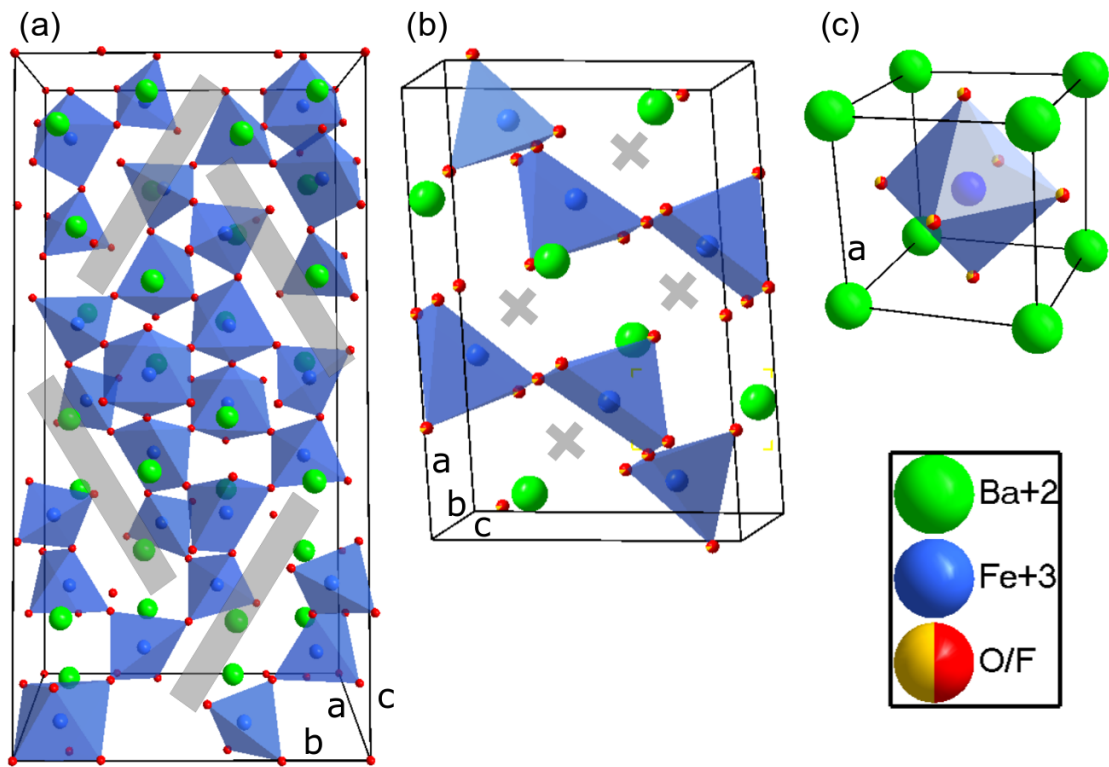


Figure 3.16.: Defect structure of (a) BaFeO_{2.5} ($P2_1/c$) and (b) BaFeO_{2.67}/BaFeO_{2.33}F_{0.33} ($P2_1/m$) with bars/crosses indicating oxygen vacancy channels/relaxations [12, 33], (c) depicts a defect free structure of BaFeO₂F ($Pm\bar{3}m$). Though BaFeO_{2.67} is confirmed to have the same overall anion content BaFeX_{2.67} than BaFeO_{2.33}F_{0.33}, neutron diffraction studies are yet needed to confirm the identical vacancy ordering pattern within the $\sqrt{6} \times \sqrt{2} \times \sqrt{3}$ monoclinic superstructure of the cubic perovskite modification.

3.2.2. Experimental

3.2.2.1. Sample Preparation

Nanocrystalline powder of BaFeO_{2.5} (BFO) was synthesized using the nebulized spray pyrolysis (NSP) method, see Figure 3.17. The aqueous precursor solution contained the nitrate salts of the corresponding metals with a concentration of $c(\text{Ba}^{2+}) = c(\text{Fe}^{3+}) = 0.06 \text{ mol/L}$. For that, Ba(NO₃)₂ (Sigma Aldrich, Saint Louis, Missouri, USA, 99.99%) and Fe(NO₃)₃ · 9 H₂O (Sigma Aldrich, Saint Louis, Missouri, USA, 99.99%) were weighed in the stoichiometric ratio and mixed with deionized water. The as-prepared solution was then stirred for 1 h to dissolve the salts and to form a homogenous transparent solution. The yellowish solution was nebulized inside the nebulizer unit with an ultrasonic nebulizer membrane (TDK, NB-59S-09S-0, Chuo, Pref Tokyo, Japan), which was operated at a voltage of 48 V and 0.5 mA. The mist was then carried with a constant gas stream of argon with a flow rate of 2.5 SLM (standard liter per minute) through the hot wall reactor, held at a constant temperature of 700 °C. The pressure inside the setup was kept at 900 mbar applied by a membrane pump and controlled by a butterfly valve. The precursor solution level was kept constant with a syringe pump at a rate of 1.3 mL/min. The as-synthesized powder was collected on a filter, which was kept at a temperature of 130 °C in order to prevent any condensation of water. The collected powder was then calcined in an airtight tube furnace at a temperature of 900 °C for 20 h under a constant flow of argon to achieve formation of phase pure, water-free BaFeO_{2.5}. Another identical powder was prepared at a reactor temperature of 1050 °C. The preparation of two different powders is used to emphasize the influence of the synthesis parameters onto the product powder. Previous reported synthesis approaches rely on a salt-assisted approach where the addition of NaCl to the precursor solution leads to a fine grained morphology of the product. The use of NaCl in the precursor solution of BaFeO_{2.5} resulted in the formation of chlorine containing hexagonal perovskites [90], which are structurally not easy comparable to the compounds under study here.

Symmetrical oxidic template films were produced by spin-coating a stabilized homogenous dispersion of the as-prepared powder onto YSZ8 button substrates (fuelcellmaterials, Nexceris, Lewis Center, OH, USA) followed by sintering. The homogenous dispersion was prepared by mixing the calcined powder with an acidic solution of diluted HNO₃ (pH = 4). The stability of the dispersion was investigated by a zeta potential measurement using a ZetaSizer Nano SZ (Malvern Instrument, Malvern, UK). HNO₃ and NaOH were used to adjust the pH level and NaCl was added to the solution to improve the measurement signal. An ultrasonicator was used to distribute the powder evenly in the acidic solution. The insertion of an interlayer, such as GDC, between YSZ substrate and film was not

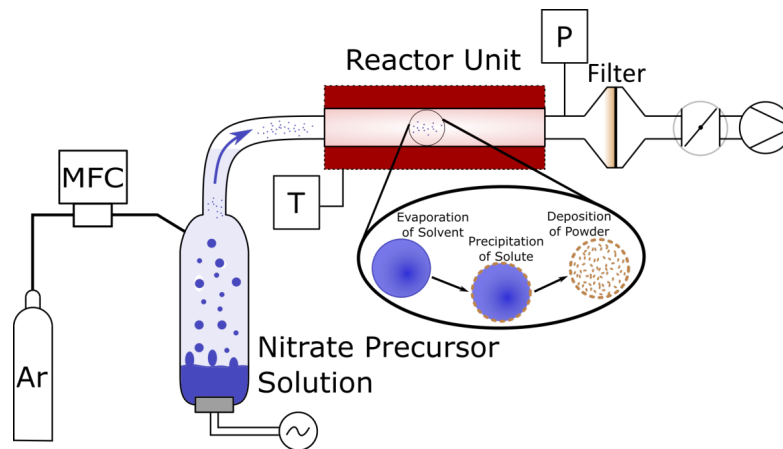


Figure 3.17.: NSP experimental setup with the schematical precipitation process.

necessary, since no reaction between YSZ and $\text{BaFeO}_{2.5}$ was observed. The as-prepared films were sintered at $1060\text{ }^\circ\text{C}$ for 1 h under a steady flow of argon.

The topochemical fluorination of the as-prepared BFO films was done in two different ways to achieve the desired fluorine content in the symmetrical films: $\text{BaFeO}_{2.33}\text{F}_{0.33}|\text{YSZ8}|\text{BaFeO}_{2.33}\text{F}_{0.33}$ and $\text{BaFeO}_2\text{F}|\text{YSZ8}|\text{BaFeO}_2\text{F}$. The films were fluorinated either via an interdiffusion or a vapor transport process, respectively; both processes are schematically depicted in Figure 3.18. The approach of interdiffusion (Figure 3.18a) allows for controlled fluorine content, whereas the vapor transport related technique (Figure 3.18b) is less aggressive method for the preparation of high fluorine content phases without decomposition into the thermodynamically stable compounds. The fluorine content of the partial fluorinated $\text{BaFeO}_{2.33}\text{F}_{0.33}|\text{YSZ8}|\text{BaFeO}_{2.33}\text{F}_{0.33}$ was adjusted by covering the pure oxide films with a sufficient amount of separately prepared $\text{BaFeO}_{2.33}\text{F}_{0.33}$ powder, which serves as a type of infinite reservoir due to its high excess in comparison to the film (the preparation of $\text{BaFeO}_{2.33}\text{F}_{0.33}$ powder is described in [12]). The films and powder were kept at a temperature of $450\text{ }^\circ\text{C}$ under argon for 20 h to enable interdiffusion and compositional equilibration between powder and film. In contrast, fully fluorinated $\text{BaFeO}_2\text{F}|\text{YSZ8}|\text{BaFeO}_2\text{F}$ was prepared by utilizing the vapor transport related technique [159]. The films and the polymer polyvinylidene fluoride (PVDF) were put into a tube furnace (Sigma Aldrich, Saint Louis, Missouri, USA) at an elevated temperature of $450\text{ }^\circ\text{C}$ and an argon gas stream. By this, the PVDF is decomposed and decomposition products such as traces of HF are transported over the samples leading to the desired topochemical under formation of the highly fluorinated state.

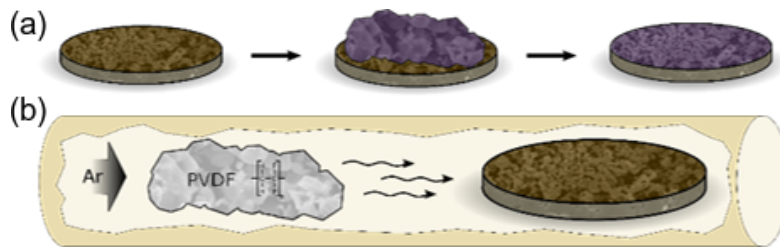


Figure 3.18.: Topochemical fluorination of oxidic films to achieve (a) partial fluorinated $\text{BaFeO}_{2.33}\text{F}_{0.33}|\text{YSZ8}|\text{BaFeO}_{2.33}\text{F}_{0.33}$ via an interdiffusion approach and (b) fully fluorinated $\text{BaFeO}_2\text{F}|\text{YSZ8}|\text{BaFeO}_2\text{F}$ via the vapor transport related technique.

We would like to emphasize that the use of an inert atmosphere during the preparation processes as well as for storage must be ensured, since it is known that $\text{BaFeO}_{2.5}$ is prone to attract moisture leading to a basic reaction with atmospheric CO_2 resulting into the decomposition into BaCO_3 and BaFe_2O_4 [177].

3.2.2.2. Ambient and Variable Temperature *In Situ* Diffraction Experiments

The ambient and variable temperature X-ray diffraction (XRD) experiments were carried out with a Bruker D8 diffractometer (Bruker, Karlsruhe, Germany). The setup uses a Bragg–Brentano geometry, a $\text{Cu-K}\alpha$ source and a PSD VANTEC detector. Ambient measurements were carried out over an angular range of 20° to 80° 2θ with a step size of 0.0066° per step and 1 s measurement time per step. For the variable temperature measurements, an HTK 1200 N temperature chamber with a TCU 1000 N (Anton–Paar) was used. The angular range was set from 20° to 60° 2θ with a step size of 0.015 and 0.22 s measurement time per step. Diffraction experiments were carried out at temperatures ranging from room temperature to 800°C under argon atmosphere. Scans were carried out in a timed interval of 30 min including a ramping with $5^\circ\text{C}/\text{min}$ and an equilibration time of 10 min for an equal temperature distribution inside the sample chamber. For each scan, the obtained data were qualitatively and quantitatively refined using the Rietveld method with the program TOPAS 6 (Bruker AXS, Karlsruhe, Germany) [73].

3.2.2.3. Scanning Electron Microscopy

The scanning electron microscopy (SEM) was carried out on a Philips XL30-FEG (Philips, Amsterdam, Netherlands) secondary electron microscope with an acceleration voltage of

20 kV. The powder samples and films were sputtered with gold to avoid electric charging of the surface.

3.2.2.4. High Temperature Impedance Spectroscopy

To investigate the electrical properties of the films, high temperature impedance spectroscopy was used and samples were measured under oxygen. The frequency range was chosen to be from 1 MHz down to 100 mHz in a temperature window of 400 °C to 600 °C with 20 °C steps. Prior to each measurement, the temperature was kept at the desired set point for 15 min for equilibration. Though the temperature is equilibrated, small temperature fluctuations in the order of ± 1 K cannot be avoided in our setup, and cause visible fluctuations in the impedance spectra only in the range of ~ 100 to 10^{-1} Hz according to our experience. Further, the temperature for the evaluation process was taken from a thermocouple directly mounted near the sample inside the furnace. An AC amplitude of 100 mV was applied. For the measurement, a Solartron 1260 (Ametek, Berwyn, Pennsylvania, USA) was used. Prior to the measurement, both sides of the films were sputter-coated with a thin gold layer for improved contacting.

3.2.3. Results and Discussion

3.2.3.1. Powder Preparation

The XRD pattern (Figure 3.19) of the precursor powder obtained via NSP at 700 °C shows a mixture which mainly consisted out of barium nitrate and iron oxide (Fe_2O_3). However, after the calcination step at 900 °C, this mixture completely reacted to $\text{BaFeO}_{2.5}$ (BFO). The SEM micrographs in Figure 3.20 show the morphology of as-prepared powder (Figure 3.20a) as well as (Figure 3.20b) after the calcination. Right after the synthesis the powder shows the typical hollow sphere morphology [84–86, 178] resulting from the precipitation at the surface of the nebulized droplets inside the reactor during the process. After the calcination, the hollow-sphere morphology is changed into finely shaped granular particles. A zeta potential measurement was used to determine the stability of the aqueous dispersion of BFO in deionized water as a function of the pH value. Figure 3.21 shows the recorded zeta potential curve for the performed measurement. The measurement indicates the highest stability of the dispersed sample material in the acidic region around $\text{pH} = 3.5$, with a maximum zeta potential of ~ 65 mV. At lower pH, the sample tends to dissolve. Taking this into account, a pH of 4 was used as the best compromise to obtain a stable dispersion in the absence of particle agglomeration. We would like to emphasize that the reactor unit temperature plays a crucial role for the preparation of BFO precursor

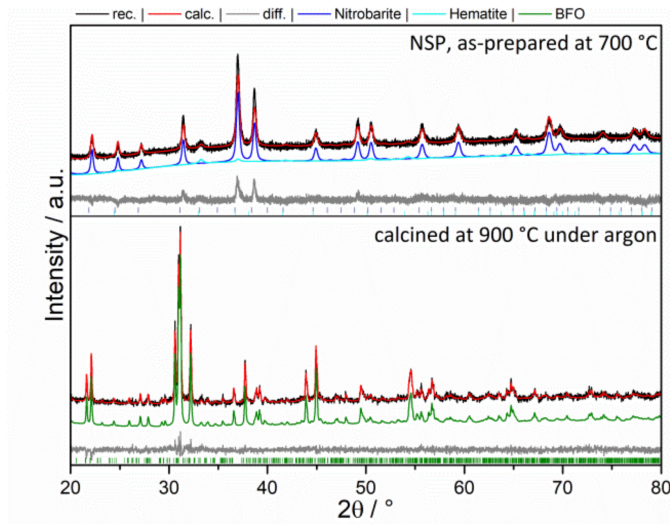


Figure 3.19.: XRD of as-prepared NSP powder and after the calcination step at 900 °C.

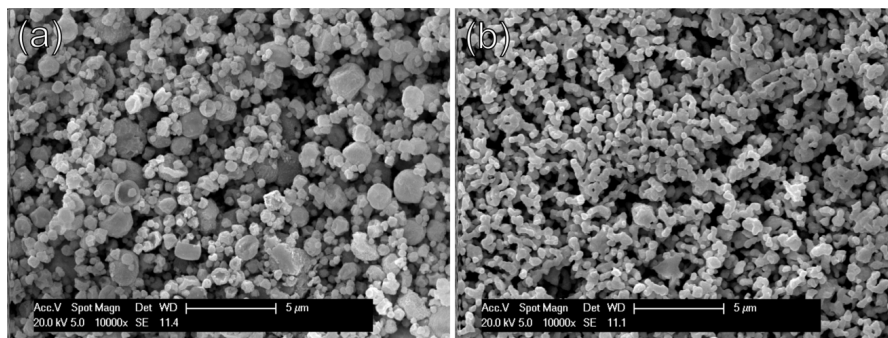


Figure 3.20.: SEM micrographs of (a) as-prepared NSP powder at 750 °C and (b) after calcination at 900 °C.

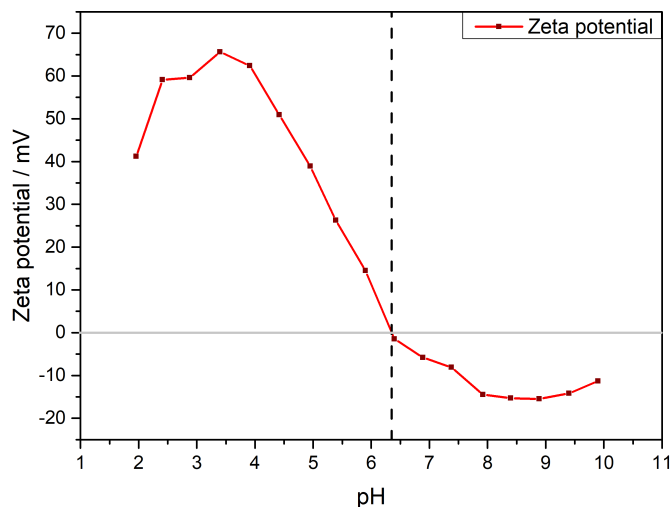


Figure 3.21.: Zeta potential measurement of an aqueous solution of BFO in the pH range from 2–10.

powders suitable for the subsequent fabrication of thin films. On increasing the reactor temperature to 1100 °C, a single phase water containing variant of $\text{BaFeO}_{2.5}$ ($\text{BFO}(\text{OH})$) is formed [117, 118], with some impurities of BaCO_3 and BaFe_2O_4 due to the sensitivity towards CO_2 , see XRD in Figure 3.22. Upon drying at 450 °C, the compound transforms into monoclinic $\text{BaFeO}_{2.5}$. The SEM micrograph of the dried powder (Figure 3.22) revealed hollow-sphere morphology. It was found that this morphology could not be broken into smaller nanoparticles by ultrasonication due to the sintering process, which already took place inside the reactor. In addition, NaCl assisted approaches which helped to obtain non-agglomerated particles for Ba-free SOFC catalysts were attempted, but resulted in the formation of a hexagonal perovskite type modification [90] due to the incorporation of chloride into the anion lattice. Though similar acidic solutions can be used for the dispersion of hollow-sphere BFO powder, attempts to manufacture symmetrical films via high temperature routes led to unstable films which delaminated easily and could not be characterized further.

3.2.3.2. Variable Temperature XRD

The metastability of oxyfluorides combined with the intention to investigate these materials for their ORR activity urges the necessity of knowing the decomposition behavior at elevated temperature. It was already shown that BaFeO_2F decomposes at elevated

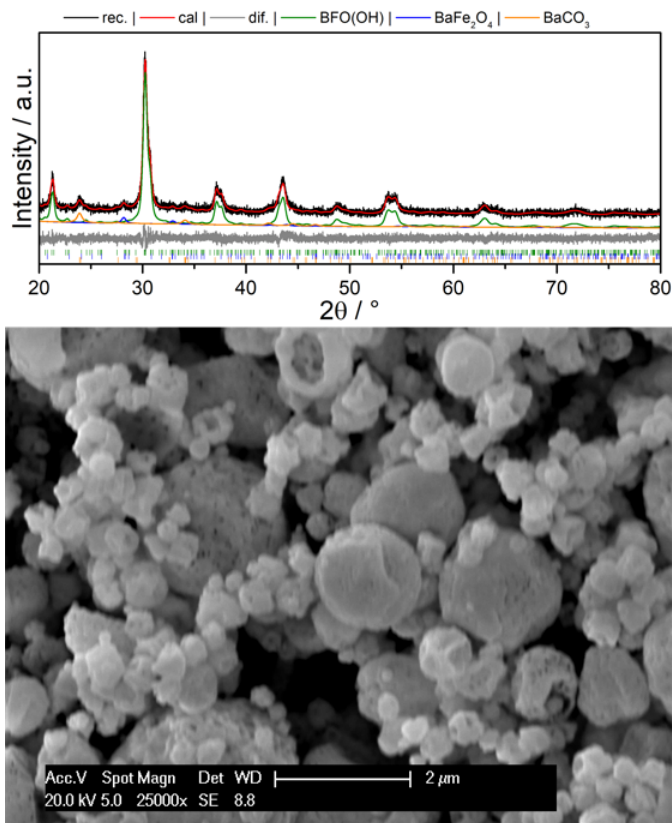


Figure 3.22.: XRD pattern of as-synthesized water-containing BFO and SEM micrograph of the dried BFO.

temperatures into BaF_2 and BaFe_2O_4 [36], however a detailed study of the temperature dependent structural stability was not performed so far. The same holds true for the decomposition of $\text{BaFeO}_{2.33}\text{F}_{0.33}$, for which no data have been reported yet. Hence, variable temperature XRD (VT-XRD) studies were performed to estimate the suitable heating limits, which might also serve as an indication in which temperature range the compounds could in principle be targeted to be used as electrode catalysts in SOFC applications.

The results of the VT-XRD studies in Figure 3.23 for BaFeO_2F and Figure 3.24 for $\text{BaFeO}_{2.33}\text{F}_{0.33}$, and representative powder patterns are depicted for the compounds around their respective temperatures of decomposition. For BaFeO_2F , a first indication for the formation of BaF_2 (reflex at $24.7^\circ 2\theta$) was given around 670°C . Between 670°C and 710°C , only

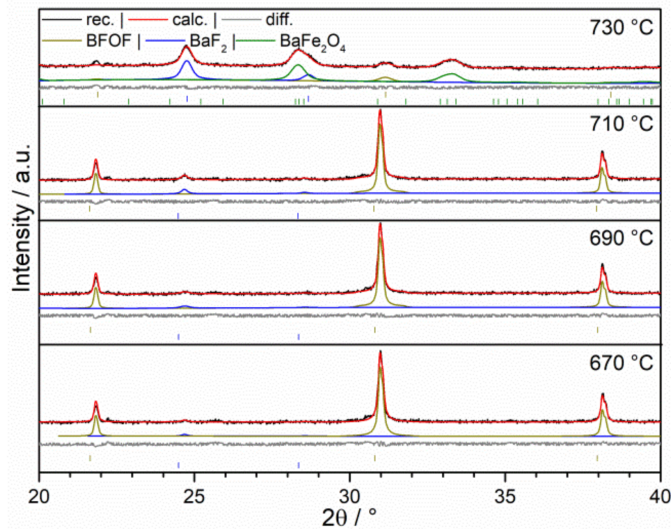


Figure 3.23.: Variable temperature XRD of BaFeO₂F under argon, 690–730 °C.

a small amount of BaF₂ (1.45 wt.%) is formed besides a stable main phase of BFOF. At around 710 °C, the amount of this phase increases, and at 730 °C the compound has decomposed into BaF₂ and BaFe₂O₄ according to



As shown previously [36], quantification of the decomposition products for BaFeO₂F can also serve to confirm the composition of the starting compound, which was also performed here and confirmed the sample to be close to BaFeO₂F within errors (48.5 mol.% of BaF₂/51.5 mol.% of BaFe₂O₄). In contrast, BaFeO_{2.33}F_{0.33} exhibits an earlier onset of degradation with extended structural changes over a broader temperature range. At 590 °C the XRD shows the formation of a small amount of BaF₂ combined with the formation of presumably one of the hexagonal perovskite polytypes, which are well known for system BaFeO_{3-y-d}F_y (6H, 10H, 12H, 15R) [38, 39, 90, 111, 113, 161, 179, 180]. The behaviors on temperature increase of the low fluorine content phase BaFeO_{2.33}F_{0.33} (onset around 590 °C) and the high fluorine content phase BaFeO₂F are partly counterintuitive. In previous works, the metastability of oxyfluorides was mainly attributed to the high stability of the alkaline earth fluorides and lanthanide oxyfluorides. This is certainly true as the general driving force, but it cannot serve to explain the findings shown here. Therefore, the structural stability (transformation between different AX₃ stacking sequences or

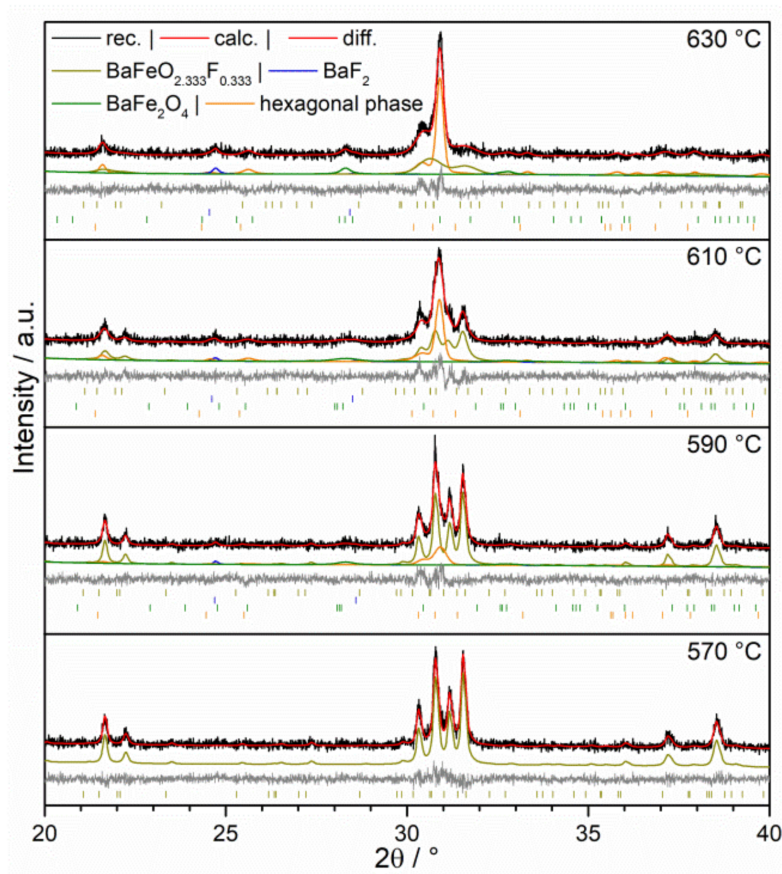


Figure 3.24.: Variable temperature XRD of $\text{BaFeO}_{2.33}\text{F}_{0.33}$ under argon, 570–630 °C.

formation of vacancy ordered modifications) dominated by the respective lattice energies as a function of fluorine content seems to be more complex than thought, indicating that fluoride richer metastable systems must not necessarily be less stable for the same A/B composition of an ABX_{3-d} perovskite type system. Nevertheless, the findings here indicate that a testing of the oxyfluoride compounds up to 600 °C is experimentally justified.

3.2.3.3. Film Preparation

Figure 3.25 shows the XRD patterns of sintered BFO films on YSZ8. A Rietveld refinement revealed the presence of exclusively BFO and YSZ8 in both cases. Hence, it is evident that there was no reaction occurring between the substrate material YSZ8 and the film compound BFO (e.g., with formation of $BaZrO_3$ [181, 182]), further confirmed by the energy dispersive X-ray EDX studies shown later within this article. The formation of phase pure products of BFO, BFOF and BFOF33 could be confirmed by the diffraction studies (again, see Figure 3.25). In addition, the cubic YSZ8 substrate ($Fm\bar{3}m$, $a = 5.17 \text{ \AA}$). This becomes clear on comparing the refined lattice parameters and crystal symmetries (which are known to be highly sensitive on the detailed composition of the anion sublattice [33]) of the compounds within the film to what has been reported in literature (see Table 3.7). The SEM analysis (Figure 3.26) reveals a film consisting of a porous network of BFO with a thickness of around 8 μm . The spin coated material, shown in Figure 3.26a, is already in a network-like arrangement before sintering, which is counterintuitive since the stabilized dispersion should guarantee a densely packed deposition of the spin coated sample powder after the evaporation of the dispersant. After sintering, Figure 3.26b, the film density is lowered; however, a certain degree of porosity is retained. Since the fluorination reaction is a low-temperature topochemical process (reaction temperature at $T \leq 450 \text{ }^\circ\text{C}$), which does not result in grain growth, the EDX in Figure 3.26c supports the observation made in the XRD pattern, and proves that no diffusion between film and substrate took place, hence, the use of an intermediate layer between film and substrate rendering an intermediate layer unnecessary, such as GDC [9, 117, 183, 184], was not required. No traces of zirconium or yttrium can be found in the film, no barium or iron diffused into the electrolyte and fluorine can only be found in the oxide film and no fluorination of the substrate occurred.

3.2.3.4. High Temperature Impedance Spectroscopy

Figure 3.27 depicts the Nyquist and Bode plots of the measured symmetrical films of BFO, BFOF33 and BFOF at selected temperatures in the range of 390 to 600 °C. In this temperature range, the Nyquist plots of BFO (Figure 3.27a) show a small semicircle

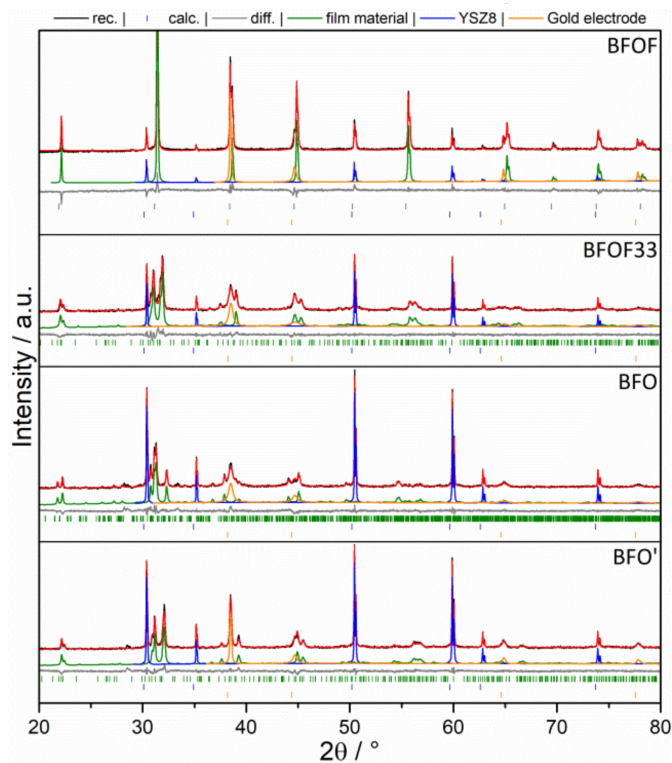


Figure 3.25.: XRD of as-prepared films with sputtered Au electrodes on top after topochemical oxidation and fluorination.

Table 3.7.: Lattice parameters and cell volume per formula unit Z of BaFeX_y ($X = \text{O}, \text{F}$) for the sintered and topochemically modified films.

Films							
Compound	Composition	SG	a (Å)	b (Å)	c (Å)	β (°)	V_Z (Å ³)
BFO	BaFeO _{2.5}	$P2_1/c$	6.9751(5)	11.7237(9)	23.4553(15)	98.865(6)	67.682(8)
BFO'	BaFeO _{2.67}	$P2_1/m$	10.1185(8)	5.6431(5)	6.9425(6)	92.298(7)	66.016(9)
BFOF33	BaFeO _{2.33} F _{0.33}	$P2_1/m$	10.1450(8)	5.6877(5)	6.9792(6)	92.246(8)	67.067(9)
BFOF	BaFeO ₂ F	$Pm\bar{3}m$	4.0583(1)	-	-	-	66.839(7)
Literature Data							
Reference	Composition	SG	a (Å)	b (Å)	c (Å)	β (°)	V_Z (Å ³)
[33]	BaFeO _{2.5}	$P2_1/c$	6.9753(1)	11.7281(2)	23.4507(4)	98.813(1)	67.692(2)
article in prep.	BaFeO _{2.67}	$P2_1/m$	10.1635(3)	5.6489(1)	6.9537(2)	92.064(2)	66.495(3)
[12]	BaFeO _{2.33} F _{0.33}	$P2_1/m$	10.1059	5.7094	6.9770(1)	93.107(1)	66.995(2)
[11]	BaFeO ₂ F	$Pm\bar{3}m$	4.05884(3)	-	-	-	66.866(1)

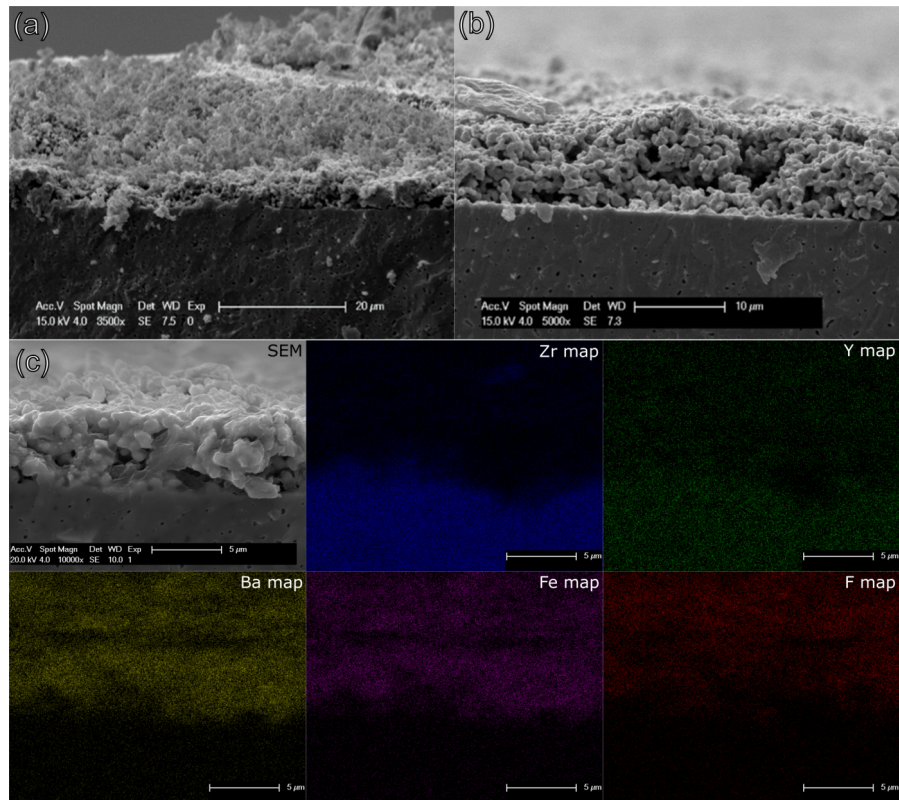


Figure 3.26.: SEM before (a) and after (b) sintering. EDX (c) of a topochemically fluorinated BFOF film, mapping the main elements of the used materials: Zr, Y, Ba, Fe, F.

at high frequencies, while in the mid frequency range the Nyquist plots first exhibit an open depressed semicircle, which closes between 434 and 450 °C into a depressed semicircle with nearly linear part with a 45° angle on its high frequency side. This mid to low frequency half tear-drop shaped response can generally be described by the Gerischer impedance element [81] and is typically found for porous mixed ionic-electronic conducting oxide cathode materials [75, 185, 186]. This response is described by:

$$Z_{\text{chem}} = \frac{R_{\text{chem}}}{\sqrt{1 + (j\omega t_{\text{chem}})^{\phi}}} \quad (3.5)$$

with R_{chem} being a chemical resistance associated with non-charge transfer processes inside the electrode, namely oxygen exchange between gas phase and electrode material and oxygen ion diffusion inside the MIEC material, and t_{chem} the corresponding time constant. The exponent ϕ turns the proposed ideal model into a “fractal” model as discussed in [186], which is comparable to the transformation of a pure capacitive into a constant phase element (CPE) related response. This equivalent circuit element represents an electrochemical non-charge transfer process, which is limited by the transport of oxygen ions with a fast exchange of oxygen at the gas phase and cathode interface. This element is derived from the model developed by Gerischer for the oxygen ion exchange on the surface of a metallic membrane [81]. Adler et al. [75] adapted this model for porous MIEC oxide cathode films, discussing the influences of the overall film morphology onto electrochemical and impedance behavior under the assumption of the electrode characteristics determined by bulk kinetics and transport processes. This Gerischer type model will be used for describing the measured response of the symmetrical BFO films. In order to account for the charge transfer processes occurring in a MIEC cathode, such as electron and oxygen ion exchange at the interfaces between cathode and gold top electrode and cathode and YSZ electrolyte, respectively, the model was extended by two additional R|CPE-elements [19]. We acknowledge that it is not always possible to resolve all processes easily. Often, the Bode plot (e.g., Figure 3.27b) only shows one broad maximum in the mid to low frequency range and one maximum at high frequencies, leading to the assumption that the non-charge transfer and charge transfer process possess a similar relaxation time. Hence, leading to the following fitting models:

$$R_S I - (R|CPE)_1 - (R|CPE)_2 - (R|CPE)_3 \text{ for } T < 435 \text{ }^{\circ}\text{C} \quad (3.6)$$

and

$$R_S I - (R|CPE)_1 - (R|CPE)_2 - G_{su} \text{ for } T > 435 \text{ }^{\circ}\text{C} \quad (3.7)$$

with G_{su} representing the fractal Gerischer model. The indices 1 and 2 represent the electronic and ionic charge transfer processes, respectively [19]. For $T < 435 \text{ }^{\circ}\text{C}$, the third

circuit $(R|CPE)_3$ may represent gas phase diffusion inside the porous cathode which then turns into the Gerischer type response at higher temperatures. In contrast, the response of BFOF33 shown in Figure 3.27c exhibits also open semicircles up to a temperature of 435 °C, with closed semicircles above this temperature. However, it does not exhibit a 45° angle of the last semi-circle in the temperature range under investigation. Hence, the response appears mainly to be of capacitive nature without a diffusive part as it has been observed in the pure oxide film. The Bode plot in Figure 3.27d consists of a broad maximum at low to mid frequencies and another one at high frequencies. From this, it was found that a plausible fitting model of a series of $(R|CPE)$ models is sufficient to achieve a satisfying fit:

$$R_S - (R|CPE)_1 - (R|CPE)_2 - (R|CPE)_{\text{chem}} \quad (3.8)$$

This is enforced by testing the models derived for the different compounds on the other compounds (e.g., the model derived for BFO' on BFOF33). Figure 3.28 compares the two discussed models on the basis of the obtained impedance data for BFO' and BFOF33. This comparison shows that

- (1) BFO' can be roughly fitted with the model used for BFO33. However, this series of $(R|CPE)_x$ elements only shows significant misfits and deviations in frequency range 10^3 to 10^1 Hz, indicating that it does not describe the occurring oxygen exchange at the gas phase/MIEC interface correctly.
- (2) In case of BFOF33 (Figure 3.28b), the $(R|CPE)$ -based fit yields a better result than a Gerischer-based, which again is expressed by systematic misfits in the frequency range of 10^3 to 10^1 Hz where the third semicircle expresses most significantly.

BFOF exhibits a different response as shown in the Nyquist and Bode plots, Figure 3.27e,f. The measured polarization resistance is three orders of magnitude higher than in case of BFO' and BFOF33. The Bode plot shows two discriminable maxima in the mid to low frequency range. It was noted that in contrast to the semicircles observed for BFO' and BFOF33, more semicircles are apparent in the high frequency range up to a temperature of 520 °C. On the other side, the Nyquist plots show two semicircles with an open end for temperatures <488 °C in the mid to low frequency range, which show up as a maximum in the frequency representation of the corresponding Bode plots. Following this argumentation, the Nyquist and Bode plots may suggest a simple series of four $(R|CPE)$ circuits. The first two semicircles, apparent only for BFOF, may correspond to a bulk and grain boundary conduction since the capacities are in the order of 10^{-12} and 10^{-10} F, respectively. Due to the comparably high ionic conductivity of YSZ, these resistive contributions must be assigned to the film material, while the contributions of

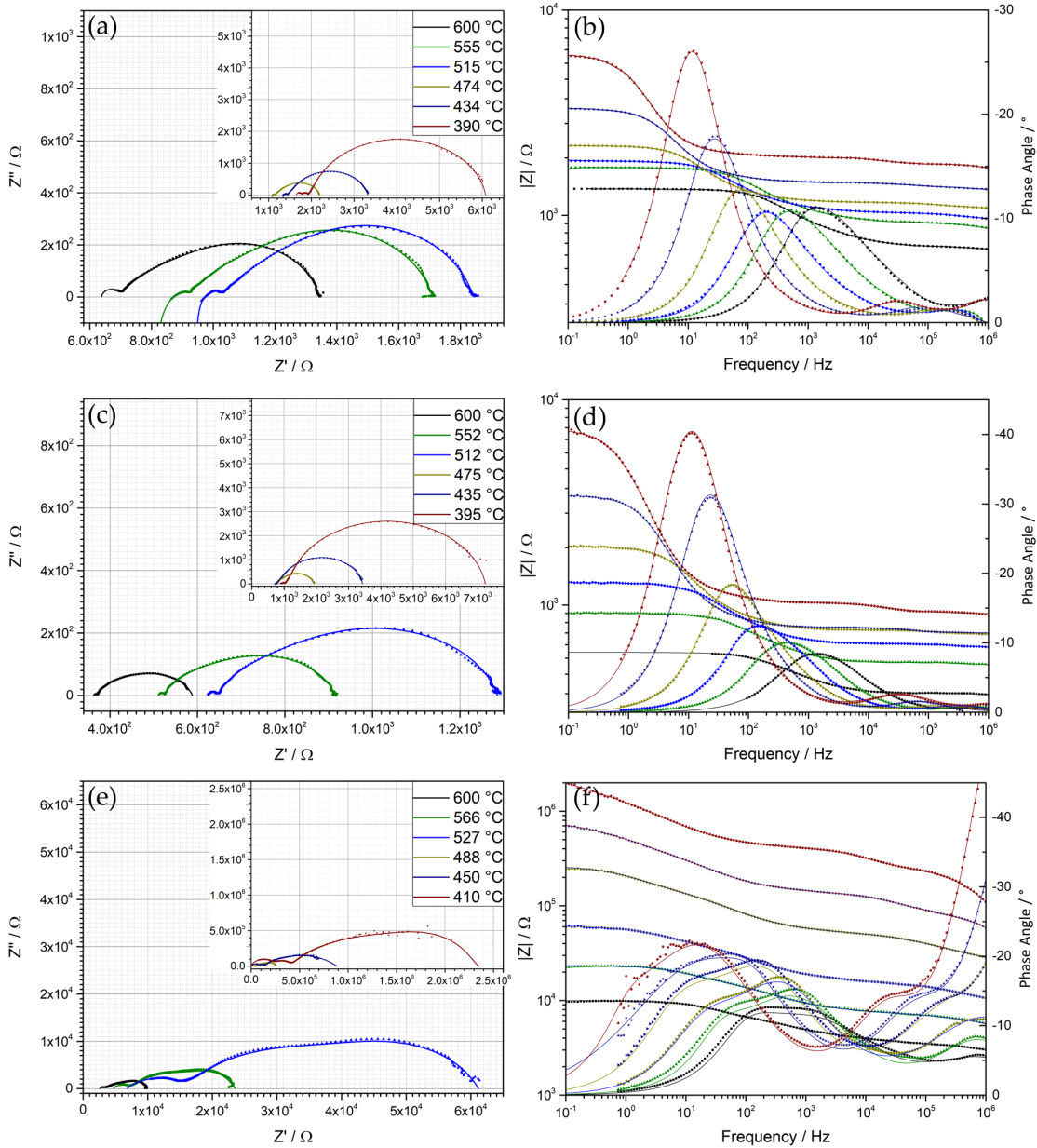


Figure 3.27.: (a,c,e) Nyquist and (b,d,f) Bode plots of symmetrical films of BFO, BFOF33 and BFOF. The recorded data are represented by symbols, while the fits are drawn with solid lines.

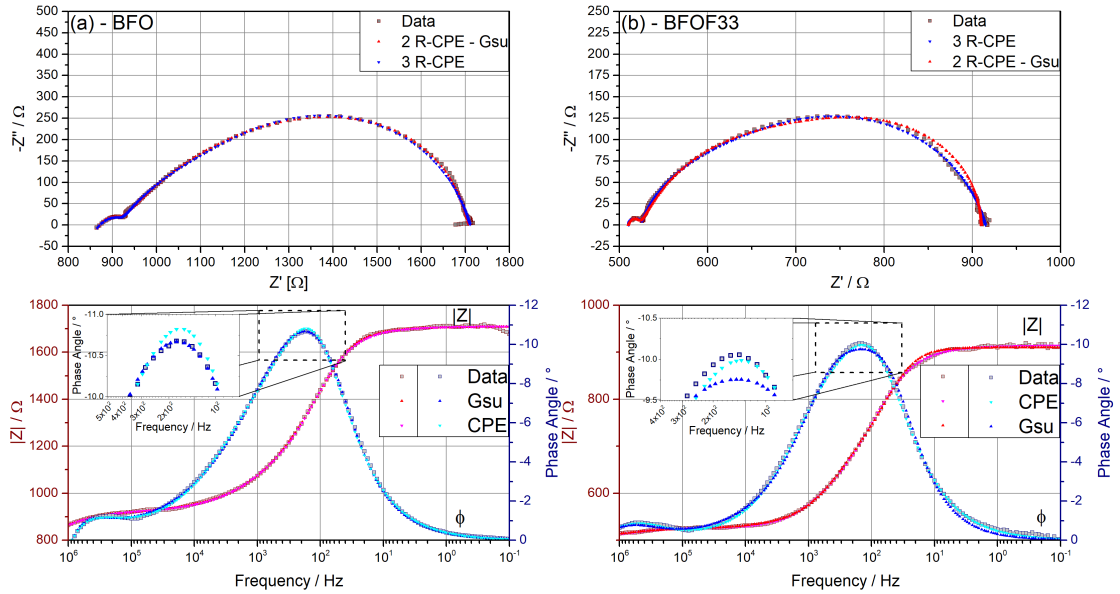


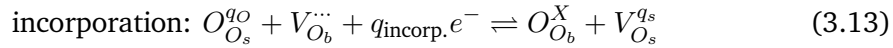
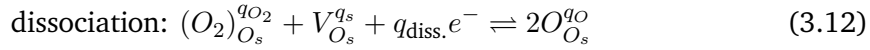
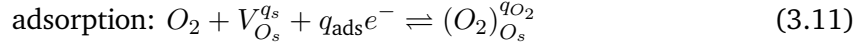
Figure 3.28.: Comparison of fitting models describing diffusive and/or capacitive responses for (a) BFO' and (b) BFOF33, where each, (a) and (b), contain a comparison of the used models inside Nyquist and Bode plots.

YSZ can be summed up in the low resistive contribution of serial resistor R_S as described in the preceding discussions. Hitherto, we described the electrochemical processes inside the MIEC with a 3D model. However, the impedance spectra observed for BFOF do not allow for the application of such a complex model due to the high resistances and less complex spectra observed. Thus, the fitted parameters were reduced to the electrochemical processes to the triple phase boundary (TPB) between electrode, electrolyte and gas phase captured by two serial (R|CPE) elements. We must acknowledge that the fits in the Nyquist and Bode representation still show systematic deviations. However, increasing the number of circuits or using other models, e.g., a Warburg-type element, did either result in over-parametrization and fit divergence or resulted in worse description of the data respectively. Hence, the following models were used for BFOF:

$$R_S - (R|CPE)_B - (R|CPE)_{GB} - (R|CPE)_1 - (R|CPE)_2 \text{ for } T < 520 \text{ }^\circ\text{C} \quad (3.9)$$

$$R_S - (R|CPE)_{GB} - (R|CPE)_1 - (R|CPE)_2 \text{ for } T > 520 \text{ }^\circ\text{C} \quad (3.10)$$

The impedance spectra recorded relate to the effects of oxygen dissociation at the electrode surface and to the incorporation into the bulk lattice of the electrode material. This can be expressed by the following formalism according to [187]:



with b and s representing the corresponding bulk and surface site, respectively. Due to the topochemical nature of the fluorination reactions, which do not enforce any significant morphological changes, microstructural effects must be expected to be low and the differences found between the oxide and oxyfluoride compounds can be assumed to relate to the processes of oxygen transfer and oxygen ion incorporation/release within the symmetrical films.

Figure 3.29 compares the area specific resistances of all three compounds. It is evident that BFO' and BFOF33 show similar EIS responses, whereas BFOF exhibits much higher resistances by three orders of magnitude. The incorporation of oxygen at the electrode requires the presence of anion vacancies, which were below the detection limit by diffraction methods for cubic BaFeO₂F [12]. This most likely also limits the generation of vacancies at the surface of the compound. Due to the nearly full occupation of the anion lattice and the pinning of the iron valency to a trivalent state, which limits electron transport, this process is strongly blocked. This well explains the difference of BFOF as compared to BFOF33 as well as BFO'. The compounds BFO' and BFOF33, which both possess a large amount of vacancies of $c_{V,\text{oxygen}} \approx 0.33$ per Fe, exhibit only smaller conceptual differences regarding the electrochemical processes expressed by the differences found for the Bode plots. The Gerischer type model considers the oxygen uptake at the gas phase/electrode interface together with the bulk diffusion as the co-limiting factors in this process. Adler et al. [19] elaborated the case of a surface limitation due to an exceeding of the utilization zone throughout the whole electrode thickness. Figure 3.30 depicts the two special cases of the penetration of the utilization region. Further, it connects the mentioned limits with the mathematical description for Z_{chem} and representation inside a Nyquist plot. Adler et al. derived the solution for these boundary conditions in [19] for the equation:

$$Z_{\text{chem}} = \frac{R_{\text{chem}}}{\sqrt{1 + j\omega t_{\text{chem}}}} \left| \text{Tanh}\left(\frac{L}{\delta} \sqrt{1 + j\omega t_{\text{chem}}}\right) \right| \quad (3.14)$$

with L as electrode thickness and δ the utilization region inside the electrode. For an infinite electrode thickness L , the term $\text{Tanh}(L/\delta)$ approaches unity, yielding Equation 3.5.

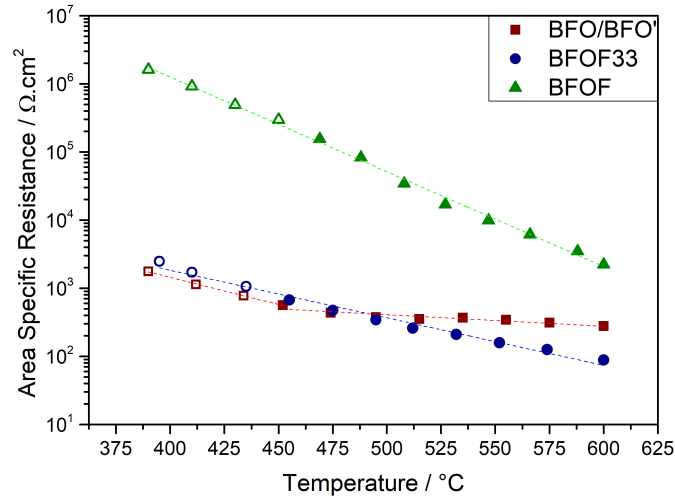


Figure 3.29.: Logarithmic plot of the area specific resistance. Dashed fitting lines highlight the behavior in case of BFOF33 (●) and BFOF (▲). BFO/BFO' (■) exhibits a bend trajectory. Hollow symbols represent the temperatures with open semicircles.

As δ becomes larger than L , Equation 3.14 turns into a linear relation, which impedance is related to $1/L$:

$$Z_{\text{chem}} = A \frac{R_{\text{chem}}}{L(1 + j\omega t_{\text{chem}})} \quad (3.15)$$

with A including thermodynamical and morphological parameters. In addition to the underlying theory of a utilization zone penetrating the electrode material, Figure 3.30 also takes into account the role of the triple phase boundary (TPB). The TPB was suggested to be the crucial region where the electrochemical process of oxygen uptake and dispersion happens. However, with the introduction of the Gerischer type impedance model, Adler et al. [75] extended the one dimensional TPB reaction into the electrode material in case of a porous mixed ionic-electronic conductor. Recent studies gave indication that the model of a spot-sized region is insufficient and does not capture the whole process [188]. The linear case results in a more semicircle like shape as depicted in Figure 3.30b. It may only occur if solid-state diffusion within the electrode is fast allowing for a utilization of the whole internal surface area for oxygen uptake limited by the film thickness L .

This behavior is in principle indicated for BFOF33 and might be interpreted as follows: The introduction of fluorine into the anion sub-lattice might provide a way to slightly

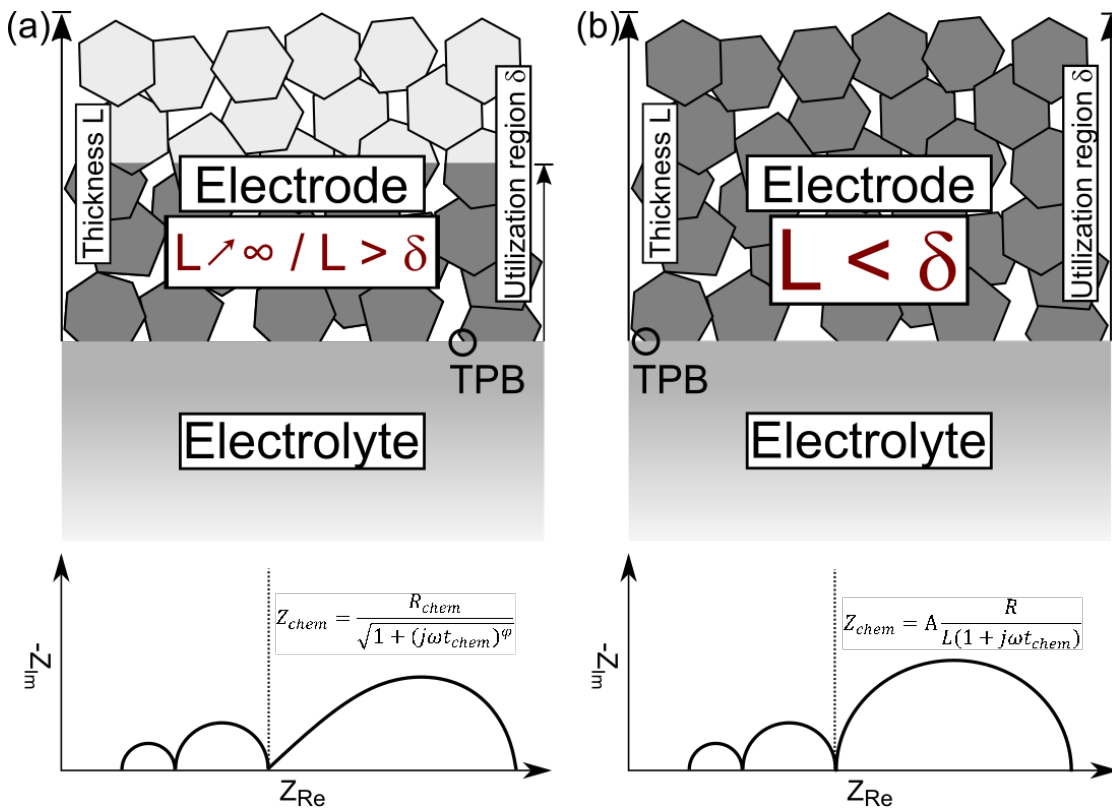


Figure 3.30.: Schematic of the penetration of the utilization region δ into the electrode in dependency of its thickness L with the corresponding impedance models: (a) depicts the relation represented by Equation 3.5; (b) illustrates the case discussed for Equation 3.15.

enhance the oxygen ion mobility within the oxyfluoride lattice once a sufficient amount of vacancies is available. In a simple picture, F^- is a more mobile ion than O^{2-} , and by this the fluoride ion might be able to allocate a vacancy to an oxide ion which is in the process of moving. Thus, the inner mobility of ions might be increased in $BaFeO_{2.33}F_{0.33}\square_{0.33}$, and the electrode limiting process might be dominated by the fast ion diffusion and the utilization of the whole electrode surface according to the model elaborated by Adler et al. [19].

Evaluation of the area specific resistance in Figure 3.29 shows that the pure oxide BFO' does not exhibit a linear Arrhenius type behavior, while the fluorinated films show Arrhenius type behavior, as indicated by the dashed lines. Within a VT-XRD study (*article in preparation*), it was found that BFO transforms to BFO' under incorporation of O_2 (hence oxidation) above 250 °C. The oxygen is then released above 500 °C and BFO' is reversed to BFO. Hence, the kink and the unsteady trajectory at temperatures above 450 °C are a result of chemical processes related to the incorporation of oxygen and the resulting phase transformation. With this oxygen uptake, BFO' becomes isotypic to BFOF33, and the linear behavior above 450 °C up to 590 °C agrees well with a fairly stable composition within this temperature range. The Gerischer related impedance response can in this case be interpreted as bulk diffusion limited, which is in agreement with the availability of high amounts of vacancies, the increase of amounts of Fe^{4+} , which acts as holes for electron transport, and the fact that ionic re-arrangements are restricted to the less mobile O^{2-} ion only.

Table 3.8 lists the activation energies extracted from the Arrhenius plots shown in Figure 3.31 (note that two activation energies were extracted for BFO due to the apparent temperature dependent differences in composition). In the temperature range 390–470 °C the activation energies for BFO' and BFOF33 appear to be similar (0.29 to 0.33 eV) and half of the value of BFOF (0.67 eV). Around 490 °C the conductivity of BFO levels and the activation energy drops down to 0.07 eV. Again, these differences in activation energies agree well with the conclusions described in the previous paragraph. Above 490 °C BFOF33 exhibits its highest conductivity reaching a value of $1 \cdot 10^{-5}$ S/cm at $T = 575$ °C, which is close to the decomposition temperature, while BFO and BFOF show values of $3 \cdot 10^{-6}$ S/cm and $2 \cdot 10^{-7}$ S/cm, respectively.

Table 3.8.: Activation energies as calculated from the Arrhenius plots in Figure 3.29.

Activation Energy, E_a	BFO/BFO'	BFOF33	BFOF	$Ba_xSr_{1-x}Co_{0.8}Fe_{0.2}O_{3-d}$ ($0.3 \leq x \leq 0.7$) [187]	$SrCo_{0.8}Fe_{0.2}O_{3-d}$ [188]	La_2NiO_4 [75]
E_a (eV)	0.07(1)/0.29(1)*	0.33(1)	0.67(2)	0.32–0.40	2.4–2.6	1.00

*: note that the extraction of an activation energy for BFO is difficult due to the structural instabilities (changes in oxygen content) beginning around 490 °C, thus a linear fit over the whole temperature range is not possible.

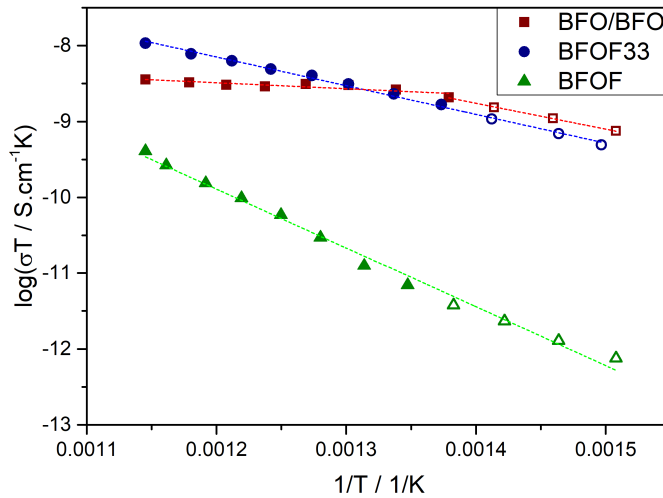


Figure 3.31.: Arrhenius plot for the conductivity of BFO/BFO' (■), BFOF33 (●) and BFOF (▲). Dashed lines represent the performed fit for the activation energy.

3.2.4. Conclusion

In this work, highly porous symmetrical films of $\text{BaFeO}_{2.67}$, $\text{BaFeO}_{2.33}\text{F}_{0.33}$ and BaFeO_2F were successfully synthesized on YSZ8 without the need of an intermediate layer. The porosity is achieved by spin coating nano-powder produced by the NSP process on YSZ substrates followed by a short sintering step. The as-prepared films feature a thickness of around $8 \mu\text{m}$. The topochemical fluorination of the films is successfully performed by an interdiffusion and vapor approach for $\text{BaFeO}_{2.33}\text{F}_{0.33}$ and BaFeO_2F , respectively. HTXRD revealed an upper temperature limit of $590 \text{ }^\circ\text{C}$ and $710 \text{ }^\circ\text{C}$ for $\text{BaFeO}_{2.33}\text{F}_{0.33}$ and BaFeO_2F , respectively. The interdiffusion approach introduced in this work has proven to give an easy option to adjust a desired fluorine level in a thin film opening up topochemical fluorination for metastable oxyfluorides, which cannot be directly synthesized.

Recent studies have already revealed an enhancing effect of fluorine doping of oxide materials on the oxygen reduction and transportation [10, 20, 99]. A small amount of fluorine may lower the activation energy for the non-charge transfer processes, such as oxygen reduction or bulk transportation. In this study, we focused on the evaluation of the impedance data by applying a 3D model developed for porous MIEC cathodes. By this, it is indicated that the non-charge transfer process is limited by the oxygen uptake rather than by bulk diffusion as it is the case for the parent oxide. In addition, the fluorine can also help to stabilize the phase of the parent oxide, especially for Ba-rich compounds

with large structural complexity. However, we have shown that it is of crucial importance to adjust the fluoride concentration to a compound specific content, as high fluorination degrees with high overall occupation of anion sites and absence of vacancies will have a detrimental effect on the overall cathode performance.

Author Contributions: “Conceptualization, S.W. and O.C.; methodology, S.W.; synthesis and characterization of materials, S.W.; writing–original draft preparation, S.W. and O.C.; writing–review and editing, S.W. and O.C.; visualization, S.W.; supervision, O.C.; project administration, O.C.; funding acquisition, O.C. All authors have read and agreed to the published version of the manuscript.

Funding: The authors acknowledge support by the German Research Foundation within the Emmy Noether Programme (grant no. CL551/2-1). We acknowledge support by the Open Access Publishing Fund of Technical University of Darmstadt.

Conflicts of Interest: The authors declare no conflict of interest.

3.3. Synthesis and characterisation of fluorinated epitaxial films of BaFeO₂F: Tailoring magnetic anisotropy via a lowering of tetragonal distortion

Akash Nair ^a, Stephan Wollstadt ^a, Ralf Witte ^b, Supratik Dasgupta ^c, Philipp Kehne ^c, Lambert Alff ^c, Philipp Komissinskiy ^{c,*}, Oliver Clemens ^{a,b,*}

^a Technische Universität Darmstadt, Institute of Materials Science, Materials Design by Synthesis Division, Alarich-Weiss-Straße 2, 64287 Darmstadt, Germany.

^b Karlsruhe Institute of Technology, Institute of Nanotechnology, Hermann-von-Helmholtz-Platz 1, 76344 Eggenstein Leopoldshafen, Germany.

^c Technische Universität Darmstadt, Institute of Materials Science, Advanced Thin Film Technology Division, Alarich-Weiss-Straße 2, 64287 Darmstadt, Germany.

* Corresponding Authors:

Fax: +49 6151 16 20699 E-Mail: komissinskiy@oxide.tu-darmstadt.de

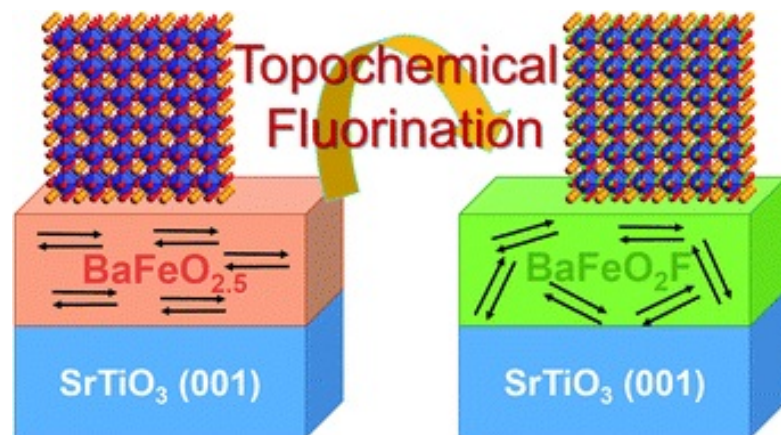
Fax: +49 6151 16 21991 E-Mail: oliver.clemens@md.tu-darmstadt.de

Received: 4th October 2019; Accepted: 25th October 2019; Published: 13th November 2019

Reproduced under the *Creative Commons BY-NC 3.0* license from Nair, A., Wollstadt, S., Witte, R., Dasgupta, S., Kehne, P., Alff, L., Komissinskiy, P., and Clemens, O. (2019). "Synthesis and characterisation of fluorinated epitaxial films of BaFeO₂F: Tailoring magnetic anisotropy via a lowering of tetragonal distortion." *RSC Advances*, 9(64), 37136-37143 with permission from the Royal Society of Chemistry.

DOI: <https://doi.org/10.1039/C9RA08039B>

Abstract In this article, we report on the synthesis and characterisation of fluorinated epitaxial films of BaFeO_2F via low-temperature fluorination of thin films of $\text{BaFeO}_{2.5+d}$ grown by pulsed laser deposition. Diffraction measurements show that fluoride incorporation only results in a contraction of the film perpendicular to the film surface, where clamping by the substrate is prohibitive for strong in-plane changes. The fluorinated films were found to be homogenous regarding the fluorine content over the whole film thickness, and can be considered as single crystal equivalent to the bulk phase BaFeO_2F . Surprisingly, fluorination resulted in the relieve of the tetragonal distortion to a nearly cubic symmetry, which results in a lowering of anisotropic orientation of the magnetic moments of the antiferromagnetically ordered compound, confirmed by Mössbauer spectroscopy and magnetic studies.



3.3.1. Introduction

Perovskite-type transition metal oxides such as the stoichiometric ABO_3 , A_2BO_4 , $A_3B_2O_7$ and non-stoichiometric ABO_{3-x} , (where A: rare earth or alkali earth ion, and B: 3d, 4d, or 5d transition metal ion) can exhibit fascinating physical and chemical properties, including multiferroicity [189–191], high temperature superconductivity [192], colossal magnetoresistance [193], and photocatalytic activity [194]. One of the most interesting aspects of these oxides is the ability to engineer/tune their physical properties by tailoring the composition of the cation sites (*i. e. the 12-fold coordinated A- and/or the 6-fold coordinated B-site*) and/or partially replacing the oxygen by other anionic species such as hydride [195, 196], fluoride [21, 37, 169, 197], or nitride [198] ions. This most often originates from a tuning of the electronic structure and coordination chemistry of the constituent species. One of the methods that has been used to incorporate fluoride ions to change oxidation states of transition metals within perovskite type (or perovskite related) materials are low-temperature topochemical fluorination routes [21, 37, 47, 169, 176]. The necessity for using low temperature topotactic fluorination routes originates from the fact that the majority of oxyfluoride perovskites are only metastable and will decompose at elevated temperature to form alkaline earth fluorides or lanthanide oxyfluorides. Therefore, for most of these compounds it is not possible to grow single crystals at elevated temperatures. Within the last years, adopted approaches have been reported for fluoride incorporation into epitaxially grown thin films [47, 168, 175, 176, 199, 200]. This does not only provide the opportunity to investigate such films as a grain boundary free model system to study bulk related properties, but also to use strain engineering [201] to further modify materials' properties. Bulk $BaFeO_{2.5}$ (BFO) crystallizes in a complex vacancy ordered modification of the cubic perovskite type structure [33, 110, 202]. This monoclinic modification is centrosymmetric with space group $P2_1/c$. This compound can be fluorinated using polymer-based routes, and $BaFeO_{2.33}F_{0.33}$ (vacancy ordered, $P2_1/m$) [12, 116] and $BaFeO_2F$ (BFOF) (no significant amounts of vacancies, cubic, $Pm\bar{3}m$) [11, 36, 203]. As is common for perovskites with trivalent iron mainly, these compounds show G-type antiferromagnetic ordering with Néel temperatures above 500 K. Although the structure of BFOF appears simple at first glance, the local structure around the iron seems to deviate significantly from having perfect octahedral symmetry. Heap et al. [11, 203] were the first to notice an unusual high atomic displacement parameters of the Fe^{3+} cations, and different configurations of fluoride ions within the FeO_4F_2 octahedra (*cis* = both fluoride ions at the same edge; *trans* = fluoride ions located at opposite corners) were discussed in the context of the compound lacking long-range anion ordering. In combination with Mössbauer spectroscopic studies, a non-centrosymmetric *cis* environment around a majority of Fe cations from mainly statistic distribution of fluoride ions was concluded [203].

The fact that there seems to be chance given for the absence of centrosymmetry around the Fe^{3+} cations makes the compound of principle interest for possessing multiferroic properties. To approach such applications, an additional understanding of the structure within fluorinated epitaxially grown thin films seems to be appreciable. Here, we report two different approaches to topochemical fluorination of epitaxially grown BFO thin films on single crystalline (001) oriented substrates of SrTiO_3 [117, 204]. We show that the films can be chemically fluorinated via different approaches under formation of BFOF without significant substrate fluorination. Via a combination of structural analysis, Mössbauer spectroscopy as well as magnetic studies, an improved understanding of the structural and magnetic behaviour of the films could be gained.

3.3.2. Experimental

3.3.2.1. Growth of BFO thin films

The BFO target was prepared using a conventional solid state synthesis route. Stoichiometric ratios of solid BaCO_3 (Alfa Aesar, >99.8%) and Fe_2O_3 (Sigma–Aldrich, >99%) were ground, uniaxially pressed and heated twice to 1100 °C for 24 h under flowing Ar with intermediate regrinding.

BFO thin films with a thickness of ~85 nm were grown on (001)-oriented SrTiO_3 (STO) substrates via pulsed laser deposition (PLD) in the custom made ultra-high vacuum PLD system which is a part of the Darmstadt Integrated System for Battery Research (DaISy–Bat). The BFO target was ablated with a KrF excimer laser ($\lambda = 248$ nm) at a repetition rate of 1 Hz and at a fluence of 1.4 Jcm^{-2} . During deposition, the substrates were heated up to a temperature of 700 °C from their back side, using a high power near infrared diode laser at 938 nm. A background oxygen pressure of 0.018 mbar was used for all depositions. After deposition, the films were cooled down to room temperature at a rate of 50 K min^{-1} . These conditions were chosen in accordance with previous experiments within our group [117, 204].

3.3.2.2. Thin Film Fluorination

Two fluorination approaches were attempted to fluorinate thin films of BFO to BFOF, which did not show strong differences with respect to the quality, structure and composition of the films reported within this article. In the first approach [47] (see Fig. 3.32), a solution of 10 wt-% of poly-(vinylidene difluoride) (PVDF) in acetone is ‘dropped’ onto an as-grown oxygen deficient BFO film. This method will be referred to as “drop fluorination” in the following. The film was then heated in air for 24 h at 375°C. In a second approach [47]

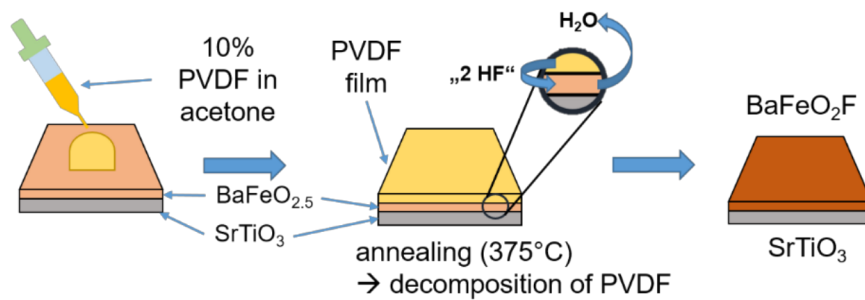


Figure 3.32.: Representation of drop fluorination method of fluorination as carried out on BFO films. The figure is recreated and related to the scheme shown in ref. [47].

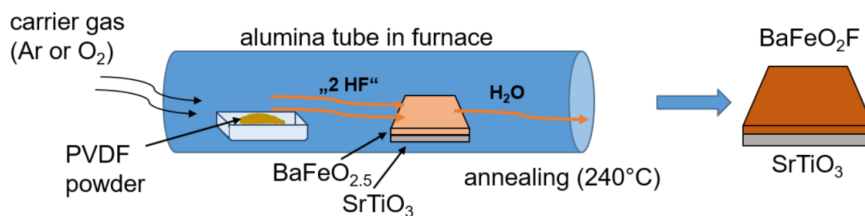
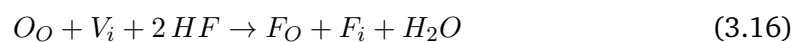


Figure 3.33.: Vapour transport process carried out on as-grown oxygen deficient BFO placed downstream from PVDF pellets in a heated alumina tube in the presence of a flowing carrier gas. The figure is recreated and related to the scheme shown in ref. [47].

(see Fig. 3.33), a PVDF powder is placed in a tube furnace heated to 240 °C in front of a BFO film with respect to the gas flow direction. Decomposition products of PVDF, such as HF or small chain components, are then carried over the film and fluorinate it. This approach will be referred to as “vapour transport” fluorination in the following. For this process, a large excess of 2 g of dry PVDF were used (the estimated amount of polymer necessary for full fluorination of the film is in the order of 1-5 µg). Within this reaction, the fluorine from the decomposition of PVDF under formation of HF can be expected to occupy the interstitial vacancies and replace oxygen from the lattice equally in the film according to



3.3.2.3. Structural characterisation

The X-ray Diffraction (XRD) θ - 2θ measurement of the BFO target was performed using a Bruker D8 Advance diffractometer in Bragg-Brentano geometry showing phase purity of the target material as reported previously [117]. The thin-film XRD θ - 2θ measurements were performed in parallel beam geometry using a Cu- $K\alpha_1$ Rigaku SmartLab X-ray diffractometer with a Ge(220) 2-bounce monochromator.

3.3.2.4. X-ray Photoelectron Spectroscopy (XPS)

X-ray photoelectron spectroscopy (XPS) measurements were performed within the DAISY-BAT system with a PHI Versaprobe 5000 spectrometer equipped with a monochromated Al K_α X-ray source at 1486.6 eV. All the measurements were carried out at room temperature at a pass energy of 23.5 eV and an energy step size of 0.1 eV. The as-grown BFO films were transferred into the XPS chamber under UHV conditions ($< 10^{-8}$ Torr) and, therefore, were not exposed to ambient atmosphere prior to the XPS measurements. For fluorinated films, adsorbates such as carbon could not be avoided on the surface of the films as the fluorination reaction was performed outside the UHV system. To probe the inward homogeneous incorporation of fluoride into the films, XPS depth profile analysis was performed via Argon ion sputtering at accelerating voltage of 4 kV and ion current of 3 μ A. The adventitious carbon contaminations were detected at the surface of the film only before Ar ion sputtering. Following the first sputtering cycle, no carbon peak could be detected.

3.3.2.5. SQUID Magnetometry

Magnetic properties of the samples were measured as a function of the applied magnetic field and temperature using a magnetic property measurement system (MPMS) by *Quantum Design*, equipped with a superconducting quantum interference device (SQUID). The magnetization data were corrected for diamagnetic contributions from the SrTiO₃ substrate. Two different sets of measurements were performed on the same films in non-fluorinated and fluorinated states. Magnetization M for each film was measured as a function of the applied magnetic field H between -2 T and 2 T at 10 K. Magnetization versus temperature curves were recorded between 298 and 10 K at $H=200$ Oe in a field cooled (FC) and zero field cooled (ZFC) regimes.

3.3.2.6. Conversion Electron Mössbauer Spectroscopy (CEMS)

Conversion Electron Mössbauer Spectroscopy (CEMS) was measured with a ^{57}Co in Rh matrix source (50 mCi) and the velocity was varied with a constant acceleration drive. The conversion electrons from the resonant absorption of gamma-rays were detected with a custom-built gas-proportional counter, with a mixture of CH_4 (4 %) in He as detector gas. The velocity scale was calibrated with a *bcc* Fe standard and all isomer shifts are given relative to *bcc* Fe at room temperature.

3.3.3. Results and discussion

3.3.3.1. Structural analysis

In agreement with our previous findings [117, 204], the XRD measurements showed, that the BFO film can be grown in a pseudo-cubic phase (see black curves in Fig. 3.34a,b). The extracted out-of-plane lattice parameter $c = 4.13 \text{ \AA}$ of the BFO film (differs strongly from the lattice parameter of the STO substrate ($a = 3.905 \text{ \AA}$). The inset in Fig. 3.34b shows a rocking curve measurement, showing a full-width at half-maximum (FWHM) of 0.05° for the (002) BFO reflection. The narrow FWHM indicates a high degree of crystallinity and low mosaicity throughout the depth of the film. The value of the lattice parameter $c = 4.13 \text{ \AA}$ lies between the values of 4.11 \AA observed by Benes et al. [117] for 200 nm thick films and of 4.15 \AA reported by Sukkurji et al. [204] for 20-30 nm thick films. This indicates that the tetragonal distortion due to the epitaxial strain depends on the film thickness. After fluorination, the BFOF films do not show any significant change in orientation or strong relaxations within the film, as no additional reflections are observed in the XRD patterns. However, strong shifts of the film (00 l) XRD reflections are observed independent of the fluorination method used (see red curves in Fig. 3.34a,b as well as Fig. 3.35), which implies a small BFOF lattice parameter $c \approx 4.066 \text{ \AA}$. Remarkably, this value is similar to what has been reported for the bulk phase of BFOF by Heap et al. [11] ($a = 4.058 \text{ \AA}$). For the BFOF film, the slightly larger FWHM= 0.08° has been extracted from the rocking curve of the (002) reflection (see Fig. 3.36) than for the BFO film (FWHM = 0.05°), which indicates a small additional broadening after fluorine incorporation. This indicates a small increase of mosaicity after the topochemical incorporation of fluoride ions. X-ray reciprocal space mapping (RSM) was carried out to determine the in-plane lattice parameter and to understand the topochemical fluorination of the film in better detail. For this purpose, mapping around the STO (103) reflection of the BFO and BFOF films was performed, as shown in Fig. 3.37a,b). The shift in the film peak of the BFO film (Fig. 3.37a) along Q_x in comparison with the one of peak from the STO substrate indicates that the lattice mismatch is too high for the growth of a fully strained film. This observation is in

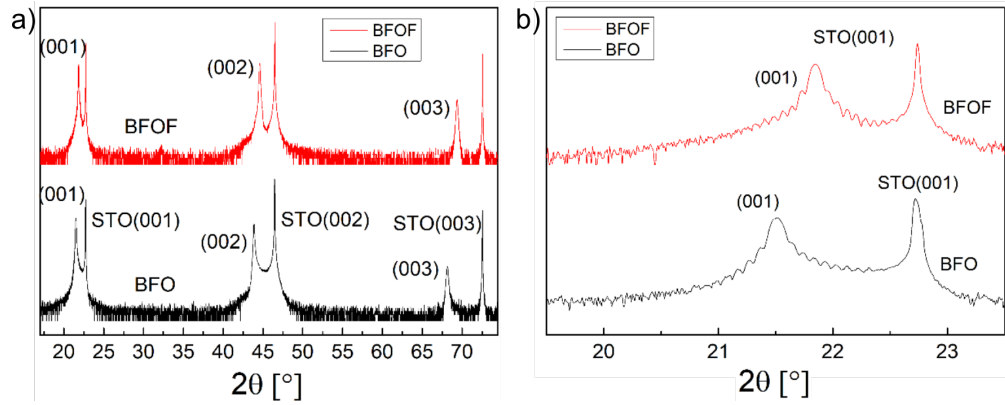


Figure 3.34.: (a) High resolution X-ray diffractograms of an as-deposited BFO (black) and fluorinated BFOF (red) films on SrTiO₃ substrate (b) Expanded view of the (001) BFO and BFOF reflections.

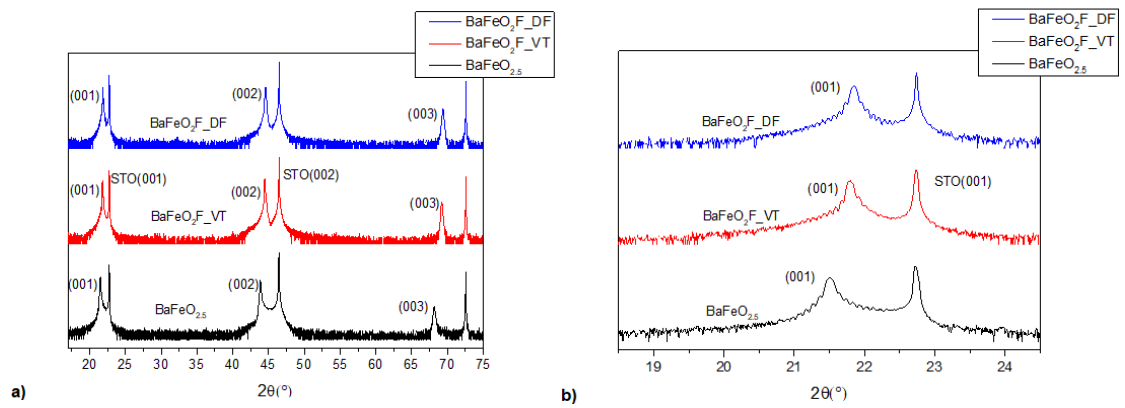


Figure 3.35.: a) XRD $2\theta - \theta$ patterns of the BFO film and BFOF films on STO. b) Expanded view of the 001 reflection. (SI)

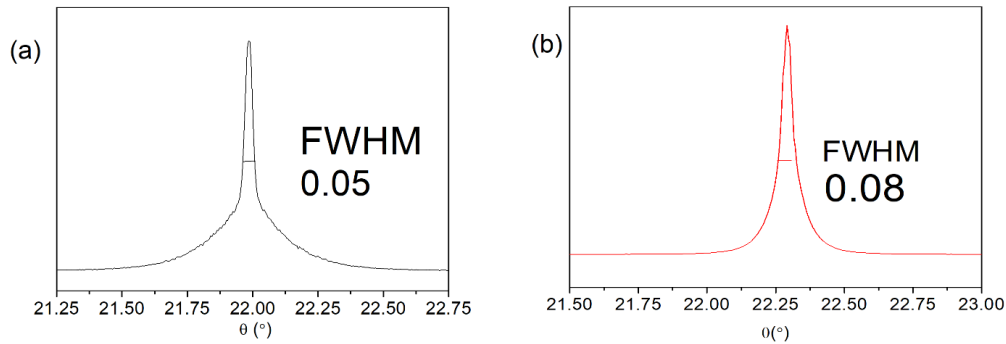


Figure 3.36.: Rocking curve scans of the (002) reflection of a film of BFO (a) and BFOF (b). (SI)

Table 3.9.: Calculated lattice parameters of the films from RSM.

Film	$a_{\text{in-plane}}$ (Å)	$c_{\text{out-of-plane}}$ (Å)
BFO	4.065(5)	4.128(6)
BFOF	4.066(3)	4.066(4)
STO	3.902	3.903

agreement with our previous study [204] which showed the presence of dislocations at the film/substrate interface. The in-plane and out-of-plane lattice parameters of $a = 4.065$ and $c = 4.128$ Å, respectively, were calculated from the RSM measurements (see Tab. 3.9). After fluorination, the BFOF film stays fully strained on the SrTiO₃ substrate and the Q_x position of the (103) BFOF film reflection is not changed (see Fig. 3.37b). This fact gives a strong support for the topotactic nature of the fluorination, which does not break clamping of the film to the substrate and allows only relaxation of the film perpendicular to the substrate plane. Meanwhile, significant changes of the RSM pattern of the BFOF are found along Q_z , implying a strong decrease of the c value to approximately 4.066 Å (Tab. 3.9). Thus, it is remarkable that the film fluorination indeed results in basically cubic cell metrics, with an average lattice parameter being close to what is found for powders of BaFeO₂F ($a = 4.058$ Å [11, 203]). Therefore, (taking into account the results of the compositional analysis presented below in Sec. 3.3.3.2, the BFOF films can be considered as being a close approximation to a single crystal of this metastable phase, which cannot be obtained by classic techniques of crystal growth.

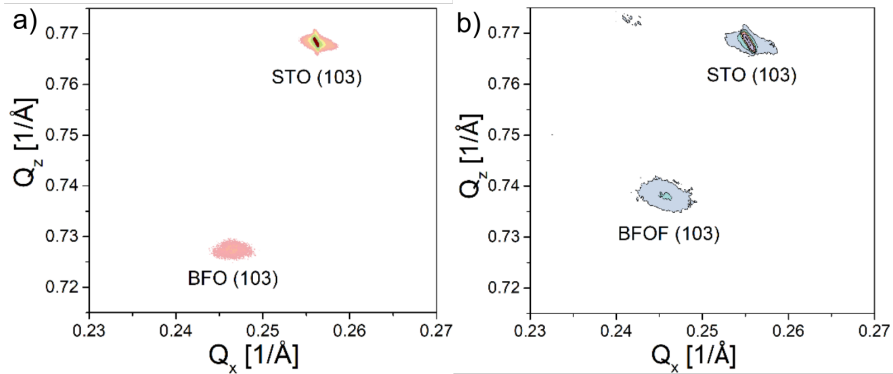


Figure 3.37.: X-ray Reciprocal Space Mapping of the (a) BFO and (b) drop-fluorinated BFO films measured around (103) STO reflection.

3.3.3.2. Compositional analysis

Fig. 3.39 shows a depth profile of the normalized elemental concentration in the BFOF film as extracted from the XPS measurements. In agreement with previous findings [47, 168, 200, 204], fluorine is only observed throughout the complete thickness of the BFOF film. No fluorine is detected in the SrTiO_3 substrate within the resolution limit of about 0.1 at.% of the XPS system. This is well plausible as PVDF does not have sufficient reductive power to form low-valent Ti species [205]. The detected sudden emergence of the Sr 3d and Ti 2p peaks indicates a sharp interface between the film and the substrate with no sign of interdiffusion of the metal species into the BFOF film. Note that in the interface region denoted with the vertical black lines, the elemental concentration is imprecise and not given. Within the BFOF film, a rather homogenous distribution of the elements Ba, Fe, O, and F could be confirmed. The Ba:Fe ratio of 1:1 in combination with a O:F ratio of 2:1 indicates the composition of BaFeO_2F , indicating a fully fluorinated state of the sample, in agreement with the Mössbauer spectra which indicate the presence of Fe^{3+} only (see section 3.3). Deviations from the ideal composition are within the reliability of the method and should be interpreted neither as anion rich films (i. e., lower oxidation states, as ruled out from Mössbauer spectroscopy, see section 3.3.3.3), nor the presence of, e. g. Ruddlesden-Popper related, Ba_2FeO_4 type defects (not indicated within the XRD analysis, see previous section). We would also like to emphasize a very similar compositional behaviour indicated the formation of BaFeO_2F films also for the second fluorination method (see Fig. 3.38). Thus, a $\text{BaFeO}_{2.33}\text{F}_{0.33}$ [12, 116] phase with intermediate fluorine concentration and ordered anion vacancies could not be synthesized

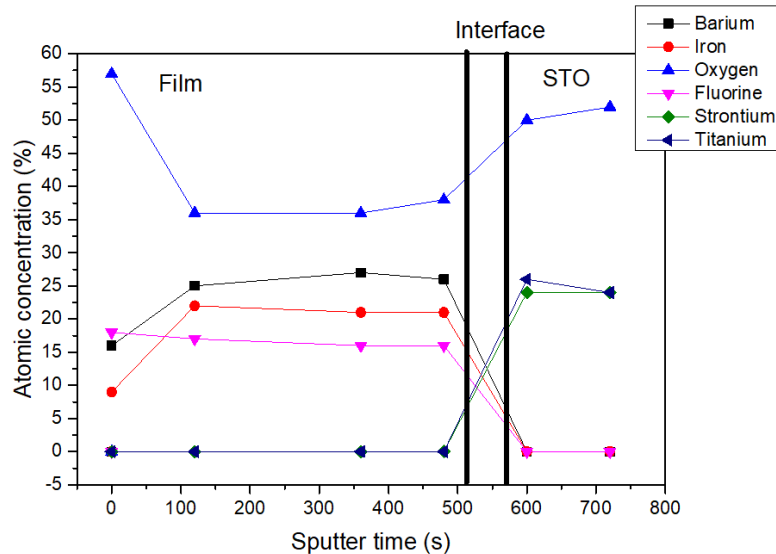


Figure 3.38.: Normalized concentration-depth profile for BFOF-VT. (SI)

with these methods. This phase is either unstable in the investigated strained BFOF films on the SrTiO_3 substrates or requires precise control of the fluorine concentration in the film at the level of about $1 \mu\text{g}$ (only few μg of fluorine are necessary for a full fluorination of the film), which has not been achieved in the presented fluorination methods.

3.3.3.3. ^{57}Fe Mössbauer spectroscopy

^{57}Fe conversion electron Mössbauer spectra were recorded for the BFO and drop-fluorinated BFOF films at 298 K (see Fig. 3.40a,b). It should be noted that the signals from the films were quite weak, which can be explained by the low thickness (85 nm) of the films. Although the signal-to-noise ratio is low, certain conclusions can still be drawn from the measurements.

- (1) The spectrum observed for BFO is similar to our previous study of 200 nm thick films [117]. It can be fitted with a similar distribution of sextets as reported for bulk $\text{BaFeO}_{2.5}$ [33] (see Tab. 3.10 and Fig. 3.40 a), which agrees with tetrahedrally (low isomer shift, sextet 2), square pyramidally, and octahedrally (high isomer shift, sextet 1 & doublet) coordinated iron species within this film. The fit shows that although no long-range ordering of anion vacancies can be obtained within a

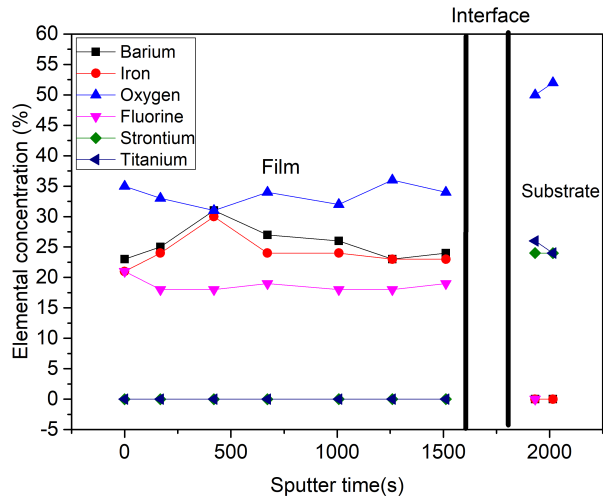


Figure 3.39.: Normalized concentration-depth profile for BFOF film corresponding to all the elements observed in XPS spectra.

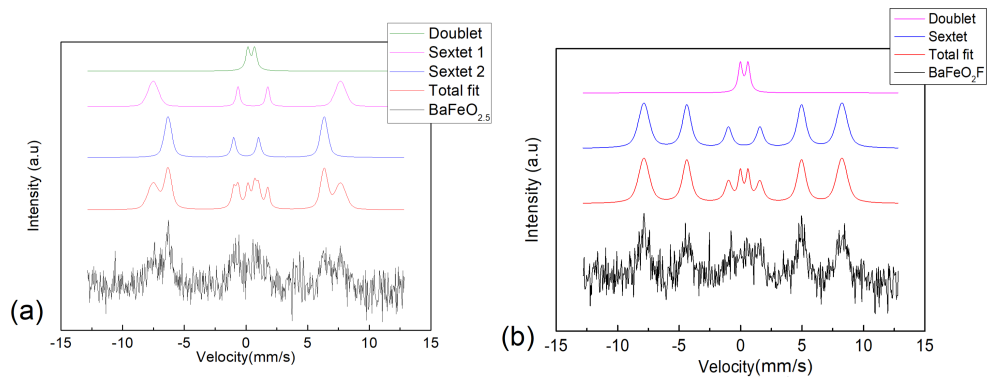


Figure 3.40.: ^{57}Fe conversion electron Mössbauer spectrum recorded from (a) BFO and (b) BFOF at room temperature.

strained film, the overall distribution of coordination polyhedra must be considered to be similar to the bulk state [117].

- (2) On fluorination of the film to BFOF, the complexity of the spectrum strongly reduces. The spectrum can then be basically fitted with one sextet and one doublet (see Tab. 3.11 and Fig. 3.40 b). All isomer shifts are indicative for iron being present in its trivalent oxidation state, in agreement with a composition following $\text{BaFe}^{+III}\text{O}_{2+x}\text{F}_{1-2x}$ ($x \sim 0$). Further, the isomer shift observed for the main sextet is indicative for octahedral environments, where the reduction compared to the octahedrally coordinated FeO_6 species in $\text{BaFeO}_{2.5}$ indicates the presence of the fluoride ions within the coordination environment, and therefore well agrees with the formation of FeO_4F_2 octahedra [161].
- (3) The presence of mainly sextet species clearly evidences magnetic ordering of films. In this respect, we observed that the intensity ratio of the individual sextet lines changed from the non-fluorinated BFO film to the fluorinated BFOF film. For BFO, magnetic anisotropy was already observed in our previous study [117], which is indicated by a change of the relative intensities of the signals of the sextets. Namely a strong decrease of the second and fifth line, which shows a alignment of the magnetic moments parallel to the gamma ray, hence in out-of-plane direction of the thin films along the c-axis of the lattice. After fluorination, the BFOF film shows a more isotropic orientation of the magnetic moments indicated by the altered relative intensities of the Mössbauer lines of the sextets towards what would be expected for a randomly oriented powder (intensity ratio of first to second to third line 4:3:1). This agrees with the absence of significant straining after fluorination and a cubic symmetry of the film and is in agreement of the literature for bulk BaFeO_2F [203]. The doublet species are commonly found for the various modifications of BaFeO_2F [161] and most likely are related to magnetically disordered regions within the films. Furthermore, the values of the observed hyperfine field splittings are high and agree with the presence of magnetically ordered high-spin Fe^{3+} at temperatures well below the magnetic ordering temperature [109].
- (4) For bulk BaFeO_2F , a random distribution of fluoride ions, forming *cis* (two fluoride ions at the same edge of the octahedron) and *trans* (two fluoride ions at opposite corners of the octahedron) was considered as the most plausible structural scenario [203]. It is difficult to determine whether more than one sextet signal is present within the BFOF film. The fact that the sextet is considerably broadened by a Gaussian distribution (width of 1.7 T) might indicate that the different crystallographic sites cannot be resolved and are thus compiled in the broad sextet.

Table 3.10.: Fitting parameters for the ^{57}Fe Mössbauer spectra for BFO.

	sextet 1 (pink, 40 %)	sextet 2 (blue, 48 %)	doublet (green, 12 %)
isomer shift (IS) (mm s^{-1})	0.43(4)	0.12(3)	0.54(5)
quadrupole splitting (QS) (mm s^{-1})	-0.49(7)	0	0.54(8)
hyperfine field (T)	47.2(4)	39.3(2)	
Lorentzian width (mm s^{-1})	0.30(11)	0.39(13)	0.4 (fixed)
Gaussian width	2.3(4)	1.2(4)	–

Table 3.11.: Fitting parameters for the ^{57}Fe Mössbauer spectra for BFOF.

	doublet (blue, 88 %)	doublet (pink, 12 %)
isomer shift (IS) (mm s^{-1})	0.35(2)	0.40(3)
quadrupole splitting (QS) (mm s^{-1})	-0.49(7)	0.62(6)
hyperfine field (T)	50.0(2)	
Lorentzian width (mm s^{-1})	0.66(11)	0.4 (fixed)
Gaussian width	1.7(4)	–

However, the small quadrupole splitting of the sextet species might indicate a nearly centrosymmetric environment, which is only the case for the trans configuration of anions within FeO_4F_2 octahedra.

3.3.3.4. Magnetic analysis

Fig. 3.41 shows the results of the magnetization measurements of the BFO and BFOF films. For both films, the measured saturation magnetic moments are below $0.015 \mu\text{B}/\text{Fe}$ at 10 K in agreement with usually observed antiferromagnetically ordered Fe^{3+} -containing perovskites [11, 33, 38, 39, 161, 203, 206, 207]. A small difference between the FC and ZFC measurements is similar to the previously reported data for bulk $\text{BaFeO}_{2.5}$ [33] and BaFeO_2F [203]. In agreement with previous discussions with respect to the magnetic hyperfine field splittings observed via Mössbauer spectroscopy [203], these results indicate a canted antiferromagnetic ordering of Fe^{3+} ions in both BFO and BFOF films with a small canting angle below 0.1° . Overall, no difference could be observed for the magnetic behaviour of the non-fluorinated BFO and the fluorinated BFOF films. Their similar low magnetic moments at low temperatures and curvature of the magnetization temperature dependence indicate that no significant change in the Fe^{3+} antiferromagnetic ordering occurs after fluorination. Thus, we cannot confirm the previously reported decrease of the Néel temperatures at higher fluorine contents (e.g. decreasing of the Néel temperatures from 750 K for LaFeO_3 to 645 K for BaFeO_2F , and even further to ~ 480 K for AgFeOF_2) [208].

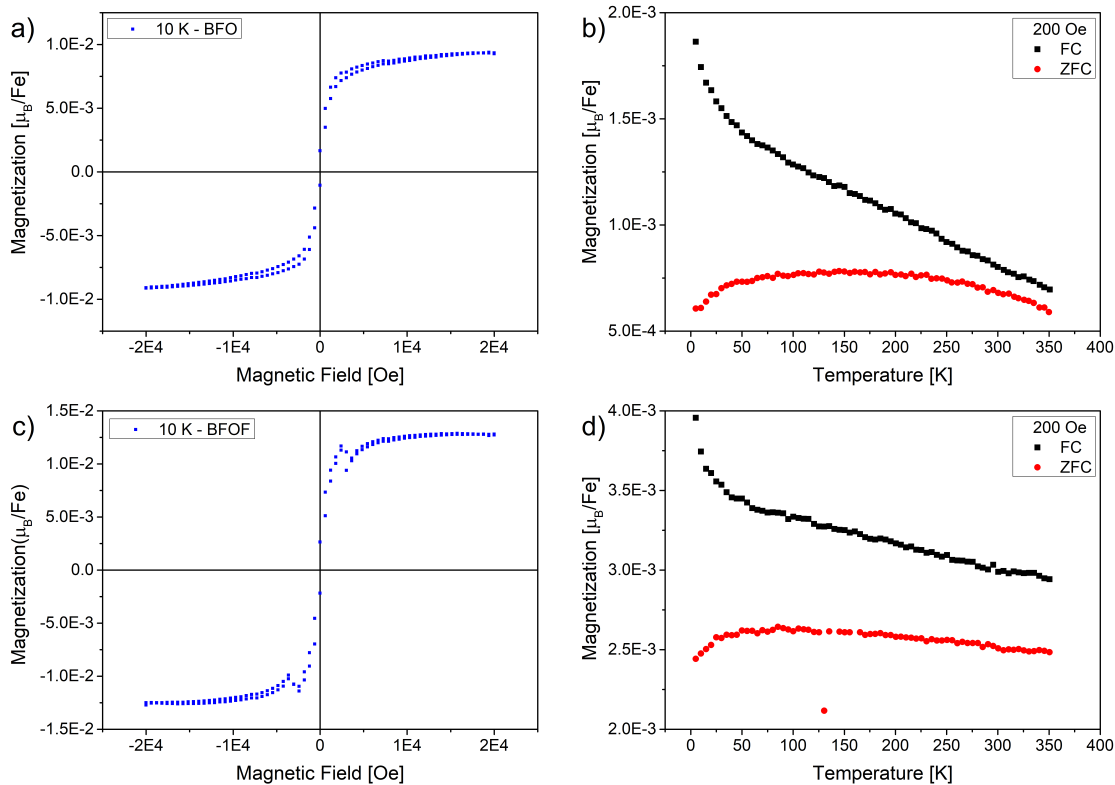


Figure 3.41.: Dependences of the magnetization from the applied magnetic field at 10 K for (a) non-fluorinated BFO and (c) drop-fluorinated BFOF films. Temperature dependence of the magnetization for (b) BFO and (d) BFOF films, measured at the applied magnetic field of 200 Oe in field-cooled (FC black) and zero-field-cooled (ZFC red) regimes. The data were corrected for the diamagnetic contribution of the SrTiO_3 substrate.

3.3.4. Conclusions

In this work we have shown that polymer based routes are efficient means in order to prepare chemically homogenous epitaxial thin films of BaFeO_2F via the low temperature topochemical fluorination of thin films of $\text{BaFeO}_{2.5}$ grown by PLD. No significant differences in film quality were found for the investigated drop-fluorination and vapour transport fluorination methods. The incorporation of fluorine results in a release of the tetragonal distortion to a cubic symmetry, which lowers the magnetic anisotropy of the film of the antiferromagnetically ordered moments. In addition, a small degree of ferromagnetic canting could be observed, similar to what is found for bulk barium ferrates [203].

In future works, our group will also focus on the preparation of strained films of BaFeO_2F by using substrates which could allow for more strict cube-on-cube growth, which could then result in additional decrease of symmetry, targeting to form novel multiferroic compounds.

3.3.5. Acknowledgments

This work was funded by the German Research Foundation, DFG, within CL551/2-1.

3.4. A kinetic study of the interdiffusion of fluorine and oxygen in the perovskite-type barium ferrate system $\text{BaFeO}_{2.5-x}\text{F}_{2x}$

Stephan Wollstadt ^{1,3}, Roger A. De Souza ², and Oliver Clemens ^{1,3,*}

¹ Fachgebiet Materialdesign durch Synthese, Institut für Materialwissenschaft, Technical University of Darmstadt, 64287 Darmstadt, Germany

² Institut für Physikalische Chemie, RWTH Aachen University, Landoltweg 2, 52056 Aachen, Germany

³ Chemische Materialsynthese, Institut für Materialwissenschaften, University of Stuttgart, 70569 Stuttgart, Germany

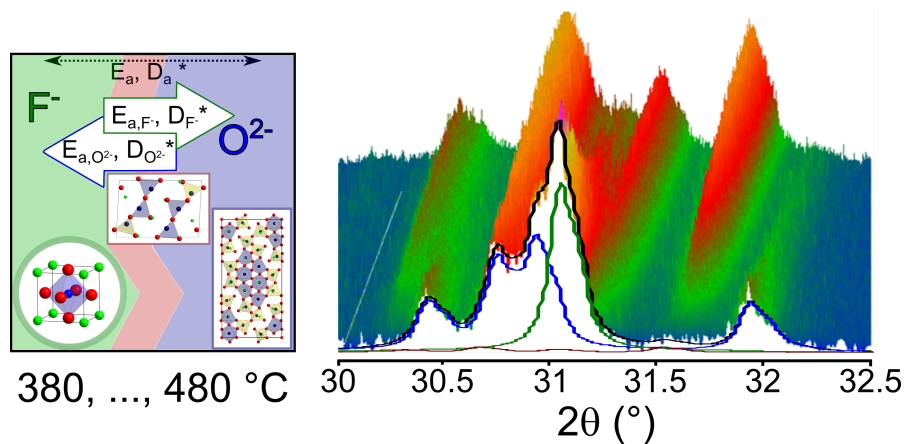
* Correspondence: oliver.clemens@imw.uni-stuttgart.de

Received: 11 November 2020; Published: 25 January 2021

Reprinted (adapted) with permission from Wollstadt, Stephan, Roger A. De Souza, and Oliver Clemens. "Kinetic Study of the Interdiffusion of Fluorine and Oxygen in the Perovskite-Type Barium Ferrate System $\text{BaFeO}_{2.5-x}\text{F}_{2x}$." *The Journal of Physical Chemistry C* 125.4 (2021): 2287-2298. Copyright 2021 American Chemical Society.

DOI: <https://doi.org/10.1021/acs.jpcc.0c10174>

Abstract Monitoring the interdiffusion of oxygen and fluorine by diffraction methods based on X-rays or neutrons is problematic because of the species' similar form factors and scattering lengths. In this study, we demonstrate through a judicious choice of system that X-ray diffraction (XRD) can be used to monitor such an interdiffusion process. Specifically, we investigated the interdiffusion process of oxide and fluoride ions in the model system $\text{BaFeO}_{2.5-x/2}\text{F}_x$, focussing on the formation of $\text{BaFeO}_{2.333}\text{F}_{0.333}$ from $\text{BaFeO}_{2.5}$ and BaFeO_2F by the exchange of two fluoride ions for one oxide ion. By virtue of their different lattice symmetries, the phases can be easily identified in isothermal, high-temperature, *in situ* XRD measurements, thus permitting the interdiffusion process to be followed. The time-dependent isothermal changes of the three phase fractions (at various temperatures between 380 °C and 480 °C) were extracted by Rietveld analysis, and these data were analysed in terms of three kinetic approaches. We show that, based on such evaluations, the activation energy for the interdiffusion reaction can be calculated assuming a first order reaction. By extracting the Johnson-Mehl-Avrami fitting parameters, the formation process of $\text{BaFeO}_{2.333}\text{F}_{0.333}$ could be further characterized, and was found to be diffusion controlled with the crystallization starting at grain boundaries. A strong temperature dependence could be shown. Employing the Boltzmann-Matano model for diffusion allowed the calculation of an average interdiffusion coefficient.

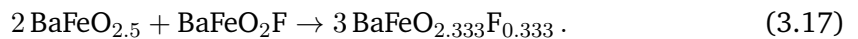


3.4.1. Introduction

Perovskite oxide materials are a possible solution for current challenges in various fields of application, also related to the rising awareness for demands of clean and green energy. Perovskite based oxyfluorides have thus gained attention in two such fields: Besides the need for extended energy-storage capabilities comparable to already well-known systems like the lithium ion battery within so-called fluoride ion batteries [209], the developing new electrode catalysts for the oxygen reduction reaction (ORR) within fuel cells is another challenging aspect [162]. For the latter application, perovskite materials in general may overcome the limits of current fuel cell systems, such as a limited power output or a high operating temperature. Solid oxide fuel cells (SOFCs) are here the system of choice. They are characterized by all-solid oxide materials, and thus require a high operating temperature ($> 800\text{ }^{\circ}\text{C}$) to guarantee a satisfying oxygen reduction reaction (ORR) and ion conduction within the compounds. This high operating temperature can in turn lead to reactions among the oxide materials decreasing their performance and lifetime. In addition, such high temperatures also require sufficient safety measures. A simple decrease in operating temperature would lead to an increase in cell polarization resistance due to the high activation energy of the ORR [5, 163]. Current SOFCs consist out of a yttria-stabilized zirconia (YSZ) electrolyte, a $\text{La}_{0.8}\text{Sr}_{0.2}\text{MnO}_3$ (LSM) perovskite cathode, and a nickel-YSZ cermet anode [7, 10, 162]. Another promising candidate for a perovskite cathode material is the system $\text{Ba}_x\text{Sr}_{1-x}\text{Co}_y\text{Fe}_{1-y}\text{O}_{3-\delta}$ (BSCF), which has shown to exhibit outstanding characteristics as a mixed ionic electronic conductor (MIEC) [8, 17, 94, 182]. It is possible to maintain a cubic symmetry with an oxygen deficiency of up to $\delta = 0.8$ [210, 211]. However, the system requires an operation temperature of $> 850\text{ }^{\circ}\text{C}$ to prevent any phase decomposition or degradation [17]. To improve the functionalities of such compounds, various doping attempts have presented promising approaches to lower the activation energy for the ORR and to increase the performance of the SOFC materials. Among them, the doping of the anion sublattice has achieved a high amount of attraction [10, 20, 99, 166]. Possible candidates for such a sublattice doping are F^- and Cl^- which reportedly increase the catalytic performance of perovskite oxides [100, 101], and it is assumed that the introduction of fluorine anions alters the electronic structure, which directly affects the surface oxygen exchange and the oxygen bulk diffusion [83, 167, 168]. However, for the synthesis and subsequent application of such oxyfluoride materials, it is important to consider that most of them are metastable and decompose at higher temperatures. Therefore, the formation of such phases, which is most often based on topochemical reactions [21] which are based on the interdiffusion of oxide and fluoride ions needs to be well understood.

Gaining such understanding poses an additional experimental challenge: the detection

and reliable estimation of the true amount of dopant inside the materials is most often not easily feasible, due to the indistinguishability of the oxide and fluoride ions within the most commonly used diffraction methods. The anions O^{2-} and F^- are equal in their electron configuration ($1s^2 2s^2 2p^6$) making it nearly impossible to distinguish between the two species by X-ray diffraction (XRD). In addition, the similar scattering lengths (5.803(4) fm and 5.654(1) fm for oxygen and fluorine, respectively [23]) and atomic form factors make them also indistinguishable by neutron diffraction [21, 22]. Therefore, suitable model systems are required to approach this interdiffusion reaction experimentally. Here, we suggest the use of vacancy-ordered $BaFeO_{2.5}$ (BFO), for which the incorporation of fluoride ions by interdiffusion leads to symmetry changes that can easily be detected by X-ray diffraction, and for which the oxyfluoride phases formed have specific compositions and crystal symmetries. BFO crystallizes in a complex oxygen-vacancy ordered monoclinic structure ($P2_1/c$). Upon fluorination, it either can form monoclinic $BaFeO_{2.333}F_{0.333}$ (BFOF33, $P2_1/m$) [12, 116] or cubic $BaFeO_2F$ (BFOF, $Pm\bar{3}m$) [203], with narrow composition dependent stability range. Since all these oxyfluorides in the Ba-Fe-O-system are metastable, their formation requires interdiffusion reactions at low temperatures in order to avoid diffusion of cations. Thus, heating above a certain transition temperature, cause BFOF and BFOF33 to decompose into their thermodynamically most stable decomposition products BaF_2 and $BaFe_2O_4$ [83], which requires a reorganisation of the cation sublattice. The aim of this study is to understand and elaborate the anion diffusion in the perovskite oxide system $BaFeO_{2.5-x/2}F_x$. Powders of the monoclinic oxide BFO and the cubic oxyfluoride BFOF were mixed in a 2:1 ratio and the time dependent phase changes were studied by in-situ X-ray diffraction. In this process, the annealing enables the interdiffusion of fluorine and oxygen between both compounds, and the formation of monoclinic $BaFeO_{2.333}F_{0.333}$ [12] according to



Since all three phases are distinguishable in X-ray diffraction, this methodology can deliver time-dependent phase fraction profiles for all phases, which then can be used for further evaluation. By this, we found that the data can be used to perform basic evaluations of kinetic parameters as well as the derivation of Johnson-Mehl-Avrami kinetic parameters [91]. Their evaluation showed that a conceptual understanding of the interdiffusion based chemical reaction can be gained by the examination of isothermal experiments via in-situ X-ray diffraction. The phase quantities and crystallite sizes obtained from XRD data enabled the revealing of underlying interdiffusion mechanisms and activation energies.

3.4.2. Experimental

3.4.2.1. Sample Preparation

BaFeO_{2.5} was prepared by mixing the stoichiometric amount of BaCO₃ and Fe₂O₃. The powder was ground in a ball mill (15 min, 300 rpm) and heated twice under air for 8 h and once under Ar for 8 h at 1100 °C with intermediate grinding steps. BaFeO₂F was prepared by mixing stoichiometric amounts of BaFeO_{2.5} with polyvinylidene fluoride (PVDF) with 4 % excess PVDF. The mixture was thoroughly ground in acetone and afterwards slowly heated (20 °C/h) in air to 375 °C (24 h dwell), to minimize the risk of BaF₂ formation [39]. The as-synthesized BaFeO_{2.5} and BaFeO₂F were then mixed in a ratio of 2:1 and ground again in acetone by using a ball mill (10 min, 300 rpm, 3 times with brakes of 20 min to avoid a warming up of the powder).

3.4.2.2. High temperature in-situ diffraction experiments

All diffraction experiments were carried out with a Bruker D8 diffractometer with Bragg-Brentano geometry and Cu anode. A PSD detector and a fixed divergence slit were used. The angular range was $20 \leq 2\theta/^\circ \leq 60$. The step size was set to 0.0075° per step with a measurement time of 0.25 seconds per step. The parameters were set in order to guarantee a satisfactory intensity output, despite the absorbing argon atmosphere, and more importantly to capture snapshots of the ongoing change in phase fractions due to the ongoing interdiffusion reaction. The temperature was controlled by using an HTK 1200 N temperature chamber with a controlling unit TCU 1000 N (Anton-Paar). Interdiffusion experiments were carried out at temperatures of 380 °C, 400 °C, 420 °C, 440 °C, 460 °C and 480 °C. Scans were carried out in a timed interval. For each scan, the obtained data was quantitatively refined using the Rietveld method with the program TOPAS 6 (Bruker AXS, Karlsruhe, Germany) [73]. Therefore, the instrumental contribution to the convolution function was extracted empirically from a set of fundamental parameters utilizing a reference scan of a LaB₆ standard (NIST 660a). The as-refined weight percentages for BaFeO_{2.5} (monoclinic, $P2_1/c$), BaFeO₂F (cubic, $Pm\bar{3}m$) and BaFeO_{2.333}F_{0.333} (monoclinic, $P2_1/m$) were used for the kinetic evaluation of the underlying diffusion process including the order of reaction and reaction rate constant k_r and extraction of the activation energy E_A , as-well as the fitting of the JMA model with fitting parameters n_{JMA} and k_{JMA} . A diffusion coefficient was estimated related to the Boltzmann-Matano method. We would like to emphasize that the estimated standard deviations (esds) reported for the phase quantities are only numerical errors from the analysis method and do not represent an interval of confidence (which is in the order of ~1-2 % for this kind of analysis).

3.4.2.3. SEM examination

The scanning electron microscopy was carried out on a Philips XL30-FEG secondary electron microscope with an acceleration voltage of 20 kV. The powder samples were sputtered with gold.

3.4.3. Results and discussion

3.4.3.1. A detailed crystallographic and chemical description of the model system

Monoclinic $\text{BaFeO}_{2.5}$ is one of the most complex perovskite-type superstructures with a large 28-fold supercell of the cubic perovskite aristotype ($P2_1/c$ $a = 6.9753(1) \text{ \AA}$, $b = 11.7281(2) \text{ \AA}$, $c = 23.4507(4) \text{ \AA}$, $\beta = 98.813(1)^\circ$, and $Z = 28$) [33]. Its complexity results from the ordering of oxygen vacancies and the tendency of Ba to maintain large coordination numbers at the same time.

$\text{BaFeO}_{2.5}$ can be fluorinated via polymer-based routes under the formation of cubic BaFeO_2F ($Pm\bar{3}m$). This phase is the fluorine-rich end-member of the series $\text{BaFeO}_{2.5-x}\text{F}_{2x}$ with $2x = 1$, which describes the substitutive fluorination of $\text{BaFeO}_{2.5}$ (under maintenance of the trivalent iron oxidation state). The symmetry relationship can be illustrated as shown in Figure 3.42, and can be used to emphasize that the Ba and Fe sublattices of both compounds are very similar, and that only the anion/vacancy sublattices undergoes the strongest relaxation.

If $\text{BaFeO}_{2.5}$ is heated with lower equivalents of PVDF, $\text{BaFeO}_{2.333}\text{F}_{0.333}$ can be formed, also a member of the aforementioned system with $2x = 0.33$. This partially fluorinated perovskite $\text{BaFeO}_{2.333}\text{F}_{0.333}$ crystallizes in the space group $P2_1/m$ ($a = 10.1059(1) \text{ \AA}$, $b = 5.7094(1) \text{ \AA}$, $c = 6.9770(1) \text{ \AA}$, $\beta = 93.107(1)^\circ$, and $Z = 6$), and this is also a subgroup structure of the aristotype $Pm\bar{3}m$ (again with maintenance of the Ba/Fe sublattices), as shown in Figure 3.43 [12].

These three phases are the only (meta)stable compositions in the system $\text{BaFeO}_{2.5-x}\text{F}_{2x}$. It was found that for $x \neq 0, 1/3, 1$, mixtures of two of the three phases are formed, which overall fluoride composition $2x$ is chosen [12].

We would like to emphasize that the symmetry tree does not necessarily describe the symmetry changes on the transformation process; since intermediate states cannot be time-resolved, it is not possible to identify a step-wise change of the anion sublattice. Hence, it is not identifiable from the tree, whether the system transforms along the branches or if it transforms through an intermediate yet unknown global (or even local) symmetry.

Due to the complexity of the unit cell, all three phases have a very characteristic reflection pattern in X-ray diffraction (see Figure 3.44). Although phase mixtures of the three phases show strongly overlapping reflections, it is therefore possible to deconvolute the phase

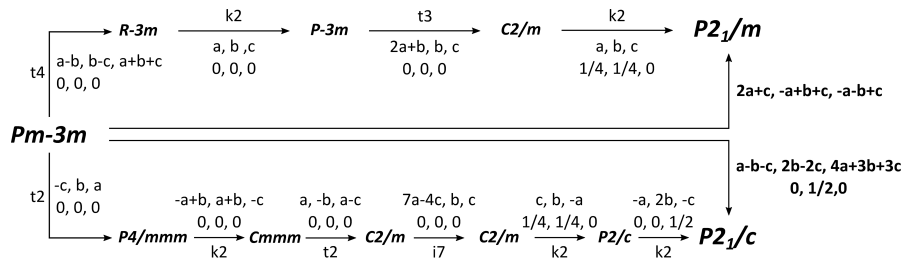


Figure 3.42.: Group-subgroup relationship of the cubic aristotype and its monoclinic derivative structures.

fraction of each phase from a Rietveld analysis under the use of reasonable constraints (demonstrated for the two (three) highest intense reflection groups, see Figure 3.45). The thermal parameters were kept the same for each atom of each phase and only small variations of the lattice parameters in comparison [12, 33, 203] were allowed; these lattice parameters were determined independently for each temperature from the measurement at $t = 0$ (for BFO and BFOF) and $t \rightarrow \infty$ (for BFOF33). The reflection width, taken into account by the crystallite size within the fundamental parameters approach chosen, was set to be identical for BFO and BFOF; this choice is justified from the fact that BFOF was prepared via a polymer based topochemical fluorination of BFO, which does not result in a change of crystal morphology and similar reflection widths (i. e., crystallite sizes). For BFOF33, an independent crystallite size parameter was used, since the width of this phase was found to strongly change on extended heating. No positional parameters of atoms were refined, and these values were fixed for the monoclinic phases $\text{BaFeO}_{2.5}$ and $\text{BaFeO}_{2.333}\text{F}_{0.333}$ to the positional parameters given in [33] and [12], respectively.

3.4.3.2. Reaction kinetic analysis

Figure 3.45 shows the start and end composition (a) as well as a changing of the main reflexes between 29° and 33° (b) for the lowest temperature of 380°C and (c) highest temperature 480°C . A quantitative Rietveld refinement of the initial pattern yields a ratio of 2:1 $\text{BaFeO}_{2.5}$ to BaFeO_2F as it would be expected from the weighing of the starting powders, see Table 3.12. As mentioned above, the conversion of BFO and BFOF into BFOF33 follows the chemical equation 3.17.

The driving force in this reaction is the concentration gradient in fluorine and oxygen concentration between BFO and BFOF. Saturation for the interdiffusion, e.g. coming to a hold, is therefore depending on steepness of the concentration gradient and the activation

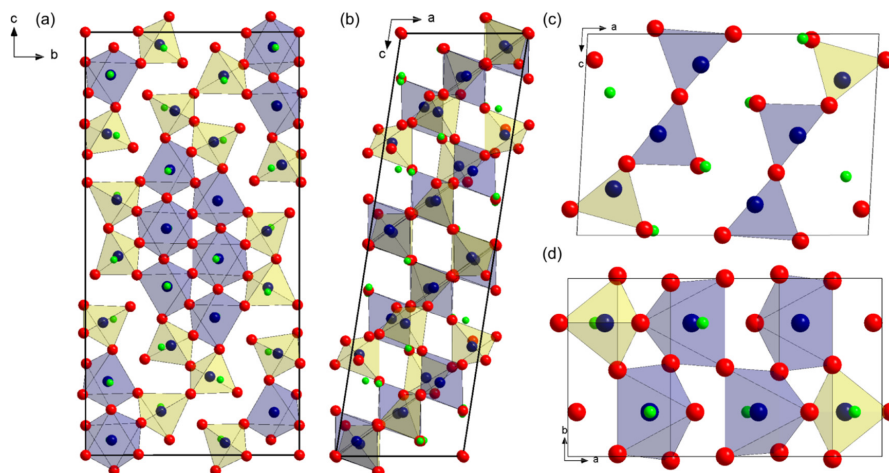


Figure 3.43.: Comparison of the coordination of iron inside the vacancy ordered structures of $\text{BaFeO}_{2.5}$ (a,b) and $\text{BaFeO}_{2.333}\text{F}_{0.333}$ (c,d). 5- and 6-fold coordinated iron atoms are surrounded by blue polyhedra, while yellow polyhedra mark tetrahedrally coordinated iron atoms. The tetrahedra form a channel-like vacancy ordering inside $\text{BaFeO}_{2.5}$.

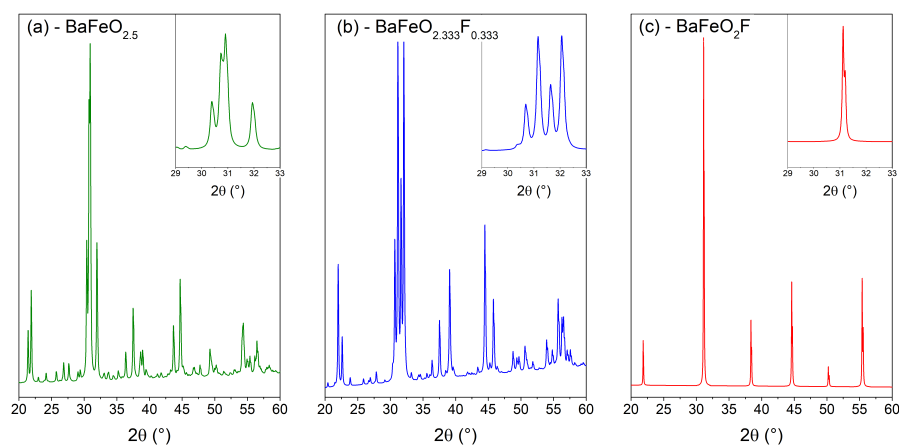
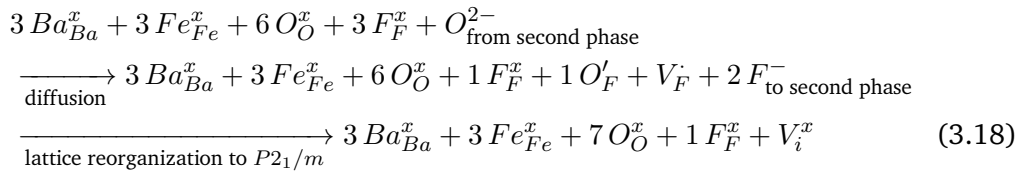
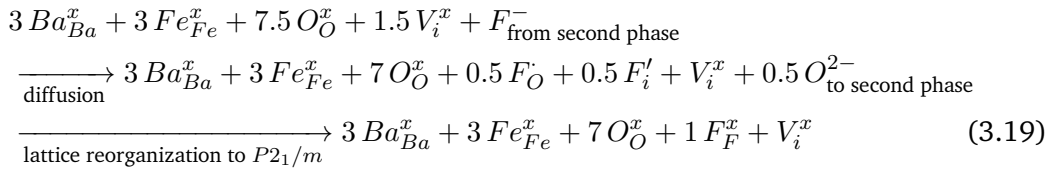


Figure 3.44.: Selected ranges of the X-ray diffraction patterns of (a) BFO, (b) BFOF33 and (c) BFOF.

energy for the interdiffusion process. To maintain charge neutrality, this interdiffusion of ions must occur simultaneously; however, at this point, it is unclear if the diffusion of fluorine or oxygen ions is rate controlling, which cannot be resolved by XRD. The performed XRD experiments mirror only the exchange of fluorine ions versus oxygen ions and vacancies from the determination of the overall amount of the respective phases. This interdiffusion reaction can be described by separating the oxygen and fluorine exchange and relaxation in the corresponding anion sublattice reaction for the starting compounds, BFO and BFOF, on the basis of previous topochemical fluorination studies [12, 21, 83, 116]: The anion sublattice of BFOF releases fluorine anions and takes up oxygen anions accompanied by the formation of interstitial vacancies and a subsequent relaxation of the lattice:



On the other hand, BFO takes up fluorine anions and releases oxygen anions, which fill up already present interstitial vacancies after the lattice has relaxed:



The above mentioned equations formalize the underlying processes according to the Kröger-Vink notation without taking into account the morphology of the sample. As explained in the beginning, the sample is a mixture of BFO and BFOF in the ratio 2:1, which means, that approximately 1 BFOF grain is surrounded by 2 BFO grains. Upon starting of the interdiffusion the ions/vacancies first have to overcome the grainboundaries; after this process and after crystallization of BFOF33 in the chemically equilibrated range, diffusion has to occur through the layer of BFOF33. By these considerations it becomes evident that first interdiffusion has to occur to result in compositional equilibration, and second BFOF33 crystallisation need to occur within the chemically equilibrated region, which then further grows into the bulk of the BFO and BFOF grains.

Upon heating the mixture, the interdiffusion starts and a refinement of the merged final four XRD patterns reveal a phase composition of 25.6(5) wt.% BFO, 13.2(7) wt.% BFOF and 61.2(7) wt.% BFOF33 after 110 h at 380 °C (see Figure 3.45 (b)). These phase

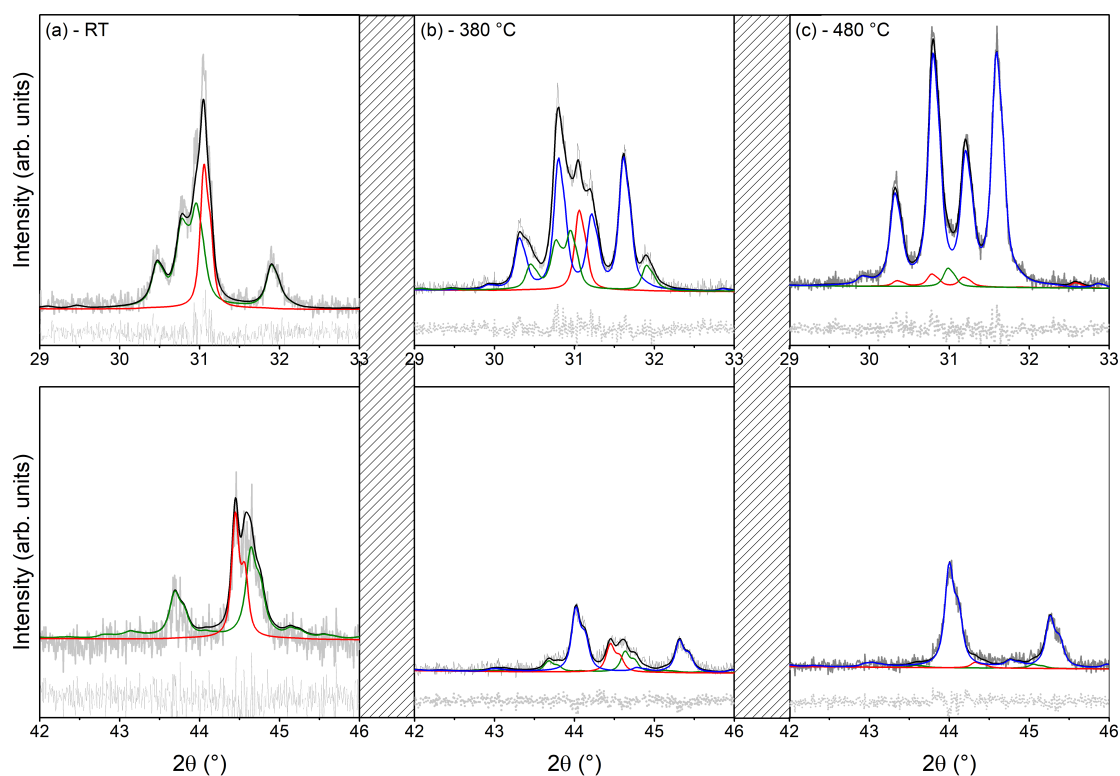


Figure 3.45.: Rietveld refinements of the mixtures at RT and at the end of the isothermal experiments at 380 °C and 480 °C with the refined phase fractions (BFO – green, BFOF – red, BFOF33 – blue) for the angular ranges 29 – 33° 2θ and 42 to 46° 2θ . The overall refinement is coloured in black. The differences are given underneath (grey dotted line). For a better signal to noise ratio, the last 4 patterns for each temperature were merged and the refined phase fractions can be found in Table 3.12.

fractions are in accordance with equation 3.17. At this temperature, the experiment does not yield a fully converted product. By increasing the temperature to 480 °C one can see a conversion to almost 100 % already after 20 h (see Figure 3.45 (c)). Therefore, these were considered as the temperature ranges to be studied to record sufficient time dependent compositions in an experimentally accessible overall reaction time. It is noteworthy, the signal to noise ratio does not allow for a precise estimation of the educt phases when their phase fraction drops below a critical value, which leads to unreliable results for the refined phase fractions. To overcome these refinement restrictions, the last four patterns of each temperature step were merged into one corresponding single pattern to increase the statistical signal. These merged patterns were then refined to estimate the final composition of the powder mixtures. The trajectories of the changes in the weight fractions for the isothermal experiments are depicted in Figure 3.46 and the final weight percentages can be found in Table 1 as well as plotted in the inset in Figure 3.47 (a). It may be noted at this point, that due to the need to find a compromise between measurement time and reaction progress, the signal to noise ratio is rather high, which results in high R_{wp} values of ~ 17 % (noise driven), with good GOF values of ~ 1.04 (signal driven). Merging the patterns reduced the R_{wp} values to ~ 8.6 % while the GOF remained around 1.05. We also would like to acknowledge that the constraints used help to avoid implausible results for the quantities of phases when their fraction turns low, which can happen without providing limits to the reflection broadening. The strong temperature dependence of the interdiffusion becomes easily evident: The diffusion process at 380 °C is rather slow compared to the fast conversion at the elevated temperature of 480 °C. Further, at low temperatures the educts are not fully reacted after a sufficient amount of time, whereas at 480 °C nearly 100 % are converted for $t = \infty$. Thus, the question arises whether the system arrives in an equilibrium state or the driving force is not strong enough to overcome the reaction barrier, namely diffusing through BFOF33 and crossing the grainboundaries. In order to be able to extract the activation energy for this process, the order of reaction has to be determined. The reduced time plot in Figure 3.47 (a) for the phase fraction of BFOF33 does not exhibit any systematic changes or deviations in dependence of the temperature and hence indicate the same mechanism for all isothermal experiments. It was found, that the interdiffusion reaction can be approximated with a first order rate law for each reaction participant i (BFO, BFOF, BFOF33):

$$-\frac{d[C_i]}{dt} = k_{r,i}[C_i] \rightarrow \ln[C_i] = -k_{r,i}t \quad (3.20)$$

Figure 3.47 (b) depicts the rate laws with fits of the linear parts. Values given are taken from the product phase BFOF33, however, the evaluation can be equally conducted from the product phases. Figure 3.47 (c) shows the corresponding Arrhenius plot for all involved

Table 3.12.: Weight percentages of the quantitative Rietveld analysis of the isothermal experiments at RT and for the merged final four measurements.

T (°C)	RT	380	400	420	440	460	480
t_{end} (h)		110	98	73	62	25	24
BFO (wt.%)	64.8(1)	25.6(5)	12.1(4)	8.2(4)	6.2(5)	4.1(4)	5.0(4)
BFOF (wt.%)	35.2(1)	13.2(7)	6.4(6)	3.7(6)	2.7(7)	3.5(6)	2.5(2)
BFOF33 (wt.%)		61.2(7)	81.5(7)	88.1(8)	91.1(9)	92.4(7)	92.5(5)

Table 3.13.: Johnson-Mehl-Avrami kinetic from fitting the model on the recorded XRD data of BFOF33.

T (°C)	380	400	420	440	460	480
n_{JMA}	0.93 ± 0.01	0.83 ± 0.01	0.76 ± 0.01	0.74 ± 0.01	0.61 ± 0.01	0.59 ± 0.02
k_{JMA}	$(6.39 \pm 0.55) \cdot 10^{-5}$	$(4.08 \pm 0.48) \cdot 10^{-5}$	$(2.14 \pm 0.24) \cdot 10^{-4}$	$(3.62 \pm 0.59) \cdot 10^{-4}$	$(2.03 \pm 0.22) \cdot 10^{-3}$	$(4.13 \pm 0.88) \cdot 10^{-3}$

compounds with the corrected values for the kinetic parameter k_r calculated from the fitting parameter in Figure 3.47 (b). The correction is made according to the reaction equation (1). It is apparent that the calculated values are in a good agreement with each other. The calculated activation energies E_a for the depletion reactions for BFO and BFOF and the formation of BFOF33 are $E_{a,\text{BFO}} = 0.48(1)$ eV, $E_{a,\text{BFOF}} = 0.50(2)$ eV and $E_{a,\text{BFOF33}} = 0.47(1)$ eV, respectively. In addition, the linear thermal expansion coefficients were calculated for the temperature range between 380 – 480 °C from the temperature dependence of the cubic (pseudocubic) lattice parameters to be $(7.09 \pm 0.7) \cdot 10^{-5} K^{-1}$, $(8.37 \pm 0.58) \cdot 10^{-5} K^{-1}$ and $(7.42 \pm 0.86) \cdot 10^{-5} K^{-1}$ for BFO, BFOF and BFOF33, respectively, showing that the structural distortions and anion compositions do not have a strong impact on the expansion behaviour of barium ferrates in general.

3.4.3.3. JMA Modell analysis

Phase formation can also be described with other models. Therefore, we found that the obtained phase fraction data of the BFOF33 phase can be well fitted with a Johnson-Mehl-Avrami (JMA) model [91, 92]:

$$\gamma(t) = (1 - e^{k_{\text{JMA}} t^{n_{\text{JMA}}}}) \quad (3.21)$$

With $\gamma(t)$ being the phase fraction percentage of BFOF33 at time t , n_{JMA} the Avrami exponent and k_{JMA} the rate constant of formation. Figure 3.48 (a) – (f) shows the trajectories of each weight percentages of BFOF33 with the corresponding JMA model fits. The fit parameters are given in Table 3.13, showing a strong temperature dependency. The Avrami exponent n_{JMA} can be interpreted as a descriptor for the underlying crystal

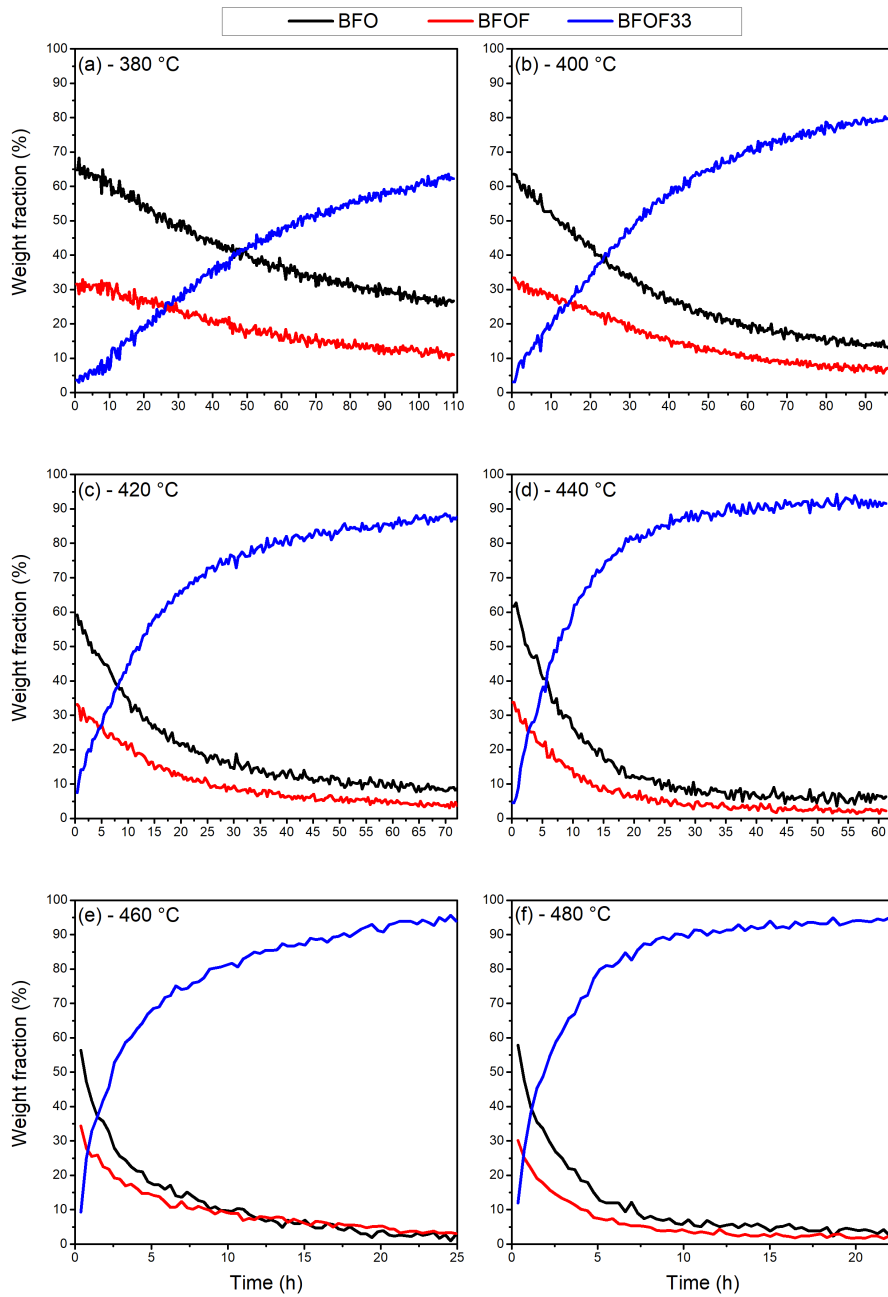


Figure 3.46.: Phase fractions over time upon heating at the different temperatures from 380 °C to 480 °C, (a) – (f).

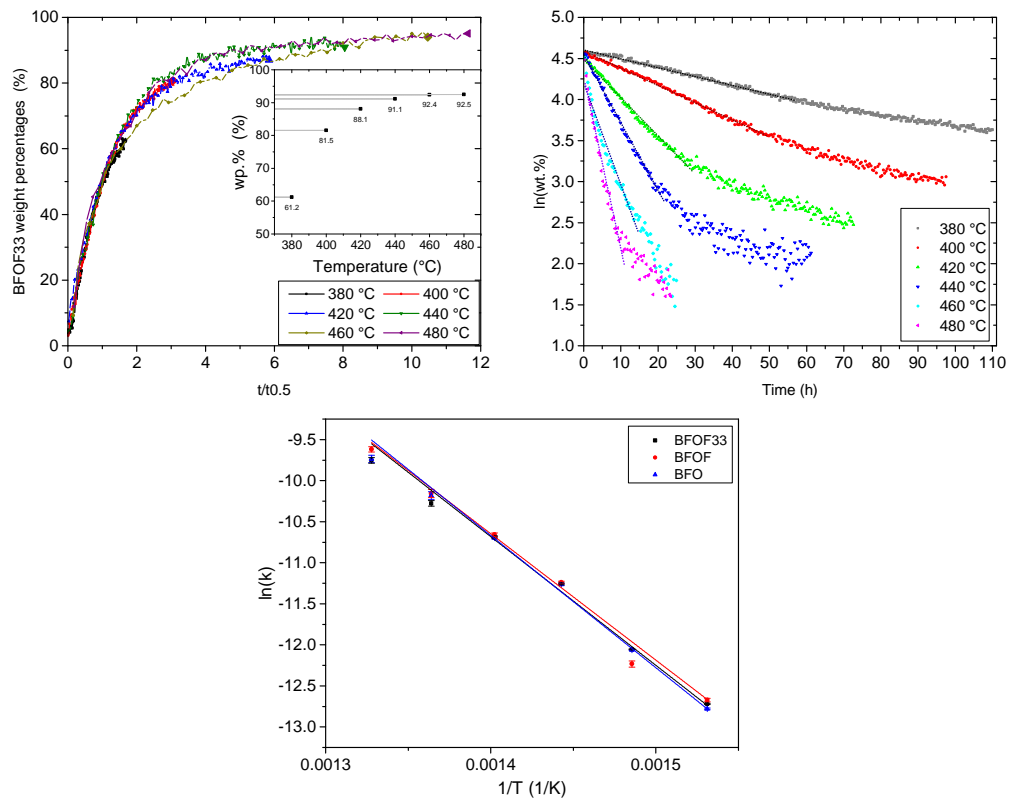


Figure 3.47.: (a) reduced time plot for the extracted weight percentages of BFOF33 (inset: depiction of the maximum phase fractions over corresponding temperature); (b) linearization of the reaction constant k for first order reaction mechanism for the formation of BFOF33 with corresponding fits (dotted lines); (c) linearized Arrhenius plot of $k(T)$ with corresponding fit (dotted line).

growth process. In literature, a value of $n_{\text{JMA}} = 0.5$ to $n_{\text{JMA}} = 1.5$ was ascribed to a diffusion controlled transformation mechanism, where $n_{\text{JMA}} = 1.5$ describes a slow diffusion process, where the transformation process takes much longer, compared to $n_{\text{JMA}} = 0.5$, which can be found for a fast diffusion resulting in a shorter time needed for the transformation [212]. In addition, a value of $n_{\text{JMA}} = 1$ can also be attributed to a grain boundary nucleation [213]. The underlying diffusion transformation reaction starts at a grain boundary, but the succeeding crystallization processes of BFOF33 in the bulk of either educt phases is penetrating further into the bulk material. The time dependency of this crystallization and formation process is obvious by comparing the plots in Figure 3.46. In addition to the phase fraction evolutions of the observed phases, the volume weighted crystallite sizes $L_{\text{Vol-IB}}$ of BFOF33 were extracted during the Rietveld refinements, plotted in Figure 3.48, blue curves. Apparently the crystallite growth is strongly depending on the temperature, but also limited to a value of around 80 to 90 nm, which is similar to the crystallite size of the initial phases. From this it follows that no recrystallization is occurring besides the exchange of oxygen and fluorine anions in the anionic sub lattice. In addition, the data also supports the assumption that for lower temperatures the diffusion path of the anions may be mainly along the grain boundaries separating the crystallites inside the particles and leading to many slowly growing nucleation sites. While for high temperatures, the diffusion can instantly occur into the bulk material. This is in well agreement with other interpretations for the values of n_{JMA} in literature, i.e. a value of $n_{\text{JMA}} \approx 1$ supports the diffusion and crystallization alongside the grain boundaries inside the particles, while approaching a value of $n_{\text{JMA}} \approx 0.5$ represents the diffusion and a more rapid crystallization into the crystallite bulk material [214].

3.4.3.4. Diffusion and SEM analysis

Based on the assumptions made concerning the reaction equation and kinetics, the analysis can be extended and the data can be used to calculate an average interdiffusion coefficient. The considerations are related to the Boltzmann-Matano method and an approach based on the root-mean-square penetration depth. In the following the work of Dayananda [52] will be outlined and introduced into this work. The formulated interdiffusion equations show, that the underlying phase formation depends on the diffusion of the anions O^{2-} and F^- . From this it follows, that the diffusing particles have to cross the grain boundary and the BFOF33 phase, formed later during the process, in both directions which results in the growth of the BFOF33 phase. It was already shown in the XRD and JMA analysis that the BFOF33 phase forms along the grain boundary and grows into the grains. This allows the introduction of the basic idea to treat the grain boundary as the Matano plane and use the penetration depth to the left and right to calculate the (inter)diffusion coefficient.

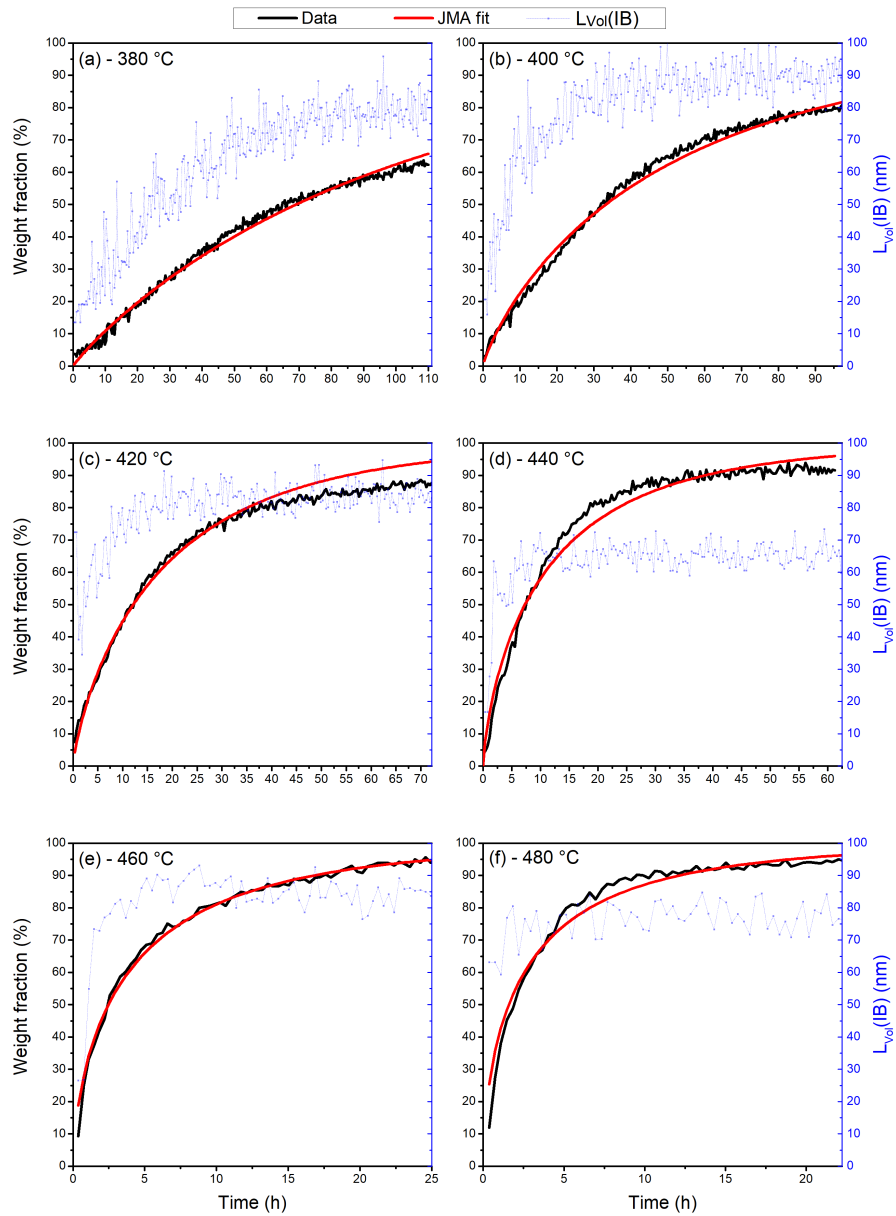


Figure 3.48.: Fitting of JMA model (red) on XRD data (black) combined with the corresponding crystallite volume (blue) of BFOF33 phase for 380 – 480 °C, (a) – (f). The crystallite size is described as the volume weighted average column length from the integral width of the reflections $L_{Vol}(IB)$.

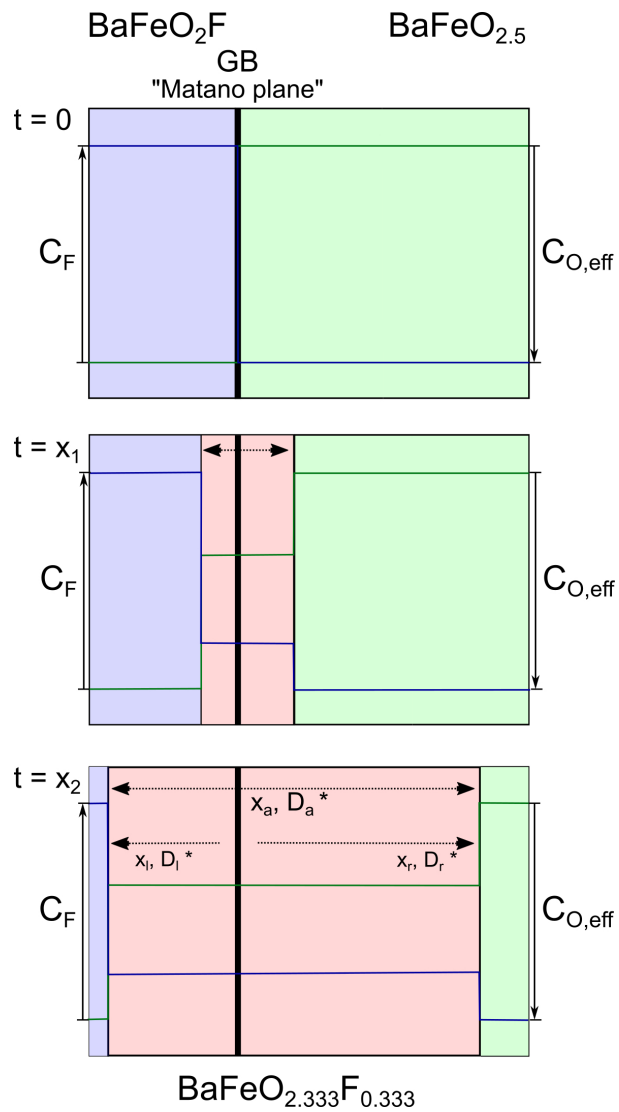


Figure 3.49.: Schematic diffusion process during an isothermal experiment at different times. The concentration profiles of fluorine and oxygen are coloured in red and green, respectively.

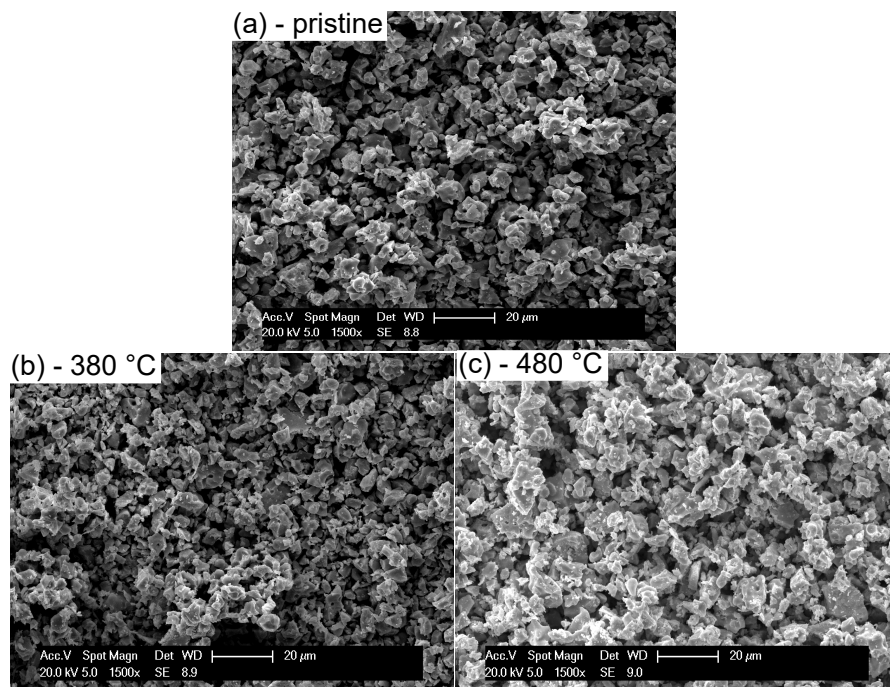


Figure 3.50.: SEM micrographs of (a) pristine powder and (b,c) powder after the isothermal interdiffusion experiment at temperatures of 380 and 480 °C, respectively.

Figure 3.49 depicts the interdiffusion schematically based on the findings of the XRD and JMA evaluations. The Boltzmann-Matano method requires the knowledge of the concentration profile inside the diffusion pair over the diffusion range x_i from the Matano plane at position x_0 after the reaction time t . From this, the interdiffusion coefficients and for the left and right hand side of the Matano plane and the average effective interdiffusion coefficient can be calculated by

$$\tilde{D}_{i,R} = \frac{\int_{C_i^+}^{C_i^0} (x - x_0)^2 dC_i}{2t[C_i^0 - C_i^+]} \quad (3.22)$$

$$\tilde{D}_{i,L} = \frac{\int_{C_i^0}^{C_i^-} (x - x_0)^2 dC_i}{2t[C_i^- - C_i^0]} \quad (3.23)$$

$$\tilde{D}_{i,C} = \frac{\int_{C_i^+}^{C_i^-} (x - x_0)^2 dC_i}{2t[C_i^- - C_i^+]} \quad (3.24)$$

respectively, where C_i^- and C_i^+ correspond to the concentration on the left and right hand side and C_i^0 equals the concentration at the Matano plane. By expressing the integrals for the left and right hand side through the mean squared distance from the Matano plane $\overline{(x - x_0)_{i,L}^2}$ and $\overline{(x - x_0)_{i,R}^2}$, the root mean-squared penetration depths $x_{i,L}$, $x_{i,R}$ and $x_{i,C}$ can be evaluated:

$$x_{i,R} = \sqrt{2\tilde{D}_{i,R}t} \quad (3.25)$$

$$x_{i,L} = \sqrt{2\tilde{D}_{i,L}t} \quad (3.26)$$

$$x_{i,C} = \sqrt{2\tilde{D}_{i,C}t} \quad (3.27)$$

The process represented here is strongly simplified by means of geometry and morphology, considering the complex morphology of the starting powders observed in the SEM micrographs in Figure 3.50. The true grain morphology is quite more irregular, which would lead to a much more complex distribution of diffusion paths. Hence, the assumptions made in the following can be seen as a basic consideration towards a simple way to estimate the interdiffusion coefficient of the present diffusion pair. The XRD evaluation revealed, that the system contains only three different phases (BFO, BFOF, BFOF33) while those are highly sensitive towards the fluorine content, e.g. that no intermediate phases occur. From this it follows, that the concentration profile during the growths of the BFOF33 phase inside the grains is comparable to a step function as shown in Figure 3.49. The

concentrations of the diffusing anions $c(F^-)$ and $c(O_{eff}^{2-})$ are then either 1, 0.333 or 0 and 1, 0.666 or 0 (note, that for sake of simplicity the concentration of O^{2-} is limited to the effective stoichiometric amount taking part in the reaction, namely 0.5). Further, it is unlikely for BFOF33 to form somewhere inside the grains beside the diffusion front. In addition, the relative weight fractions obtained from XRD evaluations strongly support the stoichiometric relation of BFOF and BFO is in the ratio of 1:2. For further discussion, it is reasonable to transform the collected weight percentage data into volume percentage data. The densities of the phases are 5.624 g/cm³, 5.975 g/cm³ and 5.745 g/cm³ for BFO, BFOF and BFOF33, respectively. Due to the minor differences between the densities, this transformation yields curves similar to the original data, but with the correct unit. The volume percentage of the BFOF33 phase can be associated with an average lateral penetration depth related to the grain size $L_{particle}$ and hence, can be connected to the above introduced mean squared penetration depth:

$$x_{BFOF33/C} = C_{V,BFOF33} \cdot L_{particle} = \sqrt{2\tilde{D}_{BFOF33/C}t} \quad (3.28)$$

$$x_{BFOF33/BFO} = 2/3 \cdot C_{V,BFOF33} \cdot L_{particle} = \sqrt{2\tilde{D}_{BFOF33/BFO}t} \quad (3.29)$$

$$x_{BFOF33/BFOF} = 1/3 \cdot C_{V,BFOF33} \cdot L_{particle} = \sqrt{2\tilde{D}_{BFOF33/BFOF}t} \quad (3.30)$$

SEM investigations before and after the isothermal experiments do not give any indication for significant particle growth or change in particle morphology. Therefore, by extracting the grain crystallite size from the SEM micrographs shown in Figure 3.50, one gets an estimated grain size $L_{particle}$ of 6.5 μm. Plotting equation 3.27 as a squared function, the interdiffusion coefficient $\tilde{D}_{BFOF33/C}$ can be extracted. Figure 3.51 (a) depicts the squared penetration depths for each isothermal experiment together with the linear fits for the extraction of the diffusion coefficients which are listed in Table 3.14. The fitting was performed in the linear regime of the curves, where the interdiffusion processes are only depending on the thermal activation. The extracted average interdiffusion coefficients $\tilde{D}_{BFOF33/C}$ for each temperature exhibit an Arrhenius type behaviour, presented in Figure 3.51 (b). The extraction of anion specific interdiffusion coefficients $\tilde{D}_{BFOF33/i}$ was not performed, due to the fact, that the interdiffusion process requires the uniform exchange of both species, thus it is limited by the slowest diffusing anion. Hence, a separate evaluation following equation 3.29 and 3.30 would not yield reliable values. The evaluation of the activation energy resulted in a value of $E_{a,\tilde{D}} = 0.46(2)$ eV, which is similar to the activation energy found for the reaction rate constant k_r (0.47 eV). The interdiffusion process of oxide and fluoride ions will be governed by the migration of the slower moving species. Examination of the literature [215, 216] indicates that activation

Table 3.14.: Average interdiffusion coefficients extracted from the squared penetration depth plots.

T (°C)	380	400	420	440	460	480
$\bar{D}_{\text{BFOF33/C}}$ ($10^{-13}\text{cm}^2/\text{s}$)	2.82 ± 0.03	5.45 ± 0.05	13.51 ± 0.14	21.72 ± 0.03	32.94 ± 0.16	60.05 ± 0.28

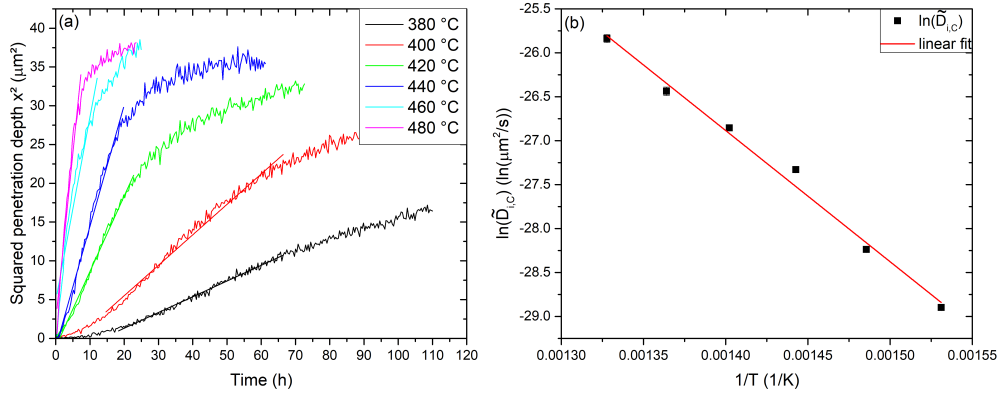


Figure 3.51.: (a) Penetration depth over time based on equation 3.30 with linear fits to extract the diffusion coefficient; (b) Arrhenius plot of the extracted diffusion coefficients.

enthalpies for oxide-ion migration in oxide perovskites are 0.5 – 1.5 eV, whereas for halide-ion migration in halide perovskites they are 0.25 – 0.54 eV. Our value lies at the border between the two, so the consideration of the activation enthalpy alone does not provide an answer. We expect, however, that the lower activation enthalpies for the singly charged ions will give rise to higher mobilities, and we thus tentatively conclude that the interdiffusion process is governed by the migration of the slower, doubly charged oxide ions.

3.4.4. Conclusion

The interdiffusion reaction between BFO and BFOF was studied using isothermal high temperature *in situ* XRD experiments. It was possible to extract the relative weight fractions of the participating phases during the interdiffusion reaction in a satisfying quality. Hence, the refined phase fractions allowed an extensive evaluation of underlying kinetic processes. The calculation of an average activation energy assuming a first order reaction was performed and found to be $E_{a,\text{BFOF33}} = 0.47(1)$ eV.

By fitting the JMA model to the experimental data, the formation kinetics of the diffusion process supported the assumption of diffusion controlled process with grain boundaries serving as crystallization sites with growth direction into the bulk material of the grains. These findings were in agreement with the results of the crystallite sizes calculated by the performed Rietveld refinements. The application of the Boltzmann-Matano method onto the present data, allowed the calculation of an average interdiffusion coefficient. By assuming step-like concentration profiles for the diffusing oxygen and fluorine anions, which was supported by the results of the JMA analysis, the derived function of the root mean-squared penetration depth could be applied. SEM micrographs indicate no significant particle growth or change in morphology during the isothermal experiments. Thus, the diffusion length, which was chosen to be the equivalent to the mean grain size, remained constant and the interdiffusion solely comprises the exchange of oxygen, fluorine and vacancies. The found average interdiffusion coefficients followed an Arrhenius-like behaviour allowing the extraction of an activation energy, $E_{a,\tilde{D}} = 0.46(2)$ eV.

The activation energies extracted for the phase formation and interdiffusion suggest the oxygen ions to be the rate limiting species in this interdiffusion reaction. The precision of the experiments and thus of the performed analysis can be enhanced by improving the experimental setup. The increase of measurement speed and the lowering of the signal to noise ratio of the diffractometer by using synchrotron based techniques would lead to more accurate Rietveld refinements. However, we show that for suitable model systems, such kinetic parameters can also be well extracted with laboratory based techniques. Therefore, this article sheds light on the interdiffusion process of anions, which normally can be hardly determined by simple diffraction techniques. The new methodology presented in this work might also be applicable to other material systems, with stoichiometric and structurally precise intermediate compounds. This would allow for a better understanding of the underlying processes or it could support findings of additional experiments.

3.4.5. Acknowledgments

This work was funded by the German Research Foundation (DFG) within the project CL551/2-1.

3.5. Supplemental and additional topics

This section contains pursuing topics which represent follow-up studies rounding up the findings reported within the publications. Thereby, the focus will lie on questions arising from the presented work. In order to give an answer or at least an educated guess to these questions, it is necessary to combine the key findings of the included publications.

3.5.1. Phases inside the system Ba-Fe-O-F

The presented work is motivated and based on the very important fact, that the oxyfluorides $\text{BaFeO}_{2.5-x}\text{F}_{2x}$ adopt either the monoclinic $P2_1/m$ or the cubic $Pm\bar{3}m$ configuration upon fluorination at a temperature of 450 °C. In contrast, hexagonal and trigonal configurations inside the system Ba-Fe-O-F can be formed through direct synthesis with BaO_2 , Fe_2O_3 and BaF_2 as precursors, or topochemical fluorination of hexagonal/trigonal oxides, such as 6H- $\text{BaFeO}_{3-\delta}$ and 15R- $\text{BaFeO}_{3-\delta}$. They will be left out during this discussion and the reader is kindly referred to literature, e.g. the work by Sturza et al. [180, 217, 218]. Any deviations from the exact stoichiometry is resolved by the formation of a phase mixture as presented in [12]. Upon fluorination, the system Ba-Fe-O-F adopts either the monoclinic $P2_1/m$ structure with the composition $\text{BaFeO}_{2.333}\text{F}_{0.333}$ or the cubic structure $Pm\bar{3}m$ with the composition BaFeO_2F . Depending on the fluorine stoichiometry $\text{BaFeO}_{2.5-x/2}\text{F}_x$, the system is either a mixture of $\text{BaFeO}_{2.5}/\text{BaFeO}_{2.333}\text{F}_{0.333}$ for $0 < x < 0.333$ or $\text{BaFeO}_{2.333}\text{F}_{0.333}$ and BaFeO_2F for $0.333 < x < 1$. The interdiffusion study in Sec. 3.4 and also the electrochemical experiments in Sec. 3.2 take advantage from this well defined composition of different compounds. Especially in Sec. 3.4 it was shown, that no intermediate phase is formed during the isothermal interdiffusion experiment.

Besides fluorination, as presented in literature and also highlighted in Sec. 3.1, the system is susceptible towards oxidation with stoichiometries between $2.5 < x < 3$. These oxidized structures can be isotypical to the metastable fluorinated phases. At this point it may be noted, that the synthesis conditions for the topochemical fluorination are much more simpler compared to the topochemical oxidation, which require precise tuning of temperature and oxygen partial pressure or the use of ozone [34]. On the other hand, the oxyfluoride compounds are metastable at room temperature and decompose at elevated temperature as presented in Sec. 3.2, Fig. 3.23 and 3.24. They are also resistant towards further oxidation [175]. $\text{BaFeO}_{2.333}\text{F}_{0.333}$ would offer oxygen vacancies, but is resistant against oxidation (see Sec. 3.2 and Sec. 3.5.4). Another important fact is, that the topochemical fluorination is purely substitutional, thus, the iron cation maintains a valence state of 3+, while the oxidation leads to a mixed valency of 3+ and 4+, eventually to almost purely 4+ in case of BaFeO_3 .

As a base for the further discussion, the cell volume of $\text{BaFeO}_{2.5}$, which is used as the educt phase for subsequent topochemical reactions, is suitable. This phase has the biggest volume per formula unit compared to the product phases. Tab. 3.15 lists the volume per formula unit for a selected range of compounds which are part of the work, except BaFeO_3 . Space groups are also given for comparison. First, it is obvious, that the system tends to reduce its volume with increasing anion content together with an increase in symmetry. Second, the oxidation leads to much smaller volumes ($\Delta = 5.1\text{\AA}^3$ (7.5%)) compared to the oxyfluoride phases ($\Delta = 0.9\text{\AA}^3$ (1.3%)). The occupation of vacancies and the breaking of the vacancy ordering leads to the volume decrease. But, as shown in Tab. 3.15, this is not equally true for oxides and oxyfluorides. The important role plays the ionic radius of each participating ion inside the compounds (the size of Ba remains equal in all cases and is thus neglected). The anion O^{2-} (140 pm) is bigger than F^- (133 pm), and the cation Fe^{4+} (58.5 pm) is much smaller than Fe^{3+} (65.5 pm), both in high spin state [219]. One might assume, that Fe^{4+} , due to its electronic configuration of $t_{2g}^3 e_g^1$ in high spin state, is responsible for an additional change in volume due to its Jahn-Teller activity and the subsequent distortion of the coordination polyhedra around it. In contrast, Fe^{3+} exhibits an electronic configuration of $t_{2g}^3 e_g^2$ and is thus not Jahn-Teller active. Surprisingly, BaFeO_3 does not show any Jahn-Teller distortion [34, 134, 220], which would result in a symmetry decrease, and prefers to remain perfectly cubic.

From this, it follows, that $\text{BaFeO}_{2.5}$ is able to be oxidized by the introduction of further oxygen, and thus, the increase of Fe^{4+} leads to a strong volume decrease, together with the occupation of oxygen vacancies. In contrast, $\text{BaFeO}_{2.333}\text{F}_{0.333}$ and BaFeO_2F cannot be further oxidized by the introduction of fluorine (or oxygen) and the iron cation maintains a valency of 3+ (see also Sec. 3.5.4 below). This points towards a higher redox potential for Fe^{4+} inside oxyfluorides, compared to the pure oxides, where $\text{BaFeO}_{2.5}$ can be oxidized. However, as seen in Fig. 3.7 a,c, the system is strongly governed by the ordering of its anion vacancies. Fig. 3.7 a,c emphasizes the conditions at which the vacancy ordered $\text{BaFeO}_{2.667}$ is stable. Though both structures are vacancy ordered, $\text{BaFeO}_{2.5}$ exhibits the lower symmetry and the much more complex unit cell. This vacancy ordering seems to be overcome, if enough activation energy is offered to take up oxygen to adopt the $P2_1/m$ ($\text{BaFeO}_{2.667}$) and $P6_3/mmc$ ($\text{BaFeO}_{2.65}$ or $\text{BaFeO}_{2.67}$) symmetry. During this oxygen uptake, the unit cell volume is reduced and Fe^{3+} becomes oxidized to Fe^{4+} which possesses a smaller ionic radius and is Jahn-Teller active. A possible Jahn-Teller distortion leads to an additional reduction of lattice enthalpy additionally to the volume reduction and symmetry increase. However, both structures become reduced to $\text{BaFeO}_{2.5}$ and adopt either again the monoclinic $P2_1/c$ structure or the cubic $Pm\bar{3}m$. Fig. 3.7 e indicates the temperature dependency since an almost linear thermal expansion relation can be seen

Table 3.15.: Unit cell volume per formula unit V_Z and space groups (SG) for selected topochemically modified phases inside the systems Ba-Fe-O and Ba-Fe-O-F.

System	Ba-Fe-O				Ba-Fe-O-F	
Phase	BaFeO _{2.5}	BaFeO _{2.667}	BaFeO _{2.82}	BaFeO ₃ [34]	BaFeO _{2.333} F _{0.333}	BaFeO ₂ F
V_Z (Å ³)	67.7	66.0	63.5	62.6	67.1	66.8
SG	$P2_1/c$	$P2_1/m$	$P4/mmm$	$Pm\bar{3}m$	$P2_1/m$	$Pm\bar{3}m$

between the $P2_1/c$ and $Pm\bar{3}m$ structure. Hence, this vacancy ordering may be broken either by a high oxygen partial pressure or by high temperature/thermal expansion which relieves the vacancy ordering. From this the conclusion may be drawn that in case of oxyfluorides the vacancy ordering is responsible for the only three stable configurations BaFeO_{2.5}F₀, BaFeO_{2.333}F_{0.333} and BaFeO₂F₁ for $x = 0, 0.333, 1$.

3.5.2. Group-subgroup relations of the structural changes observed by topochemical reactions

The cubic perovskite, which is the aristotype of the modifications described in this thesis, has the space group $Pm\bar{3}m$. This structure is either adopted if the anion sublattice is (nearly) fully occupied as in case of BaFeO_{3- δ} or if the oxygen vacancy ordering inside BaFeO_{2.5} is broken at high temperatures. By introducing fluorine into the system, the fully fluorinated BaFeO₂F can be added to the list. The work presented in Sec. 3.4 is based on the group-subgroup relations between the participating space groups $P2_1/c$ (BaFeO_{2.5}), $P2_1/m$ (BaFeO_{2.333}F_{0.333}) and $Pm\bar{3}m$ (BaFeO₂F). Also the newly found modification of BaFeO_{2.667} presented in Sec. 3.1 crystallizes in the space group $P2_1/m$ and is isotypic to BaFeO_{2.333}F_{0.333}. By further oxidizing this modification by slow cooling under an oxygen atmosphere, the compound can be described by the tetragonal space group $P4/mmm$ and a composition of BaFeO_{2.81} may be assigned. Thus, for topochemical oxidation, the phase formation upon heating could be reformulated as $P4/mmm \rightarrow P2_1/m \rightarrow P2_1/c$. Seemingly these transitions between the space groups are governed by the formation of oxygen vacancy ordering and corresponding changes of the symmetry. Figure 3.53 and 3.54 show the vacancy ordering (pink connections) inside both monoclinic structures. The symmetry relations between the compositions BaFeO_{2.5} ($P2_1/c$) [33] and BaFeO_{2.333}F_{0.333}/BaFeO_{2.667} ($P2_1/m$) [12] and the aristotype BaFeO₂F ($Pm\bar{3}m$) are well-described (see also Fig. 3.42). The transition from $P2_1/m$ to $P4/mmm$ may be taken as a cause for a deeper discussion, since $P4/mmm$ can be found in the above mentioned group-subgroup relations on the branch for $P2_1/c$. $P4/mmm$ can also be found on a branch leading to $P2_1/m$. Fig. 3.52 sketches these symmetry relations. However, BaFeO_{2.5}

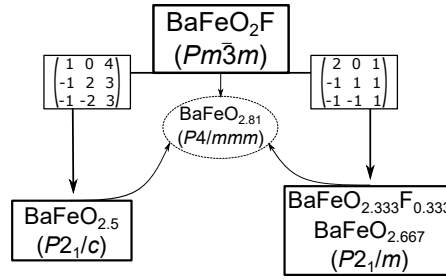


Figure 3.52.: Shortened symmetry tree for the cubic aristotype $Pm\bar{3}m$ and the monoclinic subgroups $P2_1/c$ and $P2_1/m$ with the corresponding transformation matrices and with $P4/mmm$ indicated as a possible route for the transition between both monoclinic phases.

($P2_1/c$) cannot be described as a subgroup of $\text{BaFeO}_{2.333}\text{F}_{0.333}/\text{BaFeO}_{2.667}$ ($P2_1/m$) due to different translational symmetry. This becomes clear by comparing the transformation matrices for each structure:

- $\text{BaFeO}_{2.5}$ ($P2_1/c$): $\begin{pmatrix} 1 & 0 & 4 & 0 \\ -1 & 2 & 3 & 1/2 \\ -1 & -2 & 3 & 0 \end{pmatrix}$; $\sqrt{3}|a_{cubic}|$, $\sqrt{8}|a_{cubic}|$, $\sqrt{34}|a_{cubic}|$
- $\text{BaFeO}_{2.333}\text{F}_{0.333}/\text{BaFeO}_{2.667}$ ($P2_1/m$): $\begin{pmatrix} 2 & 0 & 1 \\ -1 & 1 & 1 \\ -1 & -1 & 1 \end{pmatrix}$; $\sqrt{6}|a_{cubic}|$, $\sqrt{2}|a_{cubic}|$, $\sqrt{3}|a_{cubic}|$

The monoclinic distortion cannot occur perpendicular to the room diagonal lattice vector of the cubic aristotype, since the threefold symmetry along this axis in $Pm\bar{3}m$ can not be reduced to the twofold symmetry element along the monoclinic axis in either $P2_1/c$ or $P2_1/m$. In addition, as discussed in Sec. 3.1, the monoclinic axes a and c lie along different directions with respect to the aristotype structure.

Figure 3.53 and 3.54 depict the anion ordering inside $\text{BaFeO}_{2.5}$ [33] and $\text{BaFeO}_{2.333}\text{F}_{0.333}/\text{BaFeO}_{2.667}$ [12], respectively. The ordering of the vacancies (grey balls) is highlighted with pink channels for each structure and, in case of $\text{BaFeO}_{2.333}\text{F}_{0.333}/\text{BaFeO}_{2.667}$, the relaxation of the O4/F4 site ($2e$) to stabilize the tetragonal coordination of the Fe2 site is additionally indicated by black arrows [12]. The barium atoms are neglected to highlight the anion coordinations (blue polyhedra) around the iron atoms (blue balls) and anion vacancies. Inside $\text{BaFeO}_{2.5}$, the vacancies form interpenetrating channels along the $[0\ 1\ 1]_{P2_1/c}$ and $[0\ 1\ -1]_{P2_1/c}$ directions with non-connected layers, while inside $\text{BaFeO}_{2.333}\text{F}_{0.333}/\text{BaFeO}_{2.667}$, the vacancies ordering occurs along the b -axis in form of isolated channels. By transforming these directions back into the ideal cubic lattice with

the above transformation matrices³, one gets:

- $\text{BaFeO}_{2.5} \rightarrow \text{cubic}$: $\begin{pmatrix} -2 \\ 0 \\ 6 \end{pmatrix}$ and $\begin{pmatrix} -2 \\ 4 \\ 0 \end{pmatrix}$
- $\text{BaFeO}_{2.333}\text{F}_{0.333}/\text{BaFeO}_{2.667} \rightarrow \text{cubic}$: $\begin{pmatrix} -1 \\ 1 \\ 1 \end{pmatrix}$

Within the ideal cubic symmetry, the channels within $\text{BaFeO}_{2.5}$ would intersect with those in $\text{BaFeO}_{2.333}\text{F}_{0.333}/\text{BaFeO}_{2.667}$ at angles of $\sim 43^\circ$ and $\sim 39^\circ$.

From these considerations, the conclusion can be drawn, that in order to transform the compound $\text{BaFeO}_{2.5}$ into $\text{BaFeO}_{2.333}\text{F}_{0.333}/\text{BaFeO}_{2.667}$, i.e., $P2_1/c$ into $P2_1/m$, the system has to undergo a change in symmetry, with loss in the symmetry of the anion sublattice and maintenance of a high symmetry within the cation sublattice. By the occupation of the oxygen vacancies, the splitting of the oxygen sites during the phase formation is reversed, what results in an increase in the symmetry. Afterwards, the monoclinic distortion occurs again to form $P2_1/m$ with the new ordering of the vacancies. Above it was mentioned, that $P4/mmm$ could be found in both branches of the symmetry tree, thus, could represent the intermediate symmetry of the cation sublattice. But it could also be possible, that the transition occurs over an orthorhombic phase, since it would require a lesser increase in symmetry from the monoclinic symmetry.

3.5.3. Oxygen cycling and morphological influences

The TG/DTA experiments in Sec. 3.1 suggest that the system is capable of storing oxygen and releasing it depending on the thermodynamic conditions, such as temperature and oxygen partial pressure. Thus, this storing behaviour was investigated by TG measurements by cycling powder (prepared by high temperature NSP) of $\text{BaFeO}_{2.5}$ in a pure oxygen atmosphere. Complementary, this oxygen uptake and release was studied on symmetrical films of $\text{BaFeO}_{2.5}$ by measuring EIS under pure oxygen atmosphere and cycling the temperature. The performed cyclic TG measurements exhibited a shift in temperature for the oxygen uptake and a continuous release of oxygen over the investigated temperature range compared to the TG measurements presented in Sec. 3.1, i.e. it was indicated that the O_2 uptake/release properties are highly connected to smaller changes induced by the chosen synthesis parameters.

This synthesis dependence came to attention during the film synthesis in Sec. 3.2, the hollow-sphere morphology found for NSP-powder synthesized at high temperature (1050°C) would not sinter onto the used substrate. To overcome this issue, salt-assisted NSP was not suitable, since the chlorine prohibited the phase formation of hydrated $\text{BaFeO}_{2.5}$. The

³ $\vec{a}_{\text{monoclinic}} = \vec{a}_{\text{cubic}}P \rightarrow \vec{a}_{\text{monoclinic}}P^T = \vec{a}_{\text{cubic}}$, with P being the transformation matrix.

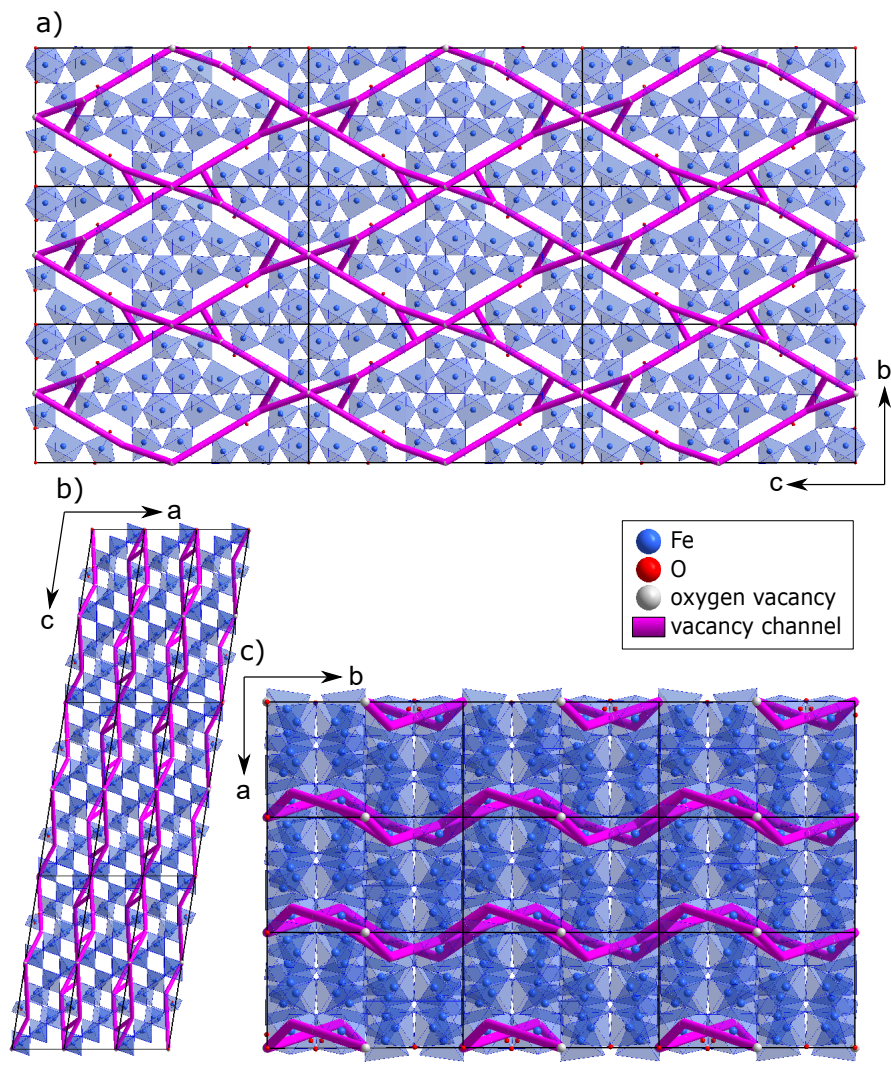


Figure 3.53.: Anion ordering in a 3×3×3 supercell of BaFeO_{2.5} viewing along (a) *a*-axis, (b) *b*-axis and (c) *c*-axis. The oxygen vacancies are depicted as grey balls with pink connections highlighting the formed oxygen vacancy channels. A detailed list of the atomic positions is given in Tab. C.2.

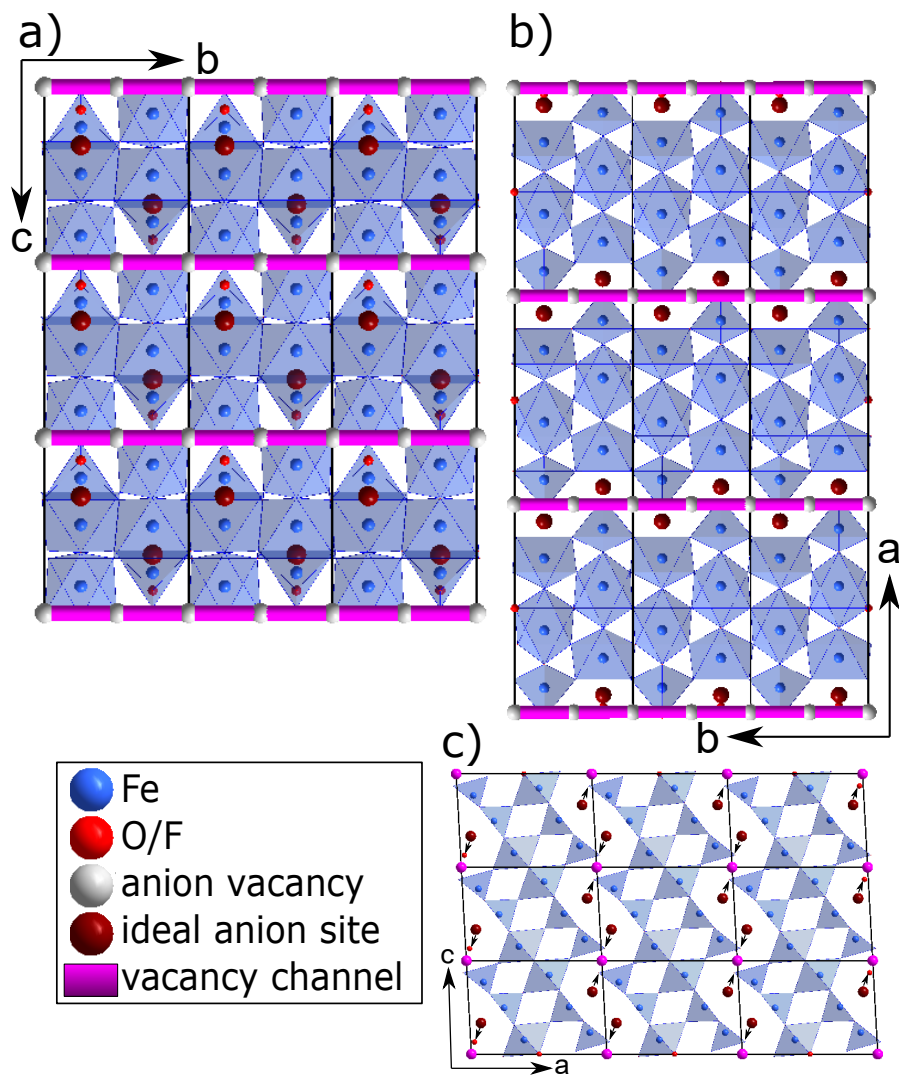


Figure 3.54.: Anion ordering in a $3 \times 3 \times 3$ supercell of $\text{BaFeO}_{2.333}\text{F}_{0.333}/\text{BaFeO}_{2.667}$ viewing along (a) a -axis, (b) c -axis and (c) b -axis. The anion vacancies are depicted as grey balls with pink connections highlighting the formed oxygen vacancy channels. Dark red balls indicate the ideal anion position and black arrows show the displacement after relaxation leading to additional vacancy positions. A detailed list of the atomic positions is given in Tab. C.1.

solution was a low temperature NSP process followed by an annealing at 900 °C under argon which resulted in fine grained powder. This low temperature powder lead to smooth films, and a similar powder (annealed for 10 h) was also used in the TG experiments in Sec. 3.1. Fig. 3.55 sketches the step-by-step synthesis routes for all powders and the subsequent film preparation step together with the crystallite sizes of each product. Due to this morphology dependency, the results from the cyclic TG and EIS measurements will be discussed with respect to the crystallite sizes of the used powders and films.

The crystallite sizes were extracted from XRD patterns of the corresponding powders and are listed in Tab. 3.16. As a result of the additional annealing for several hours at 900 °C, the low temperature powder exhibits a bigger crystallite size compared to the directly synthesized hydrated powder as refined from the XRD patterns in Fig. 3.19. A refinement yields a crystallite size of 74 nm and 24 nm for the powders synthesized at low and high temperatures, respectively, while the powder used in Sec. 3.1, which was annealed for 10 h, exhibits a crystallite size of 64 nm. Thus, the used powders differed in morphology, fine grained vs. hollow-sphere, and crystallite size. The heat treatment and the accompanied increase in crystallite size may play a crucial role.

Phase formation and changes in crystal properties can directly be related to crystallite sizes [221–225]. In case of zirconia, it was proposed by Garvie [221, 222] that the tetragonal phase can be stabilized and the transition temperature to monoclinic be shifted. This stabilization may be due to the lower surface free energy of the tetragonal phase, which dominates the overall energy term if the particle is sufficiently small. According to him, this crystallite size would be 300 Å. Based on thermodynamic requirements, the following relation is established at the transition temperature [226, 227] for two phases M1 and M2:

$$(G_{M1} - G_{M2}) + (S_{M1}\gamma_{M1} - S_{M2}\gamma_{M2}) + (V_{M1} - V_{M2}) = 0 \quad (3.31)$$

where G , S , γ and V are the free energy, molar surface, surface energy and strain energy of the phases, respectively. But it was shown, that also other factors, such as the availability of nucleation sites, may play a role, and it was always assumed, that the transformation inside zirconia is of martensitic nature. In the present case during the phase transitions, diffusion occurs when the oxygen from atmosphere is incorporated into the lattice and transported into the particles, while iron is oxidized, and vice versa. The redox reaction may be included in the first term, since the redox potential is an intrinsic factor and independent of the crystallite size. Further, no information is available on the strain energy of $\text{BaFeO}_{2.5}$ and $\text{BaFeO}_{2.667}$. But it can be assumed, that above the phase transition temperature, the free energy term is positive. From this it follows, that the second term, the surface energy term, must be negative in order to satisfy Eqn. 3.31 (by neglecting the third term). In Sec. 3.5.1 it was discussed, that $\text{BaFeO}_{2.667}$ possesses a smaller cell

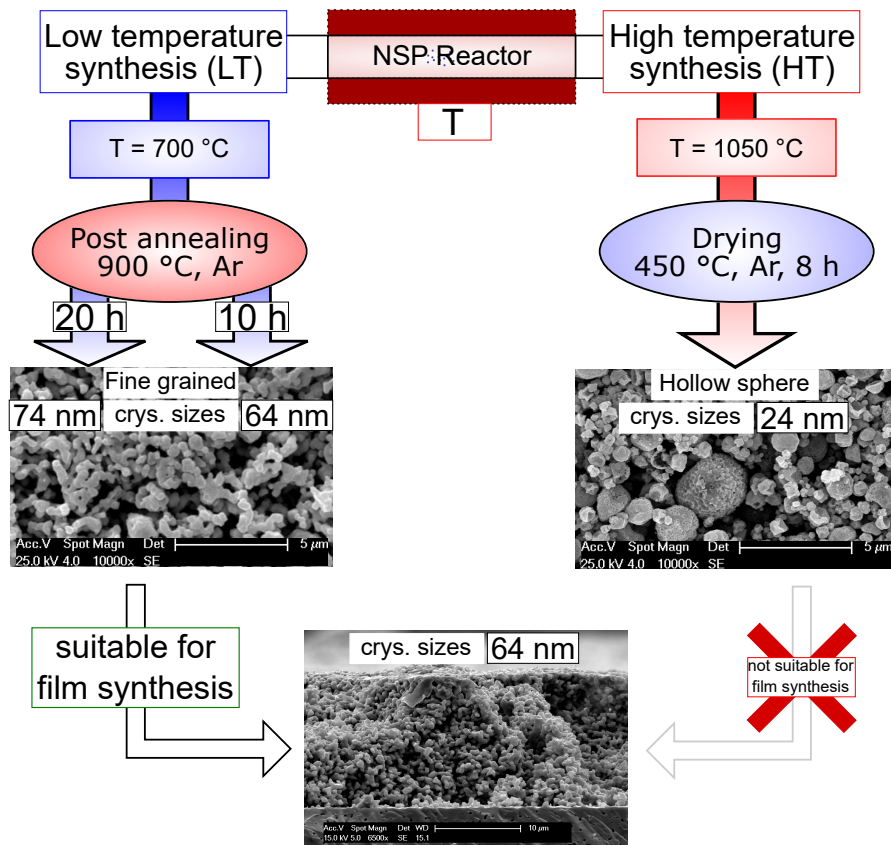


Figure 3.55.: Schematical synthesis route for the preparation of low and high temperature NSP powder and the subsequent film preparation. For both powders and the film the crystallite size and the synthesis temperature are given.

Table 3.16.: Crystallite sizes of the investigated sample powders and films depending on the synthesis temperature.

Crystallite size (nm)	LT powders		HT powder	film
	(700 °C, 20 h annealing)	(700 °C, 10 h annealing)	(1050 °C)	
	74(3)	64(4)	24(2)	64(3)

volume per formula unit than $\text{BaFeO}_{2.5}$. Assuming that the $\text{BaFeO}_{2.667}$ ($P2_1/m$) phase exhibits a much smaller surface energy than $\text{BaFeO}_{2.5}$ ($P2_1/c$), it could be concluded, that the smaller the crystallite size, the higher the phase transition temperature for the phase transition $P2_1/m \rightarrow P2_1/c$ due to a possible phase stabilization by energy minimization. In the following, the results of TG/DTA, EIS and XRD will be discussed on the background of the crystallite sizes of each powder/film.

The results of cyclic TG and EIS of directly synthesized NSP powder with a crystallite size of 24 nm, which was annealed for 1 h under argon at 900 °C prior to the measurement, will be presented and compared to the low temperature powder (crystallite size 64 nm, annealing time 10 h).

TG/DTA measurements in Sec. 3.1 under pure oxygen for the low temperature powder have shown that the oxygen stored inside $\text{BaFeO}_{2.667}$ is released over a very broad temperature range between 360 – 520 °C to only minor extents (about 0.2 % mass loss), by maintaining the $P2_1/m$ symmetry as confirmed by in situ XRD, thus, the released oxygen must lead to defects inside the anion-ordered lattice. Above 450 °C, a gradual transformation under further release of oxygen to $\text{BaFeO}_{2.5}$ ($P2_1/c$) is observed, and this phase becomes the main phase at 525 °C, according to the XRD data in Figure 3.7 a. The peculiarity of the TG measurement in Fig. 3.8 is the sudden release of oxygen and the transformation back to $\text{BaFeO}_{2.5}$.

Figure 3.56 shows two cyclic TG measurements for $\text{BaFeO}_{2.5}/\text{BaFeO}_{2.81}$ for three cycles between 420 and 650/750 °C each under pure oxygen including the heating and cooling process. The TG measurement presented in Fig. 3.8 is given as a reference (dashed grey line). It is evident, that $\text{BaFeO}_{2.5}$ is oxidized up to $\text{BaFeO}_{2.667}$ around 375 °C showing a local maximum. Afterwards the sample releases oxygen with increasing temperature up to 650 °C and takes it up again during cooling to 420 °C ($\Delta \approx 0.45\%$). The hysteresis observed results from less oxygen released than incorporated. The mean mass difference during heating, i.e. oxygen release, is around 0.31 % while 0.36 % mass is gained during cooling, i.e. oxygen uptake. After the cycling process, the hysteresis leads to a difference of 0.3 % in mass at 375 °C. Upon cooling to RT, the sample takes up further oxygen, which points towards the formation of $\text{BaFeO}_{2.81}$. In the beginning of the second measurement, the sample mass drops down to $\text{BaFeO}_{2.667}$ following the oxygen uptake

process during cooling of the prior measurement. The upper temperature limit was raised to 750 °C in order to increase the insight into the materials behaviour. Besides their cyclic trajectories, both measurements deviate strongly from the reference measurement. The sudden release of oxygen at around 500 °C could not be observed and the oxygen is released more continuously over the investigated temperature range. In addition, the mass hysteresis observed points towards an incomplete release of oxygen which means, that the incorporated oxygen partially remains in the lattice.

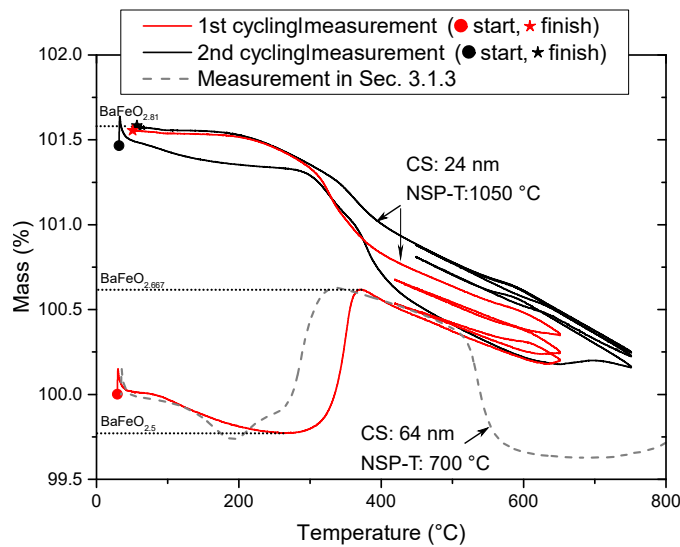


Figure 3.56.: Cyclic TG measurement of $\text{BaFeO}_{2.5}$ prepared by NSP at 1050 °C under pure oxygen between 420 and 650 °C. The start of the measurement is marked with a star and the end with a diamond. Dotted and dashed lines are guides for the eye to highlight important features. The cyclic measurement is compared to the TG measurement presented in Sec. 3.1. For both powders the crystallite size (CS) and the synthesis temperature (NSP-T) are given.

To investigate the electrical properties of $\text{BaFeO}_{2.5}$ and $\text{BaFeO}_{2.667}$ during this oxygen release/uptake, cyclic impedance spectroscopy measurements were performed in the temperature range between 440 and 540 °C on a porous symmetrical film. A porous film offers the advantage of a more homogeneous uptake and release of oxygen and it can compensate any strains arising from volume differences during the experiments due to its porosity compared to a dense pellet. Figure 3.57 shows the recorded area specific resistances (ASR) of a symmetrical $\text{BaFeO}_{2.667}$ film on a YSZ8 button substrate

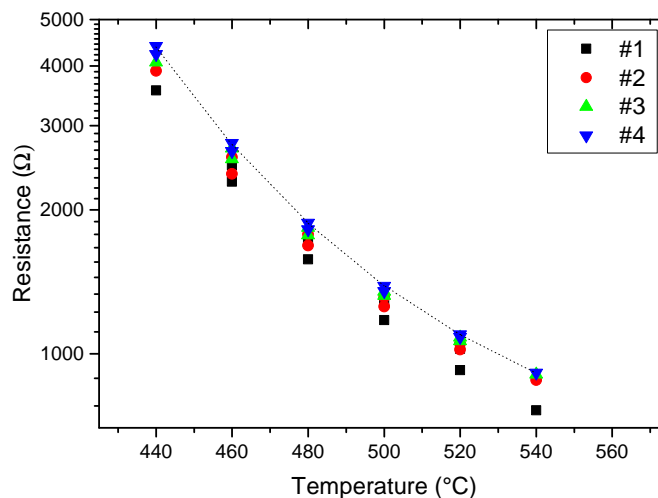


Figure 3.57.: Area specific resistance of a four-times cycled symmetrical film of $\text{BaFeO}_{2.5}$ and $\text{BaFeO}_{2.667}$. The heating and cooling ramps are indicated by solid and hollow symbols, respectively. The dashed line highlights the non-linear behaviour of the area specific resistance.

during four cycles under an oxygen atmosphere. The film differs in terms of morphology and crystallite size from the powder used for TG. The film consists of a network-like structure (compare Fig. 3.25) with a volume weighed crystallite size of roughly 64 nm (from XRD). Nyquist and Bode plots and the corresponding fits are shown in Figure D.1 and D.2. The dashed line shown in Figure 3.57 indicates the non-linear behaviour of the material even at the 4th cycle. A hysteresis in the area specific resistance can be observed similarly to the TG measurements: at 420 °C the difference in ASR from the first to last measurement is $662 \text{ } \Omega\text{cm}^2$ and at 540 °C $118 \text{ } \Omega\text{cm}^2$. The hysteresis comes with a small increase in cell volume and crystallite size, from $66.02 \text{ } \text{Å}^3/\text{f.u.}$ to $66.39 \text{ } \text{Å}^3/\text{f.u.}$ and 64 nm to 81 nm before and after the impedance measurement (see Table 3.17, film was quenched from 420 °C), respectively, derived from XRD measurements before and after thermal cycling (see Figure 3.58). The results from the TG, impedance measurements and XRD suggest a reversibility of the oxygen release and uptake. However, the hystereses observed in mass, ASR and volume uncovered during the investigations indicate a remaining of oxygen inside the lattice, what makes this redox process only partial reversible. The TG measurement of the first cycle in Fig. 3.56 suggests a residual amount of oxygen in the phase $\text{BaFeO}_{2.667+0.013}$ based on a mass difference of 0.35 %. The difference in mass before and after the TG cycling reveals that the incorporated oxygen is not released completely

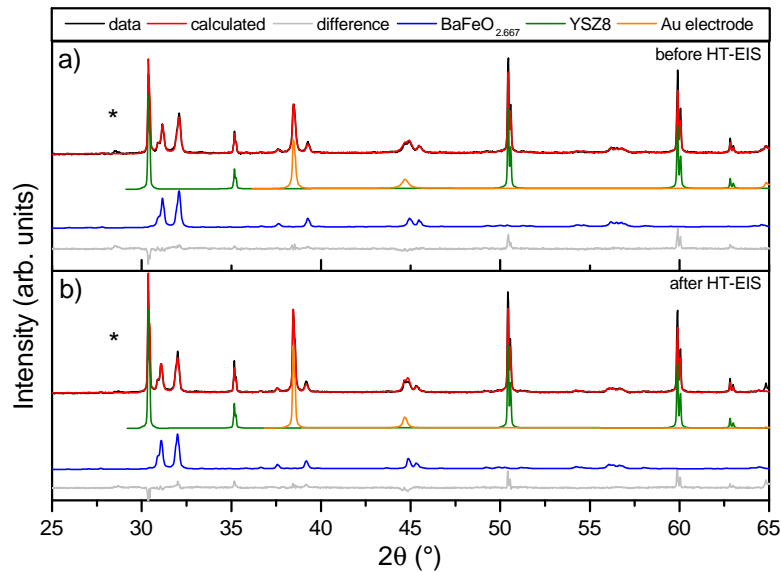


Figure 3.58.: XRD of symmetrical films of BaFeO_{2.667} on YSZ8 coated with Au electrode, recorded before (a) and after (b) the high temperature impedance spectroscopy under oxygen. The * indicates a slight impurity of BaCO₃.

and remains inside the lattice. On the other side, the XRD patterns of the films before and after the cyclic EIS measurements show an increase in crystallite size (see Tab. 3.17), which suggests that the remaining oxygen may be utilized for occupying defects in bulk and grain boundaries. The non-linear behaviour of the ASR may be attributed to the chemical changes inside the material, which arise from the formation and breaking of bonds together with a lattice relaxation, as it was observed during the HT-XRD (Figure 3.7 e). This response highlights the presence of oxygen incorporation/release accompanied by a decrease in activation energy for the oxygen ion conduction as shown in Sec. 3.2 most likely triggered by the phase changes between BaFeO_{2.5} ($P2_1/c$) and BaFeO_{2.667} ($P2_1/m$) and the flexibility of the lattice during those. On the other side, the observed hysteresis points towards a pinning of oxygen ions on their sites what leads to an overall lowered oxygen ion conduction with increasing amount of oxygen ions incorporated into the lattice as seen in the TG measurement. In addition, the phase transitions performed during each cycle lead to a repetitive volume change which may be detrimental to the structural integrity of the porous film.

The above made observations could be used to engineer a suitable material for electrocatalytic or oxygen storage applications by choosing the right morphology. As discussed

in Sec. 3.1 (see also the dashed line in Fig. 3.56), $\text{BaFeO}_{2.5}$ is capable of storing 0.08 O_2 by oxidation to $\text{BaFeO}_{2.667}$ up to a high temperature of 475 °C, with traces of $\text{BaFeO}_{2.667}$ inside the powder up to 700 °C. In addition, a second oxygen storage regime was observed at even higher temperatures of 750 °C to 950 °C, involving the reconstructive phase transition to the hexagonal modification. The precise oxygen uptake and release temperatures, coupled with the well-defined stoichiometric amount of oxygen during this process, would make this kind of $\text{BaFeO}_{2.5}/\text{BaFeO}_{2.667}$ redox couple, i.e. $\text{Fe}^{3+}/\text{Fe}^{4+}$, a suitable candidate for chemical looping with oxygen uncoupling reactions (CLOU) [228–230]. But it was previously reported that Ba-Fe-O based perovskites are susceptible for a passivation by adhesion of CO_2 . The exchange of lattice oxygen and the atmosphere is completely suppressed upon the formation of a passivation layer of adhesive CO_2 [231, 232]. Thus, there would be more experiments required to proof the performance related to this type of topochemical oxygen uptake/release between $\text{BaFeO}_{2.5}$ and $\text{BaFeO}_{2.667}$. But also the mass hysteresis observed in the cycling TG and EIS experiments has to be further investigated. Concluding it can be stated, that the crystallite size influences the reactivity of $\text{BaFeO}_{2.5}$ and $\text{BaFeO}_{2.667}$. A lower crystallite size leads to a shift in the transition temperature from $\text{BaFeO}_{2.5}$ and $\text{BaFeO}_{2.667}$, but also the release kinetics of oxygen are changed, as it was discussed in the TG analysis above. In addition, the lower crystallite size prevented the sintering between $\text{BaFeO}_{2.5}$ and the YSZ8 electrolyte. This can be connected to the discussion around Eqn. 3.31 and suggests a shift of the phase transition $\text{BaFeO}_{2.667} \rightarrow \text{BaFeO}_{2.5}$ to higher temperatures due to a minimization of the the surface energy. However, it could not be explained why $\text{BaFeO}_{2.667}$ releases oxygen over a broad temperature range, though, the sharp phase transition observed for the powder with a crystallite size of 64 nm was not present for the smaller sized powder (crystallite size of 24 nm). An inhomogeneous distribution of crystallite sizes may be the reason, but from Fig. 3.56 it can be seen that the slopes of both measurements in the temperature range 350 to 500 °C is similar, i.e. the mass loss is the same for both crystallite sizes. Also the phase transition $\text{BaFeO}_{2.5}/\text{BaFeO}_{2.667}$ occurs at higher temperatures for the smaller sized powder, which may be attributed to an increased activation energy of the phase transition. These findings are counterintuitive since a smaller crystallite size should favour kinetical processes, which appears to be outweighed by the energy minimization of the system.

3.5.4. Reduced fluorine doping

The work presented in Sec. 3.2 brings up a very critical and consequential question with respect to literature. It is assumed, that only a little amount of fluorine as a dopant is needed for improving the properties of an oxygen ion conductor in ones favour, and more important, too much fluorine leads to reversed effect [20]. In this

Table 3.17.: Lattice parameter and volume weighed crystallite sizes of BaFeO_{2.667} before and after the cyclic impedance spectroscopy. The volume per formula unit $V_{f.u.}$ is given related to the volume of one BaFeO_{2.667±d} unit.

	a (Å)	b (Å)	c (Å)	β (°)	$V_{f.u.}$ (Å ³)	L_{Vol} (IB) (nm)	strain ϵ_0 ($\cdot 10^{-4}$)
Before	10.118(1)	5.644(1)	6.942(1)	92.30(1)	66.02(1)	64(3)	3.4(3)
After	10.138(1)	5.654(1)	6.954(1)	92.19(1)	66.39(1)	81(5)	5.2(5)

study, La_{0.6}Sr_{0.4}Co_{0.2}Fe_{0.8}O_{3- δ} (LSCF) was fluorinated to La_{0.6}Sr_{0.4}Co_{0.2}Fe_{0.8}O_{2.95- δ} F_{0.05} (LSCFF0.05) and La_{0.6}Sr_{0.4}Co_{0.2}Fe_{0.8}O_{2.9- δ} F_{0.1} (LSCFF0.1). The lesser fluorinated sample LSCFF0.05 exhibited a significant performance increase ($\sim 50\%$), while LSCFF0.1 exhibited a higher area specific resistance (ASR) with a slight decrease in performance. In Sec. 3.2, comparably high amounts of fluorine were chosen as dopants, but the formed fluorinated phases were not susceptible to further oxidation and showed phase stability until their degradation/decomposition temperature. However, the important question is, how a lower amount of fluorine would affect the properties of a BaFeO_{2.5-x/2}F_x ($x < 0.333$) film. First, as already discussed in literature [12] and throughout this work, e.g. especially in Sec. 3.4, the cubic perovskite-type system Ba-Fe-O forms either the monoclinic or the cubic phase upon fluorination which possess a well-defined fluorine content. As a result, one can expect a cathode compound based on a lower level of fluorination to be a composite of BaFeO_{2.5} and BaFeO_{2.333}F_{0.333}. The question is, whether this composite combines the conduction properties found for the individual phases in Sec. 3.2, e.g. no significant improvement of properties may be observed for this composite, or if an improvement can be observed by overcoming the surface and bulk limitations due to beneficial influences of fluorination postulated by literature.

In analogy to the study in [20], a symmetrical film with a lesser fluorine stoichiometry than in BaFeO_{2.333}F_{0.333} was prepared and investigated. The following evaluation will be given on a qualitative base. The preparation was done according to the powder and film synthesis presented in Sec. 3.1 and Sec. 3.2. The fluorination agent for the fluorination via interdiffusion (see Sec. 3.2) was a mixture of BaFeO_{2.5} and BaFeO_{2.333}F_{0.333} with overall composition BaFeO_{2.43}F_{0.14}. As expected, the XRD in Fig. 3.59 a of the as-prepared film confirms the composition of the composite and BaFeO_{2.5} and BaFeO_{2.333}F_{0.333} are identifiable independently prior to the impedance measurement. Fig. 3.59 b shows the composite film after the impedance measurement after cooling down to RT. The monoclinic BaFeO_{2.5} turned into the tetragonal BaFeO_{2.81} and only slight changes in BaFeO_{2.333}F_{0.333} are visible which may be attributed to residual BaFeO_{2.667}. From the XRD data a weight percentage ratio of 38 % BaFeO_{2.333}F_{0.333} to 62 % BaFeO_{2.5} can be estimated, which results

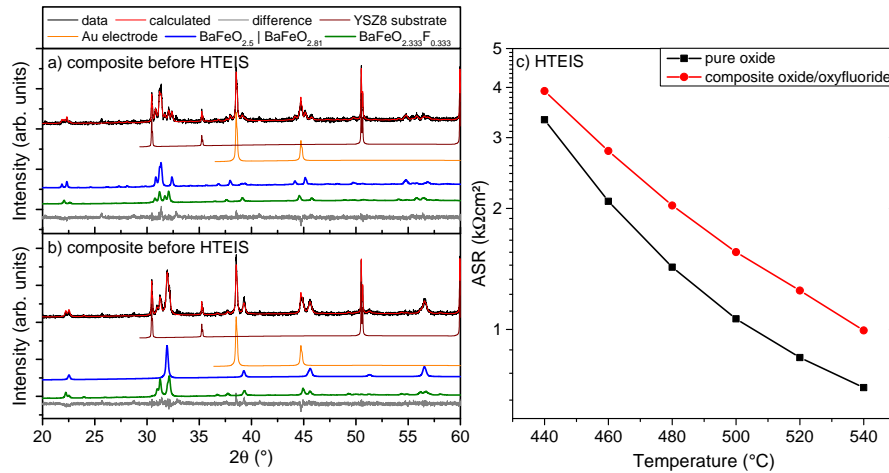


Figure 3.59.: XRD of the composite film before (a) and after (b) the electrical impedance measurement (c). The composite (red circles) is compared to a pure oxide film (black squares).

in a stoichiometric amount of fluorine of $\text{BaFeO}_{2.435}\text{F}_{0.13}$ ⁴. This relative quantification highlights the good stoichiometry transfer forced by the concentration gradient between powder and film, even though the mass of the symmetrical film is comparably low in contrast to the powder used for the interdiffusion. Fig. 3.59 c compares the results of an electrochemical impedance spectroscopy measurement of this composite film with a purely oxidic $\text{BaFeO}_{2.5}$ film (as presented in Sec. 3.1). It is evident, that the composite film shows a higher ASR (around $500 \Omega\text{cm}^2$) and thus, no improvement of the oxygen ion conduction can be observed. On the other side, the trajectory of the ASR exhibits less bending due to oxidation compared to the pure oxide which is fully susceptible towards the process of oxygen uptake and phase transformation [83]. In conclusion, a film with a low amount of fluorine comparable to literature [10, 20] could be synthesized. But the composite film does not show any significantly improved conduction properties and is still oxidized during the measurement. The results highlight the importance of phase homogeneity for samples containing low amounts of fluorine.

⁴The estimation of a reliable weight percentage is not possible due to the layered structure of the film.

4. Conclusion

Within this work, different topochemically modified compounds of the perovskite system Ba-Fe-O-F were presented and studied in terms of kinetic and electrochemical properties. Thereby, the work focussed heavily on the synthesis of these topochemically modified compounds highlighting the importance of synthesis conditions and simultaneously developing a new technique for topochemical fluorination. A key result of this work was the investigation of the interdiffusion kinetics and thermodynamics which allowed for a better understanding of electrocatalytic properties. In the following, the main conclusions will be summarized.

Besides the topochemical fluorination, the topochemical oxidation of $\text{BaFeO}_{2.5}$ led to the discovery of a yet undescribed modification of an oxygen vacancy ordered compound $\text{BaFeO}_{2.667}$, which was found to be isotypic to $\text{BaFeO}_{2.333}\text{F}_{0.333}$. A peculiarity of the oxidized $\text{BaFeO}_{2.667}$ phase is the tetrahedrally coordinated Fe^{4+} cation, which is unusual for a perovskite-type oxide derived from the cubic aristotype. On the other hand, the high temperature studies under oxygen and ambient atmosphere yielded new insights into phase formations and their stabilities inside the Ba-Fe-O system. A low temperature oxidation of $\text{BaFeO}_{2.667}$ led to the formation of the even higher oxidized tetragonal modification $\text{BaFeO}_{2.81}$.

The system Ba-Fe-O was chosen as a model system due to its well-defined structures formed upon fluorination, namely $\text{BaFeO}_{2.333}\text{F}_{0.333}$ ($P2_1/m$) and BaFeO_2F ($Pm\bar{3}m$). Porous symmetrical films of $\text{BaFeO}_{2.5}$ were synthesized and topochemically fluorinated to prepare the compounds $\text{BaFeO}_{2.333}\text{F}_{0.333}$ and BaFeO_2F . Electrochemical impedance spectroscopy revealed a surface limited conduction process for $\text{BaFeO}_{2.333}\text{F}_{0.333}$ with no significant conduction increase, compared to $\text{BaFeO}_{2.5}$, which exhibited bulk-limitation. This shift in limitations was attributed to a reduction of available oxygen ion vacancies, but also to the change in bond characteristics due to the incorporation of fluorine. On the other side, full fluorination to BaFeO_2F led to a detrimental effect on the conductivity increasing the ASR by several order of magnitudes.

In comparison to the highly porous films, epitaxial films of $\text{BaFeO}_{2.5}$ and BaFeO_2F were grown by PLD on STO substrates. The aim was to investigate possible structural properties of the FeO_4F_2 octahedron. However, the fluorination led to a relaxation of the already

strained lattice forming an almost perfect cubic structure. This also led to a homogeneous distribution of spin domains inside a G-AFM ordering. But it could be concluded, that the FeO_4F_2 octahedron exhibited a *trans*-configuration of the fluorine anions.

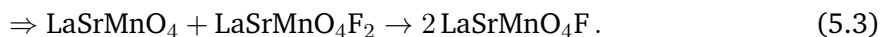
Finally, the interdiffusion kinetics and thermodynamics of the interdiffusion reaction between $\text{BaFeO}_{2.5}$ and BaFeO_2F were investigated yielding new insights into this process. The key technique inside this study were isothermal high temperature diffraction experiments coupled with Rietveld refinements for monitoring the phase fractions during the reaction. By this, the fluorine and oxygen exchange could indirectly be tracked due to the distinct formed phases. The reaction was found to be of first order and the crystallization process was controlled by the diffusion process. The adaptation of the Boltzmann-Matano method to this special experiment made it possible to calculate an interdiffusion coefficient which suggested the doubly charged oxygen anion to be the rate limiting species of the interdiffusion process.

Throughout the thesis, the range of observed symmetries was limited to $P2_1/c$ ($\text{BaFeO}_{2.5}$), $P2_1/m$ ($\text{BaFeO}_{2.333}\text{F}_{0.333}/\text{BaFeO}_{2.667}$), $P4/mmm$ ($\text{BaFeO}_{2.81}$) and $Pm\bar{3}m$ (BaFeO_2F) depending on the occupation of the anion sublattice. The monoclinic phases are subgroups of the aristotype cubic structure, while the tetragonal $P4/mmm$ can be found within the symmetry trees. This symmetry relations were discussed on the base of group-subgroup relations and the involved ordering of oxygen vacancies.

Further it was found, that the crystallite size and powder morphology played an important role for the phase stabilization and sintering behaviour. It could be shown, that the smaller crystallite size shifted the phase formation of $\text{BaFeO}_{2.667}$ to higher temperatures and hindered the reduction back to $\text{BaFeO}_{2.5}$. Also the preparation of highly porous films required a precursor powder with fine-grained morphology and a higher crystallite size. Finally, the preparation of a symmetrical film with a fluorine stoichiometry of $\text{BaFeO}_{2.435}\text{F}_{0.13}$ was prepared by interdiffusion to investigate the impact of an even lower fluorine content. The film turned out to be a composite between $\text{BaFeO}_{2.5}$ and $\text{BaFeO}_{2.333}\text{F}_{0.333}$. Electrochemical impedance spectroscopy showed no performance increase, since the limitations of each phase were still present. Further, the $\text{BaFeO}_{2.5}$ inside the composite was oxidized during the measurements, while the $\text{BaFeO}_{2.333}\text{F}_{0.333}$ remained unaffected, again highlighting the stability of the fluorine phase.

5. Outlook

The presented work offered new insights into oxyfluorides, but also highlighted the influence of vacancy ordering. The motivation of this work was to investigate the impact of topochemical fluorination onto electrochemical properties of the model system Ba-Fe-O. Simultaneously, efforts were made to achieve a deeper understanding of fluorine (inter)diffusion based on the chosen model system. The technique presented in Sec. 3.4 may be adopted for other compounds to study the (inter)diffusion kinetics under the precondition of well identifiable phases. A possible candidate for this investigation would be the system $\text{LaSrMnO}_4\text{F}_x$ ($x = 0, 1, 2$), which crystallizes in a tetragonal K_2NiF_4 structure and can be used as cathode material for fluoride ion batteries [209]. In contrast to the interdiffusion within this work, the diffusion reaction in $\text{LaSrMnO}_4\text{F}_x$ ($x = 0, 1, 2$) contains the exchange of fluorine and electrons. A diffusion reaction also includes the oxidation of Mn^{3+} to Mn^{4+} and Mn^{5+} in case of $\text{LaSrMnO}_4\text{F}_1$ and $\text{LaSrMnO}_4\text{F}_2$, respectively. This diffusion reaction can be formalized by



The K_2NiF_4 structure of $\text{LaSrMnO}_4\text{F}_x$ ($x = 0, 1, 2$) can be described by alternating layers of perovskite units (ABX_3) and rock salt units (AX) along the c -axis forming huge interstitial positions which can be occupied by anions. Depending on the degree of fluorination, the unit cell elongates along the c -axis. Thereby, the fluorine is inserted into the interstitial sites filling first one layer between perovskite and rock salt units and then the second if further fluorinated. This two-step fluorination behaviour comes with a symmetry lowering and subsequent increase from $I4/mmm$ to $P4/mmm$ and back to $I4/mmm$.

The findings and understandings of Sec. 3.2 could now be applied on other systems like the Ba-Sr-Co-Fe-O system, which is a promising candidate for SOFC applications. Recent advances in literature found stable oxyfluoride compounds using the topochemical fluorination route [233–235]. However, the topochemical fluorination route via interdiffusion established in Sec. 3.2 may enable the preparation of otherwise unexplored metastable compounds. At this point it may be noted, that the optimization of

the successfully engineered films was not an important part of this work. Hence, an improvement of the synthesis conditions may lead to better conduction performances, like the degree of film porosity and the crystallite size. But also the influence of the interface between the YSZ substrate and the porosity was not yet investigated. It was reported that the addition of electrolyte material to the film may decrease the ASR significantly [7]. Further, a combination of cation and anion doping of the Ba-Fe-O system should be considered. It was reported that Y [236] and Sn [237] improve the structural stability and electrocatalytic performance. In addition, the chosen synthesis method for the starting powders, the NSP process, proved to be an excellent method for producing phase pure BaFeO_{2.5}. A next step would be to attempt to directly synthesize fluorinated phases of promising oxide candidates, e.g. Ba_{0.5}Sr_{0.5}Co_{0.2}Fe_{0.8}O_{3-y-δ}F_y. Other methods, like nitrate-citrate or sol-gel methods, have shown to be able to produce highly crystalline oxyfluorides: Ba_{0.5}Sr_{0.5}Co_{0.2}Fe_{0.8}O_{2.9-δ}F_{0.1} [238], BaCo_{0.4}Fe_{0.4}Zr_{0.1}Y_{0.1}O_{2.95-δ}F_{0.05} [234], LaBa_{0.5}Sr_{0.5}Fe₂O_{5.875-δ}F_{0.125} [235], and more [239, 240]. In these methods, the fluorine was introduced by adding the low soluble BaF₂ or SrF₂, which would also be an issue for the NSP process, where in principle the nitrate-salts of the metal cations are dissolved in an aqueous solution.

This work boosted the understanding of fluorination and the thermodynamics of inter-diffusion, but also the role of oxygen vacancy ordering and symmetry relations could be highlighted. In addition, the utilized synthesis techniques could enable the preparation and finding of further oxide and oxyfluoride phases in complex systems.

Bibliography

1. Grove, W. R. LVI. On a new voltaic combination. *The London, Edinburgh, and Dublin Philosophical Magazine and Journal of Science* **13**, 430–431 (1838).
2. Schönbein, C. F. X. On the voltaic polarization of certain solid and fluid substances. *The London, Edinburgh, and Dublin Philosophical Magazine and Journal of Science* **14**, 43–45 (1839).
3. Cook, B. Introduction to fuel cells and hydrogen technology. *Engineering Science & Education Journal* **11**, 205–216 (2002).
4. Sun, C., Hui, R. & Roller, J. Cathode materials for solid oxide fuel cells: a review. *Journal of Solid State Electrochemistry* **14**, 1125–1144 (2010).
5. Adler, S. B. Factors governing oxygen reduction in solid oxide fuel cell cathodes. *Chemical Reviews* **104**, 4791–843 (2004).
6. Huijsmans, J. P. P., van Berkel, F. P. F. & Christie, G. M. Intermediate temperature SOFC – a promise for the 21st century. *Journal of Power Sources* **71**, 107–110 (1998).
7. Dusastre, V. & Kilner, J. A. Optimisation of composite cathodes for intermediate temperature SOFC applications. *Solid State Ionics* **126**, 163–174 (1999).
8. Shao, Z. & Haile, S. M. A high-performance cathode for the next generation of solid-oxide fuel cells. *Nature* **431**, 170–3 (2004).
9. Peña-Martínez, J. *et al.* Fuel cell studies of perovskite-type materials for IT-SOFC. *Journal of Power Sources* **159**, 914–921 (2006).
10. Zhang, Z., Zhu, Y., Zhong, Y., Zhou, W. & Shao, Z. Anion Doping: A New Strategy for Developing High-Performance Perovskite-Type Cathode Materials of Solid Oxide Fuel Cells. *Advanced Energy Materials* **7** (2017).
11. Heap, R., Slater, P. R., Berry, F. J., Helgason, O. & Wright, A. J. Synthesis and structural determination of the new oxide fluoride BaFeO₂F. *Solid State Communications* **141**, 467–470 (2007).

-
12. Clemens, O. Structural characterization of a new vacancy ordered perovskite modification found for $\text{Ba}_3\text{Fe}_3\text{O}_7\text{F}$ ($\text{BaFeO}_{2.333}\text{F}_{0.333}$): Towards understanding of vacancy ordering for different perovskite-type ferrites. *Journal of Solid State Chemistry* **225**, 261–270 (2015).
 13. Wachsman, E. D. & Lee, K. T. Lowering the temperature of solid oxide fuel cells. *Science* **334**, 935–939 (2011).
 14. Jacobson, A. J. Materials for solid oxide fuel cells. *Chemistry of Materials* **22**, 660–674 (2010).
 15. Mai, A., Haanappel, V. A. C., Uhlenbruck, S., Tietz, F. & Stöver, D. Ferrite-based perovskites as cathode materials for anode-supported solid oxide fuel cells: Part I. Variation of composition. *Solid State Ionics* **176**, 1341–1350 (2005).
 16. Mai, A., Haanappel, V., Tietz, F. & Stover, D. Ferrite-based perovskites as cathode materials for anode-supported solid oxide fuel cells: Part II. Influence of the CGO interlayer. *Solid State Ionics* **177**, 2103–2107 (2006).
 17. Shao, Z. *et al.* Investigation of the permeation behavior and stability of a $\text{Ba}_{0.5}\text{Sr}_{0.5}\text{Co}_{0.8}\text{Fe}_{0.2}\text{O}_{3-\delta}$ oxygen membrane. *Journal of Membrane Science* **172**, 177–188 (2000).
 18. Skinner, S. J. Recent advances in Perovskite-type materials for solid oxide fuel cell cathodes. *International Journal of Inorganic Materials* **3**, 113–121 (2001).
 19. Adler, S. B. Mechanism and kinetics of oxygen reduction on porous $\text{La}_{1-x}\text{Sr}_x\text{CoO}_{3-\delta}$ electrodes. *Solid State Ionics* **111**, 125–134 (1998).
 20. Liu, Y. *et al.* Enhancing oxygen reduction reaction activity of perovskite oxides cathode for solid oxide fuel cells using a novel anion doping strategy. *International Journal of Hydrogen Energy* **43**, 12328–12336 (2018).
 21. Clemens, O. & Slater, P. R. Topochemical modifications of mixed metal oxide compounds by low-temperature fluorination routes. *Reviews in Inorganic Chemistry* **33** (2013).
 22. Chantler, C. *et al.* in *NIST Chemistry WebBook, NIST Standard Reference Database Number 66* (National Institute of Standards and Technology, Gaithersburg, MD, 2005).
 23. Sears, V. F. Neutron scattering lengths and cross sections. *Neutron News* **3**, 26–37 (2006).
 24. Tilley, R. J. *Perovskites: structure-property relationships* (John Wiley & Sons, 2016).

-
25. Ishihara, T. *Perovskite oxide for solid oxide fuel cells* (Springer Science & Business Media, 2009).
 26. Janiak, C., Meyer, H.-J., Gudat, D. & Kurz, P. in *Riedel Moderne Anorganische Chemie* (eds Riedel, E. & Meyer, H.-J.) (De Gruyter, 2018).
 27. Goodenough, J., Ruiz-Diaz, J. & Zhen, Y. Oxide-ion conduction in $\text{Ba}_2\text{In}_2\text{O}_5$ and $\text{Ba}_3\text{In}_2\text{MO}_8$ (M= Ce, Hf, or Zr). *Solid State Ionics* **44**, 21–31 (1990).
 28. Gütlich, P., Bill, E. & Trautwein, A. X. *Mössbauer spectroscopy and transition metal chemistry: fundamentals and applications* (Springer Science & Business Media, 2010).
 29. Grenier, J.-C., Pouchard, M. & Hagenmuller, P. Vacancy ordering in oxygen-deficient perovskite-related ferrites. *Ferrites· Transitions Elements Luminescence*, 1–25 (1981).
 30. Poepelmeier, K. R., Leonowicz, M., Scanlon, J., Longo, J. & Yelon, W. Structure determination of CaMnO_3 and $\text{CaMnO}_{2.5}$ by X-ray and neutron methods. *Journal of Solid State Chemistry* **45**, 71–79 (1982).
 31. Spitsbergen, U. The crystal structures of BaZnO_2 , BaCoO_2 and BaMnO_2 . *Acta Crystallographica* **13**, 197–198 (1960).
 32. Tsujimoto, Y. *et al.* Infinite-layer iron oxide with a square-planar coordination. *Nature* **450**, 1062–1065 (2007).
 33. Clemens, O. *et al.* Crystallographic and magnetic structure of the perovskite-type compound $\text{BaFeO}_{2.5}$: unrivaled complexity in oxygen vacancy ordering. *Inorg Chem* **53**, 5911–21 (2014).
 34. Hayashi, N. *et al.* BaFeO_3 : a ferromagnetic iron oxide. *Angewandte Chemie International Edition* **50**, 12547–50 (2011).
 35. Bertaut, E., Blum, P. & Sagnieres, A. Structure du ferrite bicalcique et de la brown-millerite. *Acta Crystallographica* **12**, 149–159 (1959).
 36. Clemens, O., Haberkorn, R., Slater, P. R. & Beck, H. P. Synthesis and characterisation of the $\text{Sr}_x\text{Ba}_{1-x}\text{FeO}_{3-y}$ -system and the fluorinated phases $\text{Sr}_x\text{Ba}_{1-x}\text{FeO}_2\text{F}$. *Solid State Sciences* **12**, 1455–1463 (2010).
 37. McCabe, E. E. & Greaves, C. Fluorine insertion reactions into pre-formed metal oxides. *Journal of Fluorine Chemistry* **128**, 448–458 (2007).
 38. Clemens, O. *et al.* Synthesis, structural and magnetic characterisation of the fluorinated compound $15\text{R-BaFeO}_2\text{F}$. *Journal of Solid State Chemistry* **203**, 218–226 (2013).

-
39. Clemens, O., Wright, A. J., Berry, F. J., Smith, R. I. & Slater, P. R. Synthesis, structural and magnetic characterisation of the fully fluorinated compound 6H-BaFeO₂F. *Journal of Solid State Chemistry* **198**, 262–269 (2013).
 40. Clemens, O. *et al.* Electrochemical fluorination of perovskite type BaFeO_{2.5}. *Dalton Trans* **43**, 15771–8 (2014).
 41. Slater, P. & Gover, R. Synthesis and structure of the new oxide fluoride Sr₂TiO₃F₂ from the low temperature fluorination of Sr₂TiO₄F: an example of a staged fluorine substitution/insertion reaction. *Journal of Materials Chemistry* **12**, 291–294 (2002).
 42. Weng, H., Kawazoe, Y., Wan, X. & Dong, J. Electronic structure and optical properties of layered perovskites Sr₂MO₄ (M= Ti, V, Cr, and Mn): An ab initio study. *Physical Review B* **74**, 205112 (2006).
 43. Wani, B., Miller, L., Suh, B. & Borsa, F. Fluorination of Sr₂CuO₃ and high temperature superconducting oxides. *Physica C: Superconductivity* **272**, 187–196 (1996).
 44. Wu, H., Zheng, Q.-q. & Lin, H. Energy band structures of the low-dimensional antiferromagnets Sr₂CuO₃ and Sr₂CuO₂Cl₂. *Journal of Applied Physics* **87**, 4897–4899 (2000).
 45. Slater, P. Poly(vinylidene fluoride) as a reagent for the synthesis of K₂NiF₄-related inorganic oxide fluorides. *Journal of fluorine chemistry* **117**, 43–45 (2002).
 46. Kobayashi, Y., Tian, M., Eguchi, M. & Mallouk, T. E. Ion-exchangeable, electronically conducting layered perovskite oxyfluorides. *Journal of the American Chemical Society* **131**, 9849–9855 (2009).
 47. Moon, E. J. *et al.* Comparison of topotactic fluorination methods for complex oxide films. *APL Materials* **3** (2015).
 48. Matano, C. On the relation between the diffusion-coefficients and concentrations of solid metals. *Japanese Journal of Physics* **8**, 109–113 (1933).
 49. Mehrer, H. *Diffusion in solids: fundamentals, methods, materials, diffusion-controlled processes* (Springer Science & Business Media, 2007).
 50. Glicksman, M. *Diffusion in solids: field theory, solid-state principles and applications* (Wiley-Interscience, 2000).
 51. Crank, J. *The mathematics of diffusion* (Oxford university press, 1979).
 52. Dayananda, M. A. Average Effective Interdiffusion Coefficients in Binary and Multi-component Alloys. *Defect and Diffusion Forum* **95-98**, 521–536 (1993).
 53. Pecharsky, V. & Zavalij, P. *Fundamentals of powder diffraction and structural characterization of materials* (Springer Science & Business Media, 2008).

-
54. Als-Nielsen, J. & McMorrow, D. *Elements of modern X-ray physics* (John Wiley & Sons, 2011).
 55. Spieß, L., Behnken, H., Genzel, C., Schwarzer, R. & Teichert, G. *Moderne Röntgenbeugung* (Vieweg+Teubner, 2009).
 56. Birkholz, M. *Thin film analysis by X-ray scattering* (John Wiley & Sons, 2006).
 57. Von Röntgenstrahlung, B. *Moderne Röntgenbeugung* (Springer).
 58. Von Laue, M. Concerning the detection of X-ray interferences. *Nobel lecture 13* (1915).
 59. Friedrich, W., Knipping, P., Laue, M. v. & bei Röntgenstrahlen, I.-E. *Sitzungsberichte der Mathematisch-Physikalischen Classe der Königlich-Bayerischen Akademie der Wissenschaften zu München* 1912.
 60. Ewald, P. P. VII. Das „reziproke Gitter“ in der Strukturtheorie. *Zeitschrift für Kristallographie – Crystalline Materials* **56**, 129–156 (1921).
 61. Bragg, W. H. & Bragg, W. L. The reflection of X-rays by crystals. *Proceedings of the Royal Society of London. Series A, Containing Papers of a Mathematical and Physical Character* **88**, 428–438 (1913).
 62. Prince, E. & Wilson, A. J. C. *International tables for crystallography* (Kluwer, 2004).
 63. Stephens, P. W. Phenomenological model of anisotropic peak broadening in powder diffraction. *Journal of Applied Crystallography* **32**, 281–289 (1999).
 64. Maul, M. *et al.* Epitaxial CeO₂ buffer layers for YBa₂Cu₃O_{7-δ} films on sapphire. *Journal of applied physics* **74**, 2942–2944 (1993).
 65. Porod, G. The x-ray small-angle scattering of close-packed colloid systems. *Kolloid Zeitschrift* **124**, 32 (1951).
 66. Kiessig, H. Interferenz von Röntgenstrahlen an dünnen Schichten. *Physik* **10**, 715 (1931).
 67. Cheary, R. W. & Coelho, A. A fundamental parameters approach to X-ray line-profile fitting. *Journal of Applied Crystallography* **25**, 109–121 (1992).
 68. Cheary, R. W., Coelho, A. A. & Cline, J. P. Fundamental Parameters Line Profile Fitting in Laboratory Diffractometers. *Journal of Research of the National Institute of Standards and Technology* **109**, 1–25 (2004).
 69. Rietveld, H. M. The rietveld method. *Physica Scripta* **89**, 098002 (2014).
 70. Rietveld, H. Line profiles of neutron powder-diffraction peaks for structure refinement. *Acta Crystallographica* **22**, 151–152 (1967).

-
-
71. Rietveld, H. M. A profile refinement method for nuclear and magnetic structures. *Journal of applied Crystallography* **2**, 65–71 (1969).
 72. Young, R. A. *The rietveld method* (Oxford university press Oxford, 1993).
 73. AXS, B. TOPAS V6. Karlsruhe, Germany (2016).
 74. Lasia, A. *Electrochemical impedance spectroscopy and its applications* 143–248 (Springer, Boston, MA, 2002).
 75. Adler, S. B., Lane, J. A. & Steele, B. C. H. Electrode kinetics of porous mixed-conducting oxygen electrodes. *Journal of the Electrochemical Society* **143**, 3554–3564 (1996).
 76. Irvine, J. T. S., Sinclair, D. C. & West, A. R. Electroceramics: Characterization by Impedance Spectroscopy. *Advanced Materials* **2**, 132–138 (1990).
 77. Lukács, Z. The numerical evaluation of the distortion of EIS data due to the distribution of parameters. *Journal of Electroanalytical Chemistry* **432**, 79–83 (1997).
 78. Lukacs, Z. Evaluation of model and dispersion parameters and their effects on the formation of constant-phase elements in equivalent circuits. *Journal of Electroanalytical Chemistry* **464**, 68–75 (1999).
 79. Macdonald, J. R. Generalizations of “universal dielectric response” and a general distribution-of-activation-energies model for dielectric and conducting systems. *Journal of applied physics* **58**, 1971–1978 (1985).
 80. Macdonald, J. R. Power-law exponents and hidden bulk relation in the impedance spectroscopy of solids. *Journal of Electroanalytical Chemistry* **378**, 17–29 (1994).
 81. Gerischer, H. Wechselstrompolarisation von Elektroden mit einem potentialbestimmenden Schritt beim Gleichgewichtspotential. *Z. physik. Chem.* **158**, 286–297 (1951).
 82. Koyama, M. *et al.* The mechanism of porous $\text{Sm}_{0.5}\text{Sr}_{0.5}\text{CoO}_3$ cathodes used in solid oxide fuel cells. *Journal of the Electrochemical Society* **148**, A795 (2001).
 83. Wollstadt, S. & Clemens, O. On the Impact of the Degree of Fluorination on the ORR Limiting Processes within Iron Based Catalysts: A Model Study on Symmetrical Films of Barium Ferrate. *Materials (Basel)* **13** (2020).
 84. Darbandi, A. J., Enz, T. & Hahn, H. Synthesis and characterization of nanoparticulate films for intermediate temperature solid oxide fuel cells. *Solid State Ionics* **180**, 424–430 (2009).

-
85. Benel, C. *et al.* Synthesis and characterization of nanoparticulate $\text{La}_{0.6}\text{Sr}_{0.4}\text{CoO}_{3-\delta}$ cathodes for thin-film solid oxide fuel cells. *Journal of Power Sources* **229**, 258–264 (2013).
 86. Djenadic, R. *et al.* Nebulized spray pyrolysis of Al-doped $\text{Li}_7\text{La}_3\text{Zr}_2\text{O}_{12}$ solid electrolyte for battery applications. *Solid State Ionics* **263**, 49–56 (2014).
 87. Xia, B., Lenggoro, I. W. & Okuyama, K. Novel Route to Nanoparticle Synthesis by Salt-Assisted Aerosol Decomposition. *Advanced Materials* **13** (2001).
 88. Lee, S. G., Choi, S. M. & Lee, D. The role of salt in nanoparticle generation by salt-assisted aerosol method: Microstructural changes. *Thermochimica Acta* **455**, 138–147 (2007).
 89. Panatarani, C., Lenggoro, I. W. & Okuyama, K. Synthesis of single crystalline ZnO nanoparticles by salt-assisted spray pyrolysis. *Journal of Nanoparticle Research* **5**, 47–53 (2003).
 90. Serrador, L. *et al.* Chlorine Insertion Promoting Iron Reduction in Ba-Fe Hexagonal Perovskites: Effect on the Structural and Magnetic Properties. *Inorganic Chemistry* **55**, 6261–70 (2016).
 91. Johnson, W. A. & Mehl, R. F. Reaction Kinetics in Processes of Nucleation and Growth. *Transactions of the American Institute of Mining and Metallurgical Engineers* **135**, 416–442 (1939).
 92. Málek, J. The applicability of Johnson-Mehl-Avrami model in the thermal analysis of the crystallization kinetics of glasses. *Thermochimica Acta* **267**, 61–73 (1995).
 93. Richter, J., Holtappels, P., Graule, T., Nakamura, T. & Gauckler, L. J. Materials design for perovskite SOFC cathodes. *Monatshefte für Chemie - Chemical Monthly* **140**, 985–999 (2009).
 94. Zhou, W., Ran, R. & Shao, Z. Progress in understanding and development of $\text{Ba}_{0.5}\text{Sr}_{0.5}\text{Co}_{0.8}\text{Fe}_{0.2}\text{O}_{3-\delta}$ -based cathodes for intermediate-temperature solid-oxide fuel cells: A review. *Journal of Power Sources* **192**, 231–246 (2009).
 95. Mastrikov, Y. A., Kuklja, M. M., Kotomin, E. A. & Maier, J. First-principles modelling of complex perovskite $(\text{Ba}_{1-x}\text{Sr}_x)(\text{Co}_{1-y}\text{Fe}_y)\text{O}_{3-\delta}$ for solid oxide fuel cell and gas separation membrane applications. *Energy & Environmental Science* **3** (2010).
 96. Tong, J. Investigation of ideal zirconium-doped perovskite-type ceramic membrane materials for oxygen separation. *Journal of Membrane Science* **203**, 175–189 (2002).
 97. Vieten, J. *et al.* Perovskite oxides for application in thermochemical air separation and oxygen storage. *Journal of Materials Chemistry A* **4**, 13652–13659 (2016).

-
98. Mats, J. & Lemmens, P. *Crystallography and Chemistry of Perovskites* (John Wiley & Sons, Ltd, 2007).
 99. Zhu, J. *et al.* Unprecedented Perovskite Oxyfluoride Membranes with High-Efficiency Oxygen Ion Transport Paths for Low-Temperature Oxygen Permeation. *Advanced Materials* **28**, 3511–5 (2016).
 100. Dai, H. X., Ng, C. F. & Au, C. T. The catalytic performance and characterization of a durable perovskite-type chloro-oxide $\text{SrFeO}_{3-\delta}\text{Cl}_\sigma$ catalyst selective for the oxidative dehydrogenation of ethane. *Catalysis Letters* **57**, 115–120 (1999).
 101. Dai, H. X., Ng, C. F. & Au, C. T. Perovskite-Type Halo-oxide $\text{La}_{1-x}\text{Sr}_x\text{FeO}_{3-\delta}\text{X}_\sigma$ (X=F, Cl) Catalysts Selective for the Oxidation of Ethane to Ethene. *Journal of Catalysis* **189**, 52–62 (2000).
 102. Yin, W.-J., Yang, J.-H., Kang, J., Yan, Y. & Wei, S.-H. Halide perovskite materials for solar cells: a theoretical review. *Journal of Materials Chemistry A* **3**, 8926–8942 (2015).
 103. Colville, A. A. & Geller, S. The crystal structure of brownmillerite, $\text{Ca}_2\text{FeAlO}_5$. *Acta Crystallographica Section B Structural Crystallography and Crystal Chemistry* **27**, 2311–2315 (1971).
 104. Shin, S., Yonemura, M. & Ikawa, H. Order-disorder transition of $\text{Sr}_2\text{Fe}_2\text{O}_5$ from brownmillerite to perovskite structure at an elevated temperature. *Materials Research Bulletin* **13**, 1017–1021 (1978).
 105. Gallagher, P. K., MacChesney, J. B. & Buchanan, D. N. E. Mössbauer Effect in the System $\text{BaFeO}_{2.5-3.0}$. *The Journal of Chemical Physics* **43**, 516–520 (1965).
 106. MacChesney, J. B., Sherwood, R. C. & Potter, J. F. Electric and Magnetic Properties of the Strontium Ferrates. *The Journal of Chemical Physics* **43**, 1907–1913 (1965).
 107. Köhler, J. Square-Planar Coordinated Iron in the Layered Oxoferrate (II) SrFeO_2 . *Angewandte Chemie International Edition* **47**, 4470–4472 (2008).
 108. Yamamoto, T. *et al.* $(\text{Sr}_{1-x}\text{Ba}_x)\text{FeO}_2$ ($0.4 \leq x \leq 1$): A New Oxygen-Deficient Perovskite Structure. *Journal of the American Chemical Society* **134**, 11444–11454 (2012).
 109. Parras, M. *et al.* Structural aspects and Mössbauer resonance investigation of $\text{Ba}_2\text{Fe}_2\text{O}_5$. *Journal of Solid State Chemistry* **88**, 261–268 (1990).
 110. Parras, M. *et al.* A reassessment of $\text{Ba}_2\text{Fe}_2\text{O}_5$. *Materials research bulletin* **22**, 1413–1419 (1987).

-
-
111. Mori, S. Phase Transformation in Barium Orthoferrate, BaFeO_{3-x} . *Journal of the American Ceramic Society* **49**, 600–605 (1966).
 112. Suga, Y., Hibino, M., Kudo, T. & Mizuno, N. Electrochemical Oxidation of $\text{BaFeO}_{2.5}$ to BaFeO_3 . *Electrochimica Acta* **137**, 359–362 (2014).
 113. Lucchini, E., Meriani, S. & Minichelli, D. An X-ray study of two phases of BaFeO_{3-x} . *Acta Crystallographica Section B Structural Crystallography and Crystal Chemistry* **29**, 1217–1219 (1973).
 114. Gómez, M. I. *et al.* Ab Initio Structure Solution of $\text{BaFeO}_{2.8-\delta}$, a New Polytype in the System BaFeO_y ($2.5 \leq y \leq 3.0$) Prepared from the Oxidative Thermal Decomposition of $\text{BaFe}[(\text{CN})_5\text{NO}] \cdot 3\text{H}_2\text{O}$. *Journal of Solid State Chemistry* **160**, 17–24 (2001).
 115. Goldschmidt, V. M. Die Gesetze der Krystallochemie. *Die Naturwissenschaften* **14**, 477–485 (1926).
 116. Clemens, O., Reitz, C., Witte, R., Kruk, R. & Smith, R. I. Anion ordering, magnetic structure and properties of the vacancy ordered perovskite $\text{Ba}_3\text{Fe}_3\text{O}_7\text{F}$. *Journal of Solid State Chemistry* **243**, 31–37 (2016).
 117. Benes, A. *et al.* Proton Conduction in Grain-Boundary-Free Oxygen-Deficient $\text{BaFeO}_{2.5+d}$ Thin Films. *Materials (Basel)* **11** (2017).
 118. Knöchel, P. L. *et al.* Synthesis, structural characterisation and proton conduction of two new hydrated phases of barium ferrite $\text{BaFeO}_{2.5-x}(\text{OH})_{2x}$. *Journal of Materials Chemistry A* **4**, 3415–3430 (2016).
 119. Rahman, G. & Sarwar, S. Ground State Structure of BaFeO_3 : Density Functional Theory Calculations. *Journal of Superconductivity and Novel Magnetism* **31**, 413–418 (2017).
 120. Niu, Y. *et al.* A single-step synthesized cobalt-free barium ferrites-based composite cathode for intermediate temperature solid oxide fuel cells. *Electrochemistry Communications* **13**, 1340–1343 (2011).
 121. Masunaga, T., Izumi, J. & Miura, N. Reversible change in crystal structure of Ba (or Sr) $\text{FeO}_{3-\delta}$ associated with oxygen sorption/desorption by pressure variation. *Journal of the Ceramic Society of Japan* **118**, 952–954 (2010).
 122. Blöchl, P. E. Projector augmented-wave method. *Physical Review B* **50**, 17953 (1994).

-
123. Kresse, G. & Furthmüller, J. Efficiency of ab-initio total energy calculations for metals and semiconductors using a plane-wave basis set. *Computational materials science* **6**, 15–50 (1996).
 124. Kresse, G. & Joubert, D. From ultrasoft pseudopotentials to the projector augmented-wave method. *Physical Review B* **59**, 1758 (1999).
 125. Methfessel, M. & Paxton, A. High-precision sampling for Brillouin-zone integration in metals. *Physical Review B* **40**, 3616 (1989).
 126. Dudarev, S., Botton, G., Savrasov, S., Humphreys, C. & Sutton, A. Electron-energy-loss spectra and the structural stability of nickel oxide: An LSDA+ U study. *Physical Review B* **57**, 1505 (1998).
 127. Bader, R. F. W. *Atoms in Molecules. A Quantum Theory.* (Reihe: International Series of Monographs on Chemistry, Vol. 22.) Clarendon Press, Oxford, 1990. XVIII, 438 S., geb. £ 50.00.–ISBN 0-19-855168-1 1992.
 128. Yu, M. & Trinkle, D. R. Accurate and efficient algorithm for Bader charge integration. *The Journal of chemical physics* **134**, 064111 (2011).
 129. Henkelman, G., Arnaldsson, A. & Jónsson, H. A fast and robust algorithm for Bader decomposition of charge density. *Computational Materials Science* **36**, 354–360 (2006).
 130. Sanville, E., Kenny, S. D., Smith, R. & Henkelman, G. Improved grid-based algorithm for Bader charge allocation. *Journal of computational chemistry* **28**, 899–908 (2007).
 131. Tang, W., Sanville, E. & Henkelman, G. A grid-based Bader analysis algorithm without lattice bias. *Journal of Physics: Condensed Matter* **21**, 084204 (2009).
 132. Ribeiro, B., Godinho, M., Cardoso, C., Borges, R. & Gasche, T. Self-doping and the role of oxygen vacancies in the magnetic properties of cubic BaFeO_{3-δ}. *Journal of Applied Physics* **113** (2013).
 133. Cherair, I., Iles, N., Rabahi, L. & Kellou, A. Effects of Fe substitution by Nb on physical properties of BaFeO₃: A DFT+U study. *Computational Materials Science* **126**, 491–502 (2017).
 134. Cherair, I., Bousquet, E., Schmitt, M. M., Iles, N. & Kellou, A. First-principles study of strain-induced Jahn–Teller distortions in BaFeO₃. *Journal of Physics: Condensed Matter* **30**, 255701 (2018).
 135. Clevenger Jr, T. R. Effect of Fe⁴⁺ in the System SrFeO₃–SrTiO₃. *Journal of the American Ceramic Society* **46**, 207–210 (1963).

-
136. Nassau, K. A model for the Fe^{2+} - Fe^{4+} equilibrium in flux-grown yttrium iron garnet. *Journal of Crystal Growth* **2**, 215–221 (1968).
137. Waidha, A. I. *et al.* Structural, Magnetic and Catalytic Properties of a New Vacancy Ordered Perovskite Type Barium Cobaltate $\text{BaCoO}_{2.67}$. *Chemistry – A European Journal*.
138. Wollstadt, S., De Souza, R. A. & Clemens, O. Kinetic Study of the Interdiffusion of Fluorine and Oxygen in the Perovskite-Type Barium Ferrate System $\text{BaFeO}_{2.5-x}\text{F}_{2x}$. *The Journal of Physical Chemistry C* **125**, 2287–2298 (2021).
139. Li, Z., Laskowski, R., Iitaka, T. & Tohyama, T. First-principles calculation of helical spin order in iron perovskite SrFeO_3 and BaFeO_3 . *Physical Review B* **85**, 134419 (13 2012).
140. Jeannot, C., Malaman, B., Gerardin, R. & Oulladiaf, B. Synthesis, crystal and magnetic structures of the sodium ferrate (IV) Na_4FeO_4 studied by neutron diffraction and Mössbauer techniques. *Journal of Solid State Chemistry* **165**, 266–277 (2002).
141. Delattre, J. L. *et al.* Study of the structural, electronic, and magnetic properties of the barium-rich iron (IV) oxides, Ba_2FeO_4 and Ba_3FeO_5 . *Inorganic Chemistry* **41**, 2834–2838 (2002).
142. Takano, M. & Takeda, Y. Electronic State of Fe^{4+} Ions in Perovskite-Type Oxides. *Bulletin of the Institute for Chemical Research, Kyoto University* **61**, 406–425 (1983).
143. Hosaka, Y. *et al.* Two-dimensional charge disproportionation of the unusual high valence state Fe^{4+} in a layered double perovskite. *Journal of the American Chemical Society* **137**, 7468–7473 (2015).
144. Vračar, M. *et al.* Jahn-Teller distortion around Fe^{4+} in $\text{Sr}(\text{Fe}_x\text{Ti}_{1-x})\text{O}_{3-\delta}$ from X-ray absorption spectroscopy, X-ray diffraction, and vibrational spectroscopy. *Physical Review B* **76**, 174107 (2007).
145. Luo, K. *et al.* $\text{Ba}_2\text{YFeO}_{5.5}$: A Ferromagnetic Pyroelectric Phase Prepared by Topochemical Oxidation. *Chemistry of Materials* **25**, 1800–1808 (2013).
146. Hodges, J. *et al.* Evolution of oxygen-vacancy ordered crystal structures in the perovskite series $\text{Sr}_n\text{Fe}_n\text{O}_{3n-1}$ ($n = 2, 4, 8$, and ∞), and the relationship to electronic and magnetic properties. *Journal of Solid State Chemistry* **151**, 190–209 (2000).
147. Waerenborgh, J. *et al.* Fe^{4+} formation in brownmillerite $\text{CaAl}_{0.5}\text{Fe}_{0.5}\text{O}_{2.5+\delta}$. *Materials Letters* **57**, 4388–4393 (2003).
148. Bland, J. The crystal structure of barium orthotitanate, Ba_2TiO_4 . *Acta Crystallographica* **14**, 875–881 (1961).

-
149. Chamberland, B., Herrero-Fernandez, M. & Hewston, T. Magnetic behavior of tetrahedral Cr⁴⁺ compounds: Sr₂CrO₄, Ba₂CrO₄, and Ba₃CrO₅. *Journal of Solid State Chemistry* **59**, 111–115 (1985).
150. Dann, S., Weller, M. & Currie, D. The synthesis and structure of Sr₂FeO₄. *Journal of Solid State Chemistry* **92**, 237–240 (1991).
151. Mattausch, H. & Müller-Buschbaum, H. Zur Kenntnis von Ba₂CoO₄. *Zeitschrift für anorganische und allgemeine Chemie* **386**, 1–14 (1971).
152. Mattausch, H. & Müller-Buschbaum, H. Zur Kristallstruktur von Ba₂CrO₄. *Zeitschrift für anorganische und allgemeine Chemie* **407**, 129–134 (1974).
153. Feltz, A. & Schmalfuß, S. Untersuchungen an elektronenleitenden Oxidsystemen; Zur Darstellung der Verbindungen Ba₂VO₄ und Sr₂VO₄ und die Reduktion von Ca₂V₂O₇ im H₂-Strom. *Zeitschrift für Chemie* **15**, 289–291 (1975).
154. Liu, G. & Greedan, J. Synthesis and Characterization of Ba₂VO₄ with the β-Ca₂SiO₄ Structure: Comparison with Sr₂VO₄. *Journal of Solid State Chemistry* **103**, 228–239 (1993).
155. Brown, I. & Altermatt, D. Bond-valence parameters obtained from a systematic analysis of the inorganic crystal structure database. *Acta Crystallographica Section B: Structural Science* **41**, 244–247 (1985).
156. Koch, D. & Manzhos, S. On the charge state of titanium in titanium dioxide. *The Journal of Physical Chemistry Letters* **8**, 1593–1598 (2017).
157. Walsh, A., Sokol, A. A., Buckeridge, J., Scanlon, D. O. & Catlow, C. R. A. Oxidation states and ionicity. *Nature Materials* **17**, 958–964 (2018).
158. Mori, S. Preparation of Various Phases of BaFeO_{3-x}. *Journal of the American Ceramic Society* **48**, 165–165 (1965).
159. Nair, A. *et al.* Synthesis and characterisation of fluorinated epitaxial films of BaFeO₂F: tailoring magnetic anisotropy via a lowering of tetragonal distortion. *RSC Advances* **9**, 37136–37143 (2019).
160. Wollan, E. & Koehler, W. Neutron diffraction study of the magnetic properties of the series of perovskite-type Compounds [(1 - x)La,xCa]MnO₃. *Physical Review* **100**, 545 (1955).
161. Clemens, O. *et al.* Magnetic interactions in cubic-, hexagonal- and trigonal-barium iron oxide fluoride, BaFeO₂F. *J Phys Condens Matter* **28**, 346001 (2016).
162. Chen, Y. *et al.* Advances in Cathode Materials for Solid Oxide Fuel Cells: Complex Oxides without Alkaline Earth Metal Elements. *Advanced Energy Materials* **5** (2015).

-
163. Ding, D., Li, X., Lai, S. Y., Gerdes, K. & Liu, M. Enhancing SOFC cathode performance by surface modification through infiltration. *Energy & Environmental Science* **7** (2014).
164. Leng, Y., Chan, S., Jiang, S. & Khor, K. Low-temperature SOFC with thin film GDC electrolyte prepared in situ by solid-state reaction. *Solid State Ionics* **170**, 9–15 (2004).
165. Gao, P. *et al.* VOCl as a Cathode for Rechargeable Chloride Ion Batteries. *Angewandte Chemie International Edition* **55**, 4285–90 (2016).
166. Chen, L., Zhuang, L., Xue, J., Wei, Y. & Wang, H. Tuning the separation performance of hydrogen permeable membranes using an anion doping strategy. *Journal of Materials Chemistry A* **5**, 20482–20490 (2017).
167. Dong, F., Chen, Y., Chen, D. & Shao, Z. Surprisingly high activity for oxygen reduction reaction of selected oxides lacking long oxygen-ion diffusion paths at intermediate temperatures: a case study of cobalt-free BaFeO_{3-δ}. *ACS Applied Materials & Interfaces* **6**, 11180–9 (2014).
168. Moon, E. J. *et al.* Fluorination of epitaxial oxides: synthesis of perovskite oxyfluoride thin films. *J Am Chem Soc* **136**, 2224–7 (2014).
169. Greaves, C. & Francesconi, M. G. Fluorine insertion in inorganic materials. *Current Opinion in Solid State and Materials Science* **3**, 132–136 (1998).
170. Burbano, M. *et al.* Oxygen Vacancy Ordering and the Conductivity Maximum in Y₂O₃-Doped CeO₂. *Chemistry of Materials* **24**, 222–229 (2011).
171. Hagiwara, T., Yamamura, H. & Nishino, H. Relationship between oxide-ion conductivity and ordering of oxygen vacancy in the Ln₂Zr₂O₇ (Ln = La, Nd, Eu) system having a pyrochlore composition. *IOP Conference Series: Materials Science and Engineering* **18** (2011).
172. Bouwmeester, H. J. M., Den Otter, M. W. & Boukamp, B. A. Oxygen transport in La_{0.6}Sr_{0.4}Co_{1-y}Fe_yO_{3-δ}. *Journal of Solid State Electrochemistry* **8**, 599–605 (2004).
173. Grenier, J. C. *et al.* Sur le système BaFeO_{3-y} (0 < y ≤ 0.50). *Journal of Solid State Chemistry* **80**, 6–11 (1989).
174. Waidha, A. I. *et al.* Synthesis of bifunctional BaFe_{1-x}Co_xO_{3-y-δ}(OH)_y catalysts for the oxygen reduction reaction and oxygen evolution reaction. *Journal of Materials Chemistry A* **8**, 616–625 (2020).
175. Sukkurji, P. A. *et al.* Anion Doping of Ferromagnetic Thin Films of La_{0.74}Sr_{0.26}MnO_{3-d} via Topochemical Fluorination. *Materials (Basel)* **11** (2018).

-
176. Katayama, T. *et al.* Topotactic fluorination of strontium iron oxide thin films using polyvinylidene fluoride. *Journal of Materials Chemistry C* **2**, 5350–5356 (2014).
177. Fujishiro, F., Fukasawa, K., Hashimoto, T. & Chou, K. CO₂ Absorption and Desorption Properties of Single Phase Ba₂Fe₂O₅ and Analysis of Their Mechanism Using Thermodynamic Calculation. *Journal of the American Ceramic Society* **94**, 3675–3678 (2011).
178. Darbandi, A. J. & Hahn, H. Nanoparticulate cathode thin films with high electrochemical activity for low temperature SOFC applications. *Solid State Ionics* **180**, 1379–1387 (2009).
179. Iga, F., Nishihara, Y., Katayama, T., Murata, K. & Takeda, Y. Magnetic and transport properties of BaFeO_{3-y}. *Journal of Magnetism and Magnetic Materials* **104-107**, 1973–1975 (1992).
180. Sturza, M., Daviero-Minaud, S., Kabbour, H., Gardoll, O. & Mentré, O. Fluorination of Iron Hexagonal Perovskites Promoting Low Temperature Oxygen Mobility. *Chemistry of Materials* **22**, 6726–6735 (2010).
181. Anderson, M. D., Stevenson, J. W. & Simner, S. P. Reactivity of lanthanide ferrite SOFC cathodes with YSZ electrolyte. *Journal of Power Sources* **129**, 188–192 (2004).
182. Duan, Z. *et al.* Ba_{0.5}Sr_{0.5}Co_{0.8}Fe_{0.2}O_{3-δ} as a cathode for IT-SOFCs with a GDC interlayer. *Journal of Power Sources* **160**, 57–64 (2006).
183. Leonide, A., Rüger, B., Weber, A., Meulenberg, W. A. & Ivers-Tiffée, E. Impedance Study of Alternative (La,Sr)FeO_{3-δ} and (La,Sr)(Co,Fe)O_{3-δ} MIEC Cathode Compositions. *Journal of The Electrochemical Society* **157** (2010).
184. Lim, Y. H., Lee, J., Yoon, J. S., Kim, C. E. & Hwang, H. J. Electrochemical performance of Ba_{0.5}Sr_{0.5}Co_xFe_{1-x}O_{3-δ} (x=0.2–0.8) cathode on a ScSZ electrolyte for intermediate temperature SOFCs. *Journal of Power Sources* **171**, 79–85 (2007).
185. Boukamp, B. A. & Bouwmeester, H. J. M. Interpretation of the Gerischer impedance in solid state ionics. *Solid State Ionics* **157**, 29–33 (2003).
186. Flura, A. *et al.* Application of the Adler-Lane-Steele Model to Porous La₂NiO_{4+δ} SOFC Cathode: Influence of Interfaces with Gadolinia Doped Ceria. *Journal of The Electrochemical Society* **163**, F523–F532 (2016).
187. Adler, S., Chen, X. & Wilson, J. Mechanisms and rate laws for oxygen exchange on mixed-conducting oxide surfaces. *Journal of Catalysis* **245**, 91–109 (2007).
188. Horita, T. *et al.* Imaging of oxygen transport at SOFC cathode/electrolyte interfaces by a novel technique. *Journal of Power Sources* **106**, 224–230 (2002).

-
189. Catalan, G. & Scott, J. F. Physics and applications of bismuth ferrite. *Advanced Materials* **21**, 2463–2485 (2009).
190. Cheng, X., Wang, X., Yang, H., Ruan, K. & Li, X. Multiferroic properties of the layered perovskite-related oxide $\text{La}_6(\text{Ti}_{0.67}\text{Fe}_{0.33})_6\text{O}_{20}$. *Journal of Materials Chemistry C* **3**, 4482–4489 (2015).
191. Ma, J., Hu, J., Li, Z. & Nan, C.-W. Recent progress in multiferroic magnetoelectric composites: from bulk to thin films. *Advanced Materials* **23**, 1062–1087 (2011).
192. Rao, C. Perovskite oxides and high-temperature superconductivity. *Ferroelectrics* **102**, 297–308 (1990).
193. Raveau, B., Maignan, A., Martin, C. & Hervieu, M. Colossal magnetoresistance manganese perovskites: relations between crystal chemistry and properties. *Chemistry of Materials* **10**, 2641–2652 (1998).
194. Imada, M., Fujimori, A. & Tokura, Y. Metal-insulator transitions. *Reviews of Modern Physics* **70**, 1039 (1998).
195. Hayward, M. A. & Rosseinsky, M. J. Cool conditions for mobile ions. *Nature* **450**, 960–961 (2007).
196. Yajima, T. *et al.* Epitaxial thin films of $\text{ATiO}_{3-x}\text{H}_x$ (A= Ba, Sr, Ca) with metallic conductivity. *Journal of the American Chemical Society* **134**, 8782–8785 (2012).
197. Wissel, K. *et al.* Topochemical fluorination of $\text{La}_2\text{NiO}_{4+d}$: Unprecedented ordering of oxide and fluoride ions in $\text{La}_2\text{NiO}_3\text{F}_2$. *Inorganic Chemistry* **57**, 6549–6560 (2018).
198. Yoon, S., Son, K., Ebbinghaus, S. G., Widenmeyer, M. & Weidenkaff, A. Ferromagnetism in nitrogen and fluorine substituted BaTiO_3 . *Journal of Alloys and Compounds* **749**, 628–633 (2018).
199. Kawahara, K. *et al.* Topotactic fluorination of perovskite strontium ruthenate thin films using polyvinylidene fluoride. *CrystEngComm* **19**, 313–317 (2017).
200. Chikamatsu, A. *et al.* Selective fluorination of perovskite iron oxide/ruthenium oxide heterostructures via a topotactic reaction. *Chemical Communications* **55**, 2437–2440 (2019).
201. Copie, O. *et al.* Chemical strain engineering of magnetism in oxide thin films. *Advanced Materials* **29**, 1604112 (2017).
202. Zou, X. *et al.* The complex perovskite-related superstructure $\text{Ba}_2\text{Fe}_2\text{O}_5$ solved by HREM and CIP. *Acta Crystallographica Section A: Foundations of Crystallography* **49**, 27–35 (1993).

-
-
203. Berry, F. J. *et al.* Structure and magnetic properties of the cubic oxide fluoride BaFeO₂F. *Journal of Solid State Chemistry* **184**, 1361–1366 (2011).
 204. Sukkurji, P. A. *et al.* Structure and conductivity of epitaxial thin films of barium ferrite and its hydrated form BaFeO_{2.5-x+δ}(OH)_{2x}. *Journal of Physics D: Applied Physics* **50**, 115302 (2017).
 205. Wissel, K. *et al.* Developing intercalation based anode materials for fluoride-ion batteries: topochemical reduction of Sr₂TiO₃F₂ via a hydride based defluorination process. *Journal of Materials Chemistry A* **6**, 22013–22026 (2018).
 206. Berry, F. J. *et al.* Magnetic order in perovskite-related SrFeO₂F. *Journal of Physics: Condensed Matter* **20**, 215207 (2008).
 207. Clemens, O. *et al.* A neutron diffraction study and mode analysis of compounds of the system La_{1-x}Sr_xFeO_{3-x}F_x (x=1, 0.8, 0.5, 0.2) and an investigation of their magnetic properties. *Journal of Solid State Chemistry* **206**, 158–169 (2013).
 208. Takeiri, F. *et al.* AgFeOF₂: A fluorine-rich perovskite oxyfluoride. *Inorganic Chemistry* **57**, 6686–6691 (2018).
 209. Nowroozi, M. A., Wissel, K., Rohrer, J., Munnangi, A. R. & Clemens, O. LaSrMnO₄: Reversible Electrochemical Intercalation of Fluoride Ions in the Context of Fluoride Ion Batteries. *Chemistry of Materials* **29**, 3441–3453 (2017).
 210. McIntosh, S., Vente, J., Haije, W., Blank, D. & Bouwmeester, H. Structure and oxygen stoichiometry of SrCo_{0.8}Fe_{0.2}O_{3-δ} and Ba_{0.5}Sr_{0.5}Co_{0.8}Fe_{0.2}O_{3-δ}. *Solid State Ionics* **177**, 1737–1742 (2006).
 211. Mueller, D. N., De Souza, R. A., Yoo, H.-I. & Martin, M. Phase Stability and Oxygen Nonstoichiometry of Highly Oxygen-Deficient Perovskite-Type Oxides: A Case Study of (Ba,Sr)(Co,Fe)O_{3-δ}. *Chemistry of Materials* **24**, 269–274 (2012).
 212. Zhi-Xiong, C. & Yimei, Z. Dislocation-assisted-diffusion model for the kinetics of bismuth cuprate 2212-to-2223 transformation. *IEEE Transactions on Applied Superconductivity* **9**, 2714–2717 (1999).
 213. Christian, J. W. *The Theory of Transformations in Metals and Alloys* (Pergamon, Oxford, 2002).
 214. Mueller, D. N. *et al.* A kinetic study of the decomposition of the cubic perovskite-type oxide Ba_{1-x}Sr_xCo_{0.8}Fe_{0.2}O_{3-d} (BSCF) (x = 0.1 and 0.5). *Phys Chem Chem Phys* **12**, 10320–8 (2010).

-
215. De Souza, R. A. & Barboni, D. Iodide-ion conduction in methylammonium lead iodide perovskite: some extraordinary aspects. *Chemical Communications* **55**, 1108–1111 (2019).
216. De Souza, R. A. Limits to the rate of oxygen transport in mixed-conducting oxides. *Journal of Materials Chemistry A* **5**, 20334–20350 (2017).
217. Sturza, M. *et al.* High dilution of anionic vacancies in $\text{Sr}_{0.8}\text{Ba}_{0.2}\text{Fe}(\text{O},\text{F})_{2.5}$. *Inorganic Chemistry* **50**, 12499–12507 (2011).
218. Sturza, M. *et al.* Unprecedented robust antiferromagnetism in fluorinated hexagonal perovskites. *Journal of the American Chemical Society* **133**, 10901–10909 (2011).
219. Shannon, R. D. Revised effective ionic radii and systematic studies of interatomic distances in halides and chalcogenides. *Acta Crystallographica Section A* **32**, 751–767 (1976).
220. Maznichenko, I. V. *et al.* Impact of oxygen doping and oxidation state of iron on the electronic and magnetic properties of $\text{BaFeO}_{3-\delta}$. *Physical Review B* **93** (2016).
221. Garvie, R. C. The occurrence of metastable tetragonal zirconia as a crystallite size effect. *The Journal of Physical Chemistry* **69**, 1238–1243 (1965).
222. Garvie, R. Stabilization of the tetragonal structure in zirconia microcrystals. *The Journal of Physical Chemistry* **82**, 218–224 (1978).
223. Stichert, W. & Schüth, F. Influence of crystallite size on the properties of zirconia. *Chemistry of Materials* **10**, 2020–2026 (1998).
224. D’Innocenzo, V., Srimath Kandada, A. R., De Bastiani, M., Gandini, M. & Petrozza, A. Tuning the light emission properties by band gap engineering in hybrid lead halide perovskite. *Journal of the American Chemical Society* **136**, 17730–17733 (2014).
225. Friedrich, M. & Armbrüster, M. Crystallite Size Controls the Crystal Structure of $\text{Cu}_{60}\text{Pd}_{40}$ Nanoparticles. *Chemistry of Materials* **21**, 5886–5891 (2009).
226. Bailey, J., Lewis, D., Librant, Z. & Porter, L. Phase transformations in milled zirconia. *Transactions and Journal of the British Ceramic Society* **71**, 25–30 (1972).
227. Mitsuhashi, T., Ichihara, M. & Tatsuke, U. Characterization and stabilization of metastable tetragonal ZrO_2 . *Journal of the American Ceramic Society* **57**, 97–101 (1974).
228. Mattisson, T. Materials for chemical-looping with oxygen uncoupling. *International Scholarly Research Notices* **2013** (2013).

-
229. Zhu, X., Li, K., Neal, L. & Li, F. Perovskites as geo-inspired oxygen storage materials for chemical looping and three-way catalysis: a perspective. *ACS Catalysis* **8**, 8213–8236 (2018).
230. Lau, C. Y., Dunstan, M. T., Hu, W., Grey, C. P. & Scott, S. A. Large scale in silico screening of materials for carbon capture through chemical looping. *Energy & Environmental Science* **10**, 818–831 (2017).
231. Bucher, E., Egger, A., Caraman, G. & Sitte, W. Stability of the SOFC cathode material (Ba,Sr)(Co,Fe)O_{3-δ} in CO₂-containing atmospheres. *Journal of The Electrochemical Society* **155**, B1218 (2008).
232. Yan, A. *et al.* Investigation of a Ba_{0.5}Sr_{0.5}Co_{0.8}Fe_{0.2}O_{3-δ} based cathode IT-SOFC: I. The effect of CO₂ on the cell performance. *Applied Catalysis B: Environmental* **66**, 64–71 (2006).
233. Hu, X. *et al.* Antimony-doped strontium cobalt oxide as promising cathode for low-temperature solid oxide fuel cell with excellent carbon dioxide tolerance. *Applied Catalysis B: Environmental* **286**, 119901 (2021).
234. Wang, W. *et al.* Highly promoted performance of triple-conducting cathode for YSZ-based SOFC via fluorine anion doping. *Ceramics International* **46**, 23964–23971 (2020).
235. Li, H. & Lü, Z. High-performance fluorine-doped cobalt-free oxide as a potential cathode material for solid oxide fuel cells. *International Journal of Hydrogen Energy* **46**, 2503–2510 (2021).
236. Liu, X. *et al.* Lattice characteristics, structure stability and oxygen permeability of BaFe_{1-x}Y_xO_{3-δ} ceramic membranes. *Journal of Membrane Science* **383**, 235–240 (2011).
237. Dong, F. *et al.* An efficient electrocatalyst as cathode material for solid oxide fuel cells: BaFe_{0.95}Sn_{0.05}O_{3-δ}. *Journal of Power Sources* **326**, 459–465 (2016).
238. Xie, Y. *et al.* A Stable and Efficient Cathode for Fluorine-Containing Proton-Conducting Solid Oxide Fuel Cells. *ChemSusChem* **11**, 3423–3430 (2018).
239. Wang, W. *et al.* An excellent OER electrocatalyst of cubic SrCoO_{3-δ} prepared by a simple F-doping strategy. *Journal of Materials Chemistry A* **7**, 12538–12546 (2019).
240. Liu, J. *et al.* A novel anions and cations co-doped strategy for developing high-performance cobalt-free cathode for intermediate-temperature proton-conducting solid oxide fuel cells. *International Journal of Hydrogen Energy* **44**, 11079–11087 (2019).

A. EIS sample holder

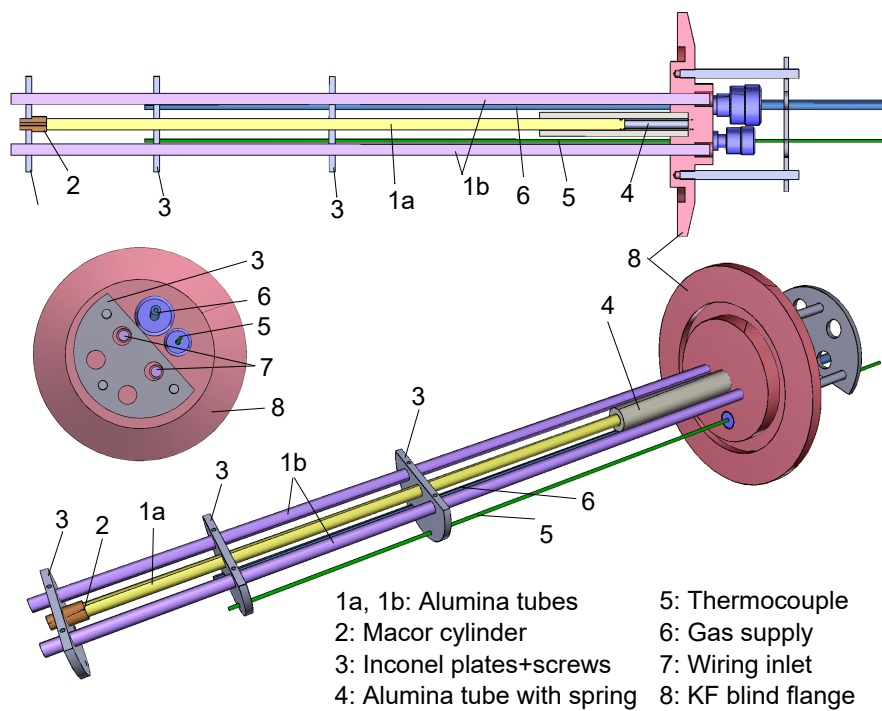


Figure A.1.: EIS sample holder.

Fig. A.1 shows a graphical representation of the sample holder manufactured for the high temperature impedance spectroscopy measurements. The project was conducted in accordance with Jochen Rank and Michael Weber of the workshop. Materials used are indicated within the drawings. The experimental conditions required the usage of high performance materials.

B. TOPAS INP Example

In the following, a commented example INP file for TOPAS 6 will be presented. This INP file was used during the analysis in Sec. 3.4. The file allowed the refinement of a set of about 300 XRD patterns in a short time combined with the extraction of the desired parameters, such as lattice parameters, weight fractions of the observed phases, crystallite sizes, sample displacement and R_{wp} values. Similar INP-files were used in Sec. 3.1

Input file

```
r_exp 15.72714833 r_exp_dash 44.41053135 r_wp 16.06194152 r_wp_dash 45.35592
484 r_p 12.48470217 r_p_dash 46.33541329
weighted_Durbin_Watson 1.935055174 gof 1.021287597
iters 100000 'iterations the refinement is running
do_errors
chi2_convergence_criteria 0.000001

'_____
'Setting a list of cell parameters (prm) for each phase
'_____
'BaFeO2.5
prm a_monoclinic 7.012079158 min =7; max =7.04; update = Val + Change;
prm b_monoclinic 11.75933297 min =11.75; max =11.816; update = Val + Change;
prm c_monoclinic 23.56297285 min =23.532; max =23.6; update = Val + Change;
prm be_monoclinic 98.97225088 min=98.90; max=99.1; update = Val + Change;
prm sc_monoclinic 8.399426949e-008 min =1e-10; max =15e-8; update = Val + Change;

'BaFeO2F
prm a_cubic 4.080132705 min =4.07; max =4.09; update = Val + Change;
prm sc_cubic =3.034023917e-005; min =1e-7; max =1e-4; update = Val + Change;

'BaFeO2.333F0.333
```

```
prm a_oxyfluorid 10.10520876 min =10.100; max =10.16; update = Val + Change;
prm b_oxyfluorid 5.690618311 min =5.67; max =5.76; update = Val + Change;
prm c_oxyfluorid 6.988258929 min =6.9; max =7.03; update = Val + Change;
prm be_oxyfluorid 93.33983537 min =92.9; max =93.34; update = Val + Change;
prm sc_oxyfluorid 6.79337935e-008 min =1e-9; max =8e-6; update = Val + Change;
```

```
'---additional parameters for the refinement---
```

```
prm sd -0.257524692 min =-0.28; max =0; update = Val + Change;
```

```
prm beq -0.08 min=-3; max=1.5; update = Val + Change;
```

```
prm csl 100 min=80; max=10000; update = Val + Change;
```

```
prm csg 100 min=80; max=10000; update = Val + Change;
```

```
prm rn = Run_Number;
```

```
num_runs 300
```

```
'_____
```

```
'Setting the output commands. First the file, then the data (parameter+output format)
```

```
'_____
```

```
out 380dC_results1.txt append
```

```
Out(rn,"%5.0f") Out(a_monoclinic,"%12.6f", "%12.6f") Out(b_monoclinic,"%12.6f", "%12.6f") Out(c_monoclinic,"%12.6f", "%12.6f") Out(be_monoclinic,"%12.6f", "%12.6f") Out(v_monoclinic,"%12.6f") Out(sc_monoclinic,"%24.20f") Out(wp_monoclinic,"%12.6f", "%12.6f") Out(a_cubic,"%12.6f", "%12.6f") Out(v_cubic,"%12.6f") Out(sc_cubic,"%24.20f") Out(wp_cubic,"%12.6f", "%12.6f") Out(a_oxyfluorid,"%12.6f", "%12.6f") Out(b_oxyfluorid,"%12.6f", "%12.6f") Out(c_oxyfluorid,"%12.6f", "%12.6f") Out(be_oxyfluorid,"%12.6f", "%12.6f") Out(v_oxyfluorid,"%12.6f") Out(sc_oxyfluorid,"%24.20f") Out(wp_oxyfluorid,"%12.6f", "%12.6f") Out(sd,"%12.6f") Out(csl,"%7.1f") Out(beq,"%12.6f", "\n")
```

```
out 380dC_rwpkof.txt append
```

```
Out(Get(r_wp), "%6.2f") Out(Get(gof), "%6.2f", "\n")
```

```
'_____
```

```
'Loading of the XRD pattern
```

```
'_____
```

```

xdd X:\Stephan\Kinetik\380dC\380dc_100h.raw
r_exp 15.72714833 r_exp_dash 44.41053135 r_wp 16.06194152 r_wp_dash 45.35592484
r_p 12.48470217 r_p_dash 46.33541329
weighted_Durbin_Watson 1.935055174 gof 1.021287597
range Run_Number
bkg @ 28.03056718 -1.2073219 6.333183325 3.194204838 1.879289311
LP_Factor( 0)
Specimen_Displacement(sd, -0.257524692)
Rp 217.5
Rs 217.5
Slit_Width(!rsw, 0.11967566)
Divergence(!fds, 0.6478928122)
Tube_Tails(!srcw, 0.1409275773,!z1, -3.136468684,!z2, 3.052708582,!fraction,
0.001156089397_LIMIT_MIN_1e-005)
axial_conv
filament_length 12
sample_length 15
receiving_slit_length 12
primary_soller_angle !soller 3.107907286
secondary_soller_angle =soller; : 3.107907286
axial_n_beta 30
User_Defined_Dependence_Convolution(lor_fwhm, 1/Cos(Th) , , 0.01249402572)
User_Defined_Dependence_Convolution(gauss_fwhm, 1/Cos(Th) , , 0.01259960982)
User_Defined_Dependence_Convolution(lor_fwhm, Tan(Th) , , 0.01783736219)
lam
ymin_on_ymax 0.001
la =1-a2-a3; : 0.6630149801 lo 1.540596 lh !lor 0.1677946017
la !a2 0.3354152679 lo 1.544443 lh =lor+0.125; : 0.2927946017
la !a3 0.001569751969_LIMIT_MIN_1e-005 lo 1.392 lh =lor; : 0.1677946017
'_____
>Loading of structures used for refinements
'_____
str
LVol_FWHM_CS_G_L( 1, 229.7566414, 0.89, 321.2017906,(csg),
1410.072299_LIMIT_MIN_0.3,(csl), 360.9008884)
r_bragg 2.403229492
phase_MAC 264.752421
phase_name "barium ferrite"

```

MVW(6528.774, 1927.839614, 0.006495399846)
prm wp_monoclinic =Get(weight_percent);
prm v_monoclinic =Get(cell_volume);
space_group P121/c1
scale =sc_monoclinic;
Phase_LAC_1_on_cm(1488.846996)
Phase_Density_g_on_cm3(5.623544408)
a = a_monoclinic;
b = b_monoclinic;
c = c_monoclinic;
be =be_monoclinic;' min =98.9; max =99.1;
site Ba1 num_posns 4 x 0.0546 y 0.3517 z 0.1145 occ Ba+2 1 beq =beq; : -0.0501627404
site Ba2 num_posns 4 x 0.25 y 0.6141 z 0.3283 occ Ba+2 1 beq =beq; : -0.0501627404
site Ba3 num_posns 4 x 0.1431 y 0.1304 z 0.3215 occ Ba+2 1 beq =beq; : -0.0501627404
site Ba4 num_posns 4 x 0.3257 y 0.6328 z 0.0379 occ Ba+2 1 beq =beq; : -0.0501627404
site Ba5 num_posns 4 x 0.0547 y 0.6176 z 0.6001 occ Ba+2 1 beq =beq; : -0.0501627404
site Ba6 num_posns 4 x 0.5603 y 0.3549 z 0.2558 occ Ba+2 1 beq =beq; : -0.0501627404
site Ba7 num_posns 4 x 0.3544 y 0.1102 z 0.0364 occ Ba+2 1 beq =beq; : -0.0501627404
site Fe1 num_posns 4 x 0.5249 y 0.3531 z 0.1038 occ Fe+3 1 beq =beq; : -0.0501627404
site Fe2 num_posns 4 x 0.3848 y 0.5816 z 0.186 occ Fe+3 1 beq =beq; : -0.0501627404
site Fe3 num_posns 4 x 0.062 y 0.3996 z 0.2595 occ Fe+3 1 beq =beq; : -0.0501627404
site Fe4 num_posns 4 x 0.1739 y 0.1525 z 0.4707 occ Fe+3 1 beq =beq; : -0.0501627404
site Fe5 num_posns 4 x 0.4359 y 0.3817 z 0.3988 occ Fe+3 1 beq =beq; : -0.0501627404
site Fe6 num_posns 4 x 0.2707 y 0.1045 z 0.1746 occ Fe+3 1 beq =beq; : -0.0501627404
site Fe7 num_posns 4 x 0.1458 y 0.6217 z 0.4644 occ Fe+3 1 beq =beq; : -0.0501627404
site O1 num_posns 2 x 0 y 0 z 0 occ O-2 1 beq =beq; : -0.0501627404
site O2 num_posns 4 x 0.2972 y 0.7097 z 0.1485 occ O-2 1 beq =beq; : -0.0501627404
site O3 num_posns 4 x -0.0628 y 0.277 z 0.2271 occ O-2 1 beq =beq; : -0.0501627404
site O4 num_posns 4 x 0.0382 y 0.0449 z 0.4273 occ O-2 1 beq =beq; : -0.0501627404
site O5 num_posns 4 x 0.008 y 0.2474 z 0.0021 occ O-2 1 beq =beq; : -0.0501627404
site O6 num_posns 4 x 0.2954 y 0.5 z 0.4297 occ O-2 1 beq =beq; : -0.0501627404
site O7 num_posns 4 x 0.7133 y 0.2597 z 0.0766 occ O-2 1 beq =beq; : -0.0501627404
site O8 num_posns 4 x 0.0559 y 0.1195 z 0.1079 occ O-2 1 beq =beq; : -0.0501627404
site O9 num_posns 4 x 0.406 y -0.0138 z 0.1436 occ O-2 1 beq =beq; : -0.0501627404
site O10 num_posns 4 x 0.4063 y 0.2443 z 0.147 occ O-2 1 beq =beq; : -0.0501627404
site O11 num_posns 4 x 0.1173 y 0.0036 z 0.2168 occ O-2 1 beq =beq; : -0.0501627404
site O12 num_posns 4 x 0.45 y 0.1263 z 0.2497 occ O-2 1 beq =beq; : -0.0501627404
site O13 num_posns 4 x 0.1944 y 0.4907 z 0.211 occ O-2 1 beq =beq; : -0.0501627404

site O14 num_posns 4 x 0.5416 y 0.4917 z 0.1449 occ O-2 1 beq =beq; : -0.0501627404
site O15 num_posns 4 x 0.3115 y 0.2406 z 0.4261 occ O-2 1 beq =beq; : -0.0501627404
site O16 num_posns 4 x 0.3596 y 0.3923 z 0.0364 occ O-2 1 beq =beq; : -0.0501627404
site O17 num_posns 4 x 0.2515 y 0.3583 z 0.3225 occ O-2 1 beq =beq; : -0.0501627404
site O18 num_posns 4 x 0.653 y 0.3669 z 0.4636 occ O-2 1 beq =beq; : -0.0501627404

str

LVol_FWHM_CS_G_L(1, 229.7566414, 0.89, 321.2017906,(csg),
1410.072299_LIMIT_MIN_0.3,(csl), 360.9008884)

r_bragg 1.142321915

phase_MAC 231.2330478

phase_name "BFOF"

MVW(269.2919239, 68.26612365, 0.0004985955391)

prm wp_cubic=Get(weight_percent);

prm v_cubic =Get(cell_volume);

space_group Pm-3m

scale = sc_cubic;

Phase_LAC_1_on_cm(1514.667767)

Phase_Density_g_on_cm3(6.550394856)

Cubic(=a_cubic;)

site O num_posns 3 x 0.5 y 0.5 z 0 occ O-2 o_O2 0.9921875307_LIMIT_MIN_0.5 min
=0.5; max =1; beq =beq; : -0.0501627404

site Ba num_posns 1 x 0 y 0 z 0 occ Ba+2 1 beq =beq; : -0.0501627404

site Fe num_posns 1 x 0.5 y 0.5 z 0.5 occ Fe+3 1 beq =beq; : -0.0501627404

site F num_posns 3 occ F-1 =1-o_O2; : 0.007812469281 min =0; max =0.5; beq =beq; :
-0.0501627404 x 0.5 y 0.5 z 0

str

LVol_FWHM_CS_G_L(1, 229.7566414, 0.89, 321.2017906,(csg),
1410.072299_LIMIT_MIN_0.3,(csl), 360.9008884)

r_bragg 2.533414295

phase_MAC 260.9463226

phase_name "barium iron oxide fluoride"

MVW(1421.020406, 410.5826738, 0.00263944218)

prm wp_oxyfluorid=Get(weight_percent);

prm v_oxyfluorid =Get(cell_volume);

space_group P121/m1

scale =sc_oxyfluorid;

Phase_LAC_1_on_cm(1499.685771)
Phase_Density_g_on_cm3(5.747104445)
a = a_oxyfluorid;
b =b_oxyfluorid;
c =c_oxyfluorid;
be =be_oxyfluorid;
site Ba1 num_posns 2 x 0.2615 y 0.25 z -0.0223 occ Ba+2 1 beq =beq; : -0.0501627404
site Ba2 num_posns 2 x 0.9129 y 0.25 z 0.7089 occ Ba+2 1 beq =beq; : -0.0501627404
site Ba3 num_posns 2 x 0.5713 y 0.25 z 0.341 occ Ba+2 1 beq =beq; : -0.0501627404
site Fe1 num_posns 2 x 0.2602 y 0.25 z 0.4961 occ Fe+3 1 beq =beq; : -0.0501627404
site Fe2 num_posns 2 x 0.8823 y 0.25 z 0.2302 occ Fe+3 1 beq =beq; : -0.0501627404
site Fe3 num_posns 2 x 0.606 y 0.25 z 0.8474 occ Fe+3 1 beq =beq; : -0.0501627404
site O1 num_posns 2 x 0.769 y 0.25 z 0.028 occ O-2 0.875 beq =beq; : -0.0501627404
site O2 num_posns 2 x 0.5 y 0 z 0 occ O-2 0.875 beq =beq; : -0.0501627404
site O3 num_posns 2 x 0.405 y 0.25 z 0.655 occ O-2 0.875 beq =beq; : -0.0501627404
site O4 num_posns 2 x 0.028 y 0.25 z 0.129 occ O-2 0.875 beq =beq; : -0.0501627404
site O5 num_posns 4 x 0.673 y 0.023 z 0.689 occ O-2 0.875 beq =beq; : -0.0501627404
site O6 num_posns 4 x 0.842 y -0.014 z 0.355 occ O-2 0.875 beq =beq; : -0.0501627404
site F1 num_posns 2 x 0.769 y 0.25 z 0.028 occ F-1 0.125 beq =beq; : -0.0501627404
site F2 num_posns 2 x 0.5 y 0 z 0 occ F-1 0.125 beq =beq; : -0.0501627404
site F3 num_posns 2 x 0.405 y 0.25 z 0.655 occ F-1 0.125 beq =beq; : -0.0501627404
site F4 num_posns 2 x 0.028 y 0.25 z 0.129 occ F-1 0.125 beq =beq; : -0.0501627404
site F5 num_posns 4 x 0.673 y 0.023 z 0.689 occ F-1 0.125 beq =beq; : -0.0501627404
site F6 num_posns 4 x 0.842 y -0.014 z 0.355 occ F-1 0.125 beq =beq; : -0.0501627404

C. Atomic positions in BaFeO_{2.5} and BaFeO_{2.333}F_{0.333}/BaFeO_{2.667} for Sec. 3.5.2

Table C.1.: Atomic parameters of BaFeO_{2.333}F_{0.333} [12] used for Fig. 3.54 plus the anion vacancies.

Atom	Wyck.	Site	x/a	y/b	z/c
Ba1	2e	m	0.2615(2)	1/4	-0.0223(3)
Ba2	2e	m	0.9129(2)	1/4	0.7089(3)
Ba3	2e	m	0.5713(2)	1/4	0.3410(4)
Fe1	2e	m	0.2602(5)	1/4	0.4961(7)
Fe2	2e	m	0.8823(5)	1/4	0.2302(6)
Fe3	2e	m	0.6060(5)	1/4	0.8474(7)
O1/F1	2e	m	0.769(1)	1/4	0.028(2)
O2/F2	2b	-1	1/2	0	0
O3/F3	2e	m	0.405(2)	1/4	0.655(2)
O4/F4	2e	m	0.028(1)	1/4	0.129(2)
O5/F5	4f	1	0.673(1)	0.023(2)	0.689(2)
O6/F6	4f	1	0.842(1)	-0.014(2)	0.355(1)
Vac.	2a	-1	0	0	0
Vac. _{ideal}	2e	m	1/12	1/4	1/3

Table C.2.: Atomic parameters of BaFeO_{2.5} [33] used for Fig. 3.53 plus the oxygen vacancies.

Atom	Wyck.	Site	x/a	y/b	z/c
Ba1	4e	1	0.0546(9)	0.3517(6)	0.1145(3)
Ba2	4e	1	0.250(1)	0.6141(6)	0.3283(3)
Ba3	4e	1	0.1431(9)	0.1304(6)	0.3215(3)
Ba4	4e	1	0.3257(10)	0.6328(5)	0.0379(4)
Ba5	4e	1	0.0547(11)	0.6176(7)	0.6001(4)
Ba6	4e	1	0.5603(10)	0.3549(6)	0.2558(3)
Ba7	4e	1	0.3544(13)	0.1102(5)	0.0364(4)
Fe1	4e	1	0.5249(8)	0.3531(5)	0.1038(3)
Fe2	4e	1	0.3848(8)	0.5816(4)	0.1860(3)
Fe3	4e	1	0.0620(9)	0.3996(5)	0.2595(3)
Fe4	4e	1	0.1739(10)	0.1525(5)	0.4707(3)
Fe5	4e	1	0.4359(9)	0.3817(5)	0.3988(3)
Fe6	4e	1	0.2707(9)	0.1045(5)	0.1746(3)
Fe7	4e	1	0.1458(11)	0.6217(4)	0.4644(4)
O1	2a	-1	0	0	0
O2	4e	1	0.2972(13)	0.7097(8)	0.1485(4)
O3	4e	1	-0.0628(13)	0.2770(8)	0.2271(4)
O4	4e	1	0.0382(14)	0.0449(7)	0.4273(4)
O5	4e	1	0.0080(14)	0.2474(9)	0.0021(5)
O6	4e	1	0.2954(15)	0.5000(9)	0.4297(5)
O7	4e	1	0.7133(14)	0.2597(9)	0.0766(4)
O8	4e	1	0.0559(15)	0.1195(10)	0.1079(5)
O9	4e	1	0.4060(15)	-0.0138(9)	0.1436(5)
O10	4e	1	0.4063(13)	0.2443(8)	0.1470(5)
O11	4e	1	0.1173(15)	0.0036(10)	0.2168(5)
O12	4e	1	0.4500(14)	0.1263(9)	0.2497(5)
O13	4e	1	0.1944(16)	0.4907(10)	0.2110(5)
O14	4e	1	0.5416(13)	0.4917(8)	0.1449(4)
O15	4e	1	0.3115(14)	0.2406(10)	0.4261(5)
O16	4e	1	0.3596(16)	0.3923(7)	0.0364(6)
O17	4e	1	0.2515(16)	0.3583(8)	0.3225(5)
O18	4e	1	0.653(2)	0.3669(7)	0.4636(6)
Vac.1	4e	1	0.21400	0.62500	0.82100
Vac.2	4e	1	0.14300	0.75000	0.21400
Vac.3	4e	1	0.07100	0.87500	0.60700
Vac.4	2c	-1	0	1/2	0

D. EIS data for Sec. 3.5.3

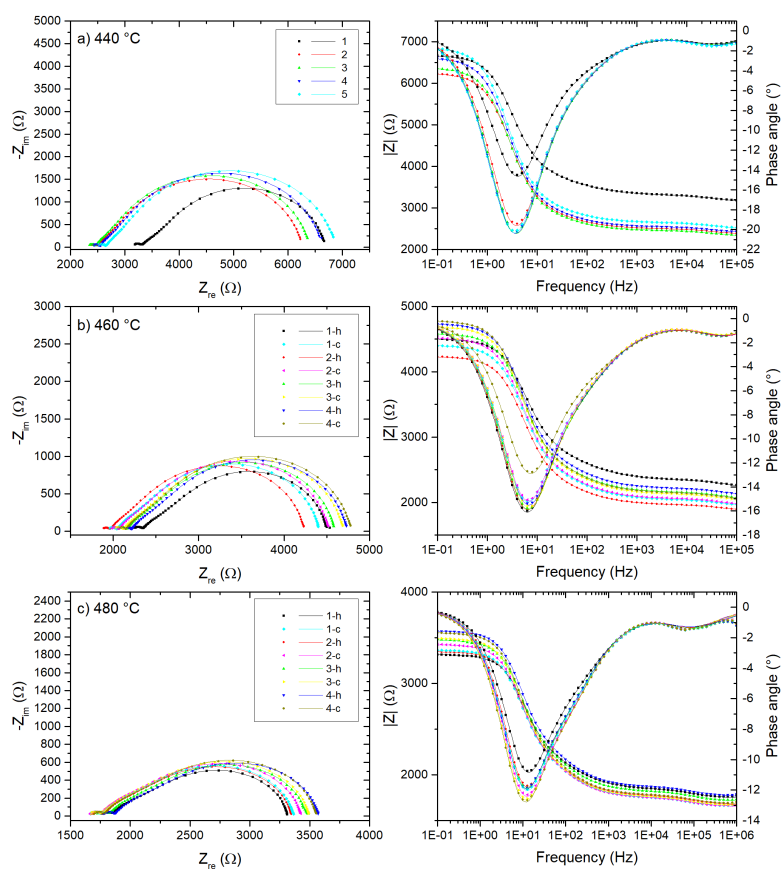


Figure D.1.: Electrical impedance spectra (Nyquist and Bode plots) of BaFeO_{2.667} symmetrical films at the temperatures a) 440 °C, b) 460 °C and c) 480 °C. The number denominates the cycle, while h and c indicate heating and cooling, respectively.

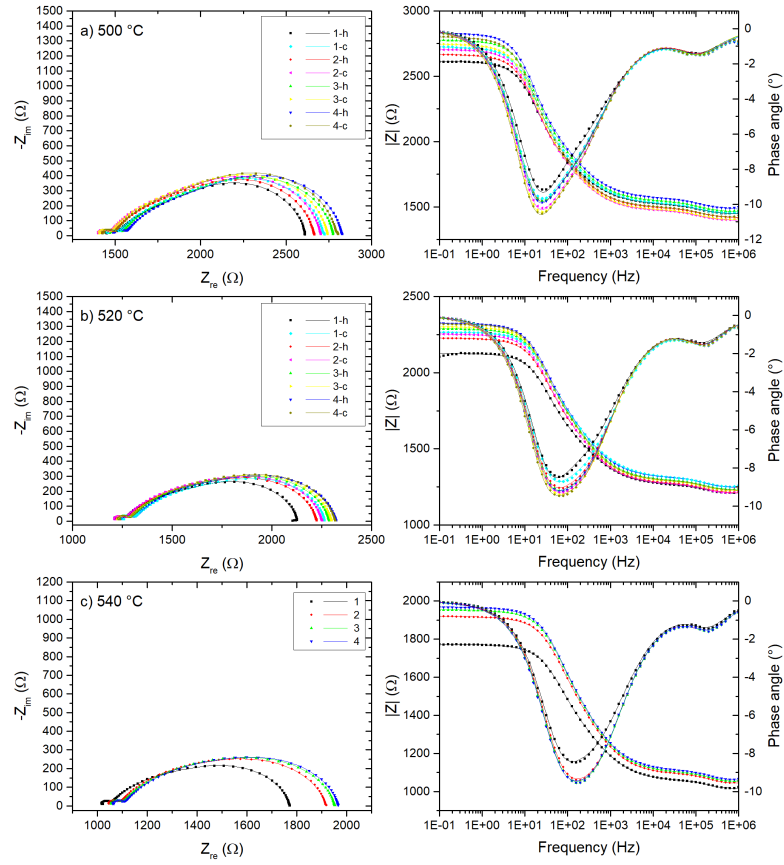


Figure D.2.: Electrical impedance spectra (Nyquist and Bode plots) of BaFeO_{2.667} symmetrical films at the temperatures a) 500 °C, b) 520 °C and c) 540 °C. The number denominates the cycle, while h and c indicate heating and cooling, respectively.